Propriétés spectrales et optiques des Matériaux corrélés.

Jan Martin Tomczak

▶ To cite this version:

Jan Martin Tomczak. Propriétés spectrales et optiques des Matériaux corrélés.. Physique [physics]. Ecole Polytechnique X, 2007. Français. NNT : . pastel-00003163

HAL Id: pastel-00003163
https://pastel.hal.science/pastel-00003163

Submitted on 23 Jul 2010

Spectral and Optical Properties
of
Correlated Materials

Jan M. Tomczak

2007

Centre de Physique Théorique
Ecole Polytechnique
France

The major concern of this thesis is the calculation and interpretation of spectral and optical properties of correlated materials within electronic structure techniques using many-body approaches.

With sizable electron correlations at present, the many-body problem of condensed matter physics is no longer, even on a qualitative level, describable by standard band-structure methods that treat the system under consideration on the basis of an effective one-particle problem. Today's state-of-the-art approaches therefore combine genuine many-body techniques with established band-structure methods, to treat correlation effects of a subset of orbitals in a more accurate fashion.

A powerful many-body approach is the dynamical mean-field theory (DMFT), which has, in particular, enlightened our understanding of the Mott transition. With its realistic extension, the combination LDA+DMFT with density functional theory (DFT) in the local density approximation (LDA), the calculation of the electronic excitation spectrum of previously untreatable systems has become possible. To put our work into context, the first part of this thesis gives a general introduction to the field of modern electronic structure calculations.

Though LDA+DMFT has led to considerable insight into correlated materials, the number of experimental observables that are calculable within the scheme is until now rather restricted, and most works have limited themselves to the local spectral function, which is in principle accessed by (inverse) photoemission spectroscopy.

In the second part of the thesis we extend the variety of physcial quantities that can actually be calculated, by introducing an analytical continuation scheme that will enable us to derive the real-frequency LDA+DMFT self-energy from imaginary time quantum Monte Carlo calculations in the most general (cluster) context. As we will see, the self-energy itself already renders the interpretation of numerical DMFT data more transparent. Within some approximation, it furthermore allows for the calculation of linear response functions. In this vein, the second emphasis of the technical development in this thesis is on optical properties, in particular the calculation of the optical conductivity for realistic LDA+DMFT calculations. For the latter we have devised a formalism that relies on a formulation of the solid in terms of a localized basis set. The commonly used Peierls substitution approach for the coupling of the light field to the solid is generalized to the case of multi-atomic unit cells. This will result in an approach of great versatility, since the entire formulation is independent of the underlying electronic structure method.

The third part of the thesis is devoted to applying the newly developed tools to actual compounds of physical interest.

In the case of vanadium dioxide, VO_2, we focus on the nature of the insulating low temperature phase and its degree of correlation with respect to the metallic phase. Indeed we find that while the latter is characterized by strong signatures of correlations, the former is, as concerns its excitation spectrum, close to a description within a one-particle approach, that we will define. Our picture of the insulating phase emerges as a "many-body Peierls" scenario, in which correlations are at the origin of the insulating behaviour,

yet, without causing appreciable lifetime effects in spectral properties. In a full-orbital setup that goes beyond the downfolded description, we calculate the optical conductivity of both, the metallic and the insulating phase, and find our theoretical result in satisfactory agreement with recent experiments. From the conductivity we, in particular, deduce the colour of the compound.

A compound that has been considered as a textbook example of a Mott-Hubbard transition is vanadium sesquioxide V_2O_3. In our analysis, we find a correlation enhanced crystal-field splitting at the origin of its metal to insulator transition that occurs upon Cr-doping. Besides making predictions for angle-resolved photoemission experiments, we further evidence an orbital selectivity in the quasi-particle coherence temperature, which will in particular allow for an understanding of the temperature dependence of recent optical measurements. Indeed, all qualitative features of the experimental data are reproduced, which thus allow for an interpretation from the point of view of our electronic structure calculation.

Finally, we study the optical properties of the light rare-earth sesquioxide series RE_2O_3 (RE=Ce, Pr, Nd, Pm). These compounds are wide-gap Mott insulators that are not well described in density functional theory, due to the localized character of the RE4f orbitals. In our analysis, we, in particular, track the influence of these localized 4f orbitals as a function of the filling along the rare-earth series and find quantitative agreement for the evolution of the optical gap and a reasonable overall shape of the optical conductivity.

Paris, July 2007

Contents

Part I

Introduction

Chapter 1

Correlated Materials

A   Physics of strongly correlated materials

Ideal solids are composed of a regular array of charged nuclei or motifs thereof. When neglecting dynamic lattice deviations, which are an important subject on their own, the Hamiltonian of the system and the translation operator have common eigenstates, which leads to the very foundation of solid state physics, namely Bloch's theorem.

That solids are stable with respect to their isolated constituencies is owing to the fact that the bonding lowers the free energy of the system. However not all electrons partake in the bonding. Electrons that are tightly bound to the ionic cores are indeed more akin to atomic-like orbitals, and only modify the periodic potential seen by all the other electrons. It is the latter, called valence electrons, that are preponderantly determining the electronic, magnetic, optical and thermal properties of the system.

Within the independent particle picture, the periodicity of the lattice results into an excitation spectrum that is discrete and exhibits allowed and forbidden regions. This eventuates in the formation of a band-structure. According to the Pauli principle, each "band" can accommodate two electrons with opposite spins. The energy up to which the bands are filled is called the Fermi level. Herewith one may distinguish very roughly two different kinds of solids : In insulators, the Fermi level falls into a forbidden region, which needs to be overcome when exciting the system. In a metal, the density of states at the Fermi level is finite, accounting for the itinerant behaviour of the charge carriers.

However, nature is considerably more complicated than the independent particle picture. Yet, in case of only moderate correlations, Landau theory allows for the casting of interaction effects of low-energy excitation states into particle-like entities called quasi-particles, which are again independent. These quasi-particles are only accounting for the coherent part of the spectrum, the incoherent spectral weight is intrinsically beyond Landau theory of Fermi liquids.

With considerable correlations at present, even the quasi-particle concept breaks down. All in all, correlations are at the origin of a very rich panoply of phenomena that are beyond any one-particle theory. This is in particular true for transition metals, their oxides and rare earth or actinide compounds, since their d and f orbitals are closer to the

nucleus than other orbitals. This is especially verified for the 3d and 4f orbitals, as their orthogonality to other orbitals can be assured by the angular part of their wavefunctions, since they are the lowest orbitals for the given angular quantum number. Therewith these orbitals do not behave like regular bond forming orbitals. Yet, they are not completely localized either. Indeed they struggle between localization and itineracy.

A signature of this is already found in crystal properties. Indeed when filling a shell of electrons that do not contribute to the bonding, the unit-cell volume does not change significantly. This is e.g. the case for the Lanthanide series (see however Chapter 7 for what is called the lanthanide contraction). When following the transition metal series Lu, Hf–Au, on the contrary, the volume strongly depends of the filling of the 5d shell, and is roughly parabolic with a minimum at about half-filling, which can be understood from a consideration, due to Friedel, in which a flat density of states with low lying bonding and high lying anti-bonding states gets gradually filled.

A high degree of localization is concomitant with two characteristics. On the one hand, the hopping elements between different atoms, given by the matrix elements of the kinetic operator will be small, resulting in narrow bands in the one-particle picture. Moreover, the localization yields a large Coloumb repulsion for electrons of the same atom. When integrating out uncorrelated orbitals and limiting the interactions of the correlated ones to the local contributions, one ends up with a description of the solid in terms of the Hubbard model, as will be derived in the next section.

This model, though appearing simple at first sight, contains highly non-trivial physics. The Hubbard model manifestly describes the struggle between itineracy and localization of the charge carriers : While the kinetic part of the Hubbard model is diagonal in momentum space, corresponding to the itinerant character of charge carriers, the local Coulomb interaction term is diagonal in real-space, reminiscent of atomic-like physics.

Herewith, the many-body implications allow for the realization of insulating behaviour beyond the band-insulator, namely the Mott insulator. The concept of the latter is actually quite simple and does not require the quantum-mechanical machinery needed to explain a band-insulator : Beyond a certain ratio of interaction over bandwidth, the Coulomb repulsion prevails upon the itineracy of the charge carriers and localizes them on their atomic sites. As a consequence, an insulator can be stabilized for an integer occupation. This is called the Mott phenomenon. Apart from the completely filled and empty orbital, band-theory would always predict metallic behaviour in these cases.

As a matter of fact this concept is realized in actual compounds. Prominent examples can be found among transition metal oxides, rare-earth compounds and actinides. Some examples of materials that exhibit a behaviour that is beyond standard electronic structure methods are :

- The d^1 systems $LaTiO_3$ or $YTiO_3$ that are metals within band-theory, while photoemission experiments clearly evidence a charge gap. Indeed these systems are Mott insulators, and are well described in modern many-body theories [Pavarini *et al.* (2004)].

- Other transition metal oxides that exhibit a metal-insulator transition, such as VO_2, V_2O_3. See Part III.

- δ-Plutonium, in which the unit-cell volume is underestimated by about 30% in band-structure methods. Also this can be improved on with the many-body techniques that we introduce below [Savrasov *et al.* (2001)].

B   The Solid in a localized basis : The Hubbard model as caricature

The Hamiltonian for the electronic degrees of freedom of a solid can be written as

$$\mathbf{H} \;=\; \mathbf{H}_0 + \mathbf{H}_{int} \tag{1.1}$$

where we have separated into the one-particle part

$$\mathbf{H}_0 \;=\; \sum_\sigma \int \mathrm{d}^3\mathrm{r} \; \Psi_\sigma^\dagger(\mathbf{r}) \left[-\frac{\hbar^2}{2m}\Delta + V^{ion}(\mathbf{r}) \right] \Psi_\sigma(\mathbf{r}) \tag{1.2}$$

that contains the kinetic energy as well as the ionic potential. When denoting the electron density by $\mathbf{n}_\sigma(\mathbf{r}) = \Psi_\sigma^\dagger(\mathbf{r})\Psi_\sigma(\mathbf{r})$, the interaction part of the Hamiltonian reads

$$\mathbf{H}_{int} \;=\; \frac{1}{2}\sum_{\sigma\sigma'} \int \mathrm{d}^3\mathrm{r} \int \mathrm{d}^3\mathrm{r}' \; n_\sigma(\mathbf{r})V^{ee}(\mathbf{r},\mathbf{r}')n_{\sigma'}(\mathbf{r}') \tag{1.3}$$

which we have restricted to two-body interactions only. As a matter of fact, the influence of this term on a mean-field level, i.e. by decoupling the two-particle term into $AB \rightarrow A\langle B\rangle + \langle A\rangle B - \langle AB\rangle$, can be cast into a local effective one-particle potential $v^{eff}[\rho](\mathbf{r})$, that can be absorbed into the one-particle part of the Hamiltonian. Therewith, however, the effective potential is a functional of the ground state density $\rho(\mathbf{r}) = \sum_\sigma \langle n_\sigma(\mathbf{r})\rangle_{\mathbf{H}}$, and has thus to be determined in a self-consistent manner, as is the usual case for mean-field type theories. As we shall see below in Section A, Chapter 2, that this is closely related to the concept of density functional theory (DFT). With this Equation (1.2) becomes

$$\mathbf{H}_0 \;=\; \sum_\sigma \int \mathrm{d}^3\mathrm{r} \; \Psi_\sigma^\dagger(\mathbf{r}) \left[-\frac{\hbar^2}{2m}\Delta + V^{ion}(\mathbf{r}) + v^{eff}[\rho](\mathbf{r}) \right] \Psi_\sigma(\mathbf{r}) \tag{1.4}$$

the residual interactions of Equation (1.3) are (see e.g. [Auerbach(1994)])

$$n_\sigma(\mathbf{r})\widetilde{V}^{ee}(\mathbf{r},\mathbf{r}')n_{\sigma'}(\mathbf{r}') =$$
$$n_\sigma(\mathbf{r})V^{ee}(\mathbf{r},\mathbf{r}')n_{\sigma'}(\mathbf{r}') - \left(v^{eff}[\rho](\mathbf{r})\rho(\mathbf{r}') + v^{eff}[\rho](\mathbf{r}')\rho(\mathbf{r}) \right)/N_e \tag{1.5}$$

This remaining term is a true two-particle interaction. Throughout this manuscript we shall refer to "correlation effects" as being caused by interaction influences that are beyond any such mean-field treatment. This thus constitutes a definition of "correlations". Band theory methods try to optimize the effective potential v^{eff}, but completely ignore the remaining interaction $\widetilde{V}^{ee}$.

The above formulas are defined in the continuum. We chose to develop the field operators into a localized "Wannier"-like basis $\chi_{\mathbf{R}L}(\mathbf{r})$:

$$\Psi_\sigma(\mathbf{r}) = \sum_{\mathbf{R},L} \chi_{\mathbf{R}L}(\mathbf{r}) \mathbf{c}_{\mathbf{R}L\sigma} \tag{1.6}$$

Here, L= (n, l, m, γ) is a combined index denoting orbital (n, l, m) of atom γ. The real space positions of the atoms are thus given by the sum of the unit cell coordinate $\mathbf{R}$ and the displacement within the unit cell ρ_γ[1]. With this, the above Equation (1.2), Equation (1.3), can equivalently be written :

$$\mathbf{H}_0 = \sum_{\mathbf{R}\mathbf{R}',LL',\sigma} t_{\mathbf{R}\mathbf{R}'}^{LL'} \mathbf{c}_{\mathbf{R}L\sigma}^\dagger \mathbf{c}_{\mathbf{R}'L'\sigma} \tag{1.7}$$

$$\mathbf{H}_{int} = \frac{1}{2} \sum_{\mathbf{R}\mathbf{R}',\mathbf{T}\mathbf{T}'} \sum_{LL',MM'} \sum_{\sigma\sigma'} U_{\mathbf{R}\mathbf{R}'\mathbf{T}\mathbf{T}'}^{LL'MM'} \mathbf{c}_{\mathbf{R}L\sigma}^\dagger \mathbf{c}_{\mathbf{R}'L'\sigma} \mathbf{c}_{\mathbf{T}M\sigma'}^\dagger \mathbf{c}_{\mathbf{T}'M'\sigma'} \tag{1.8}$$

where we have defined the real-space hopping amplitudes

$$t_{\mathbf{R}\mathbf{R}'}^{LL'} = \int \mathrm{d}^3\mathrm{r}\, \chi_{\mathbf{R}L}^*(\mathbf{r}) \left[-\frac{\hbar^2}{2m}\Delta + V^{ion}(\mathbf{r}) + v^{eff}[\rho](\mathbf{r}) \right] \chi_{\mathbf{R}'L'}(\mathbf{r}) \tag{1.9}$$

and the interaction parameters

$$U_{\mathbf{R}\mathbf{R}'\mathbf{T}\mathbf{T}'}^{LL'MM'} = \int \mathrm{d}^3\mathrm{r} \int \mathrm{d}^3\mathrm{r}'\, \chi_{\mathbf{R}L}^*(\mathbf{r}) \chi_{\mathbf{T}M}^*(\mathbf{r}') V^{ee}(\mathbf{r},\mathbf{r}') \chi_{\mathbf{T}'M'}(\mathbf{r}') \chi_{\mathbf{R}'L'}(\mathbf{r}) \tag{1.10}$$

In state of the art methods for strongly correlated materials[2], the one particle part of the Hamiltonian is provided by a band-structure calculation, which is assumed to reasonably take into account longer range interactions. Then the most important residual interactions, that are to be treated with a true many-body technique, are identified as the local ones. The above Coulomb interaction is not explicitly spin dependent. Yet the different possible symmetry combinations of the wavefunctions lead to an effective spin dependence, resulting in the well-known Hund's rule coupling. Thus, when constraining

---

[1]The choice of basis is of course arbitrary at this point, yet, as we shall see later on in Section C, Chapter 2, a basis with well-defined momentum is best suited for the dynamical mean-field approach, on which will rely most of the work in this thesis.

[2]anno 2007.

the interaction further to only density-density terms, the Hamiltonian of the system can be written as

$$
\mathbf{H} \;=\; \sum_{\mathbf{k},LL',\sigma} H_0^{LL'}(\mathbf{k})\mathbf{c}^{\dagger}_{\mathbf{k}L\sigma}\mathbf{c}_{\mathbf{k}L'\sigma} + \sum_{\mathbf{R},LL',\sigma\sigma'} U_{LL'}^{\sigma\sigma'}\mathbf{n}_{\mathbf{R}L\sigma}\mathbf{n}_{\mathbf{R}L'\sigma'}
\tag{1.11}
$$

which is nothing else but the multi-orbital generalization of the famous Hubbard model [Hubbard(1963), Gutzwiller(1963), Kanamori(1963)]. Derived from the continuum formulation of a solid, the latter now is a lattice model, in which electrons can hop from one discrete site to another, and subjected to a purely local Coulomb repulsion that sanctions double occupations. All continuous dependencies have been cast into the matrix elements that constitute the hopping amplitudes and the interaction parameters.

In the last formula we have further Fourier transformed the kinetic part of the Hamiltonian. This clearly shows the dilemma of the model : While the one-particle part is diagonal in momentum space, the interaction is diagonal in real space. Therewith the model has so far resisted any attempt of finding an exact solution beyond the special case of one dimension.

Chapter 2

Theories for the Many-Body Problem

In (quantum) many-body physics exact results are scarce and limited to very special cases. While being able to write down the Schrödinger equation of an arbitrary system, the determination of even its stationary solution is, in general, beyond the scope of any analytical or computational method. While making statements about small finite systems might still be possible, the exponential growth of degrees of freedoms with the system size, quickly makes any computational approach, led alone by-hand calculations, unfeasible. Thus, while often being capable to conceive a complete set of equations that governs the system under consideration, modern physics entirely depends on finding intelligent ways to make controllable approximations to it, such as to be able to extract the essence of the ongoing processes. It is indeed the spirit of physics to seek simplified models, from which it is possible to extract selected phenomena that are inherent to the overwhelming diversity of nature.

A paramount concept in this vein is the introduction of a *reference system*, which is both, simple enough to be resolved, yet sufficiently sophisticated to exhibit a close resemblance with the initial problem under the view point one is interested in. More well controlled approaches, in the sense that they allow for an assessment of their reliability, have as a general strategy to find a *small parameter* in the full problem. Then, the *reference system* is identified as the original problem with the parameter being set to zero. Provided the reference system proves solvable, a *perturbative expansion* in the small parameter may be endeavoured.

In this thesis we will employ three approaches to the many-body problem :

Density functional theory (DFT) within the local density approximation (LDA). The Hohenberg-Kohn theorem of density functional theory (DFT) allows for the exact mapping of the many-body problem onto an effective one-particle reference system which includes a specific potential. The latter, called the Kohn-Sham potential, is constructed such as to reproduce the local density of the true system. Herewith all ground state observables become accessible. Since however, the Kohn-Sham potential is unknown, one is obliged to make further approximations. In the local density approximation (LDA), for example, the potential is taken from a homogeneous electron gas of the same density. This will be detailed in Section A.

Perturbation theory and the GW approximation. In the case of the Hubbard model, Equation (1.11), two perturbative approaches are obvious : One can start from the atomic limit ($t = 0$) and expand in the hopping amplitude t, which is called a strong coupling approach. In a weak coupling expansion, on the other hand, the reference system corresponds to the non-interacting limit ($U = 0$), and the Coulomb interaction U is treated as a perturbation. By Dyson's equation this eventuates in the well-known diagrammatic expansion of the electron self-energy. The GW approximation that we will use for some of our calculations, and which we introduce in Section B, is such a weak coupling expansion, albeit in a slightly modified interaction parameter as will be explained below.

Both perturbative techniques of course have their merits and flaws. Important phenomena in condensed matter physics cannot be elucidated with either of the two precedent expansions. Outstanding examples are (high T_c) superconductivity and the Kondo effect. Both require a methodology that is non-perturbative in the interaction parameters.

Dynamical mean field theory (DMFT). As a matter of fact, beyond the obvious parameters of the kinetic and interaction energies there is another potentially small parameter : The inverse of the spatial dimension d, or the inverse lattice coordination. Indeed, zeroth order expansions in $1/d$ lead to the well-known concept of Mean Field Theories (MFT). There, local variables are replaced by their average values ("mean field"). This average has to be determined in a self-consistent manner, such that it produces the best local representation of the full problem. Intuitively, this approach becomes better, with a growing number of interacting particles, since by the central limit theorem, fluctuations around the mean values decrease. In *dynamical* mean field theory, as discussed in Section C, the reference system, in the above sense, is an atom that is coupled to a self-consistently obtained energy-dependent medium. In other words, the reference is an Anderson impurity model [Anderson(1961)] with an effective hybridization function. The merit of mean field theories, in general, is that they are non-perturbative in the interaction strength. They can thus be applied within the entire phase diagram of a model with somewhat equal justification[1].

A   Density Functional Theory (DFT)

We discussed in Section B, Chapter 1 that some parts of the many-body interactions, namely their mean-field approximation, can be cast into an effective one-particle potential $v^{eff}[\rho](\mathbf{r})$. The addition "effective" refers to the fact that the potential itself depends on the ground state density ρ_{gs}, and has thus to be determined self-consistently. Yet, beyond this potential, true many-body interactions persist.

We shall see that within the Kohn-Sham approach to Hohenberg-Kohn density functional theory, as far as the calculation of *ground state properties* is concerned, there exists

---

[1]Yet, we note that in the vicinity of a phase transition, such as the Mott-Hubbard one, non-local fluctuations become important. In this vein the non-perturbative single site dynamical mean-field theory is a less good approximation in the transition region than it is deep within the Fermi liquid or the Mott insulating regime.

an effective one-particle potential such that the *entire* many-body problem becomes separable, and one ends up with the task of solving one-particle Schrödinger equations subject to a self-consistency condition for the effective potential.

This enormous simplification of the many-body problem, though being in principle rigorous for the ground state, requires certain approximations in actual calculations. Still, for numerous classes of compounds this scheme proved reliable and ever since enjoys a great popularity. Yet, this thesis would be futile if band-structure methods were perfect. For reviews on DFT see e.g. [Jones and Gunnarsson(1989), Dreizler and Gross(1990)].

A.a   The Hohenberg-Kohn theorem

In a nutshell, the Hohenberg-Kohn theorem [Hohenberg and Kohn(1964)] states

- The existence of a one-to-one mapping between a given external potential v^{ext} and the ground state density ρ_{gs}. When considering the ground state energy as a functional of the external potential, this can be viewed as a Legendre transform [Lieb(1983)].

- The fact that for any observable $\mathcal{O}$, the ground state expectation value is a functional of the ground state density only : $\langle \mathcal{O} \rangle_{gs} = \mathcal{F}_{\mathcal{O}}[\rho_{gs}]$
  This is quite akin to the Green's function formalism, in which the ground state *and* the excited state expectation value of any one-particle operator can be calculated from the knowledge of the one-particle Green's function.

- A variational principle for the ground state energy $E_{gs} = E[\rho_{gs}]$, namely that $E_{gs} < E[\rho]$ for all ρ. This follows from the Rayleigh-Ritz variational principle.

Though no miracles appear in the derivation, the apparent simplifications of the many-body problem are tremendous : For ground state properties *all* interactions[2] are equivalent to an effective one-particle potential. Density functional theory within its realm of ground state properties is *exact*.

The major catch to the above scheme is the following : First of all, the Hohenberg-Kohn theorem is non-constructive, since it proofs the existence of an effective potential, yet, gives no indication on how to calculate it. In practice one is forced to employ approximations. These approximations, one of which we will briefly mention in the next subsection, are not completely well-controlled and may lead to even qualitatively wrong results.

The Hohenberg-Kohn effective potential is unknown. A strategy to minimize the ignorance thereof is to take out parts of it that are known, in the same spirit as was done with the mean-field terms in Section B, Chapter 1. The hope is that this procedure renders the actual ignorance "smaller". In the work of [Hohenberg and Kohn(1964)], the energy functional of the ground state density was split into :

$$E_{gs}[\rho] \; = \; \langle P^2/2m \rangle_{gs} + \int \mathrm{d}^3\mathrm{r} \; v^{ext}(\mathbf{r})\rho(\mathbf{r}) + \frac{1}{2} \int \mathrm{d}^3\mathrm{r} \; \mathrm{d}^3\mathrm{r}' \; \frac{\rho(\mathbf{r})\rho(\mathbf{r}')}{|\mathbf{r} - \mathbf{r}'|} + E_{xc}[\rho] \quad (2.1)$$

---

[2]Not only the mean field-like ones

where the first part is the expectation value of the kinetic energy (of the many-body system), the second terms an external potential, the third the Hartree contribution to the interaction, and the fourth term, finally, defines the *exchange correlation energy* E_{xc} which is the unknown quantity of DFT.

A.b   The Kohn-Sham equations

So far, if one was to perform a DFT calculation, once an approximation for the exchange correlation energy is chosen, one would perform a variational computation of the ground state energy with respect to the density.

In [Kohn and Sham(1965)] was proposed an approach that leads a different calculation scheme, which, ever since, has enjoyed a great popularity. The idea to introduce a reference system of non-interacting nature and to minimize the lack of knowledge of the exchange-correlation energy. This procedure brings back into play the Schrödinger equation. Indeed, if we assume the existence of a *fictitious non-interacting system* that, subjected to an external potential v^{KS}, has the same ground state density as the interacting system, we may write the Equation (2.1) as :

$$E_{gs}[\rho] = \sum_i \langle \Phi_i | P^2/2m | \Phi_i \rangle + \int \mathrm{d}^3\mathrm{r}\, v^{ext}(\mathbf{r})\rho(\mathbf{r}) + \frac{1}{2} \int \mathrm{d}^3\mathrm{r}\, \mathrm{d}^3\mathrm{r}'\, \frac{\rho(\mathbf{r})\rho(\mathbf{r}')}{|\mathbf{r} - \mathbf{r}'|} + \widetilde{E}_{xc}[\rho] \tag{2.2}$$

where the $|\Phi_i\rangle$ is the ground state eigenfunctions of the *one-particle reference system* of particle i, and the difference in kinetic energy between the true and the fictitious system, i.e. the difference to the first term in Equation (2.1), has been cast into a redefined exchange-correlation energy $\widetilde{E}_{xc}$.

Since, by construction, the above energy functional is stationary with respect to the true ground state density, one can define the Kohn-Sham potential

$$v^{KS}[\rho](\mathbf{r}) = v^{ext}(\mathbf{r}) + \int \mathrm{d}^3\mathrm{r}'\, \frac{\rho(\mathbf{r}')}{|\mathbf{r} - \mathbf{r}'|} + v^{xc}[\rho](\mathbf{r}) \tag{2.3}$$

with the introduction of the exchange-correlation *potential*

$$v^{xc}[\rho](\mathbf{r}) = \frac{\delta \widetilde{E}_{xc}[\rho]}{\delta \rho(\mathbf{r})} \tag{2.4}$$

Herewith, as announced above, the many-body Schrödinger equation becomes separable and the problem reduces to finding solutions to the independent differential equations :

$$\left(-\frac{\hbar^2 \Delta}{2m} + v^{KS}[\rho](\mathbf{r}) \right) \Phi_i(\mathbf{r}) = \epsilon_i \Phi_i(\mathbf{r}) \tag{2.5}$$

Once a choice on the form of the exchange-correlation potential is made, these have to be solved self-consistently with the Kohn-Sham potential given by Equation (2.3), where the density is determined by $\rho(\mathbf{r}) = \sum_i |\Phi_i(\mathbf{r})|^2$.

In the end, what is this approach telling us about the many-body problem from the outset ? In the above sense, a reference system of decreased sophistication was introduced, tailored to retain the ground state density. Thus, as a matter of fact, the only thing that the fictitious one-particle problem and the many-body problem have in common is precisely their ground state density. Neither the spectrum of the operator given by the kinetic part plus the Kohn-Sham potential, nor the corresponding eigenstates do have any correspondence to the true problem. They are but *auxiliary quantities* devoid of physical meaning. Any procedure that identifies the Kohn-Sham spectrum with the excitations of the system, or uses the wavefunctions for further calculations, such as for the random-phase approximation used in the GW, see below, is not well-founded. Still, as we will mention later, this approach gives surprisingly good results, which is responsible for its great popularity.

A.c   Exchange-correlation potentials and the local density approximation (LDA)

The exact exchange-correlation potential being unknown, one has to find a reasonable approximation to it. The most commonly adapted approximation is the one of the *local density* :

$$E_{xc} \;\; = \;\; \int \mathrm{d}^3\mathbf{r} \; \rho(\mathbf{r})\epsilon_{xc}^{LDA}(\rho(\mathbf{r})) \tag{2.6}$$

where $\epsilon_{xc}^{LDA}(\rho(\mathbf{r}))$ is the exchange-correlation energy density of the homogeneous electron gas, which thus serves as a reference system, evaluated at the same density as the true system under consideration, *locally* evaluated at the position $\mathbf{r}$. Therewith, the energy density $\epsilon_{xc}^{LDA}[\rho](\mathbf{r})$, which in general will be a functional of the density becomes a mere function of it : $\epsilon_{xc}(\rho(\mathbf{r}))$. Even though this function is not known analytically, interpolation formulas based on Quantum Monte Carlo studies are available, which makes this approximation rather handy to use.

Several other approximations to the exchange-correlation potential are in existence, especially in quantum chemistry. Though some of these might give results slightly closer to experimental findings, their theoretical foundation is not completely rigorous.

A.d   Implementations of DFT – Basis sets

There exist numerous implementations of density functional theory. Beyond the different exchange-correlation potentials that one might choose from, the approaches differ in particular in the basis sets that are employed in the calculation. Here we shall only briefly

mention some aspects, geared to put into perspective the implementations that are suited for our concerns.

Correlation effects beyond the LDA involve in particular local Coulomb interactions in the fashion of the Hubbard model. In order to cast the realistic solid into a form like in Equation (1.11), a description in terms of a localized basis is needed.

A suitable concept is that of Wannier functions [Wannier(1962),Anisimov *et al.* (2005), Lechermann *et al.* (2006)]. Although a transformation between e.g. Wannier functions and plane wave derived basis sets is in principle possible, there exist electronic structure techniques that directly work in a minimal and localized basis.

In particular worth mentioning are muffin-tin orbitals (MTO), in the linear version (LMTO) [Andersen(1975)], and the Nth-order (NMTO) [Andersen and Saha-Dasgupta(2000)] ones. Here we are not going into details, but only mention merits and weaknesses of these approaches. With well-chosen muffin-tin radii, L/NMTO codes may reach the same degree of precision, when comparing with plane wave techniques. Yet, there are undeniable advantages on the side of the muffin tin orbitals. Foremost, the orbitals form an adaptive minimal set of basis functions, which means that orbital matrices, like the Hamiltonian have a smaller size, than when using plane waves. This is in particular true for orbitals with a high degree of localization, for whom a lot of plane waves are needed to describe them. Moreover, since the L/NMTO functions are atomic like, they have a well-defined momentum. As we have said in the introduction the size of matrix elements of the local Coulomb interaction are expected to depend largely on the orbital character. As to the localization of the orbitals, NMTO function are about as localized as maximumally localized Wannier functions [Marzari and Vanderbilt(1997),Lechermann *et al.* (2006)].

A.e   Merits and shortcomings of DFT-LDA

Practical implementations of density functional theory, especially in the local density approximation, enjoy great popularity in the solid-state community. This is first of all because of the fact that for wide classes of materials this approach yields astonishingly good results with respect to experiment for e.g. the crystal structure. A further advantage of DFT undeniably is that computations are reasonably fast and thus the applicability to more and more complex systems becomes feasible with growing computer power.

However, DFT is a theory for the ground state, while experiments that probe the electronic structure, such as photoemission, optics or transport, inevitably measure the excitation spectrum of the system. In the above we indeed stressed that within the Kohn-Sham scheme, both eigenvalues and wavefunctions of the effective one-particle problem are but auxiliary quantities, bare of a well-founded physical meaning. Still, the Kohn-Sham scheme makes it very tempting to identify the Kohn-Sham energies with the true excitations. This strictly speaking unjustified procedure often yields reasonable results, which is why this identification has become a tacit habit.

Yet, since implementations of DFT have to resort to approximations, such as the local density approximation (LDA), since, even if DFT predicts the existence of an effective one-particle potential, its precise form is unknown. This leads in many cases to contradictions

with experiments, even as far as ground-state properties are concerned. Most problematic are systems with open 3d- or 4f-shells, such as transition metals and their oxides or rare-earth compounds, whose electrons struggle between itineracy (band-picture) and localization (Mott insulator [Imada *et al.* (1998)]). Thus, DFT-LDA e.g. fails in describing the volume of δ-Pu [Savrasov *et al.* (2001)], and the phase-diagram of the vanadium oxides V_2O_3 and VO_2, two famous examples of compounds that undergo metal-insulator transitions (MIT) as a function of doping, pressure or temperature which will be our concern in Part III.

For such materials one needs to go well beyond the LDA for capturing correlation effects. Two common approaches are discussed in the next sections.

B   GW

B.a   Hedin's equations

New insights into old problems can often be gained by looking at them from a different perspective or by reformulating them in another language. Using a Green's function formalism, [Hedin(1965)] found a set of coupled equations, whose solutions would yield the exact answer to the many-body problem. The key quantities are the one-particle Green's function G and the screened interaction W, in terms of which will be given the electron self-energy Σ, whence the name of the scheme.

Here we shall state Hedin's equation without derivation. For details see the original work [Hedin(1965)] or the reviews [Aryasetiawan and Gunnarsson(1998), Hedin(1999), Aryasetiawan(2000), Onida *et al.* (2002)].

In the following, all space-time dependencies are written in terms of the combined index $1 = (\mathbf{r}_1, t_1)$.

$$G(1,2) = G_0(1,2) + \int \mathrm{d}(34) G_0(1,3)\Sigma(3,4)G(4,2) \tag{2.7}$$

$$\Gamma(1,2,3) = \delta(1,2)\delta(1,3) + \int \mathrm{d}(4567)\frac{\delta\Sigma(1,2)}{\delta G(4,5)}G(4,6)G(7,5)\Gamma(6,7,3) \tag{2.8}$$

$$P(1,2) = -\imath \int \mathrm{d}(3,4)G(1,3)\Gamma(3,4,2)G(4,1^+) \tag{2.9}$$

$$W(1,2) = v(1,2) + \int \mathrm{d}(34)v(1,3)P(3,4)W(4,2) \tag{2.10}$$

$$\Sigma(1,2) = \imath \int \mathrm{d}(3,4)G(1,3^+)W(1,4)\Gamma(3,2,4) \tag{2.11}$$

We note again that the above coupled equations are *exact*. It is so far not completely clear, whether the above equations allow for a recursive solution, in which one starts with a guess for the Green's function G and the self-energy Σ, and obtains a new G and Σ by going through the GW cycle, that are then used to compute a first correction to the vertex Equation (2.8). This might be iterated until self-consistency. Yet, the above equations

prove quite formidable, not only from the point of view of numerical cost, but also due to the fact that non-causalities may turn up in the course of such an iterative procedure In this vein, the reformulation of the many-body problem only makes sense at all, when already a single cycle yields satisfying results.

B.b   The GW approximation

The most common and simplest use of the above equations is made by the GW *approximation* (GWA) [Hedin(1965)]. In this approximation, the Green's function is initialized by the non-interacting Green's function G_0, into which one might incorporate the interactions on a mean-field level by a suitable potential, and the starting self-energy by $\Sigma = 0$. Therewith the above equations simplify to

$$
\begin{align}
G(1,2) &= G_0(1,2) \tag{2.12}\\
\Gamma(1,2,3) &= \delta(1,2)\delta(1,3) \tag{2.13}\\
P(1,2) &= -\imath G(1,2)G(2,1^+) \tag{2.14}\\
W(1,2) &= v(1,2) + \int d(34)v(1,3)P(3,4)W(4,2) \tag{2.15}\\
\Sigma(1,2) &= \imath G(1,2)W(2,1^+) \tag{2.16}
\end{align}
$$

This is also known as G_0W_0. We see that the self-energy is given by a Hartree-Fock-like expression, albeit with a dynamically screened interaction W, which, as apparent from above, is calculated using a random phase approximation (RPA) polarization. On general grounds nothing justifies rigorously the applicability of this scheme, it is the actual ability of the GWA to yield results in close agreement with experiment for some classes of materials, which establish the use of the approach. Intuitively, one might say that an expansion in the screened interaction W should be more sensible than an expansion in the bare interaction at a given order, due to the reduction of the interaction by screening processes. However, the diagrammatic expansion is not well-defined term by term, since it is not absolutely convergent. A merit is the fact that dynamical effects are partly being captured by the RPA polarization. For the example of the Hubbard molecule, we e.g. show in Appendix B that indeed G_0W_0 is much superior to a Hartree-Fock treatment, since it captures most of the qualitative features of the exact solution in the low and intermediate coupling regime.

B.c   Further remarks

Several remarks are to be made : The result of the G_0W_0 approach evidently depends on the "non-interacting" starting point G_0. In realistic calculations some material specific input has to be chosen. What is normally done is to use a Green's function obtained from an LDA calculation and to compute a self-energy correction to the local density exchange correlation potential. This we will employ for the insulating phase of VO_2 in Section C, Chapter 5. Yet, since band-gaps are notoriously underestimated within LDA, a simple

loop of the GW equations may prove insufficient to capture the correction that the GWA might be able to give.

Another point is that the G_0W_0 is a technique that does not conserve the particle number [Schindlmayr(1997)] and thus the chemical potential is ill-defined. Though a "limited degree of self-consistency" [Hedin(1965), Schindlmayr(1997)], namely such as to align the chemical potential in a way that the one of the non-interacting and the interacting Green's function coincide yields improved spectral functions, this is seldom done in realistic calculations, mainly due to the numerical cost.

Nowadays, several paths are pursued towards a self-consistent GWA : While still keeping the order of the perturbation, one tries to get rid of the starting point dependency. In an application to NiO, a self-consistency scheme was applied in which from the GW calculation a non-local potential for the d-orbitals was deduced, that was fed back into the LDA. This procedure was found to considerably improve results with respect to one-shot calculations [Aryasetiawan and Gunnarsson(1995)]. Promising results were also obtained from the quasi-particle self-consistent scheme [van Schilfgaarde *et al.* (2006)], which is quite akin to the aforementioned work. Here a frequency-independent and hermitian approximation to the full GWA self-energy is used to compute new starting eigenvalues and eigenfunctions for a next GWA iteration. Herewith the starting point still remains a one-particle one, but the result of a GWA iteration becomes independent from the LDA initialization. A slightly different approach was used in [Bruneval *et al.* (2006)].

C   Dynamical Mean Field Theory (DMFT)

Here we shall briefly review the dynamical mean field theory (DMFT). We will put our emphasis on conceptual points only, derivations and further details can be found in numerous reviews [Georges *et al.* (1996), Vollhardt(1991), Georges(2004), Pruschke *et al.* (1995), Bulla(2006)].

C.a   From the Weiss mean-field to the quantum impurity

Characteristics of a mean field theory.   The general spirit of a mean field theory for lattice models is to replace the lattice by a single site, and to cast all non-local degrees of freedom, i.e. the couplings between the sites, into an effective background, the "mean field". The latter is then determined by the request that the single site reference system reproduces the expectation value of a chosen observable of the initial lattice problem. Besides possible representability issues[3], this procedure is completely general and involves no approximations; it is but a reformulation of the original problem. However, the construction so far requires the solution of the initial model in order to fulfill the constraint for the effective medium. The mean field *approximation* now consists in identifying the above observable of the single-site system with the *local* component of the respective *lattice* quantity.

---

[3]whether the expectation value of the chosen observable is obtainable from a local model.

This procedure becomes in fact exact in the limit of infinite dimensions, which is a result of the central-limit theorem. Indeed, in the case of the Ising model, one realizes that when scaling the nearest neighbour interaction J with the inverse spatial dimension $1/d$, the deviation of the mean-field from the true local field becomes of the order of $1/\sqrt{d}$, and thus vanishes in the $d \rightarrow \infty$ limit. For a pedagogic discussion, see e.g. [Georges(2004)].

The Hubbard model in infinite dimensions. Investigations of the Hubbard model in infinite dimensions also yielded important simplifications : The self-energy becomes completely local, i.e. independent of momenta [Müller-Hartmann(1989)], which greatly simplifies diagrammatic expansions. The scaling of the hopping parameters in the $d \rightarrow \infty$ limit was found to be $t = t^*/\sqrt{2d}$ [Metzner and Vollhardt(1989)].

Yet, though simplifications occur, the Hubbard model in infinite dimensions remains a non-trivial model. The reason is that, while in the Ising model, the non-locality of the interactions results in an effective reference system of *non-interacting* spins, the $d \rightarrow \infty$ reference system of the Hubbard model remains an interacting quantum system.

The quantum impurity model and DMFT. A crucial step in the development of DMFT was the discovery that this reference system is in fact a quantum impurity model [Georges and Kotliar(1992)] : The solid is replaced by an atom that dynamically couples to a bath of free electrons that is determined self-consistently.

The notion of a dynamics accounts for the occurrence of retardation effects for electrons that hop between the single site and the bath. Indeed, for the Hubbard model, the action of the impurity model reads :

$$S^{imp} = -\int_0^\beta \mathrm{d}\tau \int_0^\beta \mathrm{d}\tau' \sum_\sigma c_\sigma^\dagger(\tau)\mathcal{G}_0^{-1}(\tau - \tau')c_\sigma(\tau') + U \int_0^\beta \mathrm{d}\tau\, n_\uparrow(\tau)n_\downarrow(\tau) \qquad (2.17)$$

where $c_\sigma^\dagger$, c_σ are the Grassmann variables associated with the impurity creation and annihilation operators, and $n_\sigma = c_\sigma^\dagger c_\sigma$ is the corresponding occupation. The impurity self-energy $\Sigma(\iota\omega_n)$ is related to the impurity Green's function

$$G_\sigma(\tau - \tau') = -\langle \mathcal{T} c_\sigma(\tau)c_\sigma^\dagger(\tau')\rangle_{S^{imp}} \qquad (2.18)$$

and its non-interacting equivalent $\mathcal{G}_0(\iota\omega_n)$ by Dyson's equation :

$$\Sigma(\iota\omega_n) = \mathcal{G}_0^{-1}(\iota\omega_n) - G^{-1}(\iota\omega_n) \qquad (2.19)$$

The lattice Green's function, on the other hand is defined by

$$G_{lattice}^{-1}(\mathbf{k}, \iota\omega_n) = \iota\omega_n + \mu - \epsilon_\mathbf{k} - \Sigma_{lattice}(\mathbf{k}, \iota\omega_n) \qquad (2.20)$$

in which $\epsilon_\mathbf{k}$ is the one-particle dispersion, and $\Sigma_{lattice}(\mathbf{k}, \iota\omega_n)$ the lattice self-energy.

The DMFT *approximation* now consists, as was described above for a mean-field theory in general, by identifying the impurity self-energy with the local self-energy of the lattice model :

$$\Sigma_{lattice}(\mathbf{k}, \imath\omega_n) = \Sigma(\imath\omega_n) \tag{2.21}$$

The self-consistency condition is then given by the requirement that the local lattice Green's function $G_{lattice}(\imath\omega_n) = 1/N \sum_{\mathbf{k}} G_{lattice}(\mathbf{k}, \imath\omega_n)$ coincides with the Green's function of the impurity :

$$G(\imath\omega_n) = \frac{1}{N} \sum_{\mathbf{k}} \left[\imath\omega_n + \mu - \epsilon_{\mathbf{k}} - \Sigma(\imath\omega_n)\right]^{-1} \tag{2.22}$$

The equations (2.18), (2.17), (2.19) and (2.22) form a closed set, which in practice is iteratively solved.

The most intricate problem in this scheme is the solution of the impurity problem, i.e. the computation of the Green's function from Equation (2.18). However, there is quite a variety of techniques available, that were mostly developed already for the context of the Anderson impurity problem. In this work, which is mainly concerning realistic, i.e. multi-band or cluster calculations, exclusive use is made of a quantum Monte Carlo algorithm that is due to [Hirsch and Fye(1986)]. Further we will use data from L. V. Pourosvskii that were obtained from a Hubbard-I solver [Hubbard(1963)]. For a discussion of these and other techniques we refer to the literature [Georges *et al.* (1996)].

Limits in which DMFT becomes exact.   Besides the case of infinite dimensions, the dynamical mean field theory becomes exact in two other limits :

In the non-interacting limit ($U = 0$) the self-energy vanishes and the self-consistency condition, Equation (2.22), shows that the solution of the model is correctly given by the non-interacting Green's function $G(\imath\omega_n) = 1/N \sum_{\mathbf{k}} \left[\imath\omega_n + \mu - \epsilon_{\mathbf{k}}\right]^{-1} = \mathcal{G}_0(\imath\omega_n)$.

Moreover, DMFT is exact in the atomic limit. In that case the model consists of isolated atoms and thus the bath Green's function $\mathcal{G}_0^{lattice}$ equals the non-interacting lattice Green's function G_0, and thus the self-energy of the lattice and the impurity are equivalent by construction.

With its non-perturbative nature, DMFT is thus correctly comprising, both the weak and the strong coupling regime. Therewith the hope arises that it is also is a reasonable approximation in between these limiting cases. Its dynamical nature indeed allows for the capturing of multiple energy scales. We will discuss DMFT results on the Hubbard model and its characteristics in the next section.

Realistic extensions – "LDA+DMFT".   For electronic structure calculations of correlated materials, one needs to find a way to introduce material specific informations into the many-body approach that one employs.

The most successful theory that combines standard band-structure methods with the DMFT is the so-called LDA+DMFT [Anisimov *et al.* (1997), Lichtenstein and Katsnelson(1998)]. In its most basic version, it is from the LDA that one takes the one-particle part of the Hamiltonian (corresponding to the band dispersion $\epsilon_{\mathbf{k}}$ in the above), which, after supplementing it with well-chosen Hubbard-type Coloumb interactions is solved within DMFT.

Here, we make only some technical remarks, for further details see the reviews [Held *et al.* (2003), Biermann(2006), Kotliar *et al.* (2006), Lechermann *et al.* (2006)]. When producing an LDA Hamiltonian for the DMFT calculation, one has to pursue the same line of reasoning that led to the lattice formulation of the Hubbard model. This means that the Hamiltonian matrix elements have to be expressed in terms of a localized basis. Well-suited electronic structure techniques in this vein are muffin tin orbital methods, such as LMTO [Andersen(1975)], or NMTO [Andersen and Saha-Dasgupta(2000)]. Of course, one can also use e.g. plane wave codes and transform the result into a Wannier-type basis [Wannier(1962)] afterwards. Moreover, as stressed in the introduction, the strength of on-site interactions depends very much on the orbital character. It is thus favourable to have a description in terms of matrix elements with well defined angular momentum.

Notwithstanding its failure to treat correlated systems, the LDA is not a theory of independent particles. In fact, some correlations are already present in the resulting band-structure. Therefore one has to correct for not accounting these effects twice. Yet, since the LDA is not particularly well-controlled, approximative schemes have to be applied for this "double counting".

In a full LDA+DMFT implementation, there is not only the DMFT self-consistency, but also a loop over the charge density. Indeed, the DMFT will alter the local density of the system. This can be fed back into the band-structure code, which, then produces a new "one-particle" Hamiltonian corresponding to the changed density. See e.g. [Minar *et al.* (2005), Pourovskii *et al.* (2007a)].

Spectral density-functional theory (SDFT). As a matter of fact, dynamical mean field theory and density functional theory, as say have been discussed above, have quite notable conceptual similarities :

In DFT, a *non-interacting* reference system was introduced, which, together with an effective *Kohn-Sham potential*, reproduced the *local density* of the true system. Therewith *ground state observables* became accessible. This construction is exact, yet one is obliged to approximate the effective potential, for example by using the LDA.

In spectral density-functional theory (SDFT) a *local* reference system is introduced, and a self-consistent *bath Green's function* assures the reproducing of the true *local Green's function*. From the latter, all *one-particle* observables are calculable. In practical schemes one has to apply approximations, and DMFT is one of them.

Indeed, all the introduced theories, DFT-LDA, GW, DMFT, and their combinations can be formulated in a functional language, as was presented for the DFT. For a review see [Kotliar *et al.* (2006)].

Quantum Monte Carlo – an impurity solver. There exist numerous techniques that have been devised for solving an Anderon impurity problem like Equation (2.17). All of them have their pros and cons.

Here we just put into perspective the approach that was almost exclusively used thoughout this work, namely a quantum Monte Carlo (QMC) algorithm, in our case

the one of [Hirsch and Fye(1986)] (HF). This algorithm is based on a discrete Hubbard-Stratonovich decoupling [Hirsch(1983)] of the interaction term. Besides the original work, see [Georges *et al.* (1996)] for details. For the multiorbital case see [Poteryaev *et al.* (2007)].

One advantage of the QMC is that it is a numerically exact technique. It is the statistic and thus the computer time that one is willig to spend which defines the precision. Moreover it is about the only really reliable technique that can treat multi-orbital and cluster impurities, though, of course, the numerical cost increases steadily.

There are some disadvantages of the (HF-)QMC that should be mentioned. First, it is not possible to reach very low temperatures, since the number of auxiliary spins in the Hubbard-Stratonovich transformation increases; the cost scales with $1/T^3$. Moreover, in the case of more than a single-site impurity, a technical problem, known as the "sign-problem", occurs. What is needed in statistical methods is a quantity that can be identified as a probability that is then used to sample within some parameter space. It is in the cluster case that the quantity that used in the HF-QMC may acquire a negative sign for specific configurations of the auxiliary Ising spins. For the absence of the sign problem in the one-impurity case see [Jaebeom Yoo and Baranger(2005)]. Concerning this thesis we are affected only in the case of the cluster calculations of [Biermann *et al.* (2005)]. Another major concern is the fact that the technique works in imaginary time, or frequency and requires an analytical continuation to the real-frequency axis. We will devote parts of Chapter 3 to this issue.

C.b The half-filled one band Hubbard model within DMFT : phase diagram and real-frequency self-energies

Here we shall review the DMFT phase diagram for the half-filled one band Hubbard model on the Bethe lattice in infinite dimensions, and the corresponding generic properties of the real-frequency self-energy $\Sigma(\omega)$[4]. We will refer to these properties in later chapters where we will discuss applications to realistic multi-band systems.

Figure 2.2 shows the schematized phase diagram of the Hubbard model at half-filling in infinite dimensions. The abscissa corresponds to the ratio of the interaction U and the bandwidth W, while the y-axis indicates temperature. We will discuss in the following the four major phases of Hubbard model within DMFT. In the absence of correlations ($U/W = 0$), the Hubbard Hamiltonian, Equation (1.11), is diagonal in momentum-space and, hence, the spectral function of a one-band system at a given momentum is a Dirac distribution and, in particular, the self-energy is zero. The total local spectral function thus coincides with the density of states, shown in Figure 2.1 for the Bethe lattice in $d = \infty$.

---

[4]The shown self-energies are obtained from the analytical continuation procedure for Quantum Monte-Carlo calculations, that we will describe in Chapter 3.
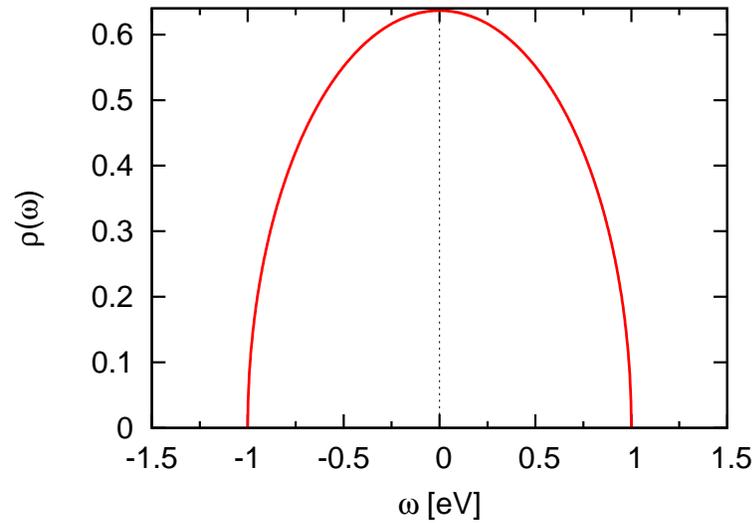
Figure 2.1 : *Density of states of the Bethe lattice with half bandwidth W/2=2t=1.0 eV.*
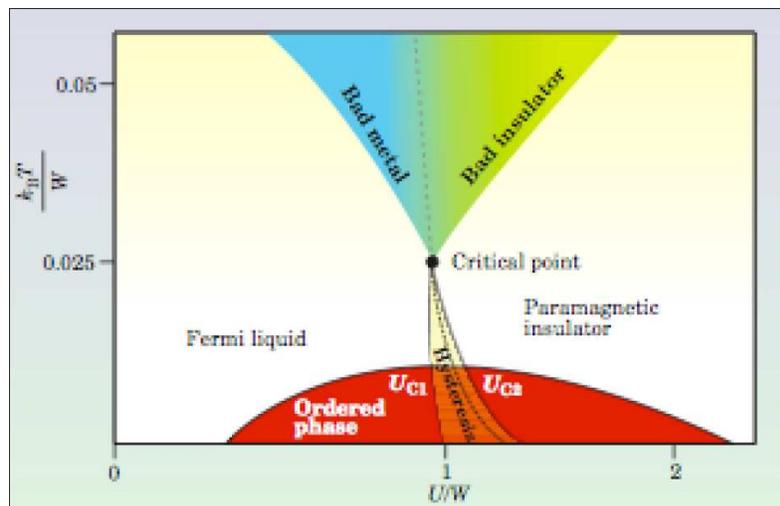

Figure 2.2 : *Schematic phase diagram of the one band, half-filled Hubbard model within DMFT. The x-axis is given by the ratio of the interaction U over the bandwidth W. The y-axis is temperature. From [Kotliar and Vollhardt(2004)].*

With correlations at present, the spectral function is given by

$$
\begin{aligned}
A(\mathbf{k}, \omega) &= -\frac{1}{\pi} \Im \frac{1}{\omega + \mu - H(\mathbf{k}) - \Re\Sigma(\omega) - i\Im\Sigma(\omega)} \\
&= -\frac{1}{\pi} \frac{\Im\Sigma(\omega)}{(\omega + \mu - H(\mathbf{k}) - \Re\Sigma(\omega))^2 + (\Im\Sigma(\omega))^2}
\end{aligned}
\tag{2.23}
$$

which can be interpreted as a Lorentzian-like curve. In this vein, the real-part is responsible for the shifting of the non-interacting excitations encoded in the Hamiltonian $H(\mathbf{k})$, whereas the imaginary part determines their width, as is familiar from e.g. finite lifetime broadening of atomic line shapes. However, the self-energy in the more interesting cases is far from being constant, but a rather strongly frequency-dependent quantity, that will account for non-trivial transfer effects of spectral weight within the entire excitation spectrum.

From the Fermi liquid to the bad metal. In regions of low temperatures and only moderate interaction strength, the solution to the DMFT equations corresponds to a Fermi liquid state[5].

The theory of Fermi liquids [Pines and Noziere(1965)] is a concept accounting for low energy excitations only. It describes the influence of correlation effects on the coherent part of the excitation spectrum by replacing, in a one-to-one correspondence, the low energy excitations of the interacting electrons by quasi-particles, that resemble free-particles that possess a renormalized mass. These particles still have well-defined momentum, however their lifetime is finite, which manifests itself in a broadening of the quasi-particle peak with respect to the Dirac distribution of the free electrons. According to Fermi liquid theory, the imaginary part of the self-energy obeys the low-frequency expansion

$$
\Im\Sigma(\omega) = -B\left[\omega^2 + (\pi T)^2\right] + O\left(\omega^4\right)
\tag{2.24}
$$

As a consequence, infinite-lifetime excitations exist only exactly on the Fermi surface and at zero temperature. Upon heating, the lifetime of the quasi-particles shortens and fades away completely beyond the coherence temperature. This is one way of inducing a finite scattering rate that results in invalidating the quasi-particle concept. Also upon leaving the Fermi surface and going to higher energies, quasi-particles become less and less defined and get incoherent.

The low energy development of the real-part of the self-energy is

$$
\Re\Sigma(\omega) = \Sigma(0) + (1 - 1/Z)\omega + O\left(\omega^3\right)
\tag{2.25}
$$

where $\Sigma(0) = 0$ in the particle-hole symmetric case, as currently considered.

$$
Z = \left(1 - \partial_\omega \Re\Sigma(\omega)\,|_{\omega=0}\right)^{-1}
\tag{2.26}
$$

---

[5]In the following we will neglect any possible magnetic orderings, thus regarding a system that is sufficiently frustrated.

is the quasi-particle renormalization factor, which, in case of a local self-energy also corresponds to the inverse of the effective mass enhancement m/m^*. With this the spectral function Equation (2.23) becomes at low energies

$$A(\mathbf{k}, \omega) \quad = \quad -\frac{1}{\pi}\Im\frac{Z}{\omega - Z(H(\mathbf{k}) - \mu) + \imath ZB(\omega^2 + \pi T^2)} \qquad (2.27)$$

which for a small scattering amplitude ($B \ll 1$) is just again a Dirac distribution. Compared with the free system ($Z = 1$) the bandwidth gets renormalized down by a factor $Z < 1$, and also the weight reduces to Z, which means that the fraction $1 - Z$ is transfered to the incoherent part of the spectrum, to which Fermi liquid theory does not give access.
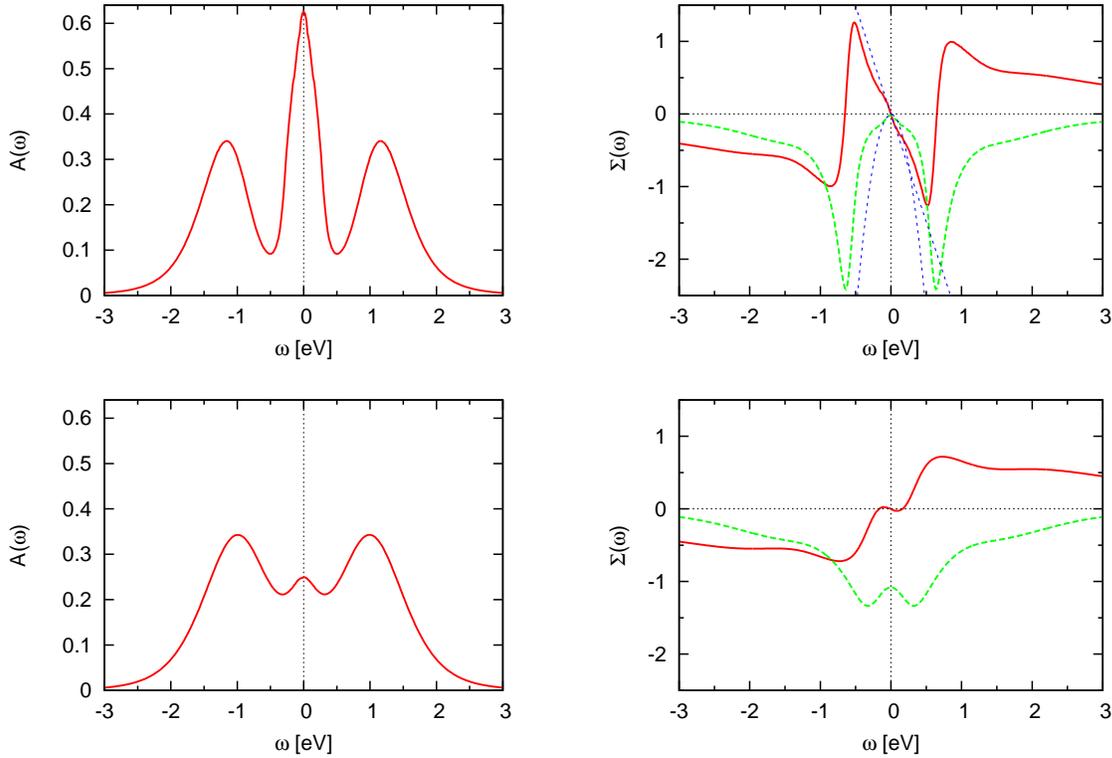
Figure 2.3 : *Spectral functions (left) and self-energies (right) in the Fermi liquid regime (top), $U = 2.0$, $\beta = 50.0$ in units of the half bandwidth, and the bad metal regime, $U = 2.0$, $\beta = 8.0$, (bottom), respectively. The real-parts of the self-energy are the solid, the imaginary parts the dashed lines.*

With DMFT, however, one possesses a theory that gives information on the electronic excitations at all energy-scales, i.e. it gives in particular information on what happens to the incoherent weight that is lost in the quasi-particle peak.

In the two top panels of Figure 2.3 is shown the DMFT spectral function (to the left) and the corresponding self-energy (to the right) for the Fermi liquid regime. Right at the Fermi level is seen the quasi-particle peak, that compared with the non-interacting case is narrower, which corresponds to the band-width narrowing by the Z-factor mentioned above. Yet, for a momentum independent self-energy, the value $A(\omega = 0)$ in the one-band or degenerate case is pinned to its non-interacting value, which means that the correlations do not modify the Fermi surface [Müller-Hartmann(1989)]. When looking at the corresponding self-energy, the characteristics of the Fermi liquid are present. As indicated by the dotted lines, the real-part is linear in frequency around the Fermi-level and the imaginary part proportional to ω^2.

Still, already at rather low energies, the self-energy deviates substantially from its low-energy behaviour[6]. In the spectral function, Figure 2.3 top left, we see the famous three peak structure[7] with the preformed Hubbard bands that remind of the atomic limit of the Hubbard model. The latter thus accommodate the weight $1-Z$ that is transferred from lower energies.

In order to produce this spectral function, the self-energy develops features that are way beyond any low-frequency expansion. While at low energy, the real-part of the self-energy is linear, with a negative slope, it has at high energy, the same behaviour as the atomic limit : $\Sigma(\omega \to \infty) \sim \frac{U^2}{4\omega}$ [8] and approaches the constant Hartree term[9]. The matching of these two very different behaviours results in a pronounced frequency dependence in the intermediate regime, leading to a prominent peak in the imaginary part (see also Section A, Chapter 3).

Upon heating, thermal fluctuations induce a finite scattering rate even at the Fermi-level, thus invalidating the quasi-particle interpretation. This is seen in Figure 2.3, bottom panels, where the temperature is well above the coherence or Kondo temperature of the system. This scattering rate is seen as a finite value in the imaginary part of the self-energy at zero energy. This results into the violation of the above mentioned pinning condition, i.e. the spectral function at zero energy is no longer bound to its non-interacting value, but is considerably reduced.

The Mott insulator. Above a critical value of the ratio U/W, the one-band Hubbard model at half-filling becomes a Mott insulator. Actually the transition is of first order, and thus shows a coexistence region in the phase diagram, Figure 2.2. At high temperature the transition line ends in a critical point, above which the transition from a high-conductivity to the high-resistivity phase is continuous. Indeed the phase diagram closely resembles the one of the liquid-gas transition, casting the phase transition into the Ising universality class [Kotliar(1999), Kotliar *et al.* (2000)], and also [Castellani *et al.* (1979)].

---

[6]In passing we note an interesting observation. Namely the that the change in slope of the real-part of the self-energy induces kinks in the effective band-structure of the interacting system that are of purely electronic origin [Byczuk *et al.* (2007), Cornaglia *et al.* (2007)].

[7]Which has become somewhat of a mascot of the field of correlated electrons...

[8]Using the Kramer-Kronig relations, one herewith obtains the sum rule : $\int_{-\infty}^{\infty} d\omega \Im\Sigma(\omega) = -\frac{\pi U^2}{4}$.

[9]which at particle-hole symmetry at half-filling is zero.

Since at half-filling, the real part of the self-energy is an anti-symmetric function, it has to vanish at zero frequency. As a consequence the elimination of spectral weight at the Fermi level can only be achieved by a divergence of the imaginary part. This results in a disappearing of the Z-factor. This is known as the Brinkman-Rice phenomenon [Brinkman and Rice(1970)].
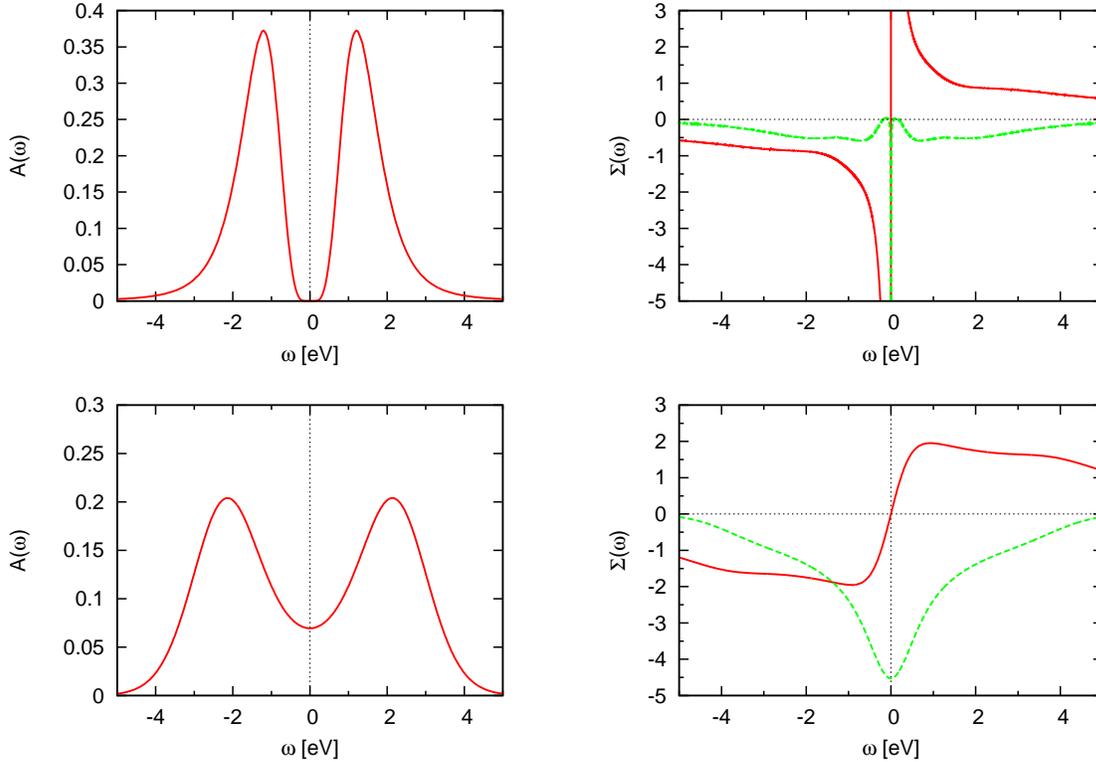
Figure 2.4 : *Spectral functions (left) and self-energies (right) in the insulating regime, $U = 3.0$, $\beta = 20$ (top) and the bad insulator (semi-conducting) regime, $U = 4.0$, $\beta = 1.0$, (bottom), respectively. The real-parts of the self-energy are the solid, the imaginary parts the dashed lines. All parameters in units of the half-bandwidth. The imaginary part of the Mott-insulating self-energy is a Delta distribution at the origin, while in the bad metal phase the $\Im\Sigma$ reaches a finite value at zero frequency.*

The top of Figure 2.4 shows an example : The imaginary part of the self-energy is indeed a Dirac distribution at the origin, and vanishes in the gap otherwise.

An increase in temperature leads to thermic filling of the gap, which is concomitant with a curing of the divergence in the imaginary part of the self-energy, which, as can be seen in the bottom of Figure 2.4, reaches a finite value at zero frequency.

In a realistic multi-band setup, the situation becomes more involved. In particular, a modification of the Fermi surface becomes possible through a local self-energy that causes charge transfers between different orbitals. Moreover the necessity of a divergent mass for a Mott transition gets relaxed. Indeed a correlation enhancement of crystal field splittings

may cause a shifting of spectral weight and thus lead to the separation of former bands at the Fermi level. Responsible for this will be the orbital dependence in the real-parts in the self-energy, which need no longer vanish at zero energy, as was the case for the half-filled one-band model. We will see actual realizations in Part III.

Part II

Technical Advances

This second part presents the technical developments that have been devised and implemented within this thesis. In the first chapter we describe an analytical continuation scheme, which allows for the deducing of the real-frequency self-energies from general multi-orbital and cluster Quantum Monte Carlo computations that are performed within the Matsubara formalism, i.e. in imaginary time or frequency. With this quantity at hand, the possibilities of numerical LDA+DMFT results will become considerably enriched.

On the one hand, the self-energy itself is much more versatile and also more conducive to interpretation than the local spectral function. In this vein it becomes for instance possible to distinguish more accurately between spectral weight that stems from a band-like excitation from those originating from incoherent satellite features. Sounding rather academical, this will for instance lead to a modified analysis of the excitation spectrum of the insulating phase of vanadium dioxide. Thus light can be shed on physical phenomena that might otherwise remain obscured. This is indeed very important since the understanding of underlying physical effects is far beyond, and more important, than a mere reproduction of selected experimental results.

In the same regard, we will introduce some notions of effective band-structures for interacting systems and discuss which prerequisites have to be met in order to allow for the latter to make sense. Indeed the artificial notion of a band-structure breaks down in the presence of correlations[10]. Yet the intuitive nature of the latter may still, as we will see in Part III, be helpful in the allocation of spectral weight to distinct characters.

Having the real-frequency self-energy at one's disposition, it becomes possible, within some approximations, to calculate response functions. The second chapter is devoted to the development of a formalism for the optical conductivity within a framework of a realistic setup for correlated materials, having in particular in mind the LDA+DMFT approach.

Starting from a continuum formulation we seek to devise a practicable working scheme within a localized description of the system under consideration. We will, first on the level of a lattice model, derive a generalized Peierls substitution approach for realistic calculations. In the case of systems with only one atom per unit cell the latter reduces to the usual Peierls term, namely to a Fermi velocity that is given by a momentum derivative of the Hamiltonian. The impact of the additional terms in the case of multi-atomic unit cell is shown to be significant. Further, by re-deriving the Peierls terms starting from the continuum description, we analyze the appearing correction terms that are beyond the Peierls approach.

The generalized Peierls approximation will give a handy way to calculate Fermi velocities without the need to compute wavefunction matrix elements other than the Hamiltonian. This is a valuable advantage, since the full matrix elements are cumbersome to compute within a band-structure method that uses localized basis functions. Therewith, the method is, moreover, independent of the electronic structure approach.

The achievements of this chapter will then be applied to several compounds in Part III, namely to vanadium di-, and sesquioxide, as well as rare-earth sesquioxides.

---

[10]as defined in Section B, Chapter 1

Chapter 3

Spectral Properties of Correlated Materials

A   Technical development and general points

In the first part of this chapter, we will describe a scheme for the analytical continuation procedure of quantum Monte Carlo data, that will result in self-energies of real frequencies.

Not only do allow the latter a much better starting point for the interpretation of numerical LDA+DMFT data, but also this makes it possible to calculate physical quantities far more interesting than the local spectral function. Among these are momentum-resolved spectral functions, and linear response quantities such as transport, the optical conductivity, and certain Raman modes, provided one neglects vertex corrections. As a consequence the interface with experimentalists becomes vastly enhanced, facilitating both the understanding of actual measurements and the assessment whether the theory captures the physics at work.

The second part of this chapter is devoted to a discussion of interacting excitation spectra and the question to which extent these might be interpreted in terms of an effective band-structure. Electronic structure calculations are still dominated by the band-picture, in which excitations are given by eigenvalues of effective one-particle systems, leading to the familiar spaghetti graphics in the respective publications. As discussed in the introduction, band-theory breaks down when pertinent correlations are at present. Still, this picture, with its intuitive interpretation, can, in a way, carry over into the realm of strongly correlated materials, where the spectral function is the appropriate quantity to discuss. Here we will present how the eigenvalue problem generalizes with a frequency-dependent self-energy, a procedure that will help the interpretation of numerical LDA+DMFT data for realistic systems as will be shown in Part III.

A.a   Calculation of real frequency self-energies from quantum Monte Carlo data

Though there exists a variety of numerical solvers for the impurity problem in the DMFT cycle, the most popular in the context of realistic calculations is the Quantum Monte Carlo (QMC) approach. This owes to the fact, that other solvers, like the numerical renormalization group (NRG), for instance, are impracticable in the case of multi-band or cluster calculations, or imply additional approximations, as is the case for the non-crossing approximation (NCA) [Keiter and Kimball(1970),Pruschke *et al.* (1993a)], or the iterated perturbation theory (IPT) [Georges and Kotliar(1992)]. Yet, the QMC works within the finite temperature Matsubara formalism, i.e. either in imaginary time or frequency. For the computation of experimental observables are, of course, real-frequency results needed.

Provided an analytical form of a function of Matsubara frequencies is known, the continuation is easily performed by the substitution $\imath\omega_n \longrightarrow \omega + \imath 0^+$. When it comes however to the analytical continuation of numerical data, things are much more complicated. If we take, e.g. the one-particle Green's function, we can write it using the spectral decomposition :

$$G(\imath\omega_n) \;\; = \;\; \int \mathrm{d}\omega \frac{A(\omega)}{\imath\omega_n - \omega} \tag{3.1}$$

which says that the Green's function on the Matsubara axis is obtained from the spectral function $A(\omega) = -1/\pi\,\Im G(\omega + \imath 0^+)$ by a Hilbert transform. The inversion of the latter is rather cumbersome, yet for numerical data without statistical noise, the Padé approximation (see e.g. [Beach *et al.* (2000)]) can be employed, in which the spectral function is expanded into a rational polynomial, whose coefficients are then determined by a least square fit. In the presence of statistical noise, however, any least square fit of this problem becomes unreliable. Fourier transforming, $G(\tau) = 1/\beta \sum_n G(\imath\omega_n)e^{\imath\omega_n\tau}$, yields

$$G(\tau) \;\; = \;\; \int \mathrm{d}\omega A(\omega) \frac{e^{-\tau\omega}}{1 + e^{-\beta\omega}} \tag{3.2}$$

which is a two-sided Laplace transform. The problem of inverting this equation is complicated due to the integration kernel $K(\tau,\omega) = e^{-\tau\omega}/\left(1 + e^{-\beta\omega}\right)$ which becomes exponentially small for large frequencies $|\omega|$.

As a consequence, two quite discernible spectral functions $A(\omega)$ may still yield Green's functions $G(\tau)$ that are indistinguishable. Given the intrinsic noise effects in the Quantum Monte Carlo approach, standard means for analytic continuation yield poor results[1].

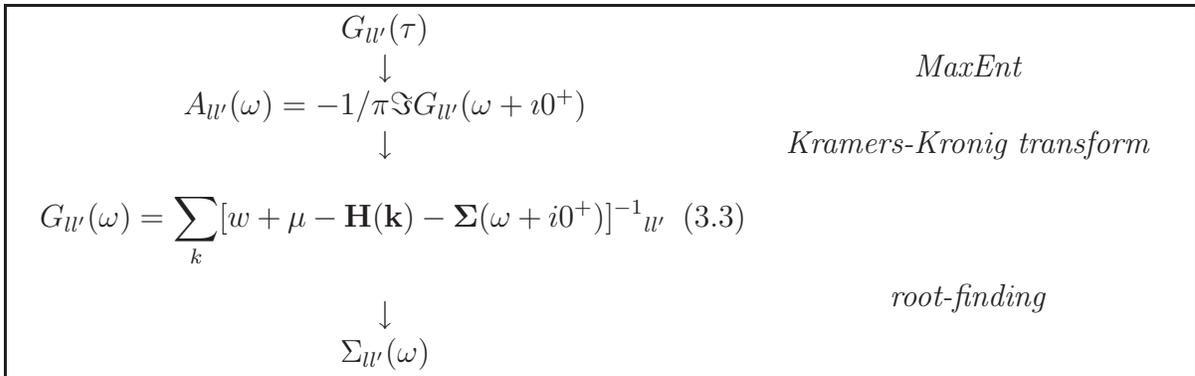The most commonly used technique for the analytical continuation of QMC data is the maximum entropy algorithm (MaxEnt), see [Jarrell and Gubernatis(1996)] for a review. The technique is based on Bayesian probability theory, which, allows for the

---

[1]It seems however that when applying e.g. the Padé approximation not to the Green's function but to the self-energy, reasonable results may be obtained from high precision QMC data.

treating of problems that have a non-unique solution, due to incomplete information. It incorporates prior knowledge of the desired quantity, such as e.g. positivity and sum rules. The principle of the method, in a nutshell, is to introduce an entropy term in the minimization procedure that shifts the minima such as to yield the most un-biased solution that is compatible with the given constraints. See e.g. [Beach(2004)] for a concise discussion.

For the continuation of the Green's function from the Matsubara formalism to real frequency the maximum entropy algorithm has become a standard approach. Yet, it would be desirable to have also the self-energy on the real-frequency axis. In the DMFT context, this was first envisioned by [Jarrell *et al.* (1995)] in the model case. In the context of realistic multi-band calculations, this has however only recently been endeavoured [Biermann(2001), Blümer(2002), Anisimov *et al.* (2005), Nekrasov *et al.* (2006)]. In the same context, the analytical continuation of momentum-resolved spectral functions was first performed by [Biermann *et al.* (2004)][2]. The calculation scheme that we present here is still based on the idea of [Jarrell *et al.* (1995)]. In this work , however, we have extended the approach to include also off-diagonal elements in the self-energy. Our implementation thus is sufficiently general to work in the multi orbital cluster DMFT case.

The following sketch outlines the most general form of the continuation procedure :

$$G_{ll'}(\tau)$$
$$\downarrow \qquad\qquad MaxEnt$$
$$A_{ll'}(\omega) = -1/\pi \Im G_{ll'}(\omega + \imath 0^+)$$
$$\downarrow \qquad\qquad Kramers\text{-}Kronig\ transform$$
$$G_{ll'}(\omega) = \sum_k [w + \mu - \mathbf{H}(\mathbf{k}) - \boldsymbol{\Sigma}(\omega + i0^+)]^{-1}{}_{ll'} \quad (3.3)$$
$$\downarrow \qquad\qquad root\text{-}finding$$
$$\Sigma_{ll'}(\omega)$$

Starting from the local Green's function in imaginary time $G(\tau)$, one performs the aforementioned MaxEnt algorithm, yielding the spectral function, which is proportional to the imaginary part of the real-frequency Green's function. The real part of this quantity is related to the former by a Kramers-Kronig transformation. The by far most difficult step in this scheme is the last one. Whereas in the one-band Hubbard model on the Bethe-lattice an exact expression for the self-energy in terms of the local Green's function exists [Georges *et al.* (1996)]

$$\Sigma(\omega) \;\; = \;\; \omega + \mu - t^2 G(\omega) - 1/G(\omega) \tag{3.4}$$

---

[2]To our experience, an application of the MaxEnt algorithm on momentum-resolved Matsubara Green's functions, $G(\mathbf{k}, \tau)$, yields spectra that are broader, with respect to momentum-resolved spectral functions that are derived from the self-energy on the real-frequency axis.

a multi-dimensional root-finding procedure [Jarrell *et al.* (1995)] has to be employed to solve (3.3) in the general multi-band case.

In the degenerate, diagonal case, the k-sum in (3.3) can be replaced by an integral over the density of states and one ends up with the simpler task of inverting the Hilbert transform

$$G_{ll}(\omega) = \int d\epsilon \frac{D(\epsilon)}{\omega + \mu - \epsilon - \Sigma_{ll}(\omega + i0^+)} \tag{3.5}$$

as has been considered e.g. in [Blümer(2002)].
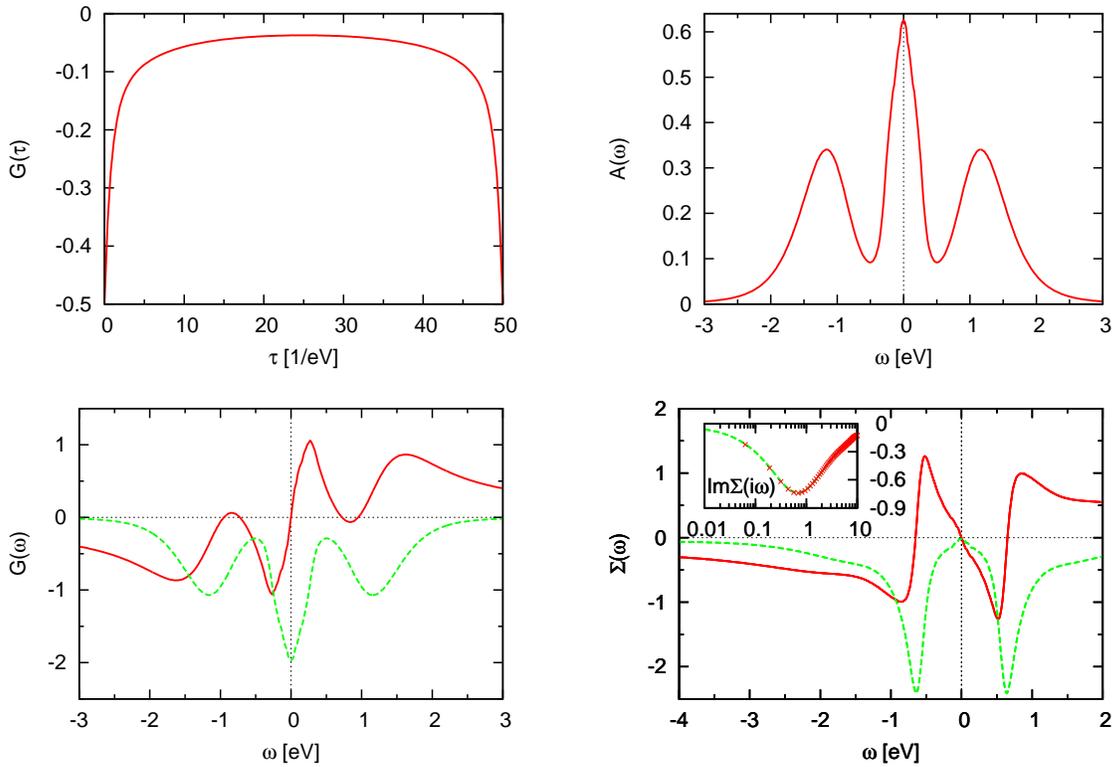
Figure 3.1 : *Example for an analytical continuation of the one-band Hubbard model on the Bethe lattice at half-filling, $U = 2.0$ and $\beta = 50$ (in units of the half-bandwidth). From the top left to the right bottom : (a) Green's function in imaginary time $G(\tau)$, (b) spectral function $A(\omega) = -1/\pi \Im G(\omega + i0^+)$, (c) the Green's function on the real frequency axis $G(\omega)$, (d) the real-frequency self-energy $\Sigma(\omega)$. Solid lines indicate the real-parts, dashed lines the corresponding imaginary parts. The inset shows a comparison between the original QMC Matsubara self-energy $\Im \Sigma(i\omega_n)$ (crosses) with the Hilbert transform, Equation (3.6), of the analytically continued one shown in the large graph (solid line).*

The inverting of Equation (3.3) in the general context is not always easy. In the non-degenerate case, where one has to work in the matrix formulation, the self-energy elements are, in particular, coupled. Practically one scans through frequency, starting

at high energies, where the solution is known and given by the Hartree self-energy, and consecutively uses the solutions as initial guesses for the root-finder at lower energies. Indeed, for well converged data, the predominant source of uncertainty of the current scheme is the MaxEnt procedure that leads to local spectral function.

By a Hilbert transform, the self-energy on the Matsubara axis can be recovered, allowing an assessment of the overall continuation quality :

$$\Sigma(\imath\omega_n) = \Sigma(\infty) - \frac{1}{\pi}\int d\omega \frac{\Im\Sigma(\omega)}{\imath\omega_n - \omega} \tag{3.6}$$

Moreover, as for the Green's function, the real and the imaginary part of the self-energy are connected by the Kramers-Kronig relations

$$\Re\Sigma(\omega) = \Sigma(\infty) - \frac{1}{\pi}\int d\omega' \frac{\Im\Sigma(\omega')}{\omega - \omega'} \tag{3.7}$$

$$\Im\Sigma(\omega) = \frac{1}{\pi}\int d\omega' \frac{\Re\Sigma(\omega')}{\omega - \omega'} \tag{3.8}$$

allowing for an internal consistency check. Figure 3.1 shows the individual steps for the analytical continuation of an example calculation for the one-band Hubbard model.

To our knowledge, the inclusion of off-diagonal elements in orbital space is new. This will in particular allow for the analytical continuation of cluster DMFT calculations, see the case of VO_2 in Part III. Still, this extensions is straight-forward, the only complication appears in the beginning, when continuing the off-diagonal Green's function. Appendix A details our procedure for these cases.

A.b   Effective band-structures

A.b.i   Poles of the Green's function

Band structure methods rely on effective one-particle theories : The Schrödinger equation is separable, and the Hilbert space therewith sufficiently small to render the eigenvalue problem of the Hamiltonian solvable. The excitation energies are then given by the resulting eigenvalues[3]. Within many-body approaches, the impact of correlation effects is encoded in the electron self-energy $\Sigma(\omega)$, which is a complex non-Hermitian quantity that is furthermore frequency-dependent[4] : As described above, the real part of the self-energy, or in the realistic multi-band case the Hermitian part of it, is responsible for the shifting of spectral weight with respect to the non-interacting problem. Supposing that the anti-Hermitian part of the self-energy is reasonably small, quasi-particle excitations are given by the poles $\omega_{\mathbf{k}}$ of the momentum-resolved Green's function, i.e. $\omega_{\mathbf{k}}$ verifies $\det(\mathbf{G}[\Re\boldsymbol{\Sigma}]^{-1}) = 0$, or

---

[3]Note, again, that this is an uncontrolled approximation in the LDA, as the Kohn-Sham energies of the effective system do not correspond to the excitations of the true N-particle system.

[4]but momentum independent in the $d = \infty$ case that we consider

$$\det \left[\mathbf{H}^{LDA}(\mathbf{k}) + \Re\mathbf{\Sigma}(\omega_{\mathbf{k}} + i0^+) - \mu - \omega_{\mathbf{k}} \right] = 0 \qquad (3.9)$$

This is closest in spirit to the band-picture, and simplifies to an eigenvalue problem in the limit of a static self-energy. Yet, in general, this equation in not an eigenvalue problem, which makes it difficult to solve numerically. We will discuss physical implications, by graphical means, in the paragraph after the next.

Another view point was taken in [Pruschke *et al.* (1996)], in which an effective band-structure was identified by the *maxima* of the one-particle spectral function. Therewith the influence of the frequency dependence of the anti-hermitian parts of the self-energy are incorporated into the finding of the positions of prominent spectral features. Moreover, experiments are measuring spectral weight and not pole positions. Yet, from a conceptual point, we prefer the notion of one-particle poles, which, especially in the multi-orbital case, are better suited to resolve individual excitations.

We shall shortly comment on our numerical procedure. In principle one might scan through frequency and search for sign changes of the determinant. This is however only possible for solutions of odd degeneracy. In case of e.g. a double degenerate solution, the determinant is zero, but does not change sign as a function of frequency. Then one would have to introduce a threshold value, and identify solutions by yielding a value below it. However, this may produce spurious solutions, even when working on a fine frequency grid. By our reckoning, an iterative procedure is to be preferred over a mere scan in frequency. When a frequency point is classified as a solution for a given threshold, the self-energy is polynomially interpolated around it on a finer grid and the scanning is repeated. Therewith different numerical solutions of the initial step collapse on each other. This procedure was tested against the sign-change method for non-degenerate solutions and was found to be reliable.

A.b.ii   Renormalized band-structure : "Z-bands"

Before commenting on the impact of the above generalization of the one-particle band-structure eigenvalue problem, we describe an even simpler way on how to assess the effects of correlations on the former (LDA) band-structure.

Indeed, besides neglecting any life-time influences by dropping the anti-hermitian parts of the self-energy, one could think of using the frequency expansion, Equation (2.25), such as to incorporate leading low-energy contributions, while remaining within a Hamiltonian, i.e. frequency independent formulation. Moreover, the procedure does not necessitate the analytical continuation to the real-frequency axis, since only the zero energy limit of the self-energy intervenes.

The, in this sense, "renormalized band-structure" is then given by the solutions $\omega_{\mathbf{k}}$ of

$$\det \left(\omega_{\mathbf{k}} - \mathbf{Z} \left[\mathbf{H}^{LDA}(\mathbf{k}) + \Re\mathbf{\Sigma}(i\omega \to 0) - \mu \right] \right) = 0 \qquad (3.10)$$

i.e. by the eigenvalues of the matrix

$$\mathbf{Z}\left[\mathbf{H}^{LDA}(\mathbf{k}) + \Re\Sigma(i\omega \to 0) - \mu\right] \tag{3.11}$$

where $\mathbf{Z}^{-1} = 1 - \partial_\omega\Im\Sigma(i\omega)|_{i\omega\to 0}$, or $\mathbf{Z}^{-1} = 1 - \partial_\omega\Re\Sigma(\omega)|_{\omega=0}$ is the renormalization (matrix) factor as obtained from the Matsubara or the real-frequency self-energy, respectively. $[i\Im\boldsymbol{\Sigma}]\,\Re\boldsymbol{\Sigma}$ denotes the [anti-] hermitian part of the self-energy, as usual. According to the validity of the low energy expansion of the self-energy, the resulting band-structure will be exact at the Fermi-level[5]. That means in particular that the correlation induced changes in the Fermi surface are correctly captured by this approach. Naturally, the renormalized band-structure will deviate from the exact pole solutions, once the self-energy is no longer in its linear regime.

In the case of a half-filled one-band case, $\Re\Sigma(0)$, is zero, and the only effect of correlations within this linearized scheme is a band-width narrowing, the dispersion $\epsilon_\mathbf{k} = H^{LDA}(\mathbf{k})$ evolving to $\widetilde{\epsilon}_\mathbf{k} = Z\epsilon_\mathbf{k}$ with $Z < 1$. Therewith the emerging "band" no longer carries the weight one, but incoherent features, on which this scheme however gives no further information, pick up the spectral weight $1 - Z$. Thus, the "counting" of bands such as to determine the occupation is no longer a sensible procedure.

In the multi-band case, the different values of $\Re\Sigma(0)$ for the individual orbitals will induce relative shifts, corresponding to correlation induced crystal field splittings. As a matter of fact, the current linearization can, mathematically, still be undertaken for an insulating phase that is realized by such an alternation of crystal fields. Yet, when using the above construction one should no longer interpret the Z values as quasi-particle weights, since the latter have no meaning in an insulator. In the case of a divergent self-energy as is the case for the insulating phase of the one-band Hubbard model, the linearization is obviously senseless.

A.b.iii   Graphical construction

In the one-band case Equation (3.9) reduces to the scalar equation

$$\omega_\mathbf{k} + \mu - \epsilon_\mathbf{k} - \Re\Sigma(\omega_\mathbf{k}) = 0 \tag{3.12}$$

i.e. solutions are given by the intersections of the real-part of the self-energy (minus μ) with a frequency stripe of slope one and a vertical width corresponding to the dispersion of $\epsilon_\mathbf{k}$.

The frequency dependence of the self-energy leads to interesting phenomena that are beyond the eigenvalue problem of the non-interacting problem. In particular the number of poles for a given momentum $\mathbf{k}$ is no longer restricted to the number of bands in the one-particle Hamiltonian. On the contrary, in a correlated system one expects to find

---

[5]We recall that we assumed the anti-hermitian part of the self-energy at low energy to be negligible.

in certain cases more poles in the Green's function, representing spectral weight in the Hubbard bands. Indeed, while in the band limit, $\Sigma(\omega) = 0$, only one possible pole per orbital arises, in the atomic limit, $\Sigma(\omega) = \frac{U^2}{4\omega}$, both, the upper and the lower Hubbard band, in the half-filled one-band Hubbard model (see above), are zeros of the denominator of the Green's function, given by $\omega_{\mathbf{k}} = \epsilon_{\mathbf{k}}/2 \pm 1/2\sqrt{\epsilon_{\mathbf{k}}^2 + U^2}$.
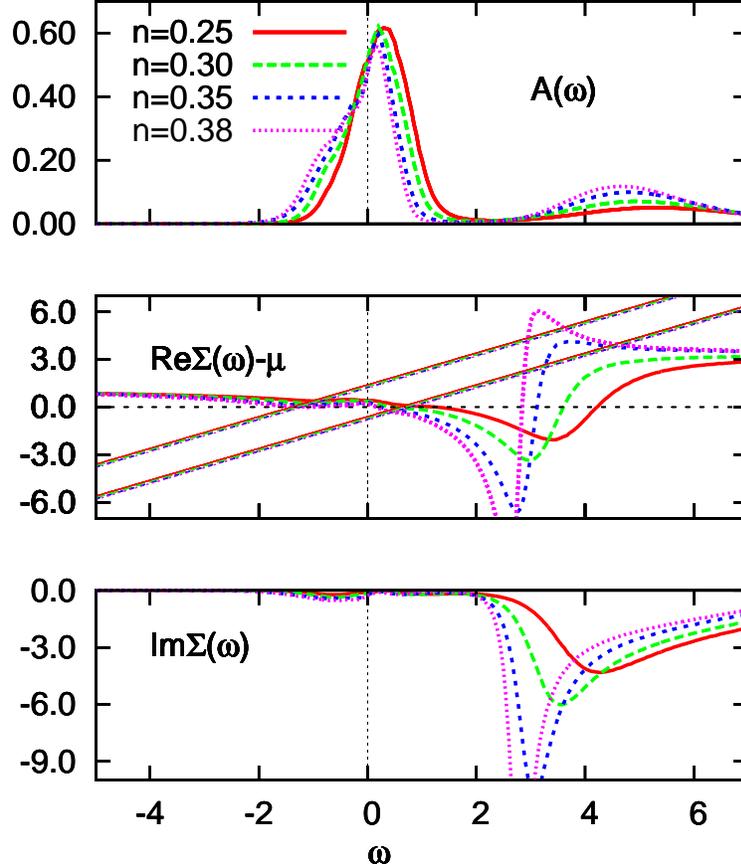
Figure 3.2 : *Graphical construction for finding one-particle poles. From top to bottom : Local spectral function $A(\omega)$, real parts of the self-energy $\Re\Sigma(\omega)$, where the frequency stripes delimits the non-interacting bandwidths, imaginary parts of the self-energy. Bethe lattice calculation with $U = 5.0$ and $\beta = 12$ for the indicated particle number.*

In between these two limits several scenarios, depending on doping and interactions, can be realized. The famous three-peak structure may in particular correspond to three solutions of the above quasi-particle equation. As we shall see for V_2O_3 and VO_2, it is possible to have an asymmetric case in which only the lower or the upper Hubbard band results from poles.

Figure 3.2 shows an example calculation : Indeed the upper Hubbard band becomes a pole of the one-particle Green's function (when assuming $\Im\Sigma = 0$) above a certain doping. Then the real-part of the self-energy crosses the indicated frequency stripe. Still, the spectral weight of the poles upon entering the stripe from low energies, is suppressed

by the enormous imaginary part, which is responsible for the depletion between the quasi-particle peak and the upper Hubbard band. The poles at higher energies, where $\Im\Sigma$ has decreased, are responsible for the spectral weight of the Hubbard band. As a matter of fact, from only the local spectral function, it is not visible whether a Hubbard band arises due to a pole like behaviour, or only because of a pole proximity. Yet, the dispersion of the two types of Hubbard bands is different.

In the non-degenerate multi-orbital case this graphical construction is no longer exact, since due to non-vanishing hybridization elements in the Hamiltonian, the determinant does no longer factorize into individual band contributions. Yet, the procedure might still give qualitative insights, as we shall see in the material specific chapters.

At this point we mention a small technicality concerning the width of the frequency stripe that intersects the self-energy. When working out the quasi-particle Equation (3.9), say with a constant and diagonal self-energy $\mathbf{\Sigma} = \begin{pmatrix} \Sigma_1 & 0 \\ 0 & \Sigma_2 \end{pmatrix}$, and a Hamiltonian $\mathbf{H}(\mathbf{k}) = \begin{pmatrix} \epsilon_{\mathbf{k}}^1 & V_{\mathbf{k}} \\ V_{\mathbf{k}}^* & \epsilon_{\mathbf{k}}^2 \end{pmatrix}$, one realizes that in the low hybridization limit $V_{\mathbf{k}} \ll \epsilon_{\mathbf{k}}$, the width of the frequency stripe is actually not quite given by the dispersion of the one-particle eigenvalues $E_{\mathbf{k}} = \frac{1}{2}\left(\epsilon_{\mathbf{k}}^1 + \epsilon_{\mathbf{k}}^2\right) \pm \frac{1}{2}\sqrt{\left(\epsilon_{\mathbf{k}}^1 - \epsilon_{\mathbf{k}}\right)^2 + 4\left|V_{\mathbf{k}}\right|^2}$, but more correctly by the "un-hybridized" dispersions $\epsilon_{\mathbf{k}}^{1,2}$. We will come back to this when discussing the oxides VO_2, and V_2O_3. Indeed, while using the concept of "un-hybridized" bands in the latter, we will find an orbital basis for the M1 phase of the former in which the self-energy and, approximately, also the Hamiltonian is diagonal, therewith rendering this graphical construction applicable.

Chapter 4

Optical Properties of Correlated Materials

A Introduction

A.a Putting optical spectroscopy into perspective

Unraveling the electronic structure of matter is at the heart of condensed matter physics. Various spectroscopic techniques have been designed to experimentally probe the electronic properties and to deepen our understanding thereof : (Angle Resolved) Photoemission spectroscopy ((AR)PES), X-ray, Raman, Electron Energy Loss Spectroscopy (EELS) and optics, to name only a few.

Optical spectroscopy is, in a way, the most natural spectroscopic technique among them. Optical detectors are sampling the response to incident light, as do our eyes, albeit accessing frequencies, and thus phenomena, that are beyond our vision.

Due to the low energy of the incident light, the optical response probes electron transitions at constant particle number, between occupied and unoccupied states of the solid. This effect of the interaction of light with matter can be cast into various response functions, that are, however, equivalent, in the sense that they contain the same information. For example, the dielectric tensor $\epsilon_{\alpha\beta}$ gives the relation between the total electric field $\mathbf{E}$ in the solid and the displacement field $\mathbf{D}$

$$D_\alpha(\mathbf{r}, t) \;\; = \;\; \int d^3r' \, dt \, \epsilon_{\alpha\beta}(\mathbf{r}, \mathbf{r}', t - t') E_\beta(\mathbf{r}', t') \tag{4.1}$$

In this chapter we shall concentrate on the optical conductivity $\sigma_{\alpha\beta}$ that gives the response relation between the electric field and the current $\mathbf{J}$

$$J_\alpha(\mathbf{r}, t) \;\; = \;\; \int d^3r' \, dt \, \sigma_{\alpha\beta}(\mathbf{r}, \mathbf{r}', t - t') E_\beta(\mathbf{r}', t') \tag{4.2}$$

When assuming a local relationship between the perturbation and the response,

$$\sigma_{\alpha\beta} = J_\alpha(\mathbf{r})/E_\beta(\mathbf{r}) \tag{4.3}$$

the response function σ does not have any Fourier component other than the one for $\mathbf{q} = 0$. This can be further justified (see below) by saying that the momentum transfer by the incident photon is negligible, leading to the dipole approximation. Furthermore, since any response function obeys causality, its real and imaginary parts are connected by a Kramers-Kronig transform, see e.g. Equation (3.7).

From Maxwell's equations it follows that the two quantities from above are simply related by[1]

$$\epsilon_{\alpha\beta}(\omega) \;\; = \;\; \epsilon_0 + \frac{\imath}{\omega}\sigma_{\alpha\beta}(\omega) \tag{4.4}$$

with the permittivity of the vacuum, $\epsilon_0 = 8.8542 \cdot 10^{-12}\frac{\text{S}}{\Omega\text{m}}$. Other optical response functions are readily computed, once one of them is known, examples are the complex refraction index

$$n_{cgs}(\omega) \;\; = \;\; \sqrt{\epsilon_{cgs}(\omega)} \tag{4.5}$$

and the reflectivity $R = |R|\, e^{\imath\theta}$. Its absolute value for incident light along the normal of the sample surface is given by

$$|R(\omega)| \;\; = \;\; \left|\frac{n_{cgs}(\omega) - 1}{n_{cgs}(\omega) + 1}\right|^2 \tag{4.6}$$

The latter quantity is what is normally measured experimentally. From its knowledge, one computes the optical conductivity or the dielectric function, which are more transparent in their physical interpretation. Experimentally accessible is the absolute value of the complex reflectivity over a finite frequency range $[\omega_{min} > 0, \omega_{max} < \infty]$[2]. However, according to the above formulas, the determination of the optical conductivity, or any other response function, necessitates the knowledge of the complex reflectivity, i.e. also of the above mentioned phase θ. In order to make use of the Kramers-Kronig relation one thus has to extrapolate the experimental data to zero and infinite frequency. Then, any other transformation is local in frequency and the desired quantities are calculable. Another way is to make an ansatz for the dielectric function and to fit the measured reflectivity. This is in particular useful when performing experiments on thin films, where one has to account for multiple reflections due to the substrate. Details can be found in experimental works, see e.g. [Zimmers(2004), Tomczak(2004)].

---

[1]The following, unless stated otherwise, all formulas are expressed in SI units. In the commonly used cgs system the current relation reads $\epsilon = 1 + \frac{4\pi\imath}{\omega}\sigma$.

[2]There exists a technique called ellipsometry which measures both the absolute value and the phase factor by changing the incident angle of the light. The setup is however rather complicated to implement into a cryostat, which is why it has so far not become a common technique beyond room-temperature measurements.

Response functions, like the optical conductivity, are genuine two-particle quantities. Yet when neglecting vertex corrections (see also Section B), which we will (have to) do throughout this thesis, the final expression for the optical conductivity is rather handy and allows for a direct interpretation of the underlying excitations.

Here, a word on methodology is in order. While it is of course desirable to calculate quantities as conceptually accurate as possible, one has to make a tradeoff between sternness and applicability. In this thesis our interest is on realistic systems. Here we therefore opt for pursuing the route of realism in favour of conceptual pureness.

We think it useful to state our end formula, Equation (4.49), of the optical conductivity, before making introductory comments :

$$\Re\sigma_{\alpha\beta}(\omega) \quad = \quad \frac{2\pi e^2 \hbar}{V} \sum_{\mathbf{k}} \int d\omega' \frac{f(\omega') - f(\omega' + \omega)}{\omega} \, \mathrm{tr}\left\{ v_\alpha(\mathbf{k})A(\mathbf{k},\omega')v_\beta(\mathbf{k})A(\mathbf{k},\omega' + \omega) \right\}$$

$$(4.7)$$

In the above, the $v_\alpha(\mathbf{k})$ are transition matrices, or Fermi velocities, and $A(\mathbf{k},\omega)$ are the momentum resolved spectral functions. Both quantities are matrices in orbital space, over which is taken the trace. The Fermi function is denoted by $f(\omega)$. Thus the conductivity is given by a simple convolution of spectral functions at the same momentum. This states nothing else than that (in the dipole approximation), transitions are vertical, in the sense that the photon does not transfer any momentum to the system. Therewith it is clear that, for an insulator, the optical gap, i.e. the energy at which absorptions sets in, may differ considerably from the gap of the band-structure or excitation spectrum, which can indeed be indirect.
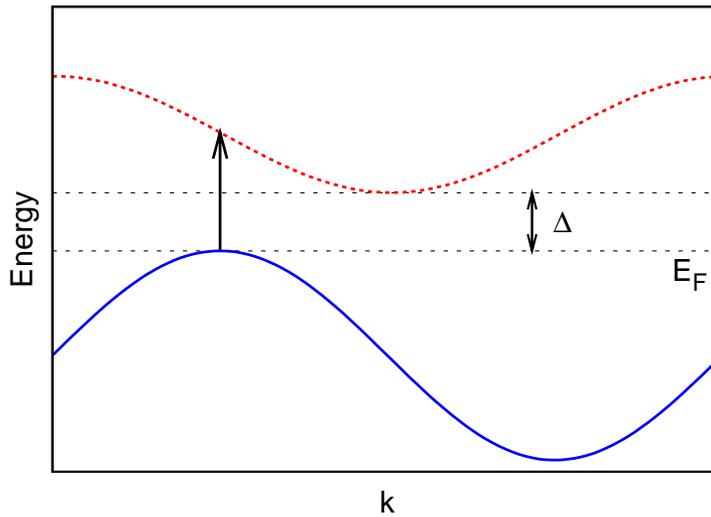

Figure 4.1 : *Schema of an optical transition in the band picture. Transitions are "vertical", since no momentum transfer occurs. Therewith the optical gap might differ considerably from the charge gap in the excitation spectrum.*

Further, the weight of a transition at a particular point in the Brillouin zone is controlled by the Fermi velocities. Contrary to photoemission experiments that can be performed angle resolved, optical spectroscopy always measures a response that is averaged over the entire Brillouin zone. However, the intervening transition matrix elements depend on the light polarization, and, hence, one can influence the weighting of different regions in momentum space by either using polarized light, or by changing the orientation of the sample.

Moreover, as compared to (AR)PES experiments, optical transition matrix elements are less involved and, as we will see below, they are given by the elements of the momentum operator, evaluated for the non-interacting system[3].

A further advantage of optical spectroscopy is that, contrary to photoemission, it is a true bulk probe, since the skin penetration depth (for metals) is typically of the order of several nm in the infrared, whereas the relevant length scale in photoemission, the electron escape depth, is only of the order of $\sim$3-30Å, depending mostly on the energy of the incident beam.

A.b   Introductory examples and phenomenology

A.b.i   The optical response of a one-particle band-structure

When using a band-structure method for the calculation of the excitation spectrum of a solid, the spectral functions $A(\mathbf{k}, \omega)$ of the system become Dirac distributions and the trace in Equation (4.7) is[4]

$$\sum_{m,n} \delta(\omega' + \nu + \mu - \epsilon_{\mathbf{k}}^m) v(\mathbf{k})_{mn} \delta(\omega' + \mu - \epsilon_{\mathbf{k}}^n) v(\mathbf{k})_{nm} \tag{4.8}$$

We see that at zero frequency $\nu = 0$, only inter-band transitions, $m \neq n$, make a contribution. Thus, in the one band case, the optical conductivity is a delta function at zero frequency. This is just the result of the fact that without interactions (electron-electron or a coupling to a bosonic mode) or disorder, the lattice momentum $\mathbf{k}$ is a constant of motion and the current thus does not decay.

A.c   The Drude model for metals

In the non-interacting case from above, the response of a metal to an electric field is infinite. It was P. Drude in 1900 who derived an expression that takes into account the finite lifetime of the electron excitations, by introducing a relaxation time τ for the charge current $j(t) = j(0)e^{-t/\tau}$. His expression for the conductivity can be recovered from

---

[3]Linear response quantities only involve expectation values of the non-perturbed system. Here, however, we mean by non-interacting, that the electron-electron interactions do not appear in the calculations of the transition matrix elements. A thorough derivation will be given below.

[4]for simplicity we assume to work in the Kohn-Sham basis, i.e. A is diagonal.

our linear response result, Equation (4.7), by assuming free particles, $\epsilon_\mathbf{k} = \frac{\hbar^2 k^k}{2m}$, and a constant self-energy $\Sigma = -\frac{i}{2\tau}$. The resulting optical conductivity is then given by

$$\Re\sigma(\omega) = \frac{ne}{m}\frac{\tau}{1+\omega^2\tau^2} \tag{4.9}$$

with n being the average charge carrier density. Hence, the response at zero frequency is finite and non-zero at finite energies. Moreover, it obeys the f-sum rule, see Section C.

A.d Phenomenology of the optical response of the one band Hubbard model

While accounting well for the response of band-like metals, the Drude formula is insufficient, even in the one-band case, in the presence of correlation effects.
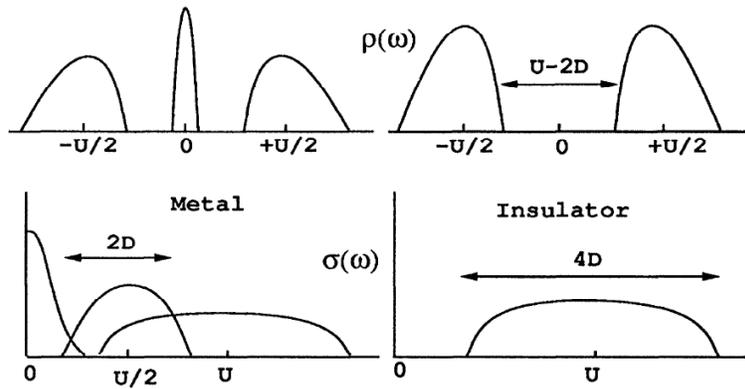
Figure 4.2 : *Schema for optical transitions in the one-band Hubbard model. The top row shows a metallic and insulating local spectral function, the bottom displays the corresponding optical conductivities. From [Rozenberg et al. (1995)].*

Indeed, the influence of correlation effects is beyond a mere broadening of bands. For the case of the one-band Hubbard model within DMFT, the paramount characteristic is the appearance of Hubbard satellites. Therewith, not only transitions within a broadened quasi-particle peak are possible, but also transitions from and to these Hubbard bands arise. Figure 4.2 shows a schematic picture. In the metal (to the left) two additional contributions arise, stemming on the one hand from transition between the quasi-particle peak and the individual Hubbard bands. This is often referred to as the mid-infrared peak, due to its location in energy in some compounds. At higher energy, transitions between the two Hubbard bands appear. In the insulating phase, only the latter survive, as shown to the right. Therewith the possible richness of optical spectra is considerably enhanced.

A.e   Prior DMFT related work – a brief review

Within the field of strongly correlated electrons, calculations of the optical conductivity within the DMFT framework were first performed by [Pruschke *et al.* (1993b), Jarrell *et al.* (1995)] for the case of the Hubbard model. In an important work, [Rozenberg *et al.* (1995), Rozenberg *et al.* (1996)] studied the phenomenology of the different optical responses of the Hubbard model throughout its phase diagram in conjunction with experiments on V_2O_3. In the realistic LDA+DMFT context, optical conductivity calculations were first performed by [Blümer(2002), Blümer and van Dongen(2003)] for the case of degenerate orbitals. A more general approach, was developed in [Pálsson(2001)] for the study of thermo-electricity. Our work goes along the lines of the mentioned approaches. We will however use a full Hamiltonian formulation, therewith allowing for the general case of non-degenerate orbitals, and we extent the intervening Fermi velocities to multi-atomic unit cells, which becomes crucial in calculations for realistic compounds.

An alternative technique was presented by [Oudovenko *et al.* (2004)]. Their idea is to diagonalize the interacting system, which allows for the analytical performing of some occuring integrals due to the "non-interacting" form of the Green's function. Owing to the frequency-dependence of the self-energy, however, the diagonalization has to be performed for each momentum and frequency separately, and involves, because of the non-hermitian nature of the problem, left and right eigenvectors, and so the procedure may become numerically expensive. So far this technique was only applied to LDA+DMFT calculations that employed approximate impurity solvers. Relying on our scheme for the analytical continuation of Matsubara self-energies, see Section , Chapter 3, we are, in our application, able to make use of numerically exact quantum Monte Carlo data.

B   Optical Conductivity –
a formalism for realistic calculations

In this section, we will present a formalism for the optical conductivity with focus on realistic correlated materials. We generalize the approach used for simple lattice systems to the case of realistic multi-orbital solids. As we shall see, the Peierls substitution, a simple way to couple the light field to a lattice model, can be extended to both, multi-band and multi-atomic systems. Yet, even in the lattice model case, this approach is not complete, since it is neglecting intra-atomic transitions.

Starting from a formulation in the continuum and developing relevant quantities in a localized basis set, we will show that the Peierls term is recovered as an approximation to the full current matrix element. In our formulation, additional contributions turn up. On the one hand we can account for intra-atomic transitions. On the other, the spatial extensions of the wavefunctions of the system generate corrections to the pure lattice model approach.

In this work, we shall entirely neglect vertex corrections. In the limit of infinite coordination the latter do vanish for a model with one atom per unit cell. In finite dimensions and in the multi-orbital context, this is however an approximation. Yet, this

allows us to compute the conductivity from the knowledge of the (momentum-resolved) one-particle Green's function. By this decoupling of the two-particle response function, particle-hole interactions are neglected.

B.a　Physical quantities

Applying an external time-dependent electric field to a solid, induces currents and changes the actual electric field in the solid. The conductivity tensor σ is defined as the response function relating the total electric field $\mathbf{E}$[5] in the solid with the current density $\mathbf{J}$.

$$\mathbf{J}(\mathbf{r}, t) = \int d^3 r' \int_{-\infty}^{t} dt' \sigma(\mathbf{r}, \mathbf{r}', t - t') \mathbf{E}(\mathbf{r}', t') \tag{4.10}$$

with the electric field

$$\mathbf{E}(\mathbf{r}, t) = \mathbf{E}_0 \exp\left[\imath(\mathbf{q} \cdot \mathbf{r} - \omega t)\right] \tag{4.11}$$

that we assume to consist of a single $(\mathbf{q}, \omega)$ mode. Supposing that the response at the position $\mathbf{r}$ to the field at $\mathbf{r}'$ only depends on the vectorial distance $\mathbf{r} - \mathbf{r}'$, i.e. $\sigma(\mathbf{r}, \mathbf{r}', t - t') = \sigma(\mathbf{r} - \mathbf{r}', t - t')$ we can write

$$\mathbf{J}(\mathbf{r}, t) = \sigma(\mathbf{q}, \omega) \mathbf{E}(\mathbf{r}, t) \tag{4.12}$$

This is true for homogeneous systems. For solids, this is however not quite justified : Looking e.g. at atomic-like core states and the symmetry of their wave-functions, it is clearly not admissible to neglect the actual positions of the perturbation and its effects. Nonetheless, we will proceed with this simplification, because of the following (see e.g. [Mahan(1990)]) :

On the one hand, optical spectroscopy is not strictly a local probe of the system. This allows us to consider a charge current that has been averaged over many unit cells. On the other hand, the wavelength of the external source is large compared to the typical relevant length scale of the solid, i.e. the penetration depth, thus, in the end, we shall neglect spatial variations of the field and take interest in the limit of long wavelengths only, i.e. in the limit of zero momentum transfer, $\mathbf{q} \to 0$.

In this spirit, the term "optical conductivity" refers to the real part of the conductivity tensor, after taking the above limit, i.e. $\Re\sigma(\mathbf{q} = 0, \omega)$. Its zero frequency limit is the usual dc conductivity.

The capital $\mathbf{J}$ above denotes the expectation value of the quantum mechanical operator for the charge current density $\mathbf{j}$.

$$\mathbf{J}(\mathbf{r}, t) = \langle \mathbf{j}(\mathbf{r}, t) \rangle \tag{4.13}$$

whose determination now follows.

---

[5]i.e. the external plus the induced one : $\mathbf{E} = \mathbf{E}^{ext} + \mathbf{E}^{ind}$

B.b   The charge current density

There are different routes to derive the charge current density stated above. The starting point is the Hamiltonian of the system, defined in the continuum, which we write

$$\mathbf{H} = \mathbf{H}_0^A + \mathbf{H}_{int} \tag{4.14}$$

where

$$\mathbf{H}_0^A = \sum_\sigma \int \mathrm{d}^3\mathrm{r} \ \Psi_\sigma^\dagger(\mathbf{r}, t) \left[\frac{1}{2m} \left(-\imath\hbar\nabla - \frac{e}{c}\mathbf{A}(\mathbf{r}, t) \right)^2 + V(\mathbf{r}) \right] \Psi_\sigma(\mathbf{r}, t) \tag{4.15}$$

is the one-particle part of the Hamiltonian with the coupling to the (classical) light field via its vector potential $\mathbf{A}(\mathbf{r}, t)$. The form of the Hamiltonian is guided by the demand of gauge invariance and the request to yield the usual Lorentz equations of motion. This is often called the minimal coupling.

Here and in the following the Coulomb gauge $\mathrm{div}\mathbf{A} = 0$ is assumed. Moreover we only consider electric fields that are transverse : $\mathrm{rot}\mathbf{E} = 0$. The relation with the vector potential then reads $\mathbf{E} = -\frac{1}{c}\partial_t\mathbf{A}$, or

$$\mathbf{A}(\mathbf{q}, \omega) = \frac{c}{\imath\omega}\mathbf{E}(\mathbf{q}, \omega) \tag{4.16}$$

$\mathbf{H}_{int}$ contains electron interactions and, in principle, couplings to bosonic modes, such as phonons that we will however not consider. Furthermore we assume the electron interactions to be of a two-body form[6].

B.b.i   Continuity equation

By Noether's theorem, each symmetry of the system corresponds to a conserved quantity. The above Hamiltonian, Equation (4.14), is clearly invariant under

$$\begin{aligned} \Psi(\mathbf{r}, t) &\rightarrow \Psi(\mathbf{r}, t)\, e^{\imath\varphi(\mathbf{r})} \\ \mathbf{A}(\mathbf{r}, t) &\rightarrow \mathbf{A}(\mathbf{r}, t) - \frac{c\hbar}{e}\nabla\varphi(\mathbf{r}) \end{aligned} \tag{4.17}$$

for any scalar field $\varphi(\mathbf{r})$. This gauge invariance leads to charge conservation, thus to the continuity equation :

$$e\, \dot\rho\,(\mathbf{r}, t) = -\mathrm{div}\mathbf{j}(\mathbf{r}, t) \tag{4.18}$$

from which we will determine the current density $\mathbf{j}(\mathbf{r}, t)$. Here

$$\rho(\mathbf{r}, t) = \sum_\sigma \rho_\sigma(\mathbf{r}, t) = \sum_\sigma \Psi_\sigma^\dagger(\mathbf{r}, t)\Psi_\sigma(\mathbf{r}, t) \tag{4.19}$$

---

[6]Thereby the interaction term commutes with the charge density, which will simplify the following. Analogous, when starting with a lattice formulation, one has to restrict the interaction vertex to terms that are of density-density type in the lattice creation and annihilation operators, which, from a conceptual point of view, is a much more limiting assumption.

is the electron density. Its equation of motion reads

$$\imath\hbar\,\dot{\rho}\,(\mathbf{r},t) = [\mathbf{H}, \rho(\mathbf{r},t)] \tag{4.20}$$

ρ being the electron density, it commutes with an interaction part $\mathbf{H}_{int}$ of the Hamiltonian, that involves two-body terms only, as assumed above. Thus, only the one-particle part enters the calculation at this stage. Evaluating the commutator yields

$$[\rho(\mathbf{r},t), \mathbf{H}] \;=\; \sum_{\sigma} \frac{\hbar^2}{2m} \mathrm{div}\left\{\Psi_\sigma^\dagger(\mathbf{r},t)\nabla\Psi_\sigma(\mathbf{r},t) - \left(\nabla\Psi_\sigma^\dagger(\mathbf{r},t)\right)\Psi_\sigma(\mathbf{r},t)\right\} \tag{4.21}$$

$$+\imath\frac{\hbar e}{mc}\mathbf{A}(\mathbf{r},t)\mathrm{div}\rho(\mathbf{r},t) \tag{4.22}$$

from which we identify

$$\mathbf{j}(\mathbf{r},t) \;=\; -\imath\frac{e\hbar}{2m}\sum_{\sigma}\left\{\Psi_\sigma^\dagger(\mathbf{r},t)\nabla\Psi_\sigma(\mathbf{r},t) - \left(\nabla\Psi_\sigma^\dagger(\mathbf{r},t)\right)\Psi_\sigma(\mathbf{r},t)\right\} + \frac{e^2}{mc}\mathbf{A}(\mathbf{r},t)\rho(\mathbf{r},t)$$

$$\;=\; -\mathcal{H}\left\{\imath\frac{e\hbar}{m}\sum_{\sigma}\Psi_\sigma^\dagger(\mathbf{r},t)\nabla\Psi_\sigma(\mathbf{r},t)\right\} + \frac{e^2}{mc}\mathbf{A}(\mathbf{r},t)\rho(\mathbf{r},t) \tag{4.23}$$

where $\mathcal{H}$ denotes the hermitian part.

B.b.ii Conjugated variables

Indeed, we notice that with the above we can write

$$\mathbf{H}_0^A \;=\; -\frac{1}{c}\int \mathrm{d}^3\mathrm{r}\,\mathbf{j}(\mathbf{r},t)\cdot\mathbf{A}(\mathbf{r},t) + \int \mathrm{d}^3\mathrm{r}\,\rho(\mathbf{r},t)V(\mathbf{r},t) \tag{4.24}$$

Hence the current density is the conjugated variable of the vector potential and, thus, the former may be *defined* as

$$\mathbf{j}(\mathbf{r},t) = -c\frac{\delta\mathbf{H}_0^A}{\delta\mathbf{A}(\mathbf{r},t)} \tag{4.25}$$

B.b.iii The paramagnetic and the diamagnetic current

The two terms of the current density (4.23) do not, on general grounds, acquire a clear physical meaning each on their own, as they are linked by the condition of gauge invariance (4.17). In the Coulomb gauge, however, they do have a clear interpretation : We can separate

$$\mathbf{j}(\mathbf{r},t) = \mathbf{j}_P(\mathbf{r},t) + \mathbf{j}_D(\mathbf{r},t) \tag{4.26}$$

into the "paramagnetic" term

$$\mathbf{j}_P(\mathbf{r}, t) = -\mathcal{H} \sum_{\sigma} \left\{ \imath \frac{e\hbar}{m} \Psi_{\sigma}^{\dagger}(\mathbf{r}, t) \nabla \Psi_{\sigma}(\mathbf{r}, t) \right\} \tag{4.27}$$

and the "diamagnetic" term

$$\mathbf{j}_D(\mathbf{r}, t) = \frac{e^2}{mc} \mathbf{A}(\mathbf{r}, t) \rho(\mathbf{r}, t) \tag{4.28}$$

Then the expectation value of the current density (4.13) reads :

$$\mathbf{J}(\mathbf{r}, t) = \langle \mathbf{j}_P(\mathbf{r}, t) \rangle + \frac{ne^2}{mc} \mathbf{A}(\mathbf{r}, t) \tag{4.29}$$

with $n = 1/V \int \mathrm{d}^3\mathbf{r} \, \langle \rho(\mathbf{r}, t) \rangle$, where, again, we have neglected spatial variations of the vector potential (see above). With Equation (4.16) and Equation (4.12) we find for the diamagnetic contribution to the conductivity tensor :

$$\sigma_{xx}(\omega) = \frac{\imath}{\omega} \frac{ne^2}{m} \tag{4.30}$$

where we have assumed a vector potential along the x-axis, $\mathbf{A} \sim (1\,0\,0)^{\mathrm{T}}$. The diamagnetic response thus has no contribution to the optical conductivity $\Re\sigma(\omega)$. However, we will see later that the above term is crucial for the optical conductivity sum rule.

B.b.iv   Interpretation

In order to elucidate the labeling of the two currents, consider an electric field pulse $\mathbf{E}(t) = \mathbf{E}_0 \delta(t)$. Then we have, with Equation (4.16), $\mathbf{A} = -\mathbf{E}_0 \theta(t) + const$ and

$$\mathbf{J}(\mathbf{r}, t) = \langle \mathbf{j}_P(\mathbf{r}, t) \rangle - \frac{ne^2}{m} \mathbf{E}_0 \theta(t) \tag{4.31}$$

Thus the diamagnetic current sets in immediately when the pulse is applied and stays forever. It is the paramagnetic current, and hence the time evolution of the wavefunction of the system that compensates for the diamagnetic part, as the total current must decay on the time scale of some inverse scattering rate [Coleman(2004)], as e.g. in the Drude model, see Section A.

B.c   Kubo formula

In order to allow for a coherent discussion of the Fermi velocity matrix elements, we shall at this point only state that the paramagnetic current, when developing it into a localized basis set, and within the dipole approximation ($\mathbf{q} = 0$), can be written as, Equation (4.67) :

$$j^\alpha(\mathbf{q}=0,\tau) \;=\; e\sum_{\mathbf{k},LL',\sigma} v_{\mathbf{k},\alpha}^{L'L}\mathbf{c}_{\mathbf{k}L'\sigma}^\dagger(\tau)\mathbf{c}_{\mathbf{k}L\sigma}(\tau) \tag{4.32}$$

with the usual fermionic creation and annihilation operators $\mathbf{c}_{\mathbf{k}L\sigma}$, where L=(n,l,m,$\gamma$) is a multi-band index (n,l,m) of atom γ in the unit cell. α denotes the cartesian coordinate of the current vector[7]. The derivation is postponed to Section B.

We then resort to the Kubo Formula of linear response theory. Given the coupling of the vector potential to the current, Equation (4.24), when assuming a vector potential along the β–direction, the response is given by [Mahan(1990), Coleman(2004)]

$$
\begin{aligned}
\langle j_P^\alpha(\mathbf{r},t)\rangle &= \frac{\imath}{\hbar c}\int_{-\infty}^t \mathrm{d}t' \int \mathrm{d}^3\mathbf{r}\,'\left\langle\left[j_P^\alpha(\mathbf{r},t),j_P^\beta(\mathbf{r}',t')\right]\right\rangle A_\beta(\mathbf{r}',t') \\
&= \frac{1}{\hbar\omega}\int_{-\infty}^t \mathrm{d}t'\left\langle\left[j_P^\alpha(\mathbf{r},t),j_P^\beta(\mathbf{q},t')\right]\right\rangle E_{0\beta}e^{-\imath\omega t'} \\
&= \frac{1}{\hbar\omega}\int_{-\infty}^t \mathrm{d}t'\left\langle\left[j_P^\alpha(\mathbf{r},t),j_P^\beta(\mathbf{q},t')\right]\right\rangle e^{\imath\omega(t-t')}e^{-\imath\mathbf{qr}}E_\beta(\mathbf{r},t) \\
&= \frac{1}{\hbar\omega}\int_0^\infty \mathrm{d}t'\left\langle\left[j_P^\alpha(\mathbf{r},t'),j_P^\beta(\mathbf{q},0)\right]\right\rangle e^{\imath\omega t'}e^{-\imath\mathbf{qr}}E_\beta(\mathbf{r},t) \tag{4.33}
\end{aligned}
$$

where use has been made of Equation (4.16), Equation (4.11) and of homogeneity of time. With Equation (4.12) it thus follows

$$\sigma_P^{\alpha\beta}(\mathbf{q},\omega) \;=\; \frac{1}{\hbar\omega}\int_0^\infty \mathrm{d}t\left\langle\left[j_P^\alpha(\mathbf{r},t),j_P^\beta(\mathbf{q},0)\right]\right\rangle e^{\imath\omega t}e^{-\imath\mathbf{qr}} \tag{4.34}$$

As mentioned before the response should be averaged over many unit cells. Hence we integrate over $\mathbf{r}$ and divide by the total volume V of the sample :

$$
\begin{aligned}
\sigma_P^{\alpha\beta}(\mathbf{q},\omega) &= \frac{1}{\hbar\omega V}\int_0^\infty \mathrm{d}t \int \mathrm{d}^3\mathbf{r}\,\left\langle\left[j_P^\alpha(\mathbf{r},t),j_P^\beta(\mathbf{q},0)\right]\right\rangle e^{-\imath(\mathbf{qr}-\omega t)} \tag{4.35}\\
&= \frac{1}{\hbar\omega V}\int_0^\infty \mathrm{d}t e^{\imath\omega t}\left\langle\left[j_P^\alpha(-\mathbf{q},t),j_P^\beta(\mathbf{q},0)\right]\right\rangle \\
&= \frac{\imath}{\omega}\int_0^\infty \mathrm{d}t\chi_P^{\alpha\beta}(\mathbf{q},t)e^{\imath\omega t} \tag{4.36}
\end{aligned}
$$

with the current-current correlation function

$$\chi^{\alpha\beta}(\mathbf{q},t) \;=\; -\frac{\imath}{\hbar}\frac{1}{V}\left\langle\left[j^\alpha(-\mathbf{q},t),j^\beta(\mathbf{q},0)\right]\right\rangle \tag{4.37}$$

---

[7]In the entire chapter, k-sums run over the Brillouin zone, and our normalization convention is $\sum_{\mathbf{k}}=N$, with N being the number of unit-cell or the number of k-points in the Brillouin zone.

where we have dropped the index for the paramagnetic component. Then the optical conductivity becomes

$$\Re\sigma^{\alpha\beta}(\mathbf{q},\omega) \;=\; -\frac{\Im\chi^{\alpha\beta}(\mathbf{q},\omega)}{\omega} \tag{4.38}$$

which is a fluctuation-dissipation type theorem. In the following we will evaluate the current-current correlation function within the Matsubara formalism. In imaginary time, Equation (4.38) reads :

$$\chi^{\alpha\beta}(\mathbf{q},\tau) \;=\; -\frac{1}{\hbar V}\left\langle \mathcal{T} j^{\alpha}(-\mathbf{q},\tau), j^{\beta}(\mathbf{q},0) \right\rangle \tag{4.39}$$

If we were to know the exact eigenstates $|n\rangle$ and eigen-energies E_n, with the ground state $|0\rangle$ and E_0, the correlation function in frequency domain becomes
(see e.g. [Maldague(1977)])

$$\chi^{\alpha\alpha}(\mathbf{q},\omega) \;=\; \frac{1}{V}\sum_{n\neq 0}|\langle 0|j^{\alpha}(\mathbf{q})|n\rangle|^{2}\left(\frac{1}{\hbar\omega + E_n - E_0 + \imath 0^{+}} - \frac{1}{\hbar\omega - E_n + E_0 + \imath 0^{+}}\right) \tag{4.40}$$

where we have written the zero temperature expression, and thus

$$\Re\sigma^{\alpha\alpha}(\mathbf{q},\omega) = \frac{\pi\hbar}{V}\sum_{n\neq 0}|\langle 0|j^{\alpha}(\mathbf{q})|n\rangle|^{2}\frac{\delta\left(\hbar|\omega| - E_n + E_0\right)}{E_n - E_0} \tag{4.41}$$

This formula is e.g. handy for finite systems, where the eigenvalue problem can actually be solved. We, on the other hand, will have to resort to a different approach. Yet the above will be used to derive the f-sum rule, see below.

B.d   Evaluation of the current-current correlation function

Within the dipole approximation we are only interested in the limit of i.e. $\mathbf{q} = 0$ (see Equation (4.65) and Equation (4.66)). Then it follows

$$\chi^{\alpha\beta}(\mathbf{q}=\mathbf{0},\tau) \;=\; -\frac{1}{\hbar V}\left\langle \mathcal{T} j^{\alpha}(-\mathbf{q}=\mathbf{0},\tau) j^{\beta}(\mathbf{q}=\mathbf{0},0) \right\rangle \tag{4.42}$$

$$= -\frac{e^{2}}{\hbar V}\sum_{\mathbf{k}\mathbf{k}',LL',PP',\sigma\sigma'} v^{L'L,\sigma}_{\mathbf{k},\alpha} v^{P'P,\sigma'}_{\mathbf{k}',\beta}\left\langle \mathcal{T} \mathbf{c}^{\dagger}_{\mathbf{k}L'\sigma}(\tau)\mathbf{c}_{\mathbf{k}L\sigma}(\tau)\mathbf{c}^{\dagger}_{\mathbf{k}'P'\sigma'}(0)\mathbf{c}_{\mathbf{k}'P\sigma'}(0)\right\rangle$$

Noting that we treat the paramagnetic case only, i.e. our Green's function is diagonal in the spin-indices, we end up, when neglecting vertex corrections :

$$\chi^{\alpha\beta}(\mathbf{q}=\mathbf{0},\tau) \;=\; -\frac{\hbar e^{2}}{V}\sum_{\mathbf{k},LL',PP',\sigma} v^{L'L,\sigma}_{\mathbf{k},\alpha} G^{LP'\sigma}_{\mathbf{k}}(\tau) v^{P'P,\sigma}_{\mathbf{k},\beta} G^{PL'\sigma}_{\mathbf{k}}(-\tau) \tag{4.43}$$

Where we have introduced the one-particle Green's function $G_{ab}(\tau) = -1/\hbar \langle \mathbf{c}_a(\tau) \mathbf{c}_b^\dagger(0) \rangle$[8]. Indeed the expectation value in Equation (4.42) involves four fermionic operators and hence is a genuine two-particle quantity. When introducing the two-particle vertex Γ, irreducible in the particle-hole channel, we have in the frequency domain the following latter series

$$
\begin{aligned}
\chi(\imath\omega_n) &= -\sum_{\mathbf{k}\nu\sigma} v_\mathbf{k}^\sigma G^\sigma(\mathbf{k}, \imath\nu) G^\sigma(\mathbf{k}, \imath\nu + \imath\omega) v_\mathbf{k}^\sigma \\
&+ \sum_{\mathbf{k}\nu\sigma} \sum_{\mathbf{k}'\nu'\sigma'} v_\mathbf{k}^\sigma G^\sigma(\mathbf{k}, \imath\nu) G^\sigma(\mathbf{k}, \imath\nu + \imath\omega) \Gamma_{\mathbf{k}\mathbf{k}'}^{\sigma\sigma'}(\imath\nu, \imath\nu', \imath\omega) G^{\sigma'}(\mathbf{k}', \imath\nu') G^{\sigma'}(\mathbf{k}', \imath\nu' + \imath\omega) v_{\mathbf{k}'}^{\sigma'} \\
&+ \cdots
\end{aligned}
\tag{4.44}
$$

where, for sake of clarity we have implied the one-orbital case, and have dropped all constants. In the limit of infinite dimensions ($d \to \infty$), though the vertex function itself does have a momentum dependence, it can, in the latter sum, be replaced by a purely local quantity [Zlatic and Horvatic(1990), Georges *et al.* (1996)]. Then the above momentum sums can be performed individually for the terms of the form

$$
\sum_{\mathbf{k}\nu\sigma} v_\mathbf{k}^\sigma G^\sigma(\mathbf{k}, \imath\nu) G^\sigma(\mathbf{k}, \imath\nu + \imath\omega)
\tag{4.45}
$$

We will see later, Section B, that the Fermi velocity, $v_\mathbf{k}$, is given by the matrix elements of the momentum operator. In the one-band case, it follows from Bloch's theorem, that $\epsilon_{-\mathbf{k}} = \epsilon_\mathbf{k}$ and $\psi_{-\mathbf{k}}(r) = \psi_\mathbf{k}^*(r)$ and thus $\langle \mathbf{k}|P|\mathbf{k}\rangle = \frac{\hbar}{\imath} \int \mathrm{d}^3 r \ \psi_\mathbf{k}^*(r) \nabla \psi_\mathbf{k} = -\langle -\mathbf{k}|P| - \mathbf{k}\rangle$, from which it follows that the Fermi velocity is odd with respect to momentum : $v_{-\mathbf{k}} = -v_\mathbf{k}$, while the Green's function is even : $G(-\mathbf{k}, \omega) = G(\mathbf{k}, \omega)$. As a consequence the above quantity, Equation (4.45), is zero [Khurana(1990)], and all vertex corrections vanish in infinite dimensions. Since this is true for *any* $\mathbf{q} = 0$ correlation function in the $d \to \infty$ limit, one further realizes [Georges *et al.* (1996)] that $\sum_\mathbf{k} v_\mathbf{k} = 0$.

In the multi-orbital case, one finds $v_{-\mathbf{k}}^{LL'} = -v_\mathbf{k}^{L'L}$, which in general does not yield a well-defined parity. Also the Green's function $G(\mathbf{k}, \imath\omega) = [\imath\omega + \mu + H(\mathbf{k}) - \Sigma(\imath\omega)]^{-1}$ is even with respect to the momentum only for systems with inversion symmetry, $H(-\mathbf{k}) = H(\mathbf{k})$. Thus, even in infinite dimensions, vertex corrections do not drop out in the multi-orbital case.

Only in the case of a constant, real self-energy $\Sigma(\imath\omega)$, the one-band reasoning holds, since then one can use an energy-independent unitary transformation $U(\mathbf{k})$ that diagonalizes both Green's functions in Equation (4.45) at the same time, and the only intervening Fermi velocity matrix elements are diagonal ones, for which, as seen above, odd parity is assured.

Though this thus is an approximation, out of simple necessity we shall neglect vertex corrections also in the multi-orbital context throughout this work. The vertex function

---

[8]With this definition, the Green's function has the unit of an inverse energy. For the diagonal elements of the spectral function, $A_{aa}(\omega) = -1/\pi \Im G_{aa}(\omega)$, we then have the normalization $\int_{-\infty}^\infty \mathrm{d}\omega \ A_{aa}(\omega) = 1/\hbar$.

is in principle obtainable from a quantum Monte Carlo calculation, but this is rather cumbersome, let alone the fact that it needed to be continued to the real-frequency axis.

Continuing from Equation (4.43), we then have, when using an (orbital-)matrix notation :

$$\chi^{\alpha\beta}(\tau) \;=\; -\frac{2\hbar e^2}{V} \sum_{\mathbf{k}} \; \mathrm{tr}\big\{ v_\alpha(\mathbf{k}) G(\mathbf{k},\tau) v_\beta(\mathbf{k}) G(\mathbf{k},-\tau) \big\} \tag{4.46}$$

The two stems from the spin summation and the matrices are now for spin up (or down) components only. Fourier-transforming leads to

$$
\begin{aligned}
\chi^{\alpha\beta}(\imath\nu_n) \;&=\; \int_0^\beta \mathrm{d}\tau\, \chi^{\alpha\beta}(\tau) e^{\imath\nu_n\tau} \\
&=\; -\frac{2\hbar e^2}{V\beta^2} \sum_{m,p}\sum_{\mathbf{k}} \int \mathrm{d}\tau\, e^{\imath(\nu_n+\omega_m-\omega_p)\tau}\, \mathrm{tr}\big\{ v_\alpha(\mathbf{k}) G(\mathbf{k},\imath\omega_p) v_\beta(\mathbf{k}) G(\mathbf{k},\imath\omega_m) \big\} \\
&=\; -\frac{2\hbar e^2}{V\beta} \sum_{\mathbf{k}}\sum_{p} \int \mathrm{d}\omega' \int \mathrm{d}\omega\, \frac{1}{\omega'-\imath\omega_p}\frac{1}{\omega+\imath\nu_n-\imath\omega_p}\, \mathrm{tr}\big\{ v_\alpha(\mathbf{k}) A(\mathbf{k},\omega') v_\beta(\mathbf{k}) A(\mathbf{k},\omega) \big\} \\
&=\; -\frac{2\hbar e^2}{V} \sum_{\mathbf{k}} \int \mathrm{d}\omega' \int \mathrm{d}\omega\, \frac{\mathrm{f}(\omega')-\mathrm{f}(\omega)}{\omega-\omega'+\imath\nu_n}\, \mathrm{tr}\big\{ v_\alpha(\mathbf{k}) A(\mathbf{k},\omega') v_\beta(\mathbf{k}) A(\mathbf{k},\omega) \big\} \tag{4.47}
\end{aligned}
$$

which finally yields the optical conductivity

$$\Re\sigma^{\alpha\beta}(\nu) \;=\; -\frac{\Im\chi^{\alpha\beta}(\imath\nu_n \to \nu+\imath 0^+)}{\nu} \tag{4.48}$$

$$\boxed{\; \Re\sigma^{\alpha\beta}(\nu) = \frac{2\pi e^2\hbar}{V} \sum_{\mathbf{k}} \int \mathrm{d}\omega'\, \frac{\mathrm{f}(\omega')-\mathrm{f}(\omega'+\nu)}{\nu}\, \mathrm{tr}\big\{ v_\alpha(\mathbf{k}) A(\mathbf{k},\omega') v_\beta(\mathbf{k}) A(\mathbf{k},\omega'+\nu) \big\} \;}$$
$$\tag{4.49}$$

Hence, the interaction part of the Hamiltonian only intervenes in the evaluation of the thermal and quantum average, leading to the spectral functions $A(\mathbf{k},\omega)$ of the interacting system. The Fermi velocity $v(\mathbf{k})$ is independent of the interactions.

We summarize the approximations that have led to this expression :

- assumption of a homogeneous response : $\sigma(\mathbf{r},\mathbf{r}') = \sigma(\mathbf{r}-\mathbf{r}')$

- linear response theory, Kubo formalism

- dipole approximation, long wave length limit $\mathbf{q} = 0$

- neglect of vertex corrections

B.e　Fermi velocities : Peierls substitution and beyond

We now turn in detail to the Fermi velocity matrices $v_\alpha(\mathbf{k})$ that determine the weight of an absorption process that enters the conductivity as a function of the position within the Brillouin zone. In the particle-hole bubble, which is our approximation for the optical conductivity, it is the velocities that connect the two Green's functions and thus mediate the transitions between different orbital components. Above, Equation (4.32), we already assumed a form of the velocities that depends only a single wave-vector $\mathbf{k}$. This will be derived in the following.

First we will review the so-called Peierls substitution approach, where one couples the vector potential of the light field directly to a Hamiltonian defined on a lattice[9]. In the case of one atom per unit cell this leads to the familiar Fermi velocities that are the momentum derivatives of the band dispersion. We will generalize this approach to the general case of multi-atomic unit cells.

Then we will come back to our approach which originated from a Hamiltonian defined in the continuum. In order to make contact with the Greens' function formalism used in the derivation for the optical conductivity above, we will expand the fermionic field operators in a localized basis set. We then show that one recovers the generalized Peierls Fermi velocity as the main contribution to the full matrix element. Yet, our approach yields terms beyond the Peierls approximation. Contrary to the latter, we fully account in particular for intra-atomic transitions. Moreover, the spatial extensions of the wavefunctions of the real solid lead to additional terms, that are absent in the Peierls lattice approach.

B.e.i　Starting from the lattice : The Peierls substitution

The idea of the Peierls substitution is to couple the vector potential of the light field directly to the lattice model in a gauge invariant way. That means that the transition to a localized description that is necessary for the application of the above Green's function formalism is made already on the level of the Hamiltonian.

When denoting unit cells (=lattice sites in the one atomic case) by i,j, and the orbitals by the multi indices $L = (n, l, m, \gamma)$, with the orbital (n,l,m) of atom γ, we can write the following lattice Hamiltonian :

$$\mathbf{H} = -\sum_{ij,LL',\sigma} t_{ij}^{L'L} \mathbf{c}_{iL'\sigma}^\dagger \mathbf{c}_{jL\sigma} + \mathbf{H}_{int} \qquad (4.50)$$

where the second term contains electron-electron interactions. For the calculation of the response to an external field, one has to couple the latter to the lattice Hamiltonian in a gauge invariant way, analogue to the case in the continuum, Equation (4.17), when considering instead of the continuous field operator $\Psi(\mathbf{r}, t)$, the lattice operators $\mathbf{c}_{iL\sigma}$. The substitution $\mathbf{c}_{iL\sigma}^\dagger \rightarrow \mathbf{c}_{iL\sigma}^\dagger e^{i\frac{e}{c\hbar} \int^{\mathbf{R}_{iL}} d\mathbf{r}\, \mathbf{A}(\mathbf{r},t)}$ verifies this requirement. When now assuming the

---

[9]For references see [Peierls(1933), Wannier(1962), Maldague(1977), Shastry and Sutherland(1990), Scalapino *et al.* (1992), Dagotto(1994), Millis(2004)]

interactions in Equation (4.50) to be of density-density type, then the above phases appear only in the kinetic part of the Hamiltonian. When additionally assuming a slowly varying vector potential such as to approximate the integral in the exponent, the Peierls approach can be seen as a substitution for the hopping amplitudes :

$$t_{ij}^{L'L} \quad \rightarrow \quad t_{ij}^{L'L} e^{i\frac{e}{\hbar c}\mathbf{A}(t)\,(\mathbf{R}_{iL'}-\mathbf{R}_{jL})} \tag{4.51}$$

It is important to note that the position $\mathbf{R}_{iL}$ depends not only on the unit cell $\mathbf{R}_i$, but also on the position ρ_γ of the atom γ within the cell. We further remark that evidently the vector potential only couples to non-local hopping elements, i.e. within this approach intra-atomic transitions $\left(i, L = (n, l, m, \gamma)\right) \rightarrow \left(i, \widetilde{L} = (n', l', m', \gamma)\right)$ are absent.

When developing the Hamiltonian up to first order in the vector potential (linear response), the paramagnetic current could then be calculated as its functional derivative with respect to the vector potential, as given by Equation (4.25). Yet, as above it can also be deduced from the usual charge continuity equation using the Hamiltonian without the coupling to the light field. Since some formulas that appear on the way will prove useful later on, we shall again pursue this path (see Equation (4.18), Equation (4.20)) :

$$\mathrm{div}\mathbf{j} \quad = \quad \frac{\imath e}{\hbar}\,[\mathbf{H}, \rho] \tag{4.52}$$

Here, and in the following, we omit all time indices, since all quantities are local in time. On the lattice we define the position operator $\mathcal{R}$ as follows

$$\mathcal{R}^\alpha = \sum_{iL\sigma} R_{iL}^\alpha \mathbf{c}_{iL\sigma}^\dagger \mathbf{c}_{iL\sigma} \tag{4.53}$$

with, as introduced above, $R_{iL}^\alpha = R_i^\alpha + \rho_\gamma^\alpha$. Then we note that $\nabla_\alpha\,[\mathbf{H}, \mathcal{R}^\alpha] = [\mathbf{H}, \rho]$ and hence

$$\mathbf{j}^\alpha \quad = \quad \frac{\imath e}{\hbar}\,[\mathbf{H}, \mathcal{R}^\alpha] \tag{4.54}$$

up to an additive constant in R_{iL}^α, which again excludes intra-atomic hoppings. Herewith we get :

$$\mathbf{j}^\alpha \quad = \quad \frac{\imath e}{\hbar} \sum_{LL',ij,\sigma} t_{ij}^{L'L}(R_{iL'}^\alpha - R_{jL}^\alpha)\mathbf{c}_{iL'\sigma}^\dagger \mathbf{c}_{jL\sigma} \tag{4.55}$$

As mentioned above, this is of course the same as can be obtained from Equation (4.25) with a vector potential along the α–direction.

Since the periodicity of the system refers to the unit cells, in the Fourier transformation of the fermionic operators, $\mathbf{c}_{iL\sigma}^\dagger = \sum_{\mathbf{k}} e^{-\imath\mathbf{k}\mathbf{R}_i}\mathbf{c}_{\mathbf{k}L\sigma}^\dagger$, only the unit cell positions $\mathbf{R}_i$ and not

the displacements within the unit cell appear. When further using the translational invariance with respect to the unit cell indices i, j, i.e. $t_{ij} = t(\mathbf{R}_i - \mathbf{R}_j)$, we see that one ends up with only those elements that are diagonal in momentum ($\mathbf{k} = \mathbf{k}'$). We can thus write

$$\mathbf{j}^\alpha \;\; = \;\; e \sum_{LL',\mathbf{k},\sigma} v_{\mathbf{k}\,\alpha}^{L'L} \, \mathbf{c}_{\mathbf{k}L'\sigma}^\dagger \mathbf{c}_{\mathbf{k}L\sigma} \tag{4.56}$$

with the velocity

$$v_{\mathbf{k}\,\alpha}^{L'L} \;\; = \;\; \frac{\imath}{\hbar} \sum_{ij} t_{ij}^{L'L} (R_{iL'}^\alpha - R_{jL}^\alpha) e^{-\imath\mathbf{k}(\mathbf{R}_i - \mathbf{R}_j)} \tag{4.57}$$

In the one atomic case, $L = (n, l, m, \gamma) = (n, l, m)$, the positions R_{iL} do not depend on the orbital index L, i.e. $R_{iL} = R_i$, and one obtains the familiar Fermi velocity

$$v_{\mathbf{k}\,\alpha}^{L'L} \;\; = \;\; \frac{1}{\hbar} \partial_{k_\alpha} \mathbf{H}_{\mathbf{k}}^{L'L} \tag{4.58}$$

which is the multi-orbital generalization of the momentum derivative of the one-particle dispersion. The Hamiltonian is defined by $\mathbf{H}_{\mathbf{k}}^{L'L} = -\sum_{ij} t_{ij}^{L'L} e^{-\imath\mathbf{k}(\mathbf{R}_i - \mathbf{R}_j)}$. The generalization to multi-atomic unit-cells is straight forward. Yet, to our knowledge, this extension is new. The atomic positions can be separated into $\mathbf{R}_{iL} = \mathbf{R}_i + \rho_L$, where the former indexes the unit cell i and the latter the atom γ within the cell. Then Equation (4.57) becomes :

$$v_{\mathbf{k}\,\alpha}^{L'L} \;\; = \;\; \frac{\imath}{\hbar} \sum_{ij} t_{ij}^{L'L} \big[(R_i^\alpha - R_j^\alpha) + (\rho_{L'}^\alpha - \rho_L^\alpha)\big] e^{-\imath\mathbf{k}(\mathbf{R}_i - \mathbf{R}_j)} \tag{4.59}$$

Clearly, the first term is again the momentum derivative of the Hamiltonian, as above, Equation (4.58). It contains hopping processes that take place between *different unit cells* i, j. While absent in the one-atomic case, the second term is crucial, once calculations of realistic materials are performed. It accounts for hopping amplitudes between *different atoms* γ', γ within the same unit cell. Again, we remark that inter-orbital intra-atomic transitions are not captured within this approach. We can write the above in the compact form

$$\boxed{v_{\mathbf{k}\,\alpha}^{L'L} = \frac{1}{\hbar}\left(\partial_{k_\alpha} \mathbf{H}_{\mathbf{k}}^{L'L} - \imath(\rho_{L'}^\alpha - \rho_L^\alpha)\mathbf{H}_{\mathbf{k}}^{L'L} \right)} \tag{4.60}$$

i.e. as compared to the one-atomic case, the Hamiltonian derivative is supplemented by a term that depends on the atomic positions within the unit cell. This generalization, of course, reduces to the one-atomic result in absence of a γ–dependence in the Hamiltonian.

Further, we note that the above expression is hermitian. Yet, in general, it has no well defined parity with respect to the momentum $\mathbf{k}$, even if assuming inversion symmetry of the Hamiltonian. Only the elements that are diagonal in the atomic γ-indices have the required odd parity that leads to the cancellation of vertex corrections in the limit of infinite coordination, according to Equation (4.44). This stresses again, that our formula for the optical conductivity is an approximation, even in the DMFT context.

B.e.ii   Starting from the continuum : Introducing a localized basis

DMFT originated from the study of lattice models. In the realistic context the notion of "sites" and locality generalizes naturally when working in a localized (Wannier type) basis. In this section we will derive expressions for the Fermi velocities when starting from the continuum formulation.

First, we develop the field operators $\Psi_\sigma(\mathbf{r}, t)$ in a Bloch-like basis $\chi_{\mathbf{k}L\sigma}(\mathbf{r})$.

$$\Psi_\sigma(\mathbf{r}, t) = \sum_{\mathbf{k},L} \chi_{\mathbf{k}L\sigma}(\mathbf{r}) \mathbf{c}_{\mathbf{k}L\sigma}(t) \tag{4.61}$$

Here, again, L= (n, l, m, γ) is a multi index denoting orbital (n,l,m) of atom γ. This means the conjugated position $\mathbf{R}$ of the Brillouin zone wavevector $\mathbf{k}$ is indexing the unit cell and not the atoms, thus the notion of local processes will require $\mathbf{R} = \mathbf{R}'$ and $\gamma = \gamma'$, just like in the discussion on the Peierls term[10]. Later on we will Fourier transform and discuss the importance of the different contributions in terms of Wannier-like functions $\chi_{\mathbf{R}L\sigma}(\mathbf{r})$.

The paramagnetic current Equation (4.27) in imaginary time then reads

$$j_P^\alpha(\mathbf{q}, \tau) = \int \mathrm{d}^3 \mathrm{r}\, j^\alpha(\mathbf{r}, \tau) e^{i\mathbf{q}\mathbf{r}} = e \sum_{\mathbf{k}'\mathbf{k}, LL', \sigma} v_{\mathbf{k}'\mathbf{k}, \alpha}^{L'L, \sigma}(\mathbf{q}) \mathbf{c}_{\mathbf{k}'L'\sigma}^\dagger(\tau) \mathbf{c}_{\mathbf{k}L\sigma}(\tau) \tag{4.62}$$

with the Fermi velocity matrix

$$v_{\mathbf{k}'\mathbf{k}, \alpha}^{L'L, \sigma}(\mathbf{q}) \;=\; -\mathcal{H}\left\{ i\frac{\hbar}{m} \int \mathrm{d}^3 \mathrm{r}\, \chi_{\mathbf{k}'L'\sigma}^*(\mathbf{r}) e^{i\mathbf{q}\mathbf{r}} \nabla_\alpha \chi_{\mathbf{k}L\sigma}(\mathbf{r}) \right\} \tag{4.63}$$

For optical transitions we limit ourselves to the usual dipole approximation, i.e. $e^{i\mathbf{q}\mathbf{R}} \approx 1$, which leads to

$$v_{\mathbf{k}'\mathbf{k}, \alpha}^{L'L, \sigma}(\mathbf{q} = \mathbf{0}) \;=\; \frac{1}{m} \mathcal{H} \langle \mathbf{k}'L' | \mathcal{P}_\alpha | \mathbf{k}L \rangle \tag{4.64}$$

where we have assumed that the wavefunctions are independent of the spin index and have introduced the momentum operator $\mathcal{P} = -i\hbar\nabla$. Since we have translational invariance, i.e. $v_{\mathbf{R}'\mathbf{R}, \alpha}^{L'L, \sigma} = v_{\mathbf{R}'+\mathbf{T}, \mathbf{R}+\mathbf{T}, \alpha}^{L'L, \sigma}$, for any lattice-vector $\mathbf{T}$, and

---

[10]N is the number of k-points in the discretized basis, or, equivalently, the number of cells in the solid. We recall our convention $\sum_{\mathbf{k}} = N$.

$v_{\mathbf{R'R},\alpha}^{L'L,\sigma} = 1/N \sum_{\mathbf{kk'}} \exp\left(-\imath\mathbf{k'R'}\right)\exp\left(\imath\mathbf{kR}\right)v_{\mathbf{k'k},\alpha}^{L'L,\sigma}$, the element is diagonal in momentum, i.e. $v_{\mathbf{k'k},\alpha}^{L'L,\sigma} \sim \delta_{\mathbf{k'k}}$. Hence, in total it follows

$$v_{\mathbf{k'k},\alpha}^{L'L,\sigma}(\mathbf{q}) \quad = \quad v_{\mathbf{k},\alpha}^{L'L,\sigma}\delta_{\mathbf{k'},\mathbf{k}}\delta_{\mathbf{q},\mathbf{0}} \tag{4.65}$$

with

$$v_{\mathbf{k},\alpha}^{L'L,\sigma} \quad = \quad \frac{1}{m}\mathcal{H}\langle\mathbf{k}L'|\mathcal{P}_\alpha|\mathbf{k}L\rangle \tag{4.66}$$

And the current is thus given by

$$j_P^\alpha(\mathbf{q},\tau) = e \sum_{\mathbf{k},LL',\sigma} v_{\mathbf{k},\alpha}^{L'L,\sigma}(\mathbf{q})\mathbf{c}_{\mathbf{k}L'\sigma}^\dagger(\tau)\mathbf{c}_{\mathbf{k}L\sigma}(\tau) \tag{4.67}$$

as was beforehand assumed.

Momentum operator matrix elements : Practicable approximations. In the case of a plane wave calculation, the dipole matrix elements, Equation (4.66), are easily calculated. In the case of LDA+DMFT calculations, however, one needs to work within a localized description, such as $L/NMTO$ functions or localized Wannier functions in general. Then the computation of the above matrix elements become rather tedious. This is why we shall here proceed an alternative path. Indeed we will show in the following that for a localized basis set the most important contributions to the matrix element can be calculated from the Hamiltonian alone, i.e. we need not perform any other integrals involving the LDA wavefunctions, in a first approximation.

The element of Equation (4.66) can be rewritten (we drop the spin index)

$$\frac{1}{m}\langle\mathbf{k}L'|\mathcal{P}_\alpha|\mathbf{k}L\rangle \quad = \quad -\frac{\imath}{\hbar}\frac{1}{N}\sum_{\mathbf{R},\mathbf{R'}}\langle\mathbf{R'}L'|e^{-\imath\mathbf{kR'}}\left[\mathcal{R}_\alpha,\mathbf{H}_0\right]e^{\imath\mathbf{kR}}|\mathbf{R}L\rangle$$

$$= \quad -\frac{\imath}{\hbar}\frac{1}{N}\sum_{\mathbf{R},\mathbf{R'}}e^{\imath\mathbf{k}(\mathbf{R}-\mathbf{R'})}\int d^3\mathbf{r}$$

$$[\langle\mathbf{R'}L'|\mathcal{R}_\alpha|\mathbf{r}\rangle\langle\mathbf{r}|\mathbf{H}_0|\mathbf{R}L\rangle - \langle\mathbf{R'}L'|\mathbf{H}_0|\mathbf{r}\rangle\langle\mathbf{r}|\mathcal{R}_\alpha|\mathbf{R}L\rangle] \tag{4.68}$$

It is important to note, that here the position operator $\mathcal{R}_\alpha$ is defined in the continuum, i.e. instead of Equation (4.53), its effect in the position representation is $\langle\mathbf{r}|\mathcal{R}_\alpha|\mathbf{R}L\rangle = r_\alpha\chi_{\mathbf{R}L}(\mathbf{r})$. One has to make a clear distinction between the continuous space variable $\mathbf{r}$ and the discrete unit cell label $\mathbf{R}$. In the (unphysical) limit of completely localized wavefunctions, $\langle\mathbf{r}|\mathbf{R}L\rangle = \chi_{\mathbf{R}L}(\mathbf{r}) \sim \delta(\mathbf{r} - \mathbf{R}_L)$, this distinction is relaxed, and we recover the expression Equation (4.60) of the Peierls approach, as we shall see.

As before we separate the positions into the site-vector and the atomic displacement within the unit cell : $R_L^\alpha = R^\alpha + \rho_L^\alpha$. By shifting in the first term $\mathbf{r} \to \mathbf{r} + \mathbf{R'} + \rho_{L'}$ and

$\mathbf{r} \to \mathbf{r} + \mathbf{R} + \rho_L$ in the second we find

$$\frac{1}{m}\langle \mathbf{k}L'|\mathbf{P}_\alpha|\mathbf{k}L\rangle = -\frac{\imath}{\hbar}\frac{1}{N}\sum_{\mathbf{R},\mathbf{R}'} e^{\imath \mathbf{k}(\mathbf{R}-\mathbf{R}')} \int \mathrm{d}^3\mathbf{r}$$

$$\left[(r_\alpha + R'_\alpha + \rho^\alpha_{L'})\langle \mathbf{R}'L'|\mathbf{r}+\mathbf{R}'+\rho_{L'}\rangle\langle \mathbf{r}+\mathbf{R}'+\rho_{L'}|\mathbf{H}_0|RL\rangle\right.$$

$$\left.-(r_\alpha + R_\alpha + \rho^\alpha_L)\langle \mathbf{R}'L'|\mathbf{H}_0|\mathbf{r}+\mathbf{R}+\rho_L\rangle\langle \mathbf{r}+\mathbf{R}+\rho_L|RL\rangle\right]$$

$$= -\frac{\imath}{\hbar}\frac{1}{N}\sum_{\mathbf{R},\mathbf{R}'} e^{\imath \mathbf{k}(\mathbf{R}-\mathbf{R}')}(R'_\alpha - R_\alpha + \rho^\alpha_{L'} - \rho^\alpha_L)\langle \mathbf{R}'L'|\mathbf{H}_0|\mathbf{R}L\rangle$$

$$-\frac{\imath}{\hbar}\frac{1}{N}\sum_{\mathbf{R},\mathbf{R}'} e^{\imath \mathbf{k}(\mathbf{R}-\mathbf{R}')} \int \mathrm{d}^3\mathbf{r}\; r_\alpha$$

$$\left[\langle \mathbf{R}'L'|\mathbf{r}+\mathbf{R}'+\rho_{L'}\rangle\langle \mathbf{r}+\mathbf{R}'+\rho_{L'}|\mathbf{H}_0|RL\rangle\right.$$

$$\left.-\langle \mathbf{R}'L'|\mathbf{H}_0|\mathbf{r}+\mathbf{R}+\rho_L\rangle\langle \mathbf{r}+\mathbf{R}+\rho_L|RL\rangle\right] \tag{4.69}$$

This shift is indeed inspired by the lattice considerations of the preceding section. As we shall see, this splitting is rather natural : The first term obviously is

$$\frac{1}{\hbar}\left(\frac{\partial}{\partial k_\alpha}\langle \mathbf{k}L'|\mathbf{H}_0|\mathbf{k}L\rangle - \imath(\rho^\alpha_{L'} - \rho^\alpha_L)\langle \mathbf{k}L'|\mathbf{H}_0|\mathbf{k}L\rangle\right) \tag{4.70}$$

which is exactly the Peierls term, Equation (4.60). The merit of the Peierls approximation in a realistic calculation is its simplicity. Indeed no matrix elements other than the Hamiltonian need to be calculated. The latter is a quantity that is anyhow required for a many-body calculation, and one thus has only to perform the directional momentum derivative[11]. For an example of the impact of the intra-cell term see Section F. From the discussion of the Peierls substitution above, it is clear that the second term in Equation (4.69)

$$-\frac{\imath}{\hbar}\frac{1}{N}\sum_{\mathbf{R},\mathbf{R}'} e^{\imath \mathbf{k}(\mathbf{R}-\mathbf{R}')} \int \mathrm{d}^3\mathbf{r}\; r_\alpha \sum_{\mathbf{\Lambda},L''}\left[\chi^*_{\mathbf{R}'L'}(\mathbf{r}+\mathbf{R}'+\rho_{L'})\chi_{\mathbf{\Lambda}L''}(\mathbf{r}+\mathbf{R}'+\rho_{L'})\langle \mathbf{\Lambda}L''|\mathbf{H}_0|\mathbf{R}L\rangle\right.$$

$$\left.-\chi^*_{\mathbf{\Lambda}L''}(\mathbf{r}+\mathbf{R}+\rho_L)\chi_{\mathbf{R}L}(\mathbf{r}+\mathbf{R}+\rho_L)\langle \mathbf{R}'L'|\mathbf{H}_0|\mathbf{\Lambda}L''\rangle\right] \tag{4.71}$$

accounts on the one hand for all atomic transitions ($\mathbf{R} = \mathbf{R}'$ and $\gamma' = \gamma$), yet it also contains contributions that arise from the fact that we started from a continuum formulation, i.e. the spatial extensions of the wavefunctions lead to inter-atomic corrections,

---

[11]We perform this derivative by using the four-point formula :
$f'(x_i)dx \approx \frac{1}{12}\left(f(x_{i-2}) - 8f(x_{i-1}) + f(x_{i+1}) - f(x_{i+2})\right)$

owing to their finite overlap. Yet, a direct evaluation of the preceding formula is an intricate undertaking, since it involves the calculation of countless integrals. This is why, in the following, we will make consecutive approximations that lead, step by step, to more simplified correction terms, that one might endeavour to take into account in an actual computation. These approximative steps will further rationalize the spatial shiftings that we have performed to split off the Peierls term as the leading contribution.

Since it is the spatial extensions of the wavefunctions that lead to the above term, the latter will decrease in relative importance with increasing localization of the orbitals. By assuming a well localized set of orbitals, we thus proceed to cut down the expression in question to the predominant terms, which will be given by the integrals that involve wave functions that have a large overlap. In the most coarse approximation, the only surviving transition elements will be given by the intra-atomic contributions, that were missing in the Peierls formulation.

Using $\chi_{\mathbf{R}L}(\mathbf{r} + \mathbf{R}) = \chi_{\mathbf{0}L}(\mathbf{r})$ the above can be written as

$$-\frac{\imath}{\hbar}\frac{1}{N}\sum_{\mathbf{R},\mathbf{R}'} e^{\imath\mathbf{k}(\mathbf{R}-\mathbf{R}')} \int \mathrm{d}^3\mathrm{r}\, r_\alpha \sum_{\mathbf{\Lambda},L''}\left[\chi^*_{\mathbf{0}L'}(\mathbf{r}+\rho_{L'})\chi_{\mathbf{0}L''}(\mathbf{r}+\mathbf{R}'-\mathbf{\Lambda}+\rho_{L'})\langle\mathbf{\Lambda}L''|\mathbf{H}_0|\mathbf{R}L\rangle\right.$$
$$\left.-\chi^*_{\mathbf{0}L''}(\mathbf{r}+\mathbf{R}-\mathbf{\Lambda}+\rho_L)\chi_{\mathbf{0}L}(\mathbf{r}+\rho_L)\langle\mathbf{R}'L'|\mathbf{H}_0|\mathbf{\Lambda}L''\rangle\right] \qquad (4.72)$$

Now, the origins of all intervening wavefunctions lie within the same unit cell, labeled "$\mathbf{0}$". In a first step, the assumed localization of the involved orbitals makes it reasonable to identify the most important terms in the sum as those, where the arguments of the wavefunctions also lie within the same unit cell. This means that the overlap will be largest when $\mathbf{\Lambda} = \mathbf{R}'$ in the first term and $\mathbf{\Lambda} = \mathbf{R}$ in the second term. We note that within this approximation, only the Hamiltonian element depends on the labels $\mathbf{R}$ and $\mathbf{R}'$, and we can thus directly perform the Fourier transformation which then yields

$$-\frac{\imath}{\hbar}\int \mathrm{d}^3\mathrm{r}\, r_\alpha \sum_{L''}\left[\chi^*_{\mathbf{0}L'}(\mathbf{r}+\rho_{L'})\chi_{\mathbf{0}L''}(\mathbf{r}+\rho_{L'})\langle\mathbf{k}L''|\mathbf{H}_0|\mathbf{k}L\rangle\right.$$

$$\left.-\chi^*_{\mathbf{0}L''}(\mathbf{r}+\rho_L)\chi_{\mathbf{0}L}(\mathbf{r}+\rho_L)\langle\mathbf{k}L'|\mathbf{H}_0|\mathbf{k}L''\rangle\right] \qquad (4.73)$$

This means that the entire momentum dependence of the matrix element, in this approximation, is carried by the Hamiltonian. The complexity of the occurring matrix elements of the position operator has been considerably reduced. In the one-atomic case, i.e. $\gamma = \gamma' = \gamma''$, and when using the short-hand notation $\mathbf{R}^{LL'}_{\alpha,0} = \langle\mathbf{0}L|\mathcal{R}_\alpha|\mathbf{0}L'\rangle$, $\mathbf{H}^{LL'}_0(\mathbf{k}) = \langle\mathbf{k}L|\mathbf{H}_0|\mathbf{k}L'\rangle$ we simply have

$$-\frac{\imath}{\hbar}\left[\mathbf{R}^{LL'}_{\alpha,0},\mathbf{H}_0(\mathbf{k})\right]_{L'L} \qquad (4.74)$$

This is reminiscent of the relation $1/m\mathcal{P} = -\imath/\hbar\,[\mathcal{R},\mathbf{H}_0]$, which we used in the beginning. Here however intervene on-site matrix elements rather than the full position

operator. Indeed these elements, $\mathbf{R}_{\alpha,0}^{LL'}$, are well known in atomic physics. They simply give the amplitudes for dipolar atomic transitions. Thus the angular part of the integral will produce the corresponding dipole selection rules ($\Delta l = \pm 1, \Delta m = 0, \pm 1$) via Clebsch-Gordon coefficients (see e.g. [Cohen-Tannoudji *et al.* (1992)]), when, as we have assumed, the wavefunctions have a well-defined angular momentum (l, m). Contrary to the atomic case, however, the Hamiltonian is momentum dependent, owing to the fact that, though regarding atomic transitions, the "atom" here is embedded in the solid from which arises the energy dispersion. Equation (4.74) thus defines an effective momentum operator, $\tilde{\mathbf{p}}_{\alpha,0}$. However, as will be explained below, it is *not* possible to use this operator in the quest for a generalization of the Peierls substitution factors to take into account local atomic transitions in a lattice formulation.

Also, the above term reminds the form of the multi-atomic correction term in Equation (4.70), only that there occurred fixed atomic positions ρ_γ, which commute with the Hamiltonian, which is why in Equation (4.70) only the non-local terms $\gamma \neq \gamma'$ survive.

Coming back to the multi-atomic case, we have to make a further approximation in order to obtain an expression containing atomic transitions only. Yet, the shifts in the wavefunctions of Equation (4.73) can be treated analogous to the unit cell coordinates : Indeed $\chi_{\mathbf{0}L}(\mathbf{r} + \rho_L)$ is centered around the position of atom γ. When, for the sake of clarity, we simply rename $\widetilde{\chi}_{\mathbf{0}L}(\mathbf{r}) = \chi_{\mathbf{0}L}(\mathbf{r} + \rho_L)$ we have

$$
-\frac{\imath}{\hbar} \int \mathrm{d}^3 \mathrm{r}\ r_\alpha \sum_{L''} \Big[\widetilde{\chi}_{\mathbf{0}L'}^*(\mathbf{r})\widetilde{\chi}_{\mathbf{0}L''}(\mathbf{r} + \rho_{L'} - \rho_{L''})\langle \mathbf{k}L''|\mathbf{H}_0|\mathbf{k}L\rangle
$$
$$
- \widetilde{\chi}_{\mathbf{0}L''}^*(\mathbf{r} + \rho_L - \rho_{L''})\widetilde{\chi}_{\mathbf{0}L}(\mathbf{r})\langle \mathbf{k}L'|\mathbf{H}_0|\mathbf{k}L''\rangle \Big] \tag{4.75}
$$

From this expression it is clear, that atomic transitions ($\gamma'' = \gamma'$ and $\gamma'' = \gamma$, respectively) are in fact predominant. When restraining ourselves to these cases, we thus drop entirely the corrections to hopping processes that stem from the finite extensions of the wave-functions and end up with the intra-atomic transitions only, that were completely missing in the Peierls approach :

intra-
atomic
overlaps
only

$$
-\frac{\imath}{\hbar} \int \mathrm{d}^3 \mathrm{r}\ r_\alpha \left[\sum_{L''}^{\gamma'' = \gamma'} \widetilde{\chi}_{\mathbf{0}L'}^*(\mathbf{r})\widetilde{\chi}_{\mathbf{0}L''}(\mathbf{r})\langle \mathbf{k}L''|\mathbf{H}_0|\mathbf{k}L\rangle - \sum_{L''}^{\gamma'' = \gamma} \widetilde{\chi}_{\mathbf{0}L''}^*(\mathbf{r})\widetilde{\chi}_{\mathbf{0}L}(\mathbf{r})\langle \mathbf{k}L'|\mathbf{H}_0|\mathbf{k}L''\rangle \right]
$$
$$
= -\frac{\imath}{\hbar} \left[\sum_{L''}^{\gamma'' = \gamma'} \langle \widetilde{\mathbf{0}L'}|\mathcal{R}_\alpha|\widetilde{\mathbf{0}L''}\rangle\langle \mathbf{k}L''|\mathbf{H}_0|\mathbf{k}L\rangle - \sum_{L''}^{\gamma'' = \gamma} \langle \widetilde{\mathbf{0}L''}|\mathcal{R}_\alpha|\widetilde{\mathbf{0}L}\rangle\langle \mathbf{k}L'|\mathbf{H}_0|\mathbf{k}L''\rangle \right] \tag{4.76}
$$

The above Equation (4.76) can sketchily be written as :

multi-
atomic
case

$$
-\frac{\imath}{\hbar} \sum_{\mathscr{L}''} \left[{}^{\gamma'}\mathbf{R}_{\alpha,0}^{\mathscr{L}'\mathscr{L}''}\ {}^{\gamma'\gamma}\mathbf{H}_0^{\mathscr{L}''\mathscr{L}}(\mathbf{k}) - {}^{\gamma''\gamma}\mathbf{H}_0^{\mathscr{L}'\mathscr{L}''}(\mathbf{k})\ {}^{\gamma}\mathbf{R}_{\alpha,0}^{\mathscr{L}''\mathscr{L}} \right] \tag{4.77}
$$

where we have split the multi-index $L = (nlm\gamma) = (\mathscr{L}\gamma)$, and have defined $^{\gamma}\mathbf{R}_{\alpha,0}^{\mathscr{L}\mathscr{L}'} = \widetilde{\langle 0\mathscr{L}\gamma|\mathbf{R}_{\alpha}|0\mathscr{L}'\gamma\rangle}$, $^{\gamma\gamma'}\mathbf{H}_{0}^{\mathscr{L}\mathscr{L}'}(\mathbf{k}) = \widetilde{\langle \mathbf{k}\mathscr{L}\gamma|\mathbf{H}_{0}|\mathbf{k}\mathscr{L}'\gamma'\rangle}$. Thus only the elements diagonal in the γ index can be written in the form of a commutator, as was the case for the one-atomic case above.

Improvements to the above approximations are obvious: One could e.g. take into account elements containing nearest-neighbour wavefunctions within the unit cell, or even account for transitions between different unit cells. In that case however, the matrix elements that one needs to evaluate are numerous and more complex since they explicitly involve the various wavefunctions. We stress again, that these terms are inter-atomic *corrections* to the Peierls term, while the intra-atomic contributions are completely absent in the Peierls formalism.

B.e.iii   Additional remarks on the Peierls phases

Connection to the lattice formulation.   The principle difference between the two approaches that we elaborated on above is given by the different notion of the spatial variables and operators. While in the lattice formalism we defined the position operator by Equation (4.53), yielding a discrete spectrum, the usual quantum mechanical position operator has a continuous spectrum. Herewith necessarily arises the distinction between labels, or quantum numbers and coordinates : When developing the field operators of the continuum in a localized basis set, one introduces a unit cell quantum number $\mathbf{R}$ which becomes the site label i in the lattice formulation. Yet, while in the former a continuous variable $\mathbf{r}$ exists, it cannot occur in the latter. Indeed all former dependencies of the continuum have to be cast into matrix elements when a pure lattice description is desired, as was the case in the derivation of the Hubbard Hamiltonian from the continuous formulation of a solid, Section B, Chapter 1.

Starting from our initial Hamiltonian, Equation (4.15), we recover the Peierls substitution in the following approximation : Developing again the field operators in the "Wannier"-like basis, $|\mathbf{R}L\rangle$, we find that, when dropping for the sake of simplicity the term that is quadratic in the vector potential, and which leads to the diamagnetic current, the coupling to the vector potential can be seen as the substitution :

$$t_{\mathbf{R}'\mathbf{R}}^{L'L} \quad \rightarrow \quad t_{\mathbf{R}'\mathbf{R}}^{L'L} + \frac{\imath e}{\hbar c}\mathbf{A}(t)\,\langle\mathbf{R}'L'|\,[\mathcal{R},\mathbf{H}_0]\,|\mathbf{R}L\rangle \tag{4.78}$$

Where, again, $1/m\mathcal{P} = -\frac{\imath}{\hbar}[\mathcal{R},\mathbf{H}_0]$ has been used. With increasing localization of the orbitals $|\mathbf{R}L\rangle$, the distinction between coordinates and quantum numbers becomes less important. Indeed, if the labels $\mathbf{R},\mathbf{R}'$ were coordinates and not quantum numbers, and thus the position operator would act on them, rather than on the states $|\mathbf{r}\rangle$ of the position representation, we would have

$$t_{\mathbf{R}'\mathbf{R}}^{L'L} \quad \rightarrow \quad t_{\mathbf{R}'\mathbf{R}}^{L'L} \cdot \left(1 + \frac{\imath e}{\hbar c}\mathbf{A}(t)\,(\mathbf{R}' - \mathbf{R})\right) \tag{4.79}$$

which is just Equation (4.51) to linear order in $\mathbf{A}$.

One is now tempted to proceed analogously with the atomic transitions, i.e. to use e.g. the matrix element of Equation (4.74) and to ask which would be the additional Peierls phase needed to reproduce the correct current element when performing a functional derivative of the Hamiltonian with respect to the vector potential. A closer examination however shows that this is not possible. Indeed the requirement of gauge invariance, Equation (4.17), can only be met by non-local hopping processes[12]. As a matter of fact, the whole concept of a current is not meaningful for local processes on a *lattice*. In the continuum formulation an atomic transition is characterized by constant position labels, while it still involves the continuous variable $\mathbf{r}$ via the wave functions. Thereby the corresponding contribution to the current does appear in the continuity Equation (4.18), since the divergence in the latter refers to the continuous space variable. In the lattice formulation, however, all continuous spatial dependencies had to be cast into transition matrix elements and the derivative of the current in the continuity Equation (4.52) is with respect to the lattice sites. Though evidently conserving the charge, an on-site current does not turn up in a continuity equation that intrinsically describes the balance of spatial charge flows. This is why in atomic physics, optical transitions are calculated à la Fermi's golden rule, i.e. by initial to final state transition probabilities, rather than current elements.

Basis dependency. An important issue in the calculation of optical properties when using the Peierls substitution is the fact that, within this approximation, it makes a difference in which basis the Fermi velocities are calculated. Indeed the derivative term in the Peierls velocities manifestly does not transform as does the Hamiltonian :

$$
\begin{aligned}
H(\mathbf{k}) \;\;\rightarrow\;\; & \widetilde{H}(\mathbf{k}) = U^\dagger(\mathbf{k}) H(\mathbf{k}) U(\mathbf{k}) \\
v(\mathbf{k}) \;\;\rightarrow\;\; & U^\dagger(\mathbf{k}) \underbrace{\Big(\partial_{\mathbf{k}} H(\mathbf{k}) \Big)}_{\widetilde{v}(\mathbf{k})} U(\mathbf{k}) + \Big(\partial_{\mathbf{k}} U^\dagger(\mathbf{k}) \Big) H(\mathbf{k}) U(\mathbf{k}) + U^\dagger(\mathbf{k}) H(\mathbf{k}) \Big(\partial_{\mathbf{k}} U(\mathbf{k}) \Big)
\end{aligned}
$$

i.e. the momentum dependence of the unitary transformation results in additional terms beyond the transformed derivative of the Hamiltonian. In other words, when using the Peierls substitution, the optical conductivity itself will be basis-dependent, which is obviously unphysical. Yet, from the above discussion we can say in which basis the Peierls substitution is possibly best evaluated. Indeed, in the beginning our Fermi velocities were completely general. As a consequence, the additional terms from above, that involve the derivative of the unitary transformations will be "compensated" by the correctional terms given by Equation (4.71). The latter however, when leaving apart purely atomic transitions, become smaller with an increasing degree of localization of the involved wavefunctions. Thus, the Peierls substitution is most justified when working in a strongly localized

---

[12]Apart from the fact, that gauge invariance is trivially granted when adding to the Hamiltonian any function of rot$\mathbf{A}$, i.e. a coupling to the magnetic field.

basis, e.g. $L/NMTO$ wavefunctions or Wannier functions à la [Gibson(1958),Marzari and Vanderbilt(1997)].

Comparisons of the Peierls and the exact velocities have so far only been performed for a Kronig-Penney model [Ahn and Millis(2000)]. A trivial example, however, is the free particle : The eigenfunctions are plane waves $\langle \mathbf{r}|\mathbf{k}\rangle = e^{\imath \mathbf{kr}}$, whose Wannier homologues are completely localized Dirac distributions $\langle \mathbf{r}|\mathbf{R}\rangle = \delta(\mathbf{R} - \mathbf{r})$. With the free particle dispersion $\epsilon_{\mathbf{k}} = \frac{\hbar^2 k^2}{2m}$, it follows the equality of the exact and the Peierls matrix-elements : $\frac{1}{m}\langle \mathbf{k}|\mathcal{P}_\alpha|\mathbf{k}\rangle = \frac{1}{\hbar}\partial_{k_\alpha}\epsilon_{\mathbf{k}} = \frac{\hbar k_\alpha}{m}$. Thus any complication in the case of a solid arises from the periodic function $u_{\mathbf{k}}(\mathbf{r})$ in Bloch's theorem, whose influence on the localization thus determines the accuracy of the Peierls approximation.

B.e.iv The Fermi velocity of the Bethe lattice

DMFT calculations are often performed using the Bethe lattice, since the corresponding self-consistency is particularly convenient. However, this lattice does not possess translational invariance, and, therefore, the above formalism can not be applied to compute the corresponding Fermi velocity.

As we shall see in the next section, the optical conductivity of a lattice model obeys a restricted sum rule. From this knowledge, one may *define* the Fermi velocity for the one-band Bethe lattice from the requirement of the validity of this sum rule, Equation (4.85). Then one finds [Chung and Freericks(1998),Chattopadhyay *et al.* (2000)]

$$v^2(\epsilon) \quad = \quad \frac{4t^2 - \epsilon^2}{3} \tag{4.80}$$

when working in an energy formulation, i.e. when replacing the momentum sum by an integral over the density of states[13].

C   Sum rules

Sum rules are a powerful tool, that allow to study, on a quantitative level, the tracking of spectral weight shifts upon the change of external parameters. Whereas in various techniques, such as photoemission, intensities are collected in arbitrary units, the knowledge of the normalization of the optical conductivity makes it possible to monitor small differences in the measured spectra.

C.a   The unrestricted sum rule

Using the Kramers-Kronig relation for the imaginary part of the conductivity, in the limit of large frequencies, we find

$$\int_0^\infty d\omega' \, \Re\sigma(\omega') \quad = \quad \frac{\pi}{2}\lim_{\omega\to\infty} \omega\Im\sigma(\omega) \tag{4.81}$$

---

[13] $1/N \sum_{\mathbf{k}} f(\mathbf{k}) \longrightarrow \int d\epsilon \, D(\epsilon) f(\epsilon)$

Since the imaginary part of the paramagnetic contribution, Equation (4.36), Equation (4.47), are going to zero with $1/\omega^2$ in the $\omega \to \infty$ limit, the only surviving term stems from the diamagnetic response, Equation (4.30), whence we get

$$\int_0^\infty \mathrm{d}\omega' \, \Re\sigma(\omega') = \frac{\pi}{2} \frac{ne^2}{m} \tag{4.82}$$

This equation is known as the f-sum rule. The presented derivation is due to [Kohn(1964)]. This means that, for a given system, the optical conductivity integrates up to a constant, independent of temperature, interaction strengths etc. When looking at finite frequency integrals over the conductivity, the above sum rule thus allows for keeping track of spectral weight transfers in distinct energy regions as a function of the mentioned parameters and hence opens the possibility of identifying the mechanisms underlying the evolution of the system. With the knowledge of the transformations between the different optical functions, analogous sum rules exist, e.g. for the dielectric function $\epsilon(\omega)$.

C.b   Restricted sum rules

In theory one often works with effective models which do not contain all electronic degrees of freedom of a realistic system. In particular the number of orbitals is restricted, and hence only a finite energy window is spanned by the model. Hereby high energy transitions, present in the real solid, are neglected. This leads, as we shall see to a modification of the above f-sum rule. Indeed, the frequency integral is found to yield not a constant but is, under certain assumptions, proportional to the kinetic energy of the model.

When working in the lattice formalism and neglecting on-site transitions, we can substitute Equation (4.54) into one of the current operators in Equation (4.41). Integrating over frequency then yields, when using the definition Equation (4.53) :

$$\int_{-\infty}^\infty \mathrm{d}\omega \, \Re\sigma(\omega) \;=\; \frac{\pi e^2}{\hbar^2 V}\langle [[\mathbf{H}, \mathcal{R}^\alpha], \mathcal{R}^\alpha]\rangle \tag{4.83}$$

$$\;=\; \frac{\pi e^2}{\hbar^2 V} \sum_{LL',ij,\sigma} t_{ij}^{L'L} \left(a_{ij,\alpha}^{L'L}\right)^2 \langle \mathbf{c}_{iL'\sigma}^\dagger \mathbf{c}_{jL\sigma}\rangle \tag{4.84}$$

with $a_{ij,\alpha}^{L'L} = R_{i,\alpha}^{L'} - R_{j,\alpha}^{L}$ being the distance between the orbital sites L, L' of the unit cells i, j. If we now further assume a one band model with only isotropic nearest-neighbour hoppings on a hyper-cubic lattice, this can be written as

$$\int_{-\infty}^\infty \mathrm{d}\omega \, \Re\sigma(\omega) = -\frac{\pi e^2}{\hbar^2 V} a^2 \langle T_\alpha\rangle \tag{4.85}$$

with the kinetic energy T_α in α–direction. In the isotropic case, one thus finds $\langle T \rangle = 3\langle T_\alpha \rangle$.

This restricted sum rule can of course also be derived from our end formula of the optical conductivity Equation (4.49), when making the same assumptions. In the one-band case, we have, with $\sigma_0 = \frac{2\pi e^2 \hbar}{V}$

$$
\begin{aligned}
\int_{-\infty}^{\infty} d\omega \, \Re\sigma(\omega) &= \sigma_0 \int d\omega \int d\omega' \sum_{\mathbf{k}} \frac{f(\omega') - f(\omega' + \omega)}{\omega} A(\mathbf{k}, \omega') A(\mathbf{k}, \omega' + \omega) v^2(\mathbf{k}) \\
&= 2\sigma_0 \int d\omega \int d\omega' \sum_{\mathbf{k}} f(\omega') \frac{A(\mathbf{k}, \omega') A(\mathbf{k}, \omega)}{\omega - \omega'} v^2(\mathbf{k})
\end{aligned}
\tag{4.86}
$$

Noticing that

$$
\begin{aligned}
A(\mathbf{k}, \omega') \int d\omega \frac{A(\mathbf{k}, \omega)}{\omega - \omega'} &= \frac{1}{\pi} G'(\mathbf{k}, \omega') G''(\mathbf{k}, \omega') \\
&= \frac{1}{2\pi} \Im\left(G^2(\mathbf{k}, \omega')\right)
\end{aligned}
\tag{4.87}
$$

and

$$
\Im\left(G^2(\mathbf{k}, \omega)\right) = -\pi \partial_{\epsilon_{\mathbf{k}}} A(\mathbf{k}, \omega)
\tag{4.88}
$$

it follows

$$
\begin{aligned}
\int_{-\infty}^{\infty} d\omega \, \Re\sigma(\omega) &= -\sigma_0 \int d\omega \sum_{\mathbf{k}} f(\omega) \left(\partial_{\epsilon_{\mathbf{k}}} A(\mathbf{k}, \omega)\right) v^2(\mathbf{k}) \\
&= -\sigma_0 \int d\omega \sum_{\mathbf{k}} f(\omega) \left(\partial_{\mathbf{k}} A(\mathbf{k}, \omega)\right) v^2(\mathbf{k}) \left(\frac{\partial \epsilon_{\mathbf{k}}}{\partial \mathbf{k}}\right)^{-1} \\
&= \sigma_0 \int d\omega \sum_{\mathbf{k}} f(\omega) A(\mathbf{k}, \omega) \partial_{\mathbf{k}} \left(\frac{v^2(\mathbf{k})}{\partial \epsilon_{\mathbf{k}} / \partial \mathbf{k}}\right)
\end{aligned}
\tag{4.89}
$$

In the last step we have specialized to the one dimensional case, in which the Fermi velocity vanishes at the Brillouin zone boundaries, and hence the partial integration only yields the term that is shown. Further, in the one-band lattice case, the Fermi velocity is just the momentum derivative of the one-particle dispersion in the direction ϵ specified by the vector potential, Equation (4.60) : $v(\mathbf{k}) = 1/\hbar(\epsilon \cdot \nabla_{\mathbf{k}})\epsilon_{\mathbf{k}}$. Here, in the one-dimensional case, we have $v(k) = 1/\hbar \partial_k \epsilon_k$, from which follows:

$$
\int_{-\infty}^{\infty} d\omega \, \Re\sigma(\omega) = \frac{\sigma_0}{\hbar^2} \sum_k \int d\omega \, f(\omega) A(\mathbf{k}, \omega) \partial_k^2 \epsilon_k
\tag{4.90}
$$

Further, when limiting ourselves to the case of nearest-neighbour hopping only, i.e. $\epsilon_k = -2t \cos(ka)$ we have $\partial_k \epsilon_k = -a^2 \epsilon_k$ and thus

$$\int_{-\infty}^{\infty} d\omega \, \Re\sigma(\omega) \;\; = \;\; -\frac{a^2 \sigma_0}{2\hbar^3} \langle T \rangle \tag{4.91}$$

with the kinetic energy

$$\langle T \rangle \;\; = \;\; 2 \sum_{k} \epsilon_k \hbar \int d\omega \, f(\omega) A(k, \omega) \tag{4.92}$$

That is to say, we recover the result of Equation (4.85).

D   Downfolding of Fermi velocity matrix elements Upfolding of the downfolded response

Many-body calculation for realistic systems mostly work in a downfolded setup. In other words, after a band-structure has been obtained from e.g. an LDA computation, orbitals that are supposed to be subject to only minor correlation effects are integrated out and linearized. These are typically high energy excitations, and thus the downfolding procedure is used to construct an effective low-energy problem, which is simpler to be tackled with a many-body approach. The linearization step preserves the Hamiltonian form of the one-particle part of the problem. Thereby the influence of correlation effects beyond the one-particle band-structure of these orbitals, and also the possible feedback on the others, are entirely neglected, and the high energy excitation spectrum fixed to the Kohn-Sham eigenvalues within LDA. The many-body calculation thus lives in an orbital subspace only, and all other orbital degrees of freedom remain unaffected. The introduction of a double-counting term, which corrects for correlation effects already taken into account by the LDA, may only adjust the center of gravity of the many-body spectrum with respect to the higher energy parts.

Although in the computation of the Fermi velocities, Equation (4.66), only the "non-interacting" band-structure results enter, several complications occur, when it comes to the deducing of optical properties from downfolded many-body calculations : Not only are transitions from and to high energy orbitals truncated, but also the optical transitions within the block of low-energy orbitals acquire wrong amplitudes, since, evidently, the computation of transition matrix elements and the downfolding procedure do not commute. Here one has to distinguish between the effect on the full matrix element from that on the Peierls velocity. As a matter of fact, when using the Peierls approach, the impact of the downfolding procedure is much worse. This is related to the aforementioned basis dependency of the Peierls conductivity. While the full velocity matrix element is only compromised by the linearization step inherent to the downfolding, the Peierls term, with its momentum derivative, suffers beyond this from the block-diagonalization as such. Indeed, the orbitals of the downfolded system are in general less localized than the ones of the original problem. For an instructive discussion on this subject see also [Millis(2004)].

Here we explain a simple strategy for the computation of the optical conductivity, applicable to many-body electronic structure calculations that were performed using a

downfolded one-particle, e.g. LDA, Hamiltonian. This procedure, though of course not rigorous, yields more sensible results than when computing the Fermi velocities directly from the downfolded system and is, in principle, not limited to the use of the Peierls approach.

The central quantity to look at in this respect is the orbital trace of the matrix product of Fermi velocities and momentum-resolved spectral functions in Equation (4.49) :

$$\mathrm{tr}\left\{v_{\mathbf{k}}A_{\mathbf{k}}(\omega')v_{\mathbf{k}}A_{\mathbf{k}}(\omega'+\omega)\right\} \tag{4.93}$$

Since the trace is invariant under unitary transformations, the above can certainly be written

$$\mathrm{tr}\left\{U_{\mathbf{k}}^{\dagger}v_{\mathbf{k}}U_{\mathbf{k}}\widetilde{A}_{\mathbf{k}}(\omega')U_{\mathbf{k}}^{\dagger}v_{\mathbf{k}}U_{\mathbf{k}}\widetilde{A}_{\mathbf{k}}(\omega'+\omega)\right\} \tag{4.94}$$

for arbitrary unitary matrices $U_{\mathbf{k}}$. In the case of a band-structure calculation (i.e. a vanishing self-energy, $\Sigma = 0$), we can chose these matrices such as that they perform the desired downfolding, i.e. both, the spectral functions $\widetilde{A}_{\mathbf{k}} = U_{\mathbf{k}}^{\dagger}A_{\mathbf{k}}U_{\mathbf{k}}$ and the transformed Hamiltonian will acquire a block-diagonal form. In the following we shall distinguish between the low energy block "L" and the high energy block "H". An LDA+DMFT calculation will normally add local Coulomb interactions only to the former after the blockdiagonalization, which will result in a self-energy that lives in this sub-block, while the orbitals of the latter will remain unchanged from the many-body (DMFT) calculation. In other words, since both sub systems are disconnected, the block-diagonality is retained throughout the calculation.

Clearly the downfolding procedure is not exact, since it linearizes the impact of the high energy orbitals. When solving the system with the full, non-downfolded, Hamiltonian [14], the matrices that block-diagonalize the full system would not be the same. They would even depend on the frequency ω due to the dynamical nature of the self-energy. Yet, when granting the approximative validity of the downfolding as such, and assuming the $U_{\mathbf{k}}$ to remain unchanged with respect to the initial band-structure, we can proceed further, and by specifying

$$\widetilde{v}_{\mathbf{k}} = U_{\mathbf{k}}^{\dagger}v_{\mathbf{k}}U_{\mathbf{k}} = \begin{pmatrix} V_1 & W \\ W^{\dagger} & V_2 \end{pmatrix}, \quad \widetilde{A}_{\mathbf{k}}(\omega') = \begin{pmatrix} L & 0 \\ 0 & H \end{pmatrix},$$
$$\text{and} \quad \widetilde{A}_{\mathbf{k}}(\omega'+\omega) = \begin{pmatrix} \bar{L} & 0 \\ 0 & \bar{H} \end{pmatrix} \tag{4.95}$$

the above trace becomes

$$LV_1\bar{L}V_1 + LW\bar{H}W^{\dagger} + HV_2\bar{H}V_2 + HW^{\dagger}\bar{L}W \tag{4.96}$$

For transitions within the block of only correlated orbitals, L , intervenes the Fermi velocity matrix V_1, which is evaluated as the low-energy block of the unitary transformed matrix element of the *full*, i.e. non-downfolded system. The resulting velocity $\widetilde{v}_{\mathbf{k}}$ is thus

---

[14]We neglect (e.g. screening related) issues concerning the interaction terms

different from the matrix element that is computed from the downfolded system. When using in particular the Peierls expression the momentum derivative of the unitary matrices $U_{\mathbf{k}}$ lead to additional terms in the latter case.

Moreover, with the above, a restriction to the low-energy block is not imperative. We can indeed calculate the complete optical response, including transitions from, to and within the high energy block[15]. The latter is entirely determined by the band-structure calculation. When comparing to experiments, this shortcoming/fact allows to assess whether it is only the relative position with respect to the low energy orbitals that needs an "adjustment", which is connected to the double counting term, correcting for correlation effects already taken into account by the LDA, or whether correlation effects modify substantially the overall spectrum of downfolded orbitals. The latter can be brought about e.g. by non-negligible life-times, or shifts that depend on the individual orbital.

We will refer to the above described scheme as "upfolding", since the downfolded orbitals are reintroduced for the sake of accounting for optical transitions from, into, and between them.

E   Colour Calculations

Among the optical functions, the reflectivity is the most natural one. Indeed, it is this quantity, that, in the region of visible light, is measured by our eyes. In order to calculate from the knowledge of the reflectivity the colours that our human detectors evidence, several parameters have to be considered. Besides the spectral response of the material, it is the spectral distribution of the light source and the colour sensitivity of our eyes that enter the calculation.

With this motivation, several colour schemes have been developed to describe the *standard observer*, i.e. the colour perception of the average human eye. This subject being a scientific branch on its own, with impact, in particular, on computer graphics, we shall not go into details, but refer to the literature : See [Nassau(2001)] and references therein.

The space of subtractive colours normally has three coordinates, referring to the three base colours, red, green, blue (RGB). The sensitivity of the response of the eye at different wavelengths is given by the *colour matching functions* $(\bar{x}, \bar{y}, \bar{z})$. Figure 4.3 shows the CIE 1964 XYZ standard functions[16]. With the colour matching functions one may calculate the *CIE XYZ colour coordinates* by

---

[15]We can thus make a distinction between different origins of spectral weight. Yet, we cannot tell apart the different contributions within the L block. While one has the possibility to suppress selected transitions by setting to zero the respective Fermi-velocity matrix elements, the different contributions are in that case not additive.

[16]The XYZ colour space is different from the standard RGB one. The advantage is that the colour matching functions are positive at all wavelength and can thus be interpreted as weighting function. This is not the case in the RGB formulation.
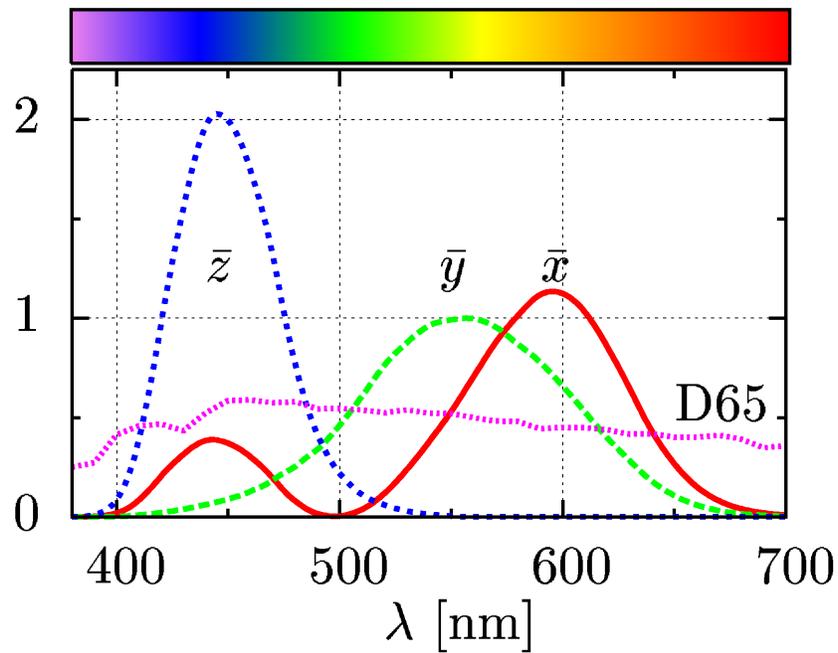
Figure 4.3 : *CIE 1964 colour matching functions ($\bar{x}$, $\bar{y}$, $\bar{z}$) as a function of wavelength, and the spectral distribution $S(\lambda)$ of the CIE day light illuminator D65 (6674 K) (illuminator values divided by 200). Data from [CVRL(2006)]. The bar on the top shows the colours corresponding to the indicated wavelengths.*

$$
\begin{aligned}
X &= k \int \mathrm{d}\lambda\, S(\lambda)R(\lambda)\bar{x}(\lambda) \\
Y &= k \int \mathrm{d}\lambda\, S(\lambda)R(\lambda)\bar{y}(\lambda) \\
Z &= k \int \mathrm{d}\lambda\, S(\lambda)R(\lambda)\bar{z}(\lambda)
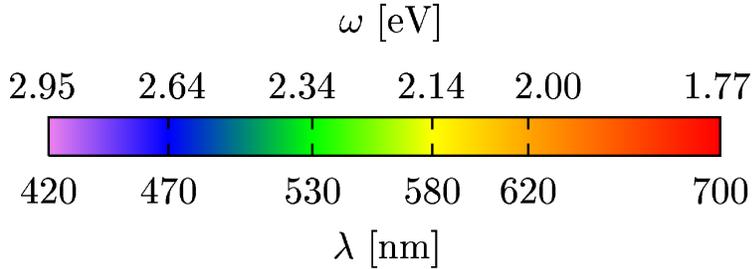\end{aligned}
\tag{4.97}
$$

Figure 4.4 : *The colour bar shows the visible spectrum in both, units of wavelength and eV.*

Here, $S(\lambda)$ is the spectral distribution of the light source. When performing actual calculations, we shall use the CIE illuminant D65, which is appropriate for usual day light. The corresponding distribution is also shown in Figure 4.3. Finally, $R(\lambda)$ is the reflectivity as calculated from the optical response functions that we introduced in the introduction to this chapter. k is a constant, that normally is chosen such that Y=100.

Then, the *chromaticity values* are defined by

$$
\begin{aligned}
x &= \frac{X}{X+Y+Z} \\
y &= \frac{Y}{X+Y+Z} \\
z &= \frac{Z}{X+Y+Z}
\end{aligned}
\tag{4.98}
$$

evidently the latter sum up to one, and they can be transformed into the usual RGB coordinates by a matrix transformation (which we take from [Hoffmann(2000)]).

F Technicalities : Examples

Simple cubic vanadium. Above we have extended the Peierls substitution to the case of multi-atomic systems. Here we shall illustrate the impact of the additional term by calculating the LDA optical response of fictitiously simple cubic vanadium in both, its primitive and a non-primitive, unit cell. Figure 4.5 shows the optical conductivity of

- cubic vanadium for the [100] polarization with one atom per unit cell. In this case the Fermi velocity is given by the momentum derivate of the Hamiltonian (red solid line)

- the same but using a non-primitive unit-cell, that with respect to the primitive one has been doubled along the x-direction, and using the generalized Peierls substitution (green dashed curve)

- the same as the latter but limiting the Fermi velocities to the momentum derivative of the Hamiltonian (blue curve).
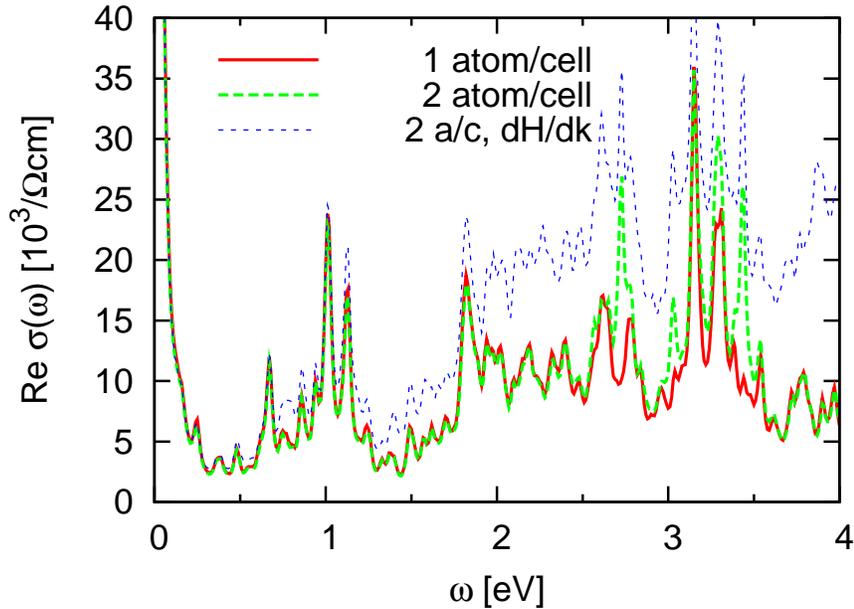

Figure 4.5 : *Optical conductivity of cubic vanadium for [100] polarization.*

We clearly see that the generalized Peierls substitution reproduces[17] the result of the primitive unit cell, while the neglecting of the additional term in the Fermi velocities induces errors up to 100%.

---

[17]Within the precision of our **k**-sampling.

Part III

Applications

The techniques developed in the preceding Part II are now applied to several examples of correlated materials : First we investigate two of the most well-known, but still not well-understood, compounds, namely the vanadium oxides VO_2 and V_2O_3.

- *In the case of VO_2, a detailed analysis of the excitation spectrum as calculated from LDA+(C)DMFT will lead to a deepened understanding of correlation effects in both, the metallic and the insulating phase. While for the former dynamical correlations and lifetime effects prevent a description in terms of quasi-particles, the excitation spectrum of the latter is found to allow for an effective band-structure. In this vein, we will construct an orbital-dependent, but energy-independent one-particle potential that reproduces the LDA+CDMFT excitation energies. Yet, though exhibiting a spectrum that is obtainable by a scissors operator, the true many-body ground state is well beyond a static one-particle description. The picture that emerges from this analysis we shall characterize as a "many-body Peierls" scenario. The seemingly contradictory result of a correlation driven metal to insulator transition in which the insulator exhibits less (spectral) signatures of correlations will thus be resolved. Moreover, we calculate the optical conductivity of both phases in a full-orbital setup, using the LDA+CDMFT self-energy. The results are in good agreement with experiment, corroborating further our picture of the electronic structure.*

- *In the case of V_2O_3, the mechanism of the doping-driven metal–insulator transition is investigated and identified to originate from a correlation enhancement of the e_g^π–a_{1g} crystal field splitting. This results in an effective de-hybridization between these orbitals. Both, the metallic and the insulating phases are found to exhibit strong satellite features in their spectral function, the dispersion of which reflects those of the renormalized one-particle excitations. Furthermore we evidence an orbital-selectivity in the coherence scale in the metallic phase : While a_{1g} excitations are found to be close to the Fermi liquid regime, e_g^π excitations remain incoherent down to the lowest temperatures of the calculation. This selectivity is confirmed by recent optical experiments. By identifying the orbital origins of different optical transitions, we explain the temperature dependence of the measured optical conductivity.*

- *The last chapter presents a study of the optical conductivity of rare-earth sesquioxides. In the series RE_2O_3, with RE=Ce, Pr, Nd, Pm, we track the behaviour of the localized f-states and their influence on the optical absorption. While the overall spectrum is dominated by O2p to RE5d orbitals, the low frequency onset of the absorption spectrum is determined by the position of the rare earth 4f states. The occupation of the latter increases along the series from one (Ce) to four (Pm) electrons. This change in filling results in a moving of the 4f Hubbard bands. In Ce_2O_3 the lower Hubbard band sits between the Fermi level and the uppermost oxygen bands and thus is fully responsible for the low-lying optical excitations, whereas already in Nd_2O_3 the Hubbard band has moved sufficiently downwards to merge with the oxygen bands, resulting in an oxygen dominated absorption edge that varies only little along the remaining rare earth series.*

Chapter 5

Vanadium Dioxide – VO$_2$

Since its discovery [Morin(1959)], almost five decades ago, the metal-insulator transition in VO$_2$ has fascinated condensed matter physicists and has been studied extensively, both, by diverse experimental techniques and numerous theoretical approaches. While a consensus even on the *nature* of the insulating phase is still lacking, VO$_2$ is on the verge of industrial applications, where use is made of its transition properties in ultra-fast switching devices [Rini *et al.* (2005)] and intelligent window coatings [Granqvist(1990)].

In the following will be given a short review on experimental and theoretical studies of VO$_2$, such as to explain the open questions and to put into context the findings of our work, whose description will follow in Section B. The starting point of our analysis are previous Cluster DMFT calculations by [Biermann *et al.* (2005)]. For a more extensive review on VO$_2$ see e.g. [Eyert(2002)] and references therein.

A Experimental findings and theoretical understanding - a brief review

It was found long ago [Morin(1959)], that VO$_2$ undergoes a first order metal-insulator transition as a function of temperature, as evidenced by the resistivity shown in Figure 5.1. The transition at 340 K is accompanied by a change in the crystal structure : The high temperature phase is of rutile (TiO$_2$) structure (P4$_2$/mnm) [Marezio *et al.* (1972)] : The oxygen ions form a hexagonal close packing. One half of the octahedral holes are filled by vanadium ions, such as to form two parallel chains of filled octahedra along the rutile c-axis, as indicated in Figure 5.2 (a). The unit cell comprises two formula units.

The monoclinic structure of the M1 phase (P2$_1$/c), Figure 5.2 (b), is characterized by the pairing up of vanadium ions that form dimers along the crystallographic c-axis, that moreover tilt, to eventuate in anisotropic zig-zag chains. This leads to a unit-cell doubling, hence a total of four formula units appear per primitive unit-cell. It is this particularity that has provoked the proposal of a simple Peierls mechanism for the insulating character of this phase, as will be detailed further below.
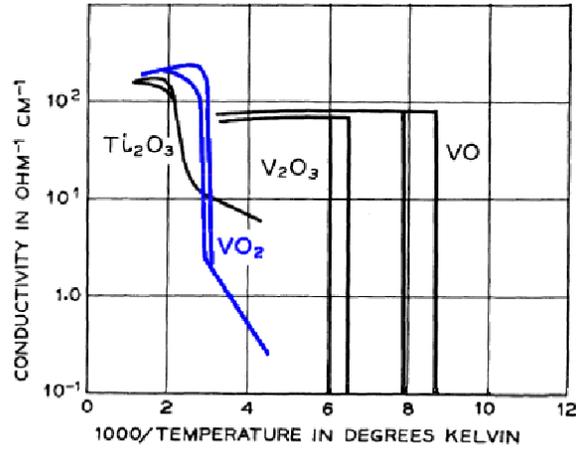
Figure 5.1 : *Resistivity of several transition metal oxides, as a function of inverse temperature. From [Morin(1959)].*
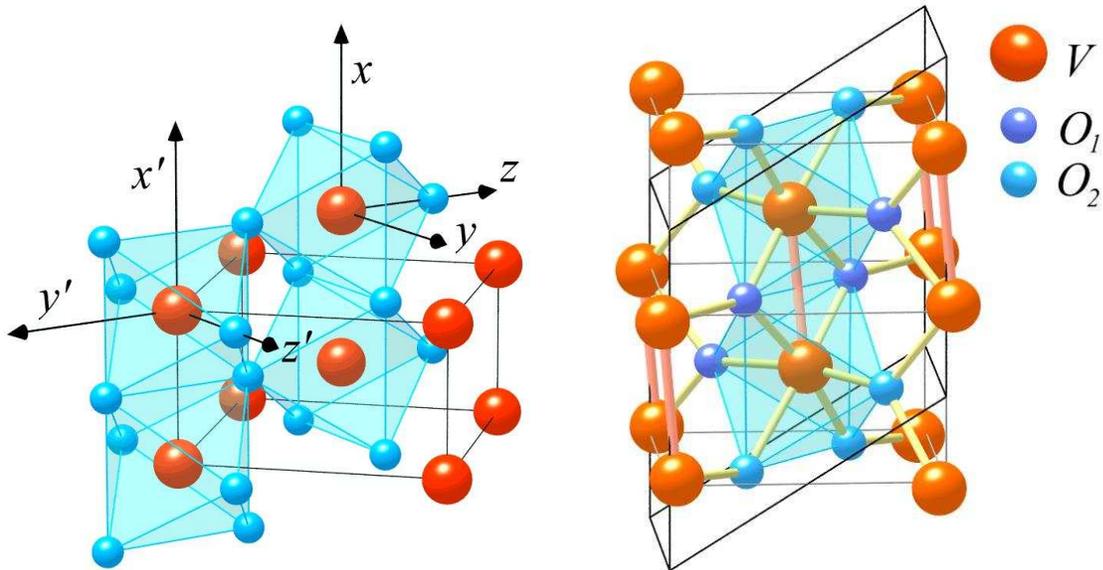

Figure 5.2 : *Crystal structure of VO$_2$ in (a) the rutile, (b) the M1 phase. The rutile c-axis is parallel to the x, x′ axis of the indicated local coordinate system in (a). From [Eyert(2002)].*

A.a The metallic rutile phase

There is considerable experimental evidence that already the metallic phase of VO$_2$ is a compound that exhibits strong correlation effects :

- The dc conductivity is found to violate [Allen *et al.* (1993), Qazilbash *et al.* (2006)] the Ioffe-Regel-Mott limit [Gunnarsson *et al.* (2003)] for resistivity saturation, i.e. the electron mean free path is comparable to, or smaller than the lattice spacing and Boltzmann transport theory breaks down.

- Further, the quasi-particle-renormalization factor Z was experimentally determined by photoemission spectroscopy [Okazaki *et al.* (2004)] and found to be rather small : $Z \sim 0.3$[1]. This is consistent with an effective mass enhancement, as evidenced by optical spectroscopy [Barker *et al.* (1966), Okazaki *et al.* (2006)], that finds $m^*/m = 4.3$[2].

- Also, photoemission experiments witness a vanadium 3d correlation satellite at binding energies higher than the lowest 3d band in LDA, see Figure 5.6 and Figure 5.9. This will be mentioned in more detail below when discussing the scenarios for the metal-insulator transition.

- Doping VO$_2$ with Niobium, $V_{1-x}Nb_xO_2$, which is thought to increase the lattice parameters and thus decrease hopping amplitudes, results in a Mott-Hubbard insulator having the rutile crystal structure [Villeneuve *et al.* (1972), Pouget *et al.* (1972), Lederer *et al.* (1972)].

A.b The insulating M1 phase and the metal-insulator transition

A.b.i Goodenough versus Mott

The formation of vanadium dimers and the resulting unit-cell doubling, led [Goodenough(1960), Goodenough(1971)] to propose a scenario in which it is the changes in the crystallography that are responsible for the metal-insulator transition. Here we shall summarize his line of reasoning.

VO$_2$ has a $3d^1$ configuration and hence the key focus lies on the d-orbitals. The cubic component of the crystal field resulting from the octahedral coordination of the vanadium ions in the rutile phase splits the d-orbitals into an e_g^σ and a t_{2g} manifold, with the latter lying lower in energy. The tetragonal contribution to the crystal field further splits the t_{2g} into two e_g^π and a single a_{1g} orbital. The former are made of d-orbitals that point towards the oxygen atoms and thus hybridize with the O2p orbitals. Due to their anti-bonding character, the e_g^π (often, as in Figure 5.3, denoted as π^*) lie higher in energy than the a_{1g} orbitals. These, on the other hand, are directed along the rutile c-axis, and are also

---

[1]When comparing the photoemission of [Okazaki *et al.* (2004)] and [Koethe *et al.* (2006)], we remark that in the former, the quasi-particle peak is less prominent, owing perhaps to more important surface effects. This however means that in particular the extracted Z factor has to be interpreted with caution.

[2]Only when supposing the electron self-energy to be local the identity $Z^{-1} = m^*/m$ holds.

called d$_\parallel$ as in the level scheme shown in Figure 5.3. In rutile VO$_2$, both these types of orbitals overlap, accounting for the metallic character of this phase. When passing to the monoclinic phase, two main effects are to be distinguished [Goodenough(1971)] :

- Due to the dimerization along the c-axis, the unit-cell doubles and the a_{1g} orbitals split into bonding / antibonding components (Peierls mechanism).

- The tilting of the dimers further leads to an increased hybridization of the e_g^π with some oxygen 2p orbitals, and thus they are shifted to higher energies with respect to the bonding a_{1g} component, whose occupation thus increases.

Both these effects favour a depletion of spectral weight at the Fermi level. Yet, the question is whether they are sufficient in magnitude to fully explain the insulating behaviour of the M1 phase : The optical gap was determined to be of the order $\sim$ 0.6 eV, e.g. [Okazaki *et al.* (2006)].
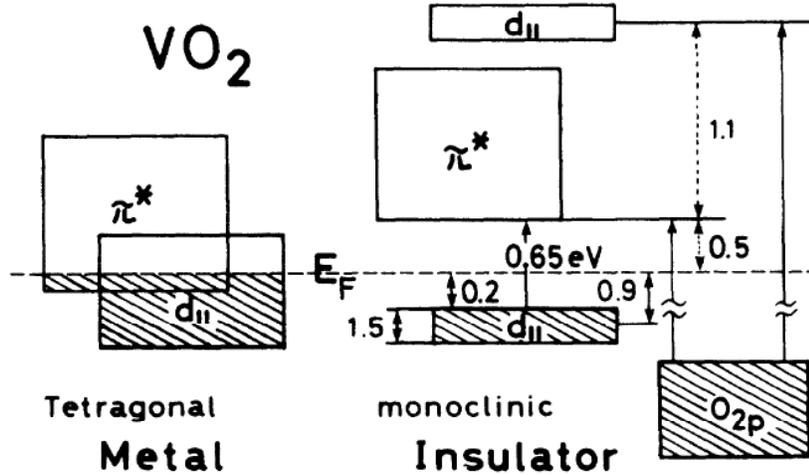

Figure 5.3 : *Schematic energy diagram for the vanadium 3d bands around the Fermi level. The energy differences are experimental estimates. From [Shin et al. (1990)].*

The second major viewpoint, initially put forward by [Zylbersztejn and Mott(1975)], emphasizes the role of electron correlations. By their reckoning, the pairing up of vanadium atoms only preempts an anti-ferromagnetic ordering, while the main reason for the insulating behaviour is the localization of carriers due to the Mott phenomenon, as described in the introduction. Thus, put simply, the opposing pictures for the insulating behaviour of the M1 phase of VO$_2$ are that of a Peierls insulator versus a Mott-Hubbard one.

In the following, we will collect experimental and theoretical evidence that has been worked out over the years, but which, however, did not yet lead to a globally accepted

consensus. Afterwards, we will show in our analysis how the two seemingly opposing pictures that have just been described, can somewhat be reconciled in a scenario in which correlations are essential for the nature of the insulating phase, but, still, they do not provoke a genuine Mott-Hubbard transition.

A.b.ii   Collecting evidence

Nuclear Magnetic Resonance and the $V_{1-x}Cr_xO_2$-phase diagram.   Besides the rutile and the M1 phase, other configuration can be realized by applying uni-axial pressure along the [110] rutile axis or by chemical substitution. The linkage between these other phases and the rutile or M1 one can give valuable information towards a better understanding of the un-doped compound at ambient pressure and was used to advocate the Mott-Hubbard scenario as will now be explained.
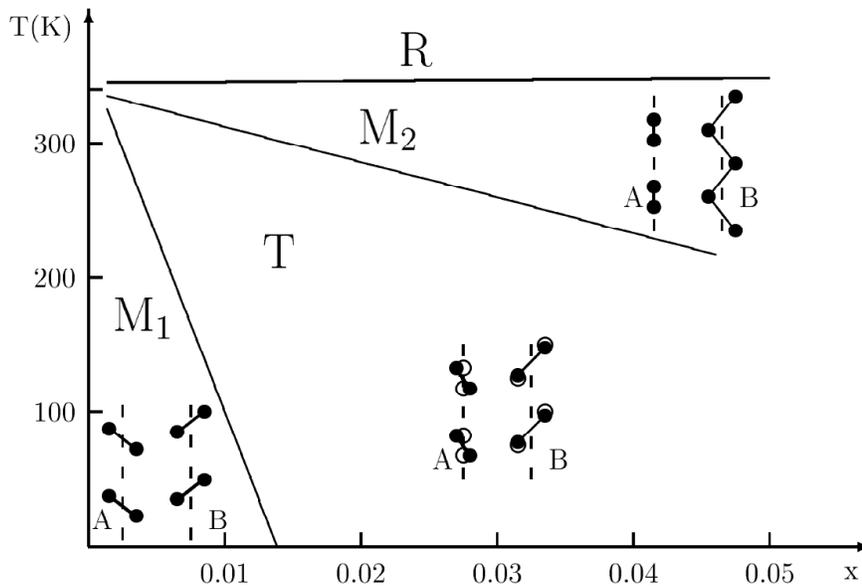

Figure 5.4 : *Phase diagram of $V_{1-x}Cr_xO_2$ after [Pouget and Launois(1976)]. Indicated are also the orientations and distortions of the vanadium chains. (open circles in the T phase refer to the positions of the M2 phase.) From [Eyert(2002)].*

Indeed, slightly different phase diagrams appear upon doping with small amounts of Cr, Fe, Al, or Ga [Marezio *et al.* (1972), Pouget *et al.* (1974)]. Figure 5.4 shows the phase diagram of Cr-doped VO$_2$ [Marezio *et al.* (1972), Pouget *et al.* (1975), Pouget *et al.* (1974)]. While at constant temperature the rutile phase persists upon doping, two new low temperature phases appear : In the insulating M2 phase, as indicated schematically in Figure 5.4, two inequivalent vanadium chains exist, in one of which only appears the dimerization while in the other only the tilting occurs. Nuclear magnetic resonance measurements [Pouget *et al.* (1974)] concluded that the tilted pairs have the magnetic response of spin 1/2 Heisenberg chains, while the dimerized chains are non-magnetic, S=0,

as is globally the case in the M1 phase. The T phase is an intermediate, or "transitional" phase between M1 and M2 at lower temperature.

[Pouget *et al.* (1975), Pouget *et al.* (1974), Pouget *et al.* (1974)] argued that the spin 1/2 chains are magnetic or Mott-Hubbard insulators. Further, since the M1 and M2 phases must be very close in their free energy and because they are linked continuously via the T phase, it was concluded that all the insulating phases of VO$_2$ are of the same type, namely the Mott-Hubbard one. In our analysis, we will put forward a slightly different scenario[3].

Also, when doping with Nb, a metal-insulator transition is induced in $V_{1-x}Nb_xO_2$ at concentrations $x \sim 0.14$, without provoking a change in the crystal symmetry, while finding a Curie-Weiss susceptibility in the insulator [Villeneuve *et al.* (1972), Pouget *et al.* (1972), Lederer *et al.* (1972)], which shows that rutile VO$_2$, as such, is indeed close to a Mott-Hubbard transition, which was thought to further corroborate the above Mott scenario for the rutile to M1 phase transition.

Band-structure methods and beyond. Arguments promoting a strong correlation scenario came from *ab initio* molecular cluster calculations. Indeed a gap of correct magnitude was opened in such an approach [Sommers and Doniach(1978)]. Furthermore, from the resulting level scheme an on-site Coulomb repulsion of $U \sim 1.22$ eV was extracted and a Heitler-London ground state, i.e. a state in which double occupancies have been projected out, was favoured over a linear combination of atomic orbitals (LCAO). The latter point will turn out to be crucial to our analysis. This will be detailed below.

Due to the considerable complexity of the compound, true band-structure calculations only became feasible decades after the discovery of the metal-insulator transition. A first attempt to describe the insulating behaviour of M1 VO$_2$ in terms of a one-particle theory was made by [Caruthers and Kleinman(1973)]. In their tight-binding linear-combination-of-atomic-orbitals (LCAO) calculation they monitored which tight-binding parameters change when going through the transition and then made the same parameters adjustable such as to reproduce, as well as possible, experimental results like the optical gap and the shape of the imaginary part of the dielectric function ϵ_2. Though in particular the opening of a gap was achieved, a reliable *ab initio* treatment of VO$_2$ remained to be awaited. Early results on the electronic structure of rutile VO$_2$ had suggested the validity of a band-like description. It was argued that the bandwidth obtained from optical and x-ray spectroscopy was too large to be subject of sizable correlations[4]. Owing to improvements both, in experiment and theory, this was however soon queried as stated already above. Indeed, e.g. modern photoemission data clearly evidences important correlation effects.

With the advent of density functional theory within the local density approximation (LDA), and increasing computer power, band-structure calculations of the monoclinic phase eventually became feasible, [Wentzcovitch *et al.* (1994)]. Although the LDA was

---

[3]In a Mott-Hubbard phase, Coulomb correlations prevail upon the itineracy of electrons, such as to localize the charge carriers on the atomic sites. This is naturally concomitant with the appearance of local moments. This is not found in M1 VO$_2$.

[4]Indeed, as we shall see, the *quasi-particle* part of the LDA+DMFT spectral function extents down in energy as much as the LDA density of states, as far as only the *occupied* spectrum is concerned.

not capable of opening a charge gap at the Fermi level, the basic tendencies of the Goodenough scenario were indeed found to take place. The formation of a pseudo gap was explained by a bond enhancement of the vanadium ions, as described by the Peierls mechanism. Also the calculation of total energies suggested that the energy gain owing to the change in crystal-symmetry was sufficient to account for the rutile to M1 transition. The failure of capturing truly insulating behaviour was ascribed to the commonly accepted gap underestimation of the local density approximation. It was thus concluded that "VO$_2$ may be more band-like than correlated" [Wentzcovitch *et al.* (1994)]. Figure 5.5 shows the LDA band-structure of M1 VO$_2$ from [Eyert(2002)]. The vertical bars indicate the contributions stemming from the a_{1g} orbitals ("fat band" representation). When comparing to the rutile structure (for an equivalent graphic for the rutile phase, see Fig. 29 in [Eyert(2002)]), an enhanced splitting of the a_{1g} is observed along with a general up-shift of the e_g^π orbitals.
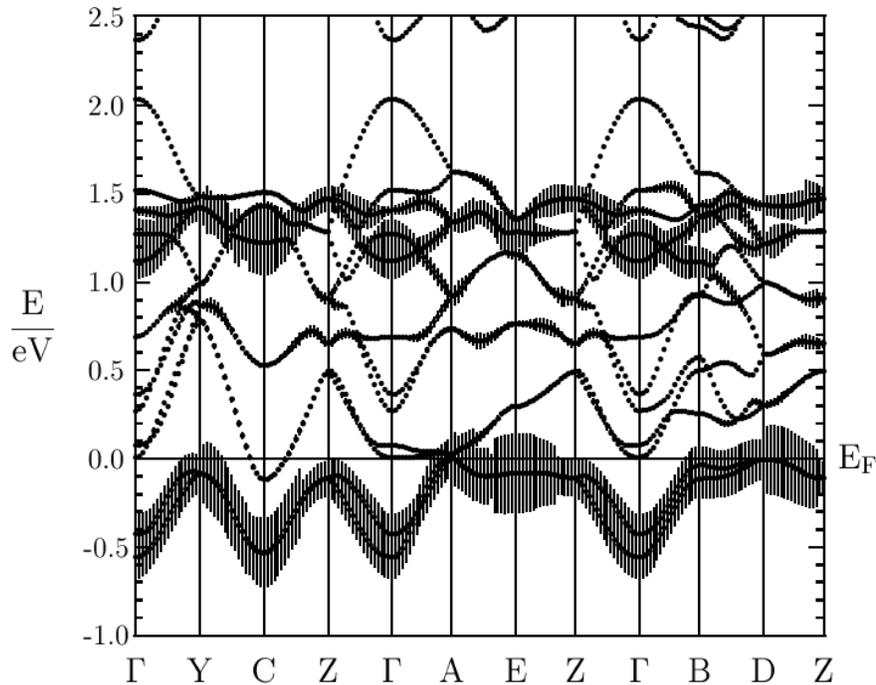

Figure 5.5 : *LDA band-structure of M1 VO$_2$. The width of the bars corresponds to the degree of a_{1g} contributions. From [Eyert(2002)].*

To further elucidate this band-like interpretation, electronic structure calculations beyond the LDA were performed. [Continenza *et al.* (1999)] used a model GW [Gygi and Baldereschi(1989)] approach, in which the screened interaction W was approximated by an inhomogeneous electron gas short-range component plus a residual interaction that was parametrized using the dielectric constant of the material[5]. This procedure opened

---

[5]Though only mentioned in the references, they apparently employed a self-consistency scheme with a full update of the wavefunctions.

a gap at the Fermi energy in good agreement with experiment. Indeed we will see below that by different means, we will arrive at a somewhat similar density of states.

Moreover, LDA+U [Anisimov *et al.* (1991)] calculations on VO$_2$ [Huang *et al.* (1998), Korotin *et al.* (2002), Liebsch *et al.* (2005)] succeeded in producing an insulating M1 phase. [Liebsch *et al.* (2005)] concluded that the important correlations are of static but non-local, or inter-orbital nature. In fact, though the Coulomb interaction U is site-diagonal, both, inter-site and momentum-dependent components are generated in the LDA+U self-energy by means of static screening processes. Further, it was shown that a gap is still opened when in the self-consistency all non-diagonal elements of the occupation matrix n$_{\alpha\beta}$ are neglected. "Non-diagonal coupling among t_{2g} orbitals" were thus argued to be unimportant for the gap opening. We will comment on this later.
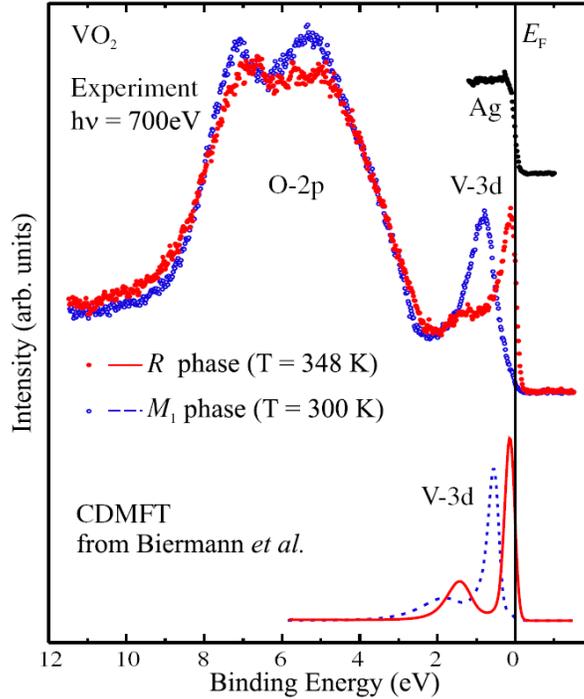

Figure 5.6 : *Photoemission spectra of VO$_2$ with 700 eV photons. From [Koethe et al. (2006)].*

Photoemission spectroscopy. Figure 5.6 shows results from a recent photoemission spectroscopy experiment [Koethe *et al.* (2006)]. Prior experiments were performed by [Sawatzky and Post(1979), Goering *et al.* (1997a), Kurmaev *et al.* (1998), Shin *et al.* (1990), Okazaki *et al.* (2004), Eguchi *et al.* (2006)]. In the rutile phase (red) a quasi-particle peak appears at the Fermi energy. At binding energies higher than 1 eV, there still is vanadium 3d weight, that reminds of a lower Hubbard band. This is clearly not captured by LDA calculations, see the density of states in Figure 5.9, and a further indication for strong correlations. Below the transition temperature (blue curve) a well defined feature appears at energies intermediate to the rutile lower Hubbard band and the rutile quasi-particle

peak. This is rather interesting : In a realistic transition, it is mostly the kinetic energy that is controlled by external parameters such as pressure or temperature, that thus are the driving force of the metal-insulator transition. Of course, due to possible changes in the crystal symmetry and thus the screening effects, also the Coulomb interaction is susceptible to variations. Yet naively, one would rather not think that the on-site interaction U is larger in the insulator than in the metal. Hence, when comparing the position of the preformed lower Hubbard band in the metal and in the insulator, it appears conceivable that it could move to higher binding energies in the latter. Here, however, the inverse seems to be the case. This is why [Koethe *et al.* (2006)], in agreement with [Biermann *et al.* (2005)] whose calculations our work is based on, and in the spirit of Goodenough, interpreted the prominent feature in the insulator as a bonding-orbital rather than a lower Hubbard band.

As concerns oxygen 2p weight in the photoemission spectra, one observes slight changes, both, in position and relative amplitudes. This is likely to be due to the modifications in the crystal symmetry and the resulting changes in the hybridizations.

An angle resolved photoemission spectroscopy experiment was performed in [Goering *et al.* (1997b)]. It was evidenced that in both, the metallic and the insulating phase, the measured bandwidth is somewhat narrower than in band-structure calculations. However, the limited experimental resolutions impeded more quantitative statements.

X-ray spectroscopy.   As regards the unoccupied part of the spectrum, insights can be gained by x-ray absorption spectroscopy. Here use is made of the mixed character of spectral weight at energies of the d-manifold. In the two experiments whose results we will mention below, the spectroscopic intensity is arising from transitions of O1s into O2p admixtures of the vanadium 3d orbitals. As for photoemission, the history of experiments for VO$_2$ is extensive : [Sawatzky and Post(1979), Bianconi(1982), Abbate *et al.* (1991), Kurmaev *et al.* (1998), Hérbert *et al.* (2002), Haverkort *et al.* (2005), Koethe *et al.* (2006), Eguchi *et al.* (2006)]. Figure 5.7 shows results for the O1s absorption edge for both, the rutile and the M1 phase from [Abbate *et al.* (1991)]. While the peaks corresponding to transitions into e_g^π (here again denoted π^*) and e_g^σ orbitals (σ^*) remain rather unaffected by the transition, clearly visible is the appearance of a third peak, at ~ 1 eV above the e_g^π, that has been attributed to transitions into the a_{1g} anti-bonding component (d$_\parallel$) following the Goodenough picture, as schematized Figure 5.3.

Due to the anisotropy of the monoclinic insulating phase, valuable information can be obtained from experiments that use polarized radiation. In the bonding / antibonding picture, the dependence of transition matrix elements on the orientation of the crystal with respect to the electric field is expected to be particularly pronounced for the a_{1g} orbitals when comparing the rutile with the M1 phase. Figure 5.8 shows recent results by [Koethe *et al.* (2006)]. Indeed the aforesaid d$_\parallel$ peak is discernible only in the spectrum where the electric field is parallel to the c-axis, along which the a_{1g} orbitals are oriented. In fact, the transitions in question are into oxygen 2p admixtures of the same symmetry, since these hybridize most with the a_{1g} orbitals. Though there is a tiny fraction of transitions of d$_\parallel$–character at lower energies, see [Koethe *et al.* (2006)], the authors identified the large main structure described above as the a_{1g} anti-bonding component, by resorting to the
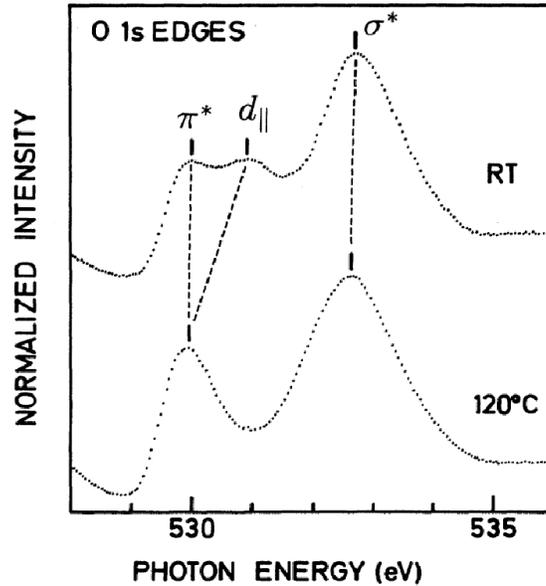
Figure 5.7 : *O1s absorption spectra at room temperature (RT) and at $T = 120°C$. From [Abbate et al. (1991)].*

Hubbard molecule. As a matter of fact, in our analysis we will rationalize the relevance of this model to the M1 phase also from the theoretical point of view. See in particular Section B and Appendix B.

Optical spectroscopy. Another experimental probe suited for the investigation of the electronic structure of correlated materials is optical spectroscopy. Chapter 4 of this thesis was devoted to developing a theoretical formalism for the calculation of optical properties for correlated systems. Above, we have already mentioned several results obtained from optical spectroscopy such as the optical gap, an estimate for the effective mass and the evidence for bad metal behaviour in the rutile phase. Although less open to interpretation, optical experiments give valuable information on low energy excitations. By appealing to sum rules, the redistribution of spectral weight as a function of temperature can be studied carefully.

Optical measurements on VO$_2$ were first performed by [Barker *et al.* (1966)], and [Verleur *et al.* (1968)]. By probing different orientations of single crystal samples, they evidenced an anisotropy in the optical response of the M1 insulator. More precisely, the conductivity depends on whether the electric field is parallel or perpendicular to the crystallographic rutile c-axis going going below the transition temperature. This is to be expected from the described changes in the crystal-structure with the unit-cell doubling along the c-axis. This anisotropy was confirmed by ultraviolet reflectance measurements [Shin *et al.* (1990)] and x-ray experiments [Abbate *et al.* (1991), Koethe *et al.* (2006)]. [Ladd and Paul(1969)] performed experiments under pressure, and noticed that c-axis stress reduces the transition temperature considerably more than is the case for hydrostatic pressure. More recently, [Okazaki *et al.* (2006)] studied reflectance spectra of thin films
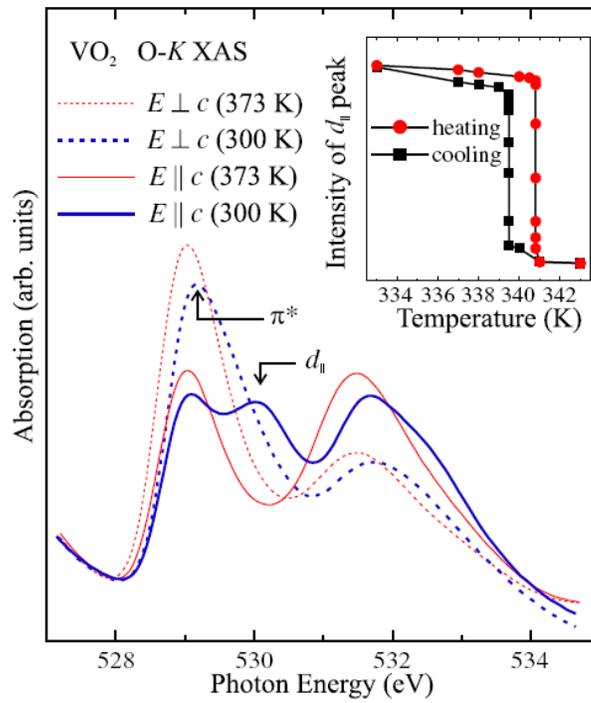
Figure 5.8 : *Polarization dependent O1s x-ray absorption spectra (XAS) of VO$_2$ above and below the transition temperature ($T_c \sim 340$ K) and for polarizations parallel and orthogonal to the crystallographic c-axis. The inset shows the temperature dependence of the $d_{\parallel}$ peak intensity across the metal-insulator transition. From [Koethe et al. (2006)].*

with an orientation such that the electric field is perpendicular to the rutile c-axis as a function of temperature, and found indications for electron-phonon couplings. New studies by [Qazilbash *et al.* (2006)] on polycrystalline films with preferential [010] orientation [Chae *et al.* (2006)] confirmed the bad metal behavior of rutile VO$_2$ evidenced already in earlier transport experiments [Ladd and Paul(1969)]. As mentioned already above, rutile VO$_2$ is found to violate [Allen *et al.* (1993), Qazilbash *et al.* (2006)] the Ioffe-Regel-Mott limit for resistivity saturation [Gunnarsson *et al.* (2003)]. As we shall see, pronounced differences in the optical response are found between the individual experiments. We will detail and comment on this in Section D, where we will also review prior theoretical work on optical properties of VO$_2$, before presenting our results on the optical conductivity using the formalism of Chapter 4.

A.c   LDA+(Cluster)DMFT

The undeniable presence of correlation effects in VO$_2$ called for a description beyond the LDA by incorporating in particular local Coulomb interactions. LDA+DMFT calculations for the rutile phase were first performed by [Liebsch *et al.* (2005), Laad *et al.* (2005), Laad *et al.* (2006a)]. Both works used a density of states implementation of LDA+DMFT[6] While Laad *et al.* used an iterated perturbation theory (IPT) solver, Liebsch *et al.* resorted to a quantum Monte Carlo algorithm to solve the DMFT impurity model. Though agreeing on the fact that rutile VO$_2$ is a strongly correlated metal, the spectral functions differ considerably in the works cited above and different conclusions are drawn as to the metal-insulator transition mechanism. Laad *et al.* stress their findings of a non-Fermi liquid in the rutile phase and conclude that already in the metal a_{1g} spectral weight is gapped out, and thus the metal-insulator transition in VO$_2$ to be "orbital-selective". Liebsch *et al.*, on the contrary, emphasized the small degree of orbital polarization in the metal, leading to small static, but considerable dynamical correlations, while the insulator was said to be mainly governed by static correlations, since LDA+U (see above) does open a gap [Huang *et al.* (1998), Korotin *et al.* (2002), Liebsch *et al.* (2005)]. Indeed, we will substantiate the viewpoint of static correlations in our analysis[7].

Cluster DMFT calculations were eventually performed by [Biermann *et al.* (2005)]. A two-site cluster was chosen as the basic unit, which is the natural choice, given the vanadium dimerization. Moreover, the calculation used a full Hamiltonian implementation instead of a partial density of states approach. In the Hamiltonian all orbitals other than the vanadium t_{2g} were downfolded.

Given the additional cluster degrees of freedom, the system was found to develop a non-local, intra-dimer a_{1g}–a_{1g} coupling in the self-energy. The physical picture that emerged from the analysis of [Biermann *et al.* (2005)] was that the a_{1g} electrons populate a bonding orbital and thus form singlets that live on the vanadium dimers and are "dynamical" due to the coupling to the CDMFT bath degrees of freedom. These singlets were found to be

---

[6]See Section B, Chapter 6 for a discussion of the implications. A small orbital anisotropy, and, correspondingly, only small charge transfers with respect to the LDA, make this approximation reasonable in the current case of rutile VO$_2$.

[7]However, as we shall see, LDA+U is not sufficient to fully account for them.

close to their Heitler-London limit, in accordance with [Sommers and Doniach(1978)].

Our work is based on these quantum Monte Carlo LDA+CDMFT calculations [Biermann *et al.* (2005)]. More details will be given below.

B   LDA+(C)DMFT – Insights by analytical continuation[8]

Summarizing the above history of experimental and theoretical results, it can be said that correlation effects must play a role in both phases of VO$_2$, yet no consensus has been reached so far, as to whether the nature of the insulating phase is dominated by the structural (Peierls) or the correlation (Mott) aspect. As a matter of fact, in our analysis we will reconcile these two viewpoints, by explaining how and why the strong correlations lead to an insulating behaviour, yet not in the fashion of a Mott-Hubbard transition. Indeed, our analysis reveals the striking tendency that the insulating phase exhibits a much higher degree of coherence than the metal. This appears counter-intuitive at first, since, as a rule of thumb, insulating behaviour of open d, or f-shell compounds is thought to be correlation driven. Actually this is also true for VO$_2$, however the correlation effects are highly non-generic : Despite their undeniable strength, they do not eventuate in important life-time effects, i.e. one-particle excitations retain their coherence to a surprising extent. Still, the position in energy of the excitations is tremendously modified with respect to band-structure calculations[9]. Below, it is shown that these modifications can even be cast into a non-local, yet static one-particle potential, that, when added to the LDA Hamiltonian, reproduces the interacting excitation spectrum, and moreover results in an optical conductivity that compares reasonably with experiment. However, as will be explained in the following, the system is in principle far from a pure one-particle description. This caused us to introduce the notion of a "many-body Peierls phase", where the referring to the Peierls mechanism emphasizes the one-particle like effects on the excitation spectrum, while the addition "many-body" indicates that for instance the ground state is quite far from a description in terms of Slater determinants of one-particle states, as will be detailed and rationalized in the following.

In the metallic rutile phase, on the other hand, correlation effects lead to strong life-time effects and incoherent satellite features. The low energy physics is dominated by strong renormalization effects, rather than static displacements. At higher energies, prominent Hubbard bands arise, further invalidating a description in terms of band-like excitations.

Usually, the analysis of realistic LDA+DMFT calculations is rather difficult, since quantities calculated by Monte Carlo techniques are derived on the Matsubara axis, which often are not obvious in their interpretation. As will become evident in the succeeding sections, our analytical continuation scheme proves especially valuable in the current case of vanadium dioxide, where it allowed for a deeper understanding of the physical mechanisms at work. Still, the case in point is also quite challenging due to its complexity :

---

[8]This work appears in two papers : [Tomczak and Biermann(2007a), Tomczak *et al.* (2007)]

[9]The Hubbard bands in f-electron materials are also coherent, due to their atomic nature. However, they are not band-like, in the sense that there are *two* Hubbard "bands" per former one-particle band. The correlations eventuate in splitting the excitation. Within the concept presented in Section A, Chapter 3, one realizes that the number of poles is not conserved when applying the local interactions. The case for M1 VO$_2$ is thus genuinely different.

Contrary to vanadium sesquioxide V$_2$O$_3$ (see next section), the self-energy in both phases is non-diagonal in orbital-space. Hence, as described in Appendix A, we perform maximum entropy algorithm calculations on unitarily-transformed orbital components. While in the rutile phase the off-diagonality arises from the choice of the local coordinate system, it is inter-site, i.e. non-local or cluster-, elements that turn up in the M1 phase. The latter will play a significant role in our picture of the nature of the insulating phase.

B.a   The metallic rutile phase

B.a.i   The local spectral function

Figure 5.9 shows the local spectral function of the rutile phase of VO$_2$, as obtained from a maximum entropy algorithm continuation of the LDA+DMFT Green's function in imaginary time by [Biermann *et al.* (2005)]. Their calculation used the value U=4.0 eV for the on-site interaction, and a Hund's coupling J=0.68 eV[10]. The temperature of the calculation was rather elevated with T=770 K ($\beta = 15$).
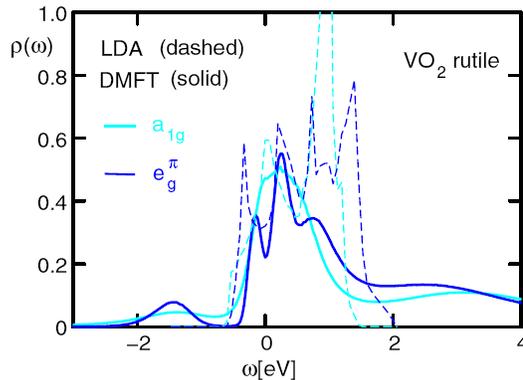

Figure 5.9 : *Rutile VO$_2$: Comparison of the LDA density of states with the LDA+DMFT local spectral function, for the indicated orbitals, from [Biermann et al. (2005)].*

As compared to the LDA density of states, corresponding to the dashed lines in the same figure, the LDA+DMFT spectral function extends over a much wider frequency range, namely from -2 eV to more than 4 eV. This is congruent with the above shown photoemission spectrum, Figure 5.6, and an indication that the correlation induced renormalizations are indeed considerable and lead to sizable satellite features, that are intrinsically beyond the LDA.

As will be seen in the following, our analytical continuation scheme for the LDA+DMFT self-energy, will allow for a more detailed analysis of the excitation spectrum, by considering the real-frequency self-energy as such and the momentum-resolved spectral function that it entails.

---

[10]It was used the usual parametrization U$_{mm}$=U, U$_{mm'}$=U-2J (m$\neq$m$'$), and J$_{mm'}$=J (m$\neq$m$'$).

B.a.ii   The real-frequency self-energy

For the sake of a better comparison, the LDA+DMFT calculation of the rutile phase was performed in a non-primitive unit cell [Biermann *et al.* (2005)], containing four formula units, as is the case for the primitive unit-cell of the M1 phase. In the metallic phase, a single-site DMFT setup was adopted. The self-energy then has the following orbital structure :

$$\Sigma_{unitcell} \quad = \quad \begin{pmatrix} \Sigma_{VO_2} & 0 & 0 & 0 \\ 0 & \Sigma_{VO_2} & 0 & 0 \\ 0 & 0 & \Sigma_{VO_2} & 0 \\ 0 & 0 & 0 & \Sigma_{VO_2} \end{pmatrix} \tag{5.1}$$

where the blocks Σ_{VO_2} are each 3x3 matrices that correspond to the t_{2g} self-energy matrices for a given VO$_2$ formula unit, which in turn look

$$\Sigma_{VO_2} \quad = \quad \begin{pmatrix} \Sigma_{a_{1g}} & 0 & 0 \\ 0 & \Sigma_{e_g^\pi} & \Sigma_{e_g^\pi - e_g^\pi} \\ 0 & \Sigma_{e_g^\pi - e_g^\pi} & \Sigma_{e_g^\pi} \end{pmatrix} \tag{5.2}$$

i.e. besides the diagonal a_{1g} and e_g^π components there is an on-site inter-e_g^π element. Alternatively, one could have worked in a basis, in which the self-energy is diagonal, with two inequivalent e_g^π elements. Indeed, in this special case of degenerate e_g^π diagonal elements, this is the way how we perform the analytical continuation of the off-diagonal component : As explained in Appendix A, a unitary orbital transformation is used to rotate the self-energy. Contrary to the general case, the rotation here yields a diagonal self-energy.

Figure 5.10 shows (a) the real and (b) the imaginary parts of the LDA+DMFT self-energy on the real frequency axis, after our analytical continuation treatment. Figure 5.11 shows a comparison between the Matsubara self-energy as obtained from the QMC and the Hilbert transformed real-frequency one. The low energy agreement is very good, while at higher energies the QMC self-energy is noisy and the processed self-energy deviates perceptibly.

Coming back to Figure 5.10, we see that the off-diagonal element, which is important to be taken into account during the continuation process, is non-negligible, yet smaller than the diagonal ones. Notwithstanding minor details in position and shape, the a_{1g} and e_g^π elements exhibit a comparable, though quite dynamical behaviour. The real-parts of the diagonal elements at zero frequency, $\Re\Sigma(0)$, that are responsible for relative shifts in the a_{1g} and e_g^π quasi-particle bands near the Fermi level are almost the same, which is in line with the quite modest change in the relative a_{1g} and e_g^π occupations as compared to the LDA [Biermann *et al.* (2005)], and with the measured rather isotropic character of rutile VO$_2$ [Haverkort *et al.* (2005)].

In an energy window of about 1 eV around the Fermi level, the diagonal real-parts are rather linear, with slopes that lead to eigenvalues of the Z-matrix, Equation (2.26), of 0.48
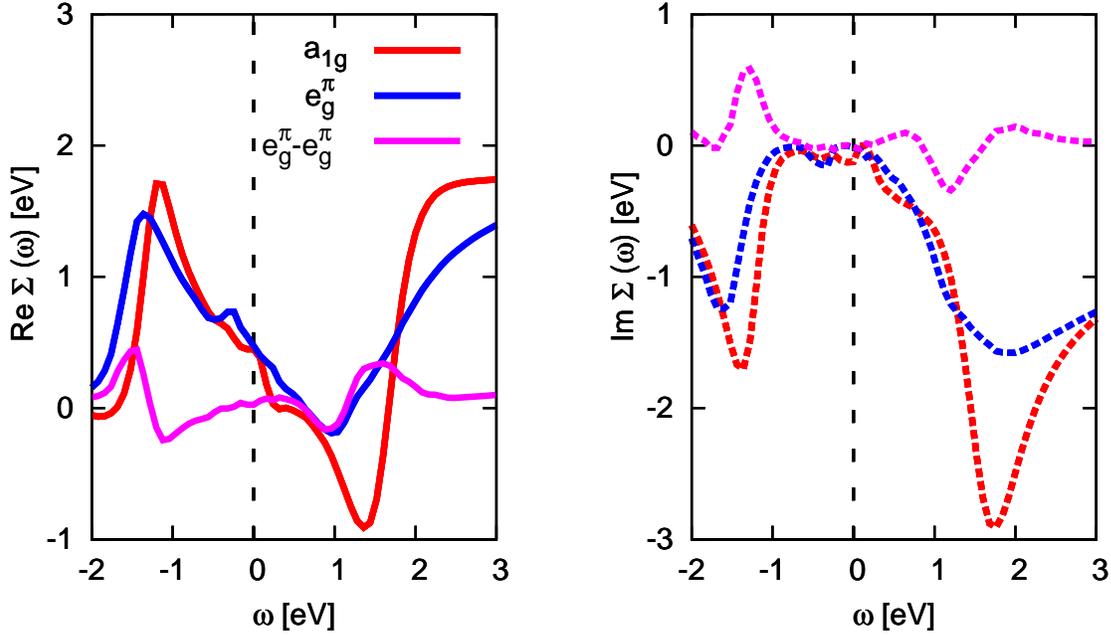
Figure 5.10 : *LDA+DMFT self-energy $(\Sigma - \mu)$ of rutile VO_2 on the real frequency axis: (a) real parts (b) imaginary parts for the indicated orbital components.*
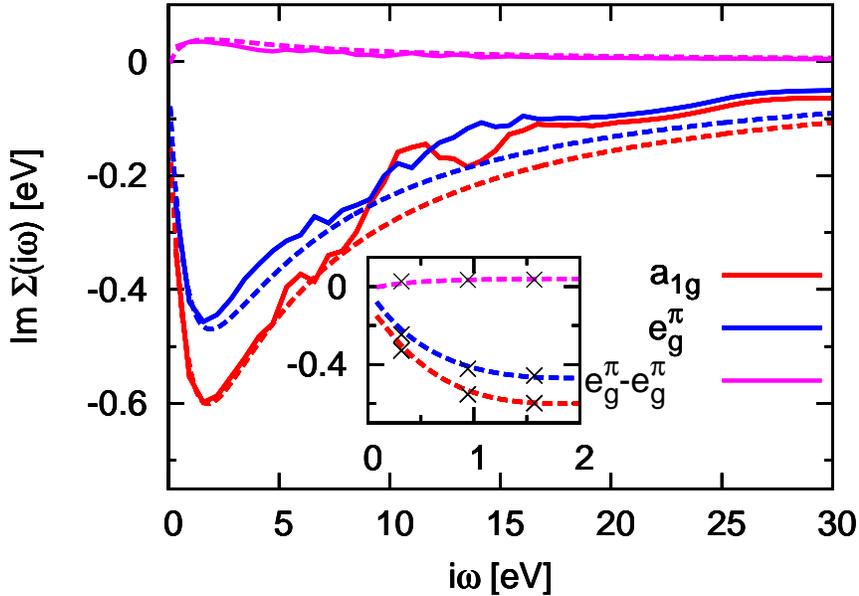

Figure 5.11 : *Comparison of the Quantum Monte Carlo self-energy on the Matsubara axis (solid lines) with the one obtained from the analytically continued one by a Hilbert transform, Equation (3.6), (dashed lines). Shown are only the imaginary parts. The insets shows the low energy regime and here the crosses indicate the discrete Matsubara self-energy from the QMC.*

for the a_{1g}, and 0.59, 0.53 for the e_g^π respectively, indicating strong renormalization effects. In comparison, photoemission experiments found indications for a Z-factor of ~ 0.3.

However, in the current case, our numerical precision for the imaginary parts around the Fermi level is not sufficient for quantitative statements about the coherence at low energy. Whether or not, the electrons are in their Fermi liquid regime, can, unfortunately, not be answered from the current analysis. Hence, we cannot assess the experimentally found bad metal behaviour, manifesting itself, as mentioned above, in the exceeding of the Ioffe-Regel-Mott limit for resistivity saturation [Qazilbash *et al.* (2006)]. Still, we realize that already below -0.5 eV and above +0.2 eV, the imaginary parts, corresponding to the inverse life-time, of both orbital components become considerable. As a result, sharp one-particle-like excitations are not to be expected beyond a quite narrow energy window around the Fermi level.

At still higher energies, prominent features develop in both real and imaginary parts of the self-energy, typical harbingers of Hubbard satellite formation.

B.a.iii Linearized band-structure

A first attempt to improve on the LDA band-structure by incorporating correlations, yet while keeping a Hamiltonian form, is to take self-energy renormalization effects into account up to linear order in frequency, as described in Section A, Chapter 3. For this procedure to make conceptual sense, we are supposing the system to be in the Fermi liquid regime, i.e. the imaginary parts of the self-energy are assumed to be sufficiently low at the Fermi level, although this cannot be fully warranted from our numerical data, as mentioned above. Herewith, the linearization is exact at the Fermi level. Figure 5.12 shows the renormalized band-structure corresponding to the Z values given in the preceding section.

As compared to the LDA, the bands get obviously renormalized towards the Fermi level, whence the overall band-narrowing. The slightly different real parts at zero frequency, $\Re\Sigma(0)$[11] lead to some modifications of the Fermi surface : The crossings with the Fermi level are changed with respect to the LDA, although only slightly[12]. Again, one has to keep in mind that the linearized bands no longer carry weight one, but $Z_{eff} < 1$ that depends on the orbital character, which in turn is momentum-dependent. It is thus not a good idea to start counting electrons in this picture.

B.a.iv Momentum-resolved spectral functions and quasi-particle poles

While the above procedure gives an accurate picture of the many-body excitation spectrum around the Fermi level, with the fully frequency-dependent LDA+DMFT self-energy we are in the position to compute the momentum-resolved spectral function. Figure 5.13 shows the result in a colour-coded representation. Also indicated are the quasi-particle poles of the Green's function when entirely neglecting life-time effects, as described in

---

[11]and in principle also the fact that in the current case the Z-matrix is non-diagonal in orbital space.

[12]In the case of degenerate bands, such as for SrVO$_3$ when downfolded onto the t_{2g} subset, the Fermi surface is not affected by correlation effects stemming from a local, i.e. momentum-independent self-energy, as mentioned in the introduction.
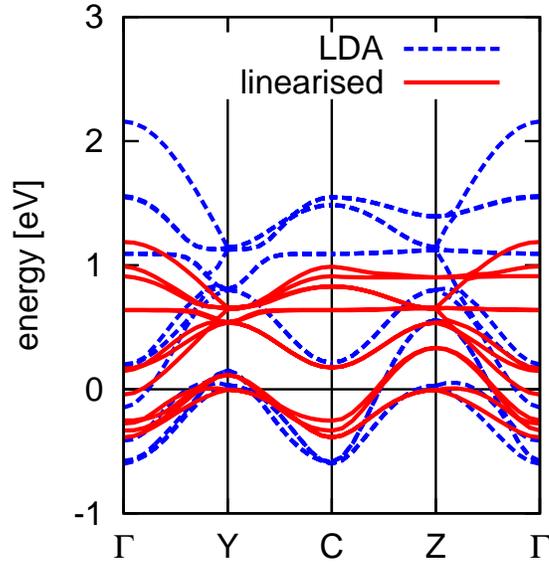
Figure 5.12 : *Comparison between LDA bands and the renormalized band-structure, constructed from a linearized self-energy, according to Section A, Chapter 3.*
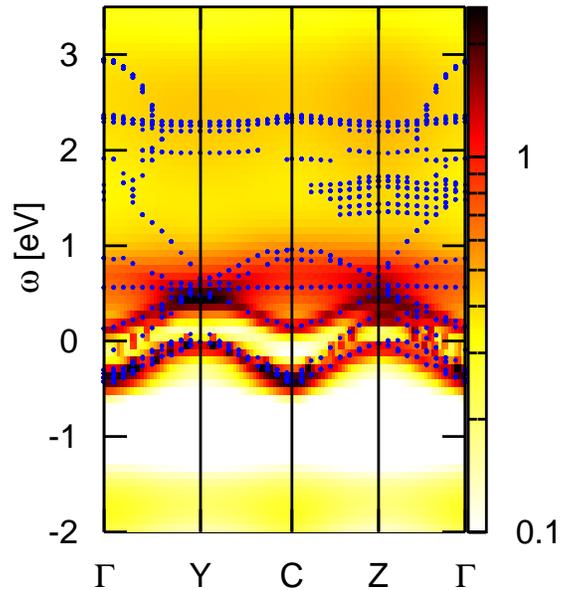

Figure 5.13 : *Momentum-resolved LDA+DMFT spectral function of rutile VO$_2$ along selected symmetry lines with colour-coded intensity, as indicated by the colour-legend to the right. The (blue) dots are solutions of the quasi-particle Equation (3.9). See text for a discussion.*
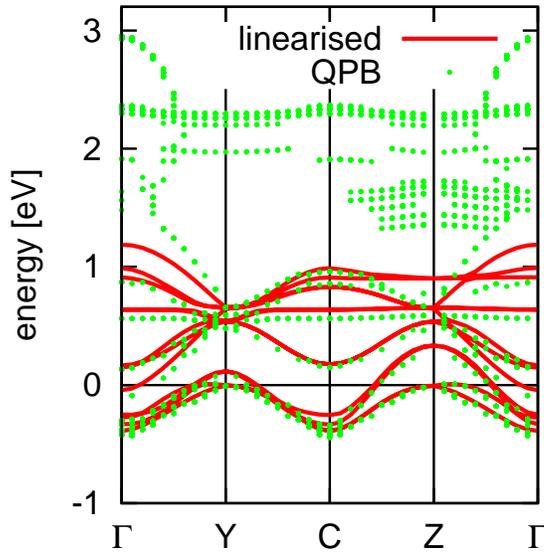
Figure 5.14 : *Comparison of the linearized band-structure, Figure 5.12, and the solutions of the quasi-particle Equation (3.9).*

Section A, Chapter 3. At low energy, the almost completely filled band of mainly a_{1g} character is discerned as quite sharply defined. As expected from the above discussion of the self-energy, the solutions of the quasi-particle Equation (3.9) follow closely the spectral intensity in this energy region. Also, as seen in Figure 5.14, the numerical solution of the quasi-particle equation coincides with the renormalized bands at the Fermi level, and at energies around it, as they should by construction. Slight deviations at higher energies, are accounting for the self-energy which is not strictly linear over the entire relevant frequency range. Still, up to the point where the upper Hubbard band emerges, the agreement between the pole structure and the linear renormalized band-structure is quite satisfactory. It is thus the *linearity* of the dynamical behaviour of the real part of the self-energy that accounts for the reshaping of the excitation energies. Yet, the attempt of constructing a global effective band-structure fails : Already above 0.2 eV, while there are regions of high intensity in the spectral function, the larger imaginary parts of the self-energy broaden the excitations, and no coherent features emerge, though the positions of some excitations of dominant e_g^π character are discernible when comparing with the pole-structure. As seen above, at high, positive and negative, energies distinctive features appear in the imaginary parts of the self-energy, that are responsible for the formation of lower and upper Hubbard bands, seen in the spectral function, both the momentum-resolved, Figure 5.13, and the local one, Figure 5.9, at around -1.7 eV and 2.5 eV, respectively.

In the range of the upper Hubbard band, a pole-structure appears whose shape is reminiscent of the low-energy quasi-particle band-structure, which is congruent with observations that quasi-particle dispersions are generally reflected in the Hubbard bands [Hubbard(1963)]. This will also be observed for V$_2$O$_3$ in the next chapter. The fact that

these poles are numerous can be rationalized from the graphical construction, Section A, Chapter 3. Indeed when the slope of the self-energy within the band-width stripe is one, or close to it, then several solutions $\omega_{\mathbf{k}}$ appear per given momentum.

B.a.v   Conclusions

In rutile VO$_2$, the excitation energies stemming from former LDA bands are strongly renormalized by the correlations. Linearizing the real-parts of the self-energy around the Fermi energy is sufficient for accounting for the full dynamical behaviour of the self-energy within the former LDA bandwidth. Yet, while giving some information on the position of spectral weight, this cannot explain, by construction, for the full physics of rutile VO$_2$, in which life-time effects are found to be non-negligible already at low energy. Moreover, important incoherent features appear in the spectral function, turning down further the quest for a global description in terms of an effective band-structure of one-particle excitations.

B.b   The insulator
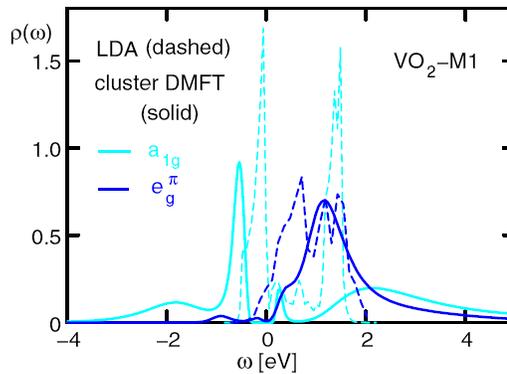
B.b.i   The local spectral function

Figure 5.15 : *M1 VO$_2$: Comparison of the LDA density of states with the LDA + Cluster DMFT spectral function for the indicated orbitals. The two inequivalent e_g^π components have been averaged for better visibility. From [Biermann et al. (2005)].*

While in the metallic rutile phase, the local spectral function could still be said to lead, yet in a less detailed way, to the above conclusions, this, we shall see, is not the case for insulating VO$_2$. Indeed, in the current phase the analytical continuation procedure allowed for the emerging of a modified interpretation of the calculation in remarkable agreement with experiment. Figure 5.15 displays the local LDA+CDMFT spectral function for the indicated orbital components[13]. Biermann *et al.* used the same parameters as for the

---

[13]For the analytical continuation we use slightly different maximum entropy parameters, which essentially modifies the lower a_{1g} "Hubbard band", that only appears as a shoulder to the sharp feature below the Fermi level, see the orbitally traced spectral function in Figure 5.20 (c).

metallic phase : U=4.0 eV for the on-site interaction, a Hund's coupling J=0.68 eV, and T=770 K ($\beta = 15$)[14].

Given the above described interpretation of [Biermann *et al.* (2005)], the spectral weight seen in photoemission of the M1 phase was ascribed to the a_{1g} bonding orbital, rather than a lower Hubbard band. Yet, the local spectral function disguised important parts of the physics of the M1 phase. Indeed, it was presumed that the correlations *renormalize downwards* the bonding / antibonding-splitting, analogous to what happens in the linearized band-structure described above for the metal, which led to the identification of the a_{1g} spectral weight at 0.5 eV as stemming from the a_{1g} anti-bonding orbital and the hump at ~ 2.0 eV to be an upper Hubbard band. In the following, it will be detailed that this is not quite the case. Actually, the M1 phase is even more dominated by the vanadium dimers than anticipated, which allows for a model discussion in terms of the Hubbard molecule, which is an isolated two-site cluster with on-site interactions only. It will be rationalized that the correlations indeed *enhance* the bonding / antibonding-splitting and that thus it is the a_{1g} anti-bonding component that emerges at ~ 2 eV and that actually only a lower a_{1g} satellite appears at ~ -1.75 eV, which corresponds to $N = 1 \rightarrow N = 2$ transitions into the low lying singlet state with little double occupancies. In this sense, one might call this satellite a molecular Hubbard band[15].

B.b.ii   The real-frequency self-energy

With four formula units in the unit cell, the M1 VO$_2$ self-energy matrix acquires the following form in orbital space :

$$\Sigma_{unitcell} \quad = \quad \begin{pmatrix} \Sigma_{dimer} & 0 \\ 0 & \Sigma_{dimer} \end{pmatrix} \tag{5.3}$$

where the blocks Σ_{dimer} are 6x6 matrices that correspond to the cluster self-energies for a given vanadium *dimer*. They may contain non-local inter-site intra-dimer components between the vanadium *ions* of a dimer. We note again, that in the CDMFT calculation, instead of a single site, the unit that is coupled to the self-consistent bath is a vanadium dimer, as schematized in the graphic below.

---
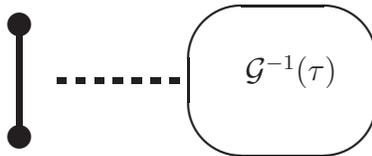
[14]Due to the cluster nature of the calculation the Hirsch-Fye algorithm suffered from sign problems (see introduction), yet the average sign being $\sim$0.8, the impact of this is thought to be small.

[15]We will come back to this later, in particular in the Appendix B

Still, when given this additional (cluster) freedom, the system is found to have in total only four non-equivalent self-energy elements. All others are zero within numerical precision. The self-energy for one dimer is found to have the structure

$$\Sigma_{dimer} \;=\; \begin{pmatrix} \Sigma_{a_{1g}} & 0 & 0 & \Sigma_{a_{1g}-a_{1g}} & 0 & 0 \\ 0 & \Sigma_{e_g^\pi 1} & 0 & 0 & 0 & 0 \\ 0 & 0 & \Sigma_{e_g^\pi 2} & 0 & 0 & 0 \\ \Sigma_{a_{1g}-a_{1g}} & 0 & 0 & \Sigma_{a_{1g}} & 0 & 0 \\ 0 & 0 & 0 & 0 & \Sigma_{e_g^\pi 1} & 0 \\ 0 & 0 & 0 & 0 & 0 & \Sigma_{e_g^\pi 2} \end{pmatrix} \tag{5.4}$$

i.e. the intra-dimer coupling is entirely due to the a_{1g} channel, as could be expected from the discussed symmetry of the system.
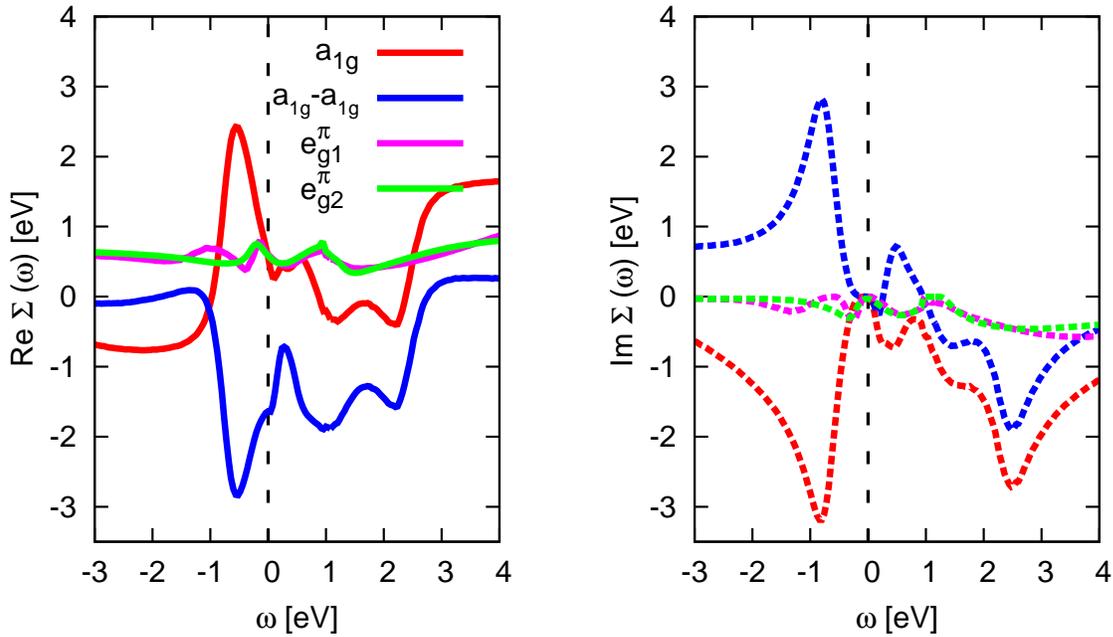

Figure 5.16 : *LDA+CDMFT self-energy $(\Sigma - \mu)$ of monoclinic VO$_2$ for the indicated orbital components. (a) real parts, (b) imaginary parts. Note in particular the frequency dependence of the a_{1g} on-site and a_{1g}–a_{1g} intra-dimer elements. Note the qualitative similarities of the a_{1g} components with those of the Hubbard molecule, see Figure B.3. See text for a discussion.*

Figure 5.16 displays the real-frequency elements of the M1 self-energy. Figure 5.17 shows a comparison between the Matsubara self-energy from the QMC and the Hilbert transformed real-frequency result. As for the rutile phase, the low energy agreement proves the reliability of our approach.

In an insulator, the suppression of spectral weight at the Fermi energy can be achieved by two distinct behaviours of the imaginary parts of the self-energy within the charge gap :

Either they diverge, as is the case for the insulating phase of the one-band Hubbard model, or they have to vanish within the gap. In the present case of M1 VO$_2$ we see, Figure 5.16, that the self-energies are all regular and their imaginary parts vanish within the gap. Hence it is not a divergence of the effective mass that is responsible for the metal-insulator transition. Indeed, when it comes to realistic materials, the realization of a divergent self-energy is rather uncommon. Also in the paramagnetic insulating phase of $(V_{1-x}M_x)_2O_3$, the self-energy is regular at zero frequency, see Figure 6.15. It thus appears that due to crystal-field effects, polarization driven transitions find a much wider realization in real compounds. Yet see the examples LaTiO$_3$ and YTiO$_3$ [Pavarini *et al.* (2004)].
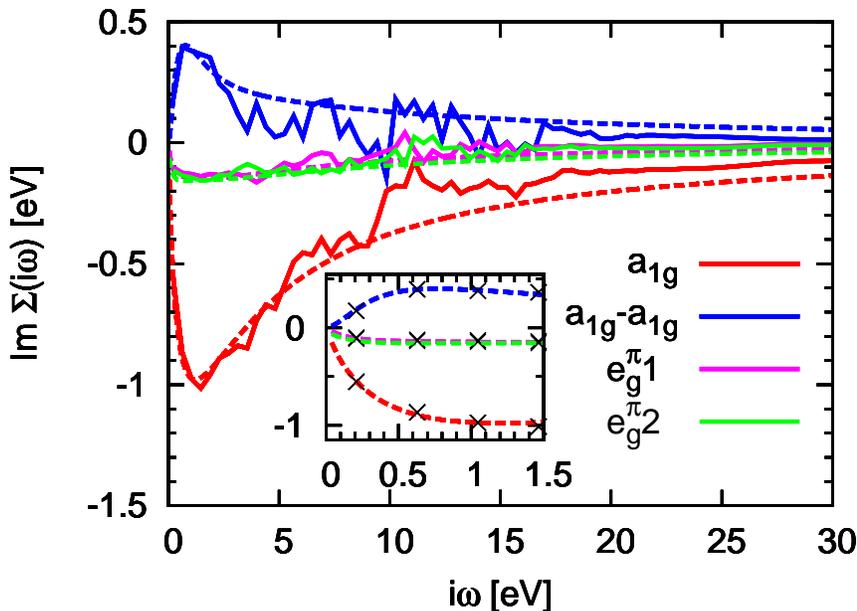

Figure 5.17 : *Comparison of the Quantum Monte Carlo self-energy on the Matsubara axis (solid lines) with the one obtained from the analytically continued one by a Hilbert transform, Equation (3.6), (dashed lines). Shown are only the imaginary parts. The insets shows the low energy regime and here the crosses indicate the discrete Matsubara self-energy from the QMC.*

Coming back to the self-energy of M1 VO$_2$, we see that concerning the e_g^π elements, both the real and the imaginary part, depend only weakly on frequency. Moreover the imaginary part is globally low in magnitude, signaling only minor life-time effects. This is a consequence of the low occupation of these orbitals which drops to merely 0.11 per vanadium ion, as compared to 0.28 in LDA. The nearly constant positive value of $\Re\Sigma_{e_g^\pi 1,2}$ corresponds to this depopulation, both seen in experiments [Haverkort *et al.* (2005)] and theoretical studies [Tanaka(2003),Biermann *et al.* (2005)]. These almost empty e_g^π orbitals only feel weak correlations, and sharply defined bands are expected in the whole energy range. Correspondingly, the transfer of e_g^π spectral weight to incoherent features will be low in magnitude as well.

The interesting physics is carried by the a_{1g} components, on which lies our key focus. Indeed, correlation effects seem to be more prominent than for the respective rutile phase components, Figure 5.10 : The imaginary part of the on-site a_{1g} self-energy becomes twice as large as its rutile counterpart, and is important already at much lower energies. Usually this is an unmistakable hallmark of an increased importance of correlation effects.

However, we argue in the following that a closer examination leads to the conclusion that the *effect* of the correlations is in fact much weaker than in the metallic phase. Indeed, the dimerization in the M1 phase leads to strong inter-site fluctuations, indicated by the significant a_{1g}–a_{1g} intra-dimer self-energy element. When examining the on-site and intra-dimer a_{1g} element, Figure 5.16, one remarks that they exhibit a rather selective dependence on frequency : In the occupied part, at negative energies, the frequency dependence is rather opposite in both, the real and the imaginary part, while in the unoccupied part the behaviour of the two elements is quite comparable in shape and form. Later on, we will refer to the Hubbard molecule, whose self-energy exhibits a similar behaviour as shown in Figure B.3.

The self-energy in the bonding / antibonding basis. This, and the molecular bonding picture in general, motivates to perform a basis transformation and to display the self-energy in the a_{1g} bonding / antibonding-basis, i.e.

$$\Sigma_{b/ab} \;\; = \;\; \Sigma_{a_{1g}} \pm \Sigma_{a_{1g}-a_{1g}} \tag{5.5}$$

in which the self-energy is diagonal in orbital space[16]. Figure 5.18 shows the result :

The a_{1g} (anti)bonding imaginary part, see Figure 5.18 (b), is low and varies little with frequency in the (un)occupied part of the spectrum, thus allowing for coherent spectral weight in the respective energy range. In the opposite regions (dotted lines) the self-energy elements have huge amplitudes. However, as far as the excitation spectrum is concerned, this has no relevance at all, as we shall see. Still, the energy dependence has important implications for the nature of the system. We will come back to this, in Section B.

Owing to its d^1-configuration, with the nearly filled a_{1g} bonding bands, and empty anti-bonding bands, this leads as for the e_g^π orbitals – but this time in a non-trivial way – to only small life-time effects. Despite the considerable on-site interactions, the complex structure of the self-energy suggests the existence of well-defined one-particle excitations. As we shall see below, this effective band-structure is however strongly rearranged as compared to the former LDA energies, due to the differences in the regions of constant real-parts :

B.b.iii One-particle excitations and momentum-resolved spectral functions

As regards one-particle excitations we can get a first, yet instructive, idea for the a_{1g} bonding / antibonding ones from the intersections

$$\omega + \mu - \epsilon_{b/ab}(\mathbf{k}) = \Re\Sigma_{b/ab}(\omega) \tag{5.6}$$

---

[16]We stress that this non-local basis transformation can only be done *after* the CDMFT calculation since the Hubbard-Hund Coulomb interaction terms would acquire an untreatable form.

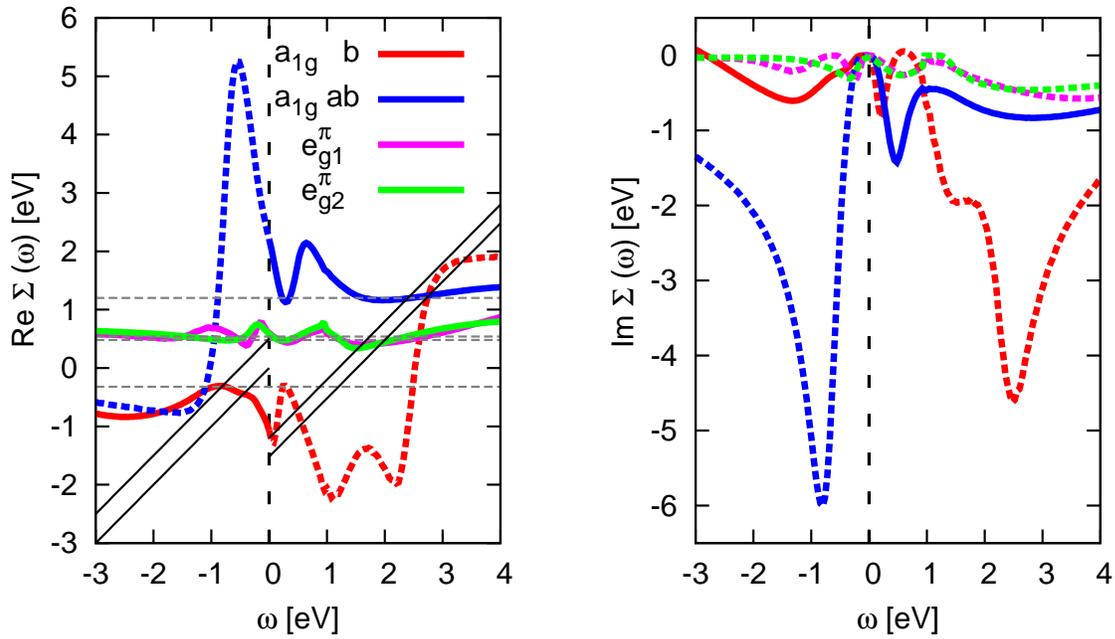**Figure 5.18 :** *LDA+CDMFT self-energy $(\Sigma - \mu)$ of monoclinic VO$_2$ in the a_{1g} bonding/antibonding basis, see Equation (5.5). (a) real parts, (b) imaginary parts. Self-energy elements are dotted in region where they are irrelevant. Note that in all other regions the real-parts are only weakly dependent on frequency, and, moreover, the imaginary-parts are low in magnitude. See text for a discussion.*

as obtained graphically in Figure 5.18 (a), where the black stripes delimit the bandwidth of the LDA a_{1g} bonding and anti-bonding components, as can be inferred from Figure 5.5. This construction is exact for a one-band model and was described in Section A, Chapter 3. In the general Hamiltonian case it is no longer exact, but might still give qualitative insights. In the present case we expect this procedure to give a rather good description, when working in the bonding / antibonding basis and limiting ourselves to a discussion of the a_{1g} orbitals only. The reason for this was discussed in Section A, Chapter 3, where it was explained that in the Hamiltonian case, it is more appropriate to work with one-particle bands, in which the hybridizations were turned off. We called these "un-hybridized bands". In the current case, the mentioned basis transformation, which diagonalizes the self-energy, is expected to also reduce off-diagonal elements in the Hamiltonian, owing to the bonding / antibonding characteristics that are preformed within the LDA (see e.g. the density of states in Figure 5.15). Indeed, if the e_g^π orbitals were empty, i.e. for isolated a_{1g} orbitals that do not hybridize with other bands, this construction would be exact.

According to Figure 5.18, the (anti)bonding band appears as the crossing of the (blue) red solid line with the frequency stripe at (positive) negative frequency. Hence, the (anti)bonding band emerges at around (2.5 eV) -0.75 eV. Still, the anti-bonding one is broadened by the anti-bonding imaginary part, $\Im\Sigma_{ab}$, that reaches a value of -1 eV in the respective energy range. To confirm this simple analysis, we have solved the quasi-particle Equation (3.9) and indicate its solutions along with the momentum resolved spectral function in Figure 5.19 (a).

As expected from the discussion of the self-energy, there are reasonably coherent features over nearly the *entire* energy range of the spectral function, from -1 to +2 eV, the positions of which coincide with the one-particle poles : The filled doubly degenerate bands are identified as the bonding bands of dominantly a_{1g} character. Above the gap, the white region in the colour-coded figure, the e_g^π bands give rise to quite sharp structures. The anti-bonding a_{1g} band, whose poles appear, as anticipated from our simple graphical construction, at around 2.5 eV, is not clearly distinguished in the momentum-resolved spectral function, since in this range, e_g^π spectral weight is dominant. Yet, it corresponds to the weight seen in the orbitally resolved local spectral function, Figure 5.15. The lower and upper "Hubbard bands" have lost most of their weight with respect to the metallic phase : a mere shoulder at -1.5 eV suggests to be the remnant of the lower Hubbard band, see Figure 5.15. Finally, contrary to rutile VO$_2$, the number of poles *equals* the orbital dimension. We will come back to this in the next section.

Before, we comment more on the somewhat astounding coherence of the system and the physical mechanisms that lead to the opening of the charge gap. At first sight, it may seem indeed surprising that despite strong local correlations – the imaginary parts of the on-site self-energies reach values of the order of -3 eV – well-defined one-particle excitations do survive. Mathematically spoken, this is the consequence of a cancellation of local and inter-site self-energies resulting in nearly negligible life-time effects for the (anti-)bonding bands at (positive) negative energies, respectively. Physically, it is enhanced inter-site hoppings that allow the electrons to avoid the strong on-site repulsion by delocalizing over the dimer. The resulting intra-dimer fluctuations reduce the net *effects* of the interactions.

Indeed as compared to isolated atoms, the probability of finding an electron on one of the sites is reduced. By this construction the electrons effectively circumvent parts of the on-site Coulomb interaction.

B.b.iv   The Hubbard molecule and the "many-body Peierls" scenario

The above can be rationalized by resorting to simple model considerations. As a matter of fact, most of the physics of the a_{1g} electrons can be understood by invoking the Hubbard molecule, which is a two-site cluster, coupled by an inter-site hopping t and subjected to an on-site Coulomb interaction U. This model can of course be solved exactly. This is done in Appendix B. In the following, we will stress the similarities between M1 VO$_2$ and the model, and conclude on the nature of the insulating phase of VO$_2$.

The dimerization of the vanadium ion in the M1 phase of VO$_2$ is mediated by the a_{1g} orbitals that are oriented along the crystallographic rutile c-axis. We have further seen, in the LDA+CDMFT calculation, that the completely filled orbitals below the Fermi level have almost pure a_{1g} character. Thus, in correspondence, the above introduced one-orbital Hubbard molecule is half-filled. Further, it is controlled by only two parameters, the inter-site, intra-molecular hopping, t, which is taken as the intra-dimer a_{1g}–a_{1g} hopping
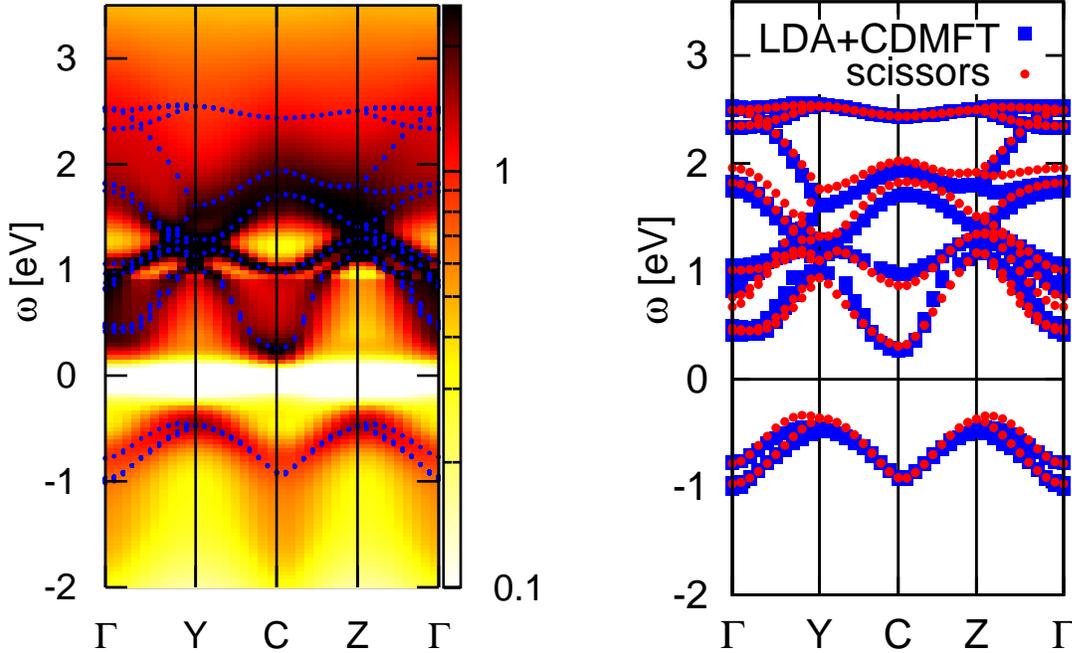

Figure 5.19 : *M1 VO$_2$: (a) momentum-resolved spectral function A(**k**,ω). (blue) dots (in (a) & (b)) are solutions of the quasi-particle Equation (3.9). (b) The (red) dots represent the eigenvalues of the LDA Hamiltonian plus the effective potential Δ. See text for discussion.*

$t = 0.7$ eV, as obtained from the LDA, and the on-site Coulomb repulsion, $U = 4.0$ eV. For the Hamiltonian of the model and details to the following statements see the Appendix B.

The ground state of the defined model is given (at zero temperature) by a non-degenerate singlet state :

$$|\psi_0^{N=2}\rangle = 1 / \sqrt{2\left(\frac{16t^2}{(\sqrt{16t^2+U^2}-U)^2}+1\right)} \times \tag{5.7}$$
$$\left\{\frac{4t}{\sqrt{16t^2+U^2}-U}\left(|\downarrow\ \uparrow\rangle - |\uparrow\ \downarrow\rangle\right) + \left(|\uparrow\downarrow\ 0\rangle + |0\ \uparrow\downarrow\rangle\right)\right\}$$

which is an intermediate state between the ground state in the non-interacting limit ($U = 0$) that is a Slater determinant of one-particle states

$$|1\ 2\rangle_{\text{SD}} = 1/\sqrt{4}\left\{|\downarrow\ \uparrow\rangle - |\uparrow\ \downarrow\rangle + |\uparrow\downarrow\ 0\rangle + |0\ \uparrow\downarrow\rangle\right\} \tag{5.8}$$

and the strong-correlation Heitler-London limit [Sommers and Doniach(1978)]

$$|1\ 2\rangle_{\text{HL}} = 1/\sqrt{2}\left\{|\downarrow\ \uparrow\rangle - |\uparrow\ \downarrow\rangle\right\} \tag{5.9}$$

in which all double-occupancies are projected out. Still, at all interaction strengths, the ground state is a singlet state for $t \neq 0$. For the above given parameters that correspond to the VO$_2$ case, the double occupations are already strongly suppressed. Their weight in the eigenstate, i.e. its projection on the double occupancy states, is merely $\sim 9\%$, i.e. 4.5% per site. In the LDA+CDMFT calculation one finds an a_{1g} double occupancy of 6.42%. This larger value is owing to that fact that calculations were performed at finite temperature[17], and the embedding of the molecule into the solid. Therewith we realize that, both, the N-particle ground state of the model and of M1 VO$_2$ are clearly *not* given by a Slater determinant of single-particle states[18].

The physical reason for the enhanced bonding-formation resides in the fact that in this state, the electrons are exposed to a reduced Coulomb interaction. Indeed, while the expectations value of the Hamiltonian Equation (B.1) is $\langle H\rangle_{\text{SD}} = {}_{\text{SD}}\langle 1\ 2|H|1\ 2\rangle_{\text{SD}} = U/2 = 2.0$ eV in the Slater determinant limit, it is reduced to merely $\langle H\rangle_{\psi_0} = \langle\psi_0^{N=2}|H|\psi_0^{N=2}\rangle = U/\frac{16t^2}{(\sqrt{16t^2+U^2}-U)^2+1} = 0.23\,U = 0.91$ eV in the true ground state.

The spectral function of the Hubbard molecule exhibits four peaks, see Figure B.2. In the parameter regime that we are interested in, the two main features are the renormalized bonding / antibonding excitations of the non-interacting model. As a matter of fact, the bonding / antibonding splitting is then given by

---

[17]Indeed, the double occupation decreases when going from $\beta = 12$ to $\beta = 15$.

[18]As a matter of fact, the good agreement of the Kohn-Sham spectrum and experimental findings for weakly correlated materials does not necessarily entail that the N-particle ground state is given by a Slater determinant.

$$\Delta_{bab} \;\; = \;\; -2t + 4t\sqrt{1 + \left(\frac{U}{4t}\right)^2} = 3.48 \text{ eV} \tag{5.10}$$

In the case of M1 VO$_2$, however, the coupling of the vanadium dimers to the bath, i.e. the embedding into the solid on a mean-field level, the hybridization with the e_g^π orbitals and the a_{1g} dispersion reduce the splitting to $\sim$3 eV, as can be inferred from the one-particle poles, Figure 5.19, in remarkable agreement with experiment [Koethe *et al.* (2006)].

Further, the two other excitation energies seen in the model, Figure B.2, do not appear as poles of the LDA+DMFT Green's function. This is again likely to be a consequence of the hybridizations and the embedding of the dimers, because these couplings work to broaden the imaginary parts of the a_{1g} self-energies that have a δ-peak structure in the model of the isolated molecule. Thereby the divergence in the corresponding real-part is suppressed, as can be seen in the graphical construction for VO$_2$, Figure 5.18 (a), where neither the a_{1g} bonding nor the anti-bonding element cross the corresponding former LDA bandwidth[19], in contrast to the case of the isolated Hubbard molecule, where the same construction is shown in Figure B.4. Yet, incoherent satellite weight does appear, since the deviation from a pole-energy is not too large. In the model case, these excitations would be expected $2t = 1.4$ eV [above] below the [anti-]bonding energies, which is also what is roughly found in M1 VO$_2$, as far as the bonding component is concerned, see Figure 5.15[20]. The two main excitation however, both in the Hubbard molecule and the realistic case, are sharply defined. In other words, the correlations, though inducing strong renormalizations, see Equation (5.10), do not eventuate in important life-time effects. As a matter of consequence, the excitation spectrum is rather band-like[21]. We can rationalize this further. First, we note that the Hubbard molecule has two evident limits : First, the non-interacting one ($U = 0$) which is a Peierls insulator at half-filling, second, the atomic limit ($t \to 0$) in which the system evolves towards a degenerate Mott insulator. In the present parameter regime, $U = 4.0$ eV and $t = 0.7$ eV, the band-derived features account for 79% and the satellites thus for only 21% of the weight in the spectral function, signaling, again, a rather coherent picture of the model. However, when computing the overlaps of the ground state wavefunction with the ground state corresponding to the two above limits[22], one finds : $|_{\text{HL}}\langle 1\,2|\psi_0\rangle|^2 = 92\%$ and $|_{\text{SD}}\langle 1\,2|\psi_0\rangle|^2 = 21\%$. In other words, despite the coherence of the system, its ground state is *far* from being an uncorrelated state. As concerns spectral properties, the correlations only enhance the one-particle

---

[19]which is why the two stripes that indicate the LDA a_{1g} bandwidths were limited to the frequency range ($\omega \gtrless 0$).

[20]As said in Footnote 13, with our parameters, the lower Hubbard band is at slightly lower binding energies, see Figure 5.20, which can however be justified, as for the bonding / antibonding splitting by the couplings to other orbitals and dimers.

[21]In the atomic limit, a one-band Mott-Hubbard insulator could also be called band-like, since the Hubbard bands correspond to sharp atomic excitations. Yet, in that case the number of poles of the Green's function doubles with respect to the non-interacting limit.

[22]which are not orthogonal

Peierls mechanism. On the eigenstate level, however, they completely invalidate a one-particle description of the system. This is why we would like to call M1 VO$_2$ to be in a *"many-body Peierls state"*, stressing both the one-particle-like effects on the excitation spectrum on the one hand, and the non-Slater-determinant nature of the ground state, on the other.

A concomitant effect is the difference between the charge and the spin gap. While in a generic band-insulator, both are equal, $\Delta_{spin} = \Delta_{charge}$, this is not true for the ground state of the Hubbard molecule ($\Delta_{spin} = 0.44$ eV for our parameters, see Appendix B), and also in M1 VO$_2$, one finds $\Delta_{spin} < \Delta_{charge}$[23], even though the charge gap is determined not by the a_{1g} bonding / antibonding splitting but by the a_{1g}–e_g^π gap.

B.b.v   Implications for the gap opening

In the realistic compound, the charge gap is not determined by the bonding / antibonding splitting, since the e_g^π orbitals lie lower in energy than the a_{1g} anti-bonding orbitals. Still, the above considerations prove useful to the following discussion.
As regards the gap-opening in M1 VO$_2$, we can thus identify two effects :

- First, as seen in both, the model considerations and the realistic system, the self-energy tremendously enhances the a_{1g} bonding / antibonding-splitting as compared to the LDA.

- Secondly, as explained above, the charge in this a_{1g} state is less exposed to local Coulomb interactions than in the e_g^π orbitals. This further contributes to the charge transfer into the a_{1g} bonding bands. Thus depleted, the e_g^π orbitals also feel only very weak Coulomb correlations. This shift, seen in the calculation as the difference in $\Re\Sigma$, eventuates in the separation of the a_{1g} and e_g^π at the Fermi level.

In conclusion, it is the local interactions that amplify the Goodenough scenario, described in Section A. Thus, for once correlations, though being at the origin of the insulating behaviour, do not invalidate the band-picture on the level of spectral properties but just reshape them.

B.b.vi   A scissors construction

A static approximation of the self-energy.   Above we have seen that the frequency dependence of the real parts of the self-energy, though shifting the excitation energies with respect to the LDA, is sufficiently low such as not to introduce new solutions to the quasi-particle Equation (3.9). Indeed, the number of poles is conserved and thus limited to the number of LDA bands. This is already a harbinger for the possibility of obtaining the excitation spectrum from a one-particle approach. Yet, even though not resulting in additional solutions, the frequency dependence might still not be fully discardable. However, when looking again at the graphical construction, Figure 5.18 (a), we note that the variation of the a_{1g} self-energy is somewhat unimportant in the relevant bandwidth windows indicated by the (black) stripes, and the e_g^π components do

---

[23]J. P. Pouget, private communication.

not vary much either, even on a global scale. This explains why the LDA+U approach, whose self-energy is purely static, succeeds in opening a gap [Huang *et al.* (1998), Korotin *et al.* (2002), Liebsch *et al.* (2005)]. Yet, being a Hartree-Fock like calculation it misses the correct bonding / antibonding splitting. This is detailed in Appendix B, where we compare the exact solution of the Hubbard molecule with approximate techniques, such as the GW and Hartree-Fock. Furthermore the imaginary parts of the self-energy in the relevant energy ranges is not too significant. Having said this, we endeavour to construct a scissors operator, Δ, as a static approximation to the dynamical self-energy *in the bonding / antibonding basis*, by evaluating the real parts of the latter at the former LDA band centers and at the pole energies for the e_g^π and a_{1g} respectively, i.e.

$$
\begin{array}{rcccr}
\Delta_{e_{g1}^\pi} & = & \Re\Sigma_{e_{g1}^\pi}(0.5 \text{ eV}) - \mu & = & 0.48 \text{ eV} \\
\Delta_{e_{g2}^\pi} & = & \Re\Sigma_{e_{g2}^\pi}(0.5 \text{ eV}) - \mu & = & 0.54 \text{ eV} \\
\Delta_b & = & \Re\Sigma_b(-0.75 \text{ eV}) - \mu & = & -0.32 \text{ eV} \\
\Delta_{ab} & = & \Re\Sigma_{ab}(2.5 \text{ eV}) - \mu & = & 1.20 \text{ eV}
\end{array}
$$

as indicated by the dashed (grey) horizontal lines in Figure 5.18 (a).

The density of states of the scissored Hamiltonian.   Given the overall behaviour of the self-energy this might look as a tremendous oversimplification. Yet, the band-structure corresponding to the eigenvalue problem of the scissored LDA Hamiltonian, $H_0(\mathbf{k}) + \Delta$, is shown in Figure 5.19 (b) : The agreement with the LDA+CDMFT-poles is excellent. The excitation energies are thus entirely reproducible with a one-particle potential. However, though being static in energy, the latter is orbital-dependent. This is why it cannot be viewed as an "improved exchange - correlation potential" in the sense of DFT. Further differences with potentials from standard band-theory are discussed at the end of this paragraph.

Figure 5.20 shows a collection of comparisons between the LDA density of states (DOS), the DOS of the scissored Hamiltonian, the LDA+CDMFT spectral function and photoemission experiments that we will discuss individually :

(a) shows the original LDA DOS and the DOS of $H_0(\mathbf{k}) + \Delta$. The changes are in line with the already discussed band-structure. Clearly seen is the opening of a gap at the Fermi level. Moreover the anti-bonding a_{1g} peak is shifted beyond all e_g^π weight and thus delimits the DOS at high energies. Indeed a density of stated that qualitatively agrees with ours was calculated by [Continenza *et al.* (1999)] using a model GW approach[24].

(b) shows a comparison of the scissored t_{2g} Hamiltonian with a full (non-downfolded) Hamiltonian (comprising in particular the oxygen 2p and the e_g^π orbitals) which also includes the scissors shiftings. This is done by replacing, in the respective Kohn-Sham basis, the eigenvalues in the t_{2g} energy window by those of the scissored, downfolded t_{2g} Hamiltonian :

---

[24]According to earlier work, [Massidda *et al.* (1995)], the model GW calculation was performed self-consistently.
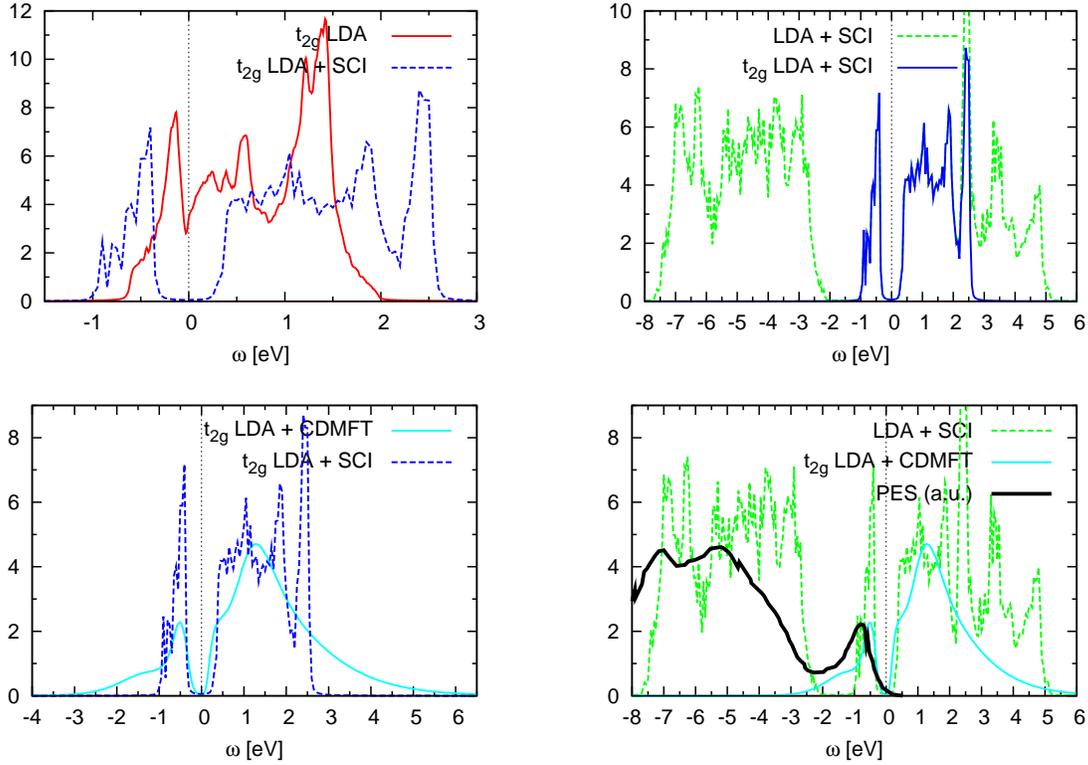
Figure 5.20 : *Density of states (DOS), spectral function and photoemission results– a comparison, from top left to bottom right : (a) DOS of the t_{2g} LDA Hamiltonian with and without the scissors operator, (b) DOS of the t_{2g} LDA Hamiltonian vs. the full LDA spd-Hamiltonian, both scissored, (c) scissored t_{2g} LDA DOS vs. LDA+CDMFT spectral function, (d) Comparison of the scissored t_{2g} LDA DOS, the LDA+CDMFT spectral function with results from photoemission [Koethe et al. (2006)], in arbitrary units.*

$$
\begin{aligned}
\mathrm{diag}(\epsilon_1^{sci}, \cdots, \epsilon_{12}^{sci}) &= U_{sci}^\dagger(\mathbf{k}) H^{sci}(\mathbf{k}) U_{sci}(\mathbf{k}) \\
\mathrm{diag}(\epsilon_a, \cdots, \epsilon_1, \cdots, \epsilon_{12}, \cdots, \epsilon_z) &= U^\dagger(\mathbf{k}) H^{LDA}(\mathbf{k}) U(\mathbf{k}) \qquad (5.11) \\
\longrightarrow \qquad \widetilde{H}(\mathbf{k}) &= U(\mathbf{k})\mathrm{diag}(\epsilon_a, \cdots, \epsilon_1^{sci}, \cdots, \epsilon_{12}^{sci}, \cdots, \epsilon_z) U^\dagger(\mathbf{k})
\end{aligned}
$$

Since in the LDA+CDMFT calculation, the oxygen O2p and also the 3d e_g^σ orbitals were not included, they do not evolve from their LDA shape and position[25]. Thus t_{2g} spectral weight that was shifted upwards in energy by the correlation effects now partly overlaps with the e_g^σ density of states, starting at ~ 2.5 eV. This observation will become important in the interpretation of our optical spectra, see below.

---

[25]Herewith, one can say, that we have chosen a specific type of double counting (see Section C, Chapter 2), which is responsible for the position of oxygen 2p and e_g^σ weight with respect to the t_{2g}. As we shall see later, in the optics section, a different double counting, which might be tuned to reproduce experimental findings, such as the found positions in photoemission or x-ray absorption, is conceivable.

(c) compares the scissored t_{2g} DOS with the LDA+CDMFT spectral function. Here we can see, that, though the scissors operator reproduces the interacting excitation energies, there are finite lifetime effects that broaden the spectrum considerably. Indeed the spectral function extents over almost twice the energy range than the shown DOS. We note in particular that both the bonding and the anti-bonding peaks are strongly suppressed in the spectral function. Moreover the transfer of spectral weight to the lower satellite at ~ 1.5 eV[26] that appears in the spectral function is clearly a dynamical effect, which is beyond the static potential Δ that led to the shown DOS.

(d) compares both the non-downfolded, but scissored Hamiltonian of Figure (b), and the LDA+CDMFT spectral function with recent photoemission experiments [Koethe *et al.* (2006)]. Three major observations can be made. First, the bonding a_{1g} peak in the calculations appears at slightly lower binding energies than in the experiment, which could be a fine-tuning problem concerning the choice of interaction parameters. Second, contrary to the density of states, both the experiment and the spectral function exhibit spectral weight at binding energies greater than ~ 1 eV, yet before oxygen contributions set in. This strengthens the LDA+CDMFT calculation which predicts a lower a_{1g} satellite, by the mechanism, discussed in Appendix B. Thirdly, when comparing oxygen spectral weight, we see that the centre of gravity of the latter is at somewhat higher binding energies in the experiment than in the LDA calculation. Indeed, model calculations[27] suggest that in full orbital setups, i.e. when renouncing from using a downfolding procedure, the spectral weight of occupied uncorrelated orbitals can be considerably shifted with respect to the LDA, which might improve also the optical spectra. The latter is the subject of Section D, in which we calculate the optical conductivity of the scissored Hamiltonian, and the full LDA+CDMFT calculation.

Conceptual differences of the scissors operator and DFT one-particle potentials.   Finally, we find it instructive to discuss conceptual differences between our scissors operator and potentials from standard band-theories :

Density functional theory guarantees the existence of an effective one-particle problem that has the same ground state density as the true system. Both, the Kohn-Sham energies and the eigenstates are however *auxiliary* quantities. The latter are, in particular, Slater determinants by construction, which needs by no means to be the case for the real system. The interpretation of the Kohn-Sham spectrum as true excitation energies is theoretically unjustified. Still, in systems devoid of sizable correlations, this yields reasonable results, which is why this correspondence is often tacitly assumed.

Our one-particle potential, on the contrary, was created such as to reproduce the interacting excitation spectrum as obtained from LDA+CDMFT. The eigenvalues of $H_0(\mathbf{k})+\Delta$ are thus *not* artificial. Still, the eigenstates, as in density functional theory, are auxiliary Slater determinants, since the effective problem is a one-particle one. The crucial point for the monoclinic M1 phase of VO$_2$ is that *spectral properties* are indeed capturable within this one-particle description, despite strong local Coulomb interactions and a ground state that is truly far from a Slater determinant, as rationalized above by alluding to the

---

[26]See the above section on the Hubbard molecule and Appendix B for a discussion on its nature.

[27]*J.M.T.*, work in progress.

Hubbard molecule. It is in this "spectral" sense that M1 VO$_2$ is exhibiting only weak correlation effects. Our scissors operator is a construction that only permits the reproduction of the excitation spectrum, while it cannot account for other properties. Yet, our LDA+CDMFT calculation yields a true many-body result. It is the frequency dependence in the self-energy that we could neglect for the spectral properties, which takes effect in the full description of the system, which as such is well beyond an effective one-particle problem.

B.b.vii   The M2 phase

Finally, we comment on the insulating M2 phase of VO$_2$, which, as mentioned in the beginning, is realized under uni-axial pressure or upon Cr-doping [Pouget and Launois(1976)]. In this phase, every second vanadium chain along the c-axis consists of untilted dimers, whereas in the other only the tilting occurs. From the above analysis we are led to the following speculation as to the underlying mechanisms of the insulating behaviour of this phase.

In M2 VO$_2$, the dimerized chains are likely to already form a_{1g} Peierls singlets as in M1 VO$_2$. The additional tilting that occurs when going towards the M1 phase will slightly change the hybridizations between the e_g^π and the oxygen 2p, such as to reduce the a_{1g}–e_g^π splitting, while a further anisotropy in the hoppings along the c-axis works in the opposite direction, namely to favour further the population of the a_{1g} bonding orbital.

The transition in the other type of chains seems more interesting. While also here the hybridizations with the oxygens change when evolving towards the M1 phase, the main effect will be the increasing anisotropy in the a_{1g} hoppings along the chains.

Indeed band-structure calculations by [Eyert(2002)] suggest that the electronic structure of the tilted chains is somewhat akin to the chains in the rutile phase, albeit with smaller hopping amplitudes along the chain, owing to the increased vanadium–vanadium distances caused by the zigzag geometry. Thus, one might even evoke a comparison with the Nb-doped compound, $V_{1-x}Nb_xO_2$ which, as mentioned above, is found to become a Mott insulator at large enough x.

Taking for granted that a_{1g} and e_g^π spectral weights do not overlap neither in the M2 phase, nor in the M1 phase and in between, such as to guarantee an insulating phase, it is quite instructive to study the evolution of only the a_{1g} channel. The following graphic schematizes a simple model for the a_{1g} orbitals. In the M2 phase the latter form an isotropic chain : The one dimensional Hubbard model. When going to the M1 phase, the hopping becomes anisotropic and, as indicated in the scheme, t'/t decreases. The Hubbard molecule corresponds to the limit $t'/t \to 0$. In all the cases the system is assumed to be half-filled.

t   t   U
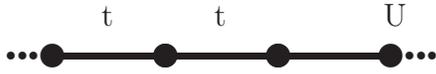
M2. The tilted chains have an isotropic hopping amplitude t. Insulating behaviour at half-filling is realized by the Mott phenomenon.

t   t′   U
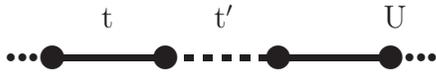
M1. The dimerization results in an anisotropic hopping $t > t'$. The system is in a many-body Peierls phase at half-filling.

t   U

Hubbard molecule. Isolated dimer corresponding to the limit $t'/t \to 0$.

In the M2 regime, insulating behaviour necessitates Mott-Hubbard physics, the self-energy $\Sigma(\mathbf{k},\omega)$ needs to diverge at zero frequency. Indeed for any finite U value the 1d Hubbard model is insulating. In the Hubbard molecule, that we already discussed previously and whose exact solution is given in Appendix B, the self-energy diverges outside the bonding / antibonding gap, at $\pm 3t$. The interactions lead to what we called a "many-body Peierls state".

It would be quite interesting to study the behaviour in between, i.e. for $t'/t < 1$. This could e.g. be accomplished with the chain-DMFT technique [Biermann *et al.* (2001)][28].

In the light of the above, we interpret the seminal work of [Pouget and Launois(1976)] as the observation of the transition from a Mott phase to a many-body Peierls one (with the above definition), taking place on the tilted chains when going from the M2 to the M1 phase. The above is in particular consistent with the finding of (S=0) S=1/2 for the (dimerized) tilted pairs.

B.b.viii   Conclusion

In conclusion, this section presented a detailed analysis of the excitation spectrum of the M1 phase of VO$_2$, with special emphasis on an effective band-structure description. Indeed, we found life-time effects to be rather negligible and the correlation effects to mainly shift and reshape the Kohn-Sham energies with respect to the starting LDA calculation. In total, the nature of the insulating phase of VO$_2$ is shown to be rather "band-like" in the sense that one-particle excitations keep their coherence. Our analytical continuation scheme for LDA+CDMFT allowed us to explicitly calculate this band-structure : The effective band scenario can be derived from a static one-particle potential. However, this does *not* imply a one-particle picture for quantities other than the excitation spectrum. In particular, the true ground state is not a Slater determinant. Correspondingly, we qualify M1 VO$_2$ as a "many-body Peierls" phase.

---

[28]A study of a slightly different model was performed in [Fabrizio *et al.* (1999)].

We argued that the surprising weakness of lifetime effects is the result of strong inter-site fluctuations that circumvent correlation effects in an otherwise strongly correlated solid. This is in striking contrast to the strong dynamical correlations in the metallic phase which is dominated by important life-time effects and the appearance of incoherent features in the spectral function.

The intra-dimer fluctuations account for the excitation spectrum, to an extent that the physics of the compound is indeed dominated by a modified Goodenough-Peierls picture and not by Mott behaviour. As regards spectral properties, the role of correlations consists in (i) pushing the a_{1g} anti-bonding band beyond the top of the e_g^π, consistent with the experimental findings, and, more importantly, in (ii) enhancing the a_{1g} bonding – e_g^π splitting due to an effectively reduced Coulomb repulsion in the a_{1g} bonding band, that favours the depopulation of the e_g^π bands. The latter results in the opening of the gap. Thus, as a matter of consequence it *is* the correlations that are responsible for the insulating state, albeit they cause it in a rather specific fashion. Indeed, the Coulomb repulsion causes a localization of charges, however, contrary to a genuine Mott-Hubbard insulator, they are not confined to the lattice sites, but form a bonding superposition near the Heitler-London limit. This might sounds like a mere question of definition, yet, we stress that the magnetic response in genuinely different : While the local moments of a Mott insulator result in an S=1/2 response, the nature of the insulating phase of M1 VO$_2$ causes a S=0 response. In this vein, we have further pointed out the relevance of the Hubbard molecule as a basic model for the M1 phase of VO$_2$, by indicating the striking similarities of the a_{1g} channel with the physics of a correlated molecule.

Further advances might by made by including the e_g^σ and oxygen 2p orbitals in the many-body setup, with the aim of correcting their positions relative to the t_{2g} spectral weight.

As an outlook, it might by enlightening to perform realistic calculations on the M2 phase, in order to assess our picture of the nature of this insulating phase, however the numerical cost is tremendous. On the experimental side, it would be most interesting to check our predictions experimentally by modern angle-resolved photoemission.

C   GW – Model and First Principles Calculations

In the electronic structure community, *ab initio* calculations enjoy great popularity. This is why the first argument against the LDA+DMFT approach often refers to the existence of adjustable parameters, namely the on-site Coulomb repulsion, whose values may be guided by techniques such as constrained LDA or GW calculations, yet indeed they are parameters of the technique. GW, on the other hand (see Section B, Chapter 2, [Hedin(1965), Aryasetiawan and Gunnarsson(1998)]), is genuine *ab initio*, which is an undeniable merit of the approach. Still, there is always a tradeoff, since as mentioned in the introduction, the perturbative nature of the GW approach does not allow for capturing the excitation spectrum of *strongly* correlated materials.

The fact that the insulating behaviour of the M1 phase is not caused by a divergence of the effective mass and that moreover its excitation spectrum can be obtained from acting with a scissors operator on the LDA Hamiltonian, reminds of the way in which GW calculations improve on the gap values of semiconductors. That the GW approach might yield reasonable results for M1 VO$_2$ was already pointed out when reviewing the model GW calculations of [Continenza *et al.* (1999)] which succeeded in describing the insulating character of the compound.

C.a   The GW approximation for the Hubbard molecule

Here, still on the model level, we will first explain, that, contrary to Hartree-Fock, the GW approximation is qualitatively yielding the correct physics for the Hubbard molecule, that we invoked in the preceding section for the discussion of the dimerization in M1 VO$_2$. At this point, we only state the major outcome of this investigation, the full calculation can be found in Appendix 2. Just like in the exact solution, which is presented in the same appendix, the self-energy in the GW approximation exhibits the typical bonding / antibonding combinations. Albeit, the poles of the self-energy are at the wrong energies and have different weights. This leads to a bonding / antibonding splitting that is way too small with respect to the exact solution for large on-site repulsions, but captures well the correlation induced enhancement at small interaction strengths (see Figure B.6). This might be said to sound trivial, since GW is a weak-coupling expansion *in the screened interaction W*. Yet, it is precisely the latter emphasis that is important. In fact the bonding / antibonding splitting enhancement is entirely due to the fact that the random phase approximation (RPA) screening leads to a screened interaction that is non-diagonal in two-particle orbital space. On the Hartree-Fock level, which could be named Gv, with v being the bare interaction, which in turn is diagonal when considering only density-density terms, the splitting remains unchanged from its non-interacting value.

However, it must be said that the Hubbard molecule, where the on-site interaction is a fixed parameter also for the GW approximation, is a much more simplistic model with reference to a realistic GW calculation for M1 VO$_2$, than was the case for the LDA+CDMFT. The reason is the following. Though being in principle capable to cope with a full-orbital setup in the realistic case, LDA+DMFT is often used as a low-energy approach that works

e.g. with a downfolded Hamiltonian comprising only the t_{2g} orbitals. Then the local inter-actions are added as parameters. In the GW the interaction is calculated in an *ab initio* fashion using the RPA. For this procedure to yield reasonable results, the screening that is due to high energy orbitals is indispensable. Moreover, the resulting screened interactions are far from being local. Thus the complex interplay of orbital degrees of freedom and also non-local corrections to the LDA might play a major role. As a consequence this model is far less appropriate in the GW context than it was in the LDA+CDMFT one. Still, already on the model level, an assessment of the GW approximation might prove useful.

C.b   The GW approximation for M1 VO$_2$

Technicalities.   The above motivated us to perform, in the realistic setup, fully *ab initio* calculations for the insulating M1 phase of VO$_2$ using the GW approximation, i.e. a one shot G_0W_0 computation on top of an LDA calculation[29].

The GW code we use takes as a starting point the Hamiltonian and the wavefunc-tions from an LMTO calculation within the atomic sphere approximation (ASA) [Ander-sen(1975)]. Then the GW equations, see Section B, Chapter 2, are followed in the Kohn-Sham basis, to yield the GW self-energy. For details of the implementation see [Aryase-tiawan(2000)].

Due to the large unit cell and thus numbers of orbitals, this is computationally very demanding for the material in question, and has become feasible only in recent years. Still, for time and memory reasons, we had to content ourselves with calculating the diagonal self-energy corrections for the t_{2g} states only. Further, we used 26 **k**-points in the irreducible Brillouin zone and computed the polarization up to frequencies of 10 eV.

The linearized band-structure.   In a first step, we then calculated the shifts with respect to the starting Kohn-Sham energies, by linearizing the self-energy [Aryaseti-awan(2000)] : When denoting the Kohn-Sham energies and wave functions by $\epsilon_{\mathbf{q}n}$, and $\psi_{\mathbf{q}n}$, respectively, and introducing the self-energy correction to the LDA exchange-cor-relation potential V_{xc}, $\Delta\Sigma_{\mathbf{q}n}(\omega) = \langle\psi_{\mathbf{q}n}|\Re\Sigma(\omega) - V_{xc}|\psi_{\mathbf{q}n}\rangle$, we can write

$$
\begin{aligned}
E_{\mathbf{q}n} &= \epsilon_{\mathbf{q}n} + \Delta\Sigma_{\mathbf{q}n}(E_{\mathbf{q}n}) \\
&\approx \epsilon_{\mathbf{q}n} + Z_{\mathbf{q}n}\Delta\Sigma_{\mathbf{q}n}(\epsilon_{\mathbf{q}n})
\end{aligned}
\tag{5.12}
$$

with

$$
Z_{\mathbf{q}n} = \left[1 - \frac{\partial\Delta\Sigma_{\mathbf{q}n}(\epsilon_{\mathbf{q}n})}{\partial\omega}\right]^{-1}
\tag{5.13}
$$

Contrary to what is done for obtaining a low-energy renormalized band-structure, see Section A, Chapter 3, here the derivative of the self-energy is evaluated at the former LDA energies. Hence, the above factor is not subject to the restriction $Z < 1$.

---

[29]For VO$_2$ this had not been done before. See however parallel work by Gatti *et al.* and forthcoming footnotes.

Figure 5.21 shows a comparison between the thus obtained GW excitation energies and the LDA+CDMFT poles from the preceding section. We note that the G_0W_0 approximation is non-conserving [Schindlmayr(1997)] and that we have in this picture shifted the chemical potential arbitrarily such that the center of gravity of the occupied bands roughly coincides with the LDA+CDMFT ones.

Several remarks are to be made. First of all, the current GW implementation succeeds in opening a gap in the excitation spectrum between the a_{1g} bonding and some e_g^π bands[30,31].

Compared with LDA+CDMFT, the magnitude of the gap is quite comparable and some of the band dispersions come out similar. Yet, the dispersion of the bonding a_{1g} bands and the unoccupied bands below 1 eV are somewhat narrower in the GW. The second major observation is that the anti-bonding a_{1g} bands are not pushed upwards such as to form the top of the t_{2g} conduction band, as is the case in LDA+CDMFT. To further illustrate this, we plot in Figure 5.22 the evolution of the Kohn-Sham energies at the Γ-point when applying the GW. We have indicated the preponderant LDA orbital character by different line styles and colours : The blue solid lines represent the a_{1g} and the dashed red lines the e_g^π energies.

We see that, while the bonding a_{1g} to e_g^π splitting, responsible for the gap opening, grows tremendously, the a_{1g} bonding / antibonding splitting actually decreases. This is to be contrasted to our model GW analysis on the Hubbard molecule, given in Appendix B, where, as stated above, an on-site Coulomb repulsion leads to a too small, yet increased bonding / antibonding splitting.

The self-energy. Figure 5.23 shows the GW t_{2g} self-energy at the Γ-point, $\Delta\Sigma_{\Gamma n}$, as defined above. Again, we have marked the components according to their LDA orbital character. It would be interesting to see, whether in the a_{1g} channel a frequency dependence similar to the one of the Hubbard molecule within GW, Figure B.5, is found. Unfortunately, we note that since we have calculated the polarization and thus the screened interaction only up to 10 eV, the frequency convolution in the equation to obtain the self-energy (given by the Fourier transform of Equation (2.16), which was written in time

---

[30]This is to be contrasted to one-shot GW calculations of Gatti *et al.* who used a pseudo-potential plane wave code. Indeed Gatti *et al.* find insulating behaviour only when performing self-consistent calculations, during which the wavefunctions considerably adjust. There are two possible explanations for the different findings. First it could be a question of which orbitals are taken into account for the calculation of the screened interaction. A too restricted choice might result in the missing of important contributions to the polarization, thus working in favour of a smaller gap value. A further possibility is the difference in wavefunctions. In our calculation the atomic sphere approximation (ASA) might have severe impacts on the wavefunctions (yet see below), while in the plane wave approach the pseudization might yield considerably different wavefunctions, too. Yet, as we have noted previously, the LDA wavefunctions have no physical meaning. Similarities between our electron energy loss spectra (EELS) $\Im\left(\epsilon(\mathbf{q},\omega)\right)^{-1}$ of our one shot calculation (not shown) and the one of Gatti *et al.* who used self-consistent wavefunctions, might suggest that the LMTO-ASA wavefunctions are closer to the self-consistent solution than the starting pseudized plane waves. This issue remains to be clarified.

[31]Preliminary full-potential GW calculations of Sakuma *et al.* show the opening of a gap on first shot, supporting our ASA result.
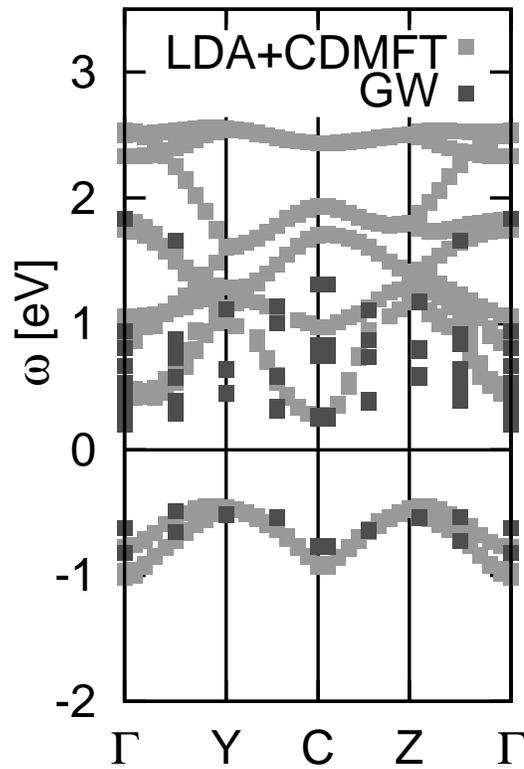
Figure 5.21 : *Comparison of the G_0W_0 renormalized Kohn-Sham energies with the poles of the LDA+CDMFT Green's function along various symmetry lines. Note that the GW chemical potential has arbitrarily shifted up such as to align the occupied bands with the respective LDA+CDMFT poles.*
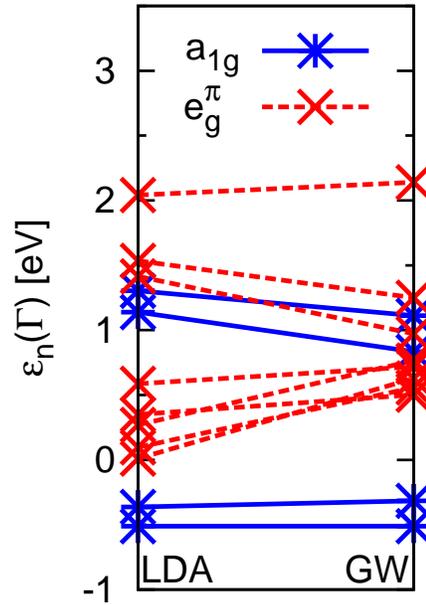
Figure 5.22 : *Comparison of the Kohn-Sham energies and the GW corrected excitation energies at the Γ-point. Here we have arbitrarily shifted the GW energies such as to freeze the lowest energy to the LDA value. The elements corresponding to Kohn-Sham energies of predominant a_{1g} (e_g^{π}) character are marked by solid blue (dashed red) lines, cf. Figure 5.5.*

space), suffers from finite range artifacts. Computations for a simpler material, Cu, revealed that the resulting self-energy is reliable up to about 1/3 of the cutoff frequency only. This is why we do not show the GW VO$_2$ t_{2g} self-energy beyond 3 eV. Calculations with an increased cutoff frequency were technically not feasible.

Hence we cannot conclude as to whether also in the *ab initio* GW approach the physics is (correctly) dominated by the vanadium dimers or not.
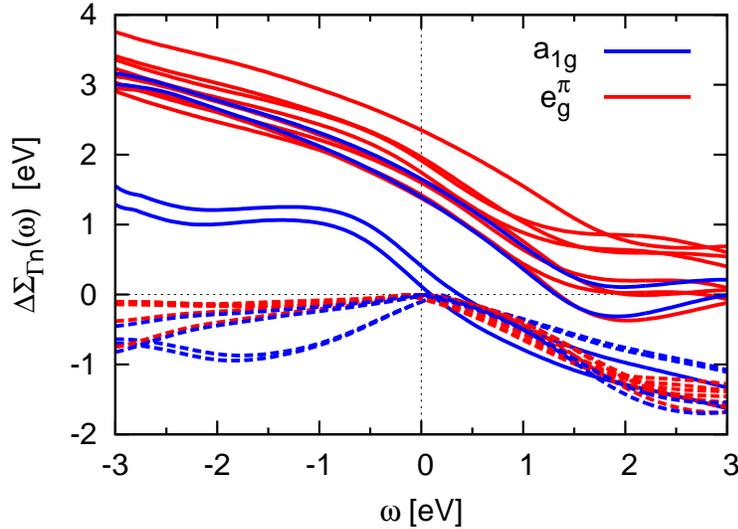

Figure 5.23 : *GW t_{2g} self-energy correction at the Γ-point. Solid lines are real parts, dashed lines imaginary parts. Also, as before we have indicated the different (LDA) orbital character.*

Coming back to Figure 5.23, we see that the shift between the bonding a_{1g} and the other components is clearly distinguishable. Yet, as expected from the above discussion of the linearized band-structure, the anti-bonding a_{1g} elements show a behaviour that is rather generic for the e_g^π elements, too. As a consequence, the gap-opening within the current approach is rather Hartree-Fock like, i.e. the different occupations of a_{1g} and e_g^π orbitals lead to different real-parts of the self-energy.

As far as the coherence of the excitations is concerned, we may compare the imaginary parts of the GW self-energy in the Kohn-Sham basis, with the LDA+CDMFT self-energy in the bonding / antibonding basis, Figure 5.18. The occupied a_{1g} orbitals thus have a quite comparable coherence, the imaginary parts reaching about -0.25 eV in the relevant energy range. The e_g^π excitations are actually slightly less coherent in GW than they are in the LDA+CDMFT, which is also seen in the spectral function, which extents over a wider frequency range in the case of GW.

The spectral function. Finally, we plot the spectral function at the Γ-point in Figure 5.24 and compare the position of spectral weight with the self-energy corrected band-structure from above. The spectral function exhibits weight roughly at the perturbatively calculated positions. Deviations are due to two effects. First, the described
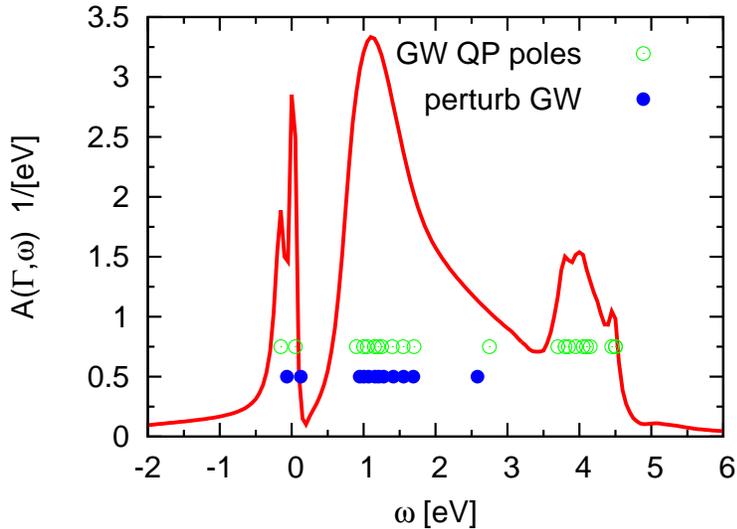
Figure 5.24 : *GW t_{2g} spectral function $A(\Gamma, \omega)$ at the Γ-point. Indicated are also the self-energy corrected Kohn-Sham energies (perturb GW) according to Equation (5.12), and the poles of the GW Green's function (GW QP poles). Here we show all quantities as they emerge from the calculation, no shift in the chemical potential was applied.*

procedure is a linearization of the quasi-particle equation. This is done for the sake of less numerical cost, since then the self-energy needs only be computed for the former LDA energies[32]. When however disposing of the frequency dependent self-energy on a fine frequency grid, we can solve the quasi-particle equation, as we have done in the context of LDA+DMFT calculations, see e.g. Section A, Chapter 3. We note that a correct treatment slightly moves the excitation energies, in particular the a_{1g} bonding and the upper e_g^π bands. Moreover the frequency dependence of the self-energy may lead to additional solutions indicating the formation of satellite features in the spectral function, as seen in Figure 5.24. As mentioned above, however, we do not trust the self-energy beyond ± 3 eV which is why we renounce from attributing a physical meaning to the features seen at around $+4$ eV in the spectral function. This, and the non-conserving nature of the GW in general, detains us from calculating the chemical potential from the constraint $N = \int^\mu d\omega A(\mathbf{k}, \omega)$, since there is considerable weight in satellite features (also at larger negative energies, not shown).

The considerable numerical cost prevented us from showing a series of momentum-resolved spectral functions, as we did for the LDA+CDMFT calculation.

Conclusions.   Within the used implementation of the GW approximation, the correct insulating behaviour is reproduced[33]. Yet, the expected bonding / antibonding physics in

---

[32]and some energies around them in order to compute the derivative of the self-energy.

[33]The fact that two different GW implementations, the one we used [Aryasetiawan(2000)] and the one of Gatti *et al.*, are yielding a qualitatively different result is rather worrisome. Above, we stated our opinion on the origin of this discrepancy. Hopefully this issue will be resolved and understood. One has

the a_{1g} channel was not clearly evidenced. In particular our one-shot GW calculation did not succeed in increasing the bonding / antibonding splitting.

Still, we dare say that the GW approach seems to reach its limits for systems like VO$_2$, since the number of calculable quantities is rather limited, which makes a thorough physical discussion cumbersome. It would be quite desirable to find ways to speed up these calculations. After all, the success of density functional theory can in large parts be ascribed to the fact that calculations are reasonably quick even for large systems.

---

to say that GW apparently still suffers from teething troubles. While DFT-LDA results are usually stable with respect of the choice of basis sets, potentials and codes, GW may not yet have reached this point.

D   The Optical Conductivity of VO$_2$[34]

Prior theoretical work.   Theoretically, the optical response of M1 VO$_2$ was investigated by means of a self-consistent model GW calculation [Continenza *et al.* (1999)], mentioned already earlier. This was found to improve on LDA results for the dielectric function, when comparing with experiments [Gavini and Kwan(1972)]. Also, a clear polarization dependence was evidenced. Yet, in these calculations, a model parametrization for the dielectric function was assumed that, moreover, used some experimental input.

Further, the dielectric response of both the metallic and the insulating phase were calculated within LDA [Mossanek and Abbate(2007)]. In the metallic phase, peak positions and the polarization dependence were qualitatively captured. The issue of the bad metallic behavior was not adressed, which is natural since a capturing of this lies way beyond band theory. As to the insulating M1 phase a rigid shift was introduced to the LDA band-structure, such as to artificially produce a gap. This procedure, again, resulted in qualitative agreement with experiment. However, we explain that by our reckoning the electronic structure is characterized by an enhanced a_{1g} bonding/anti-bonding splitting, which is, of course, not reproduced by an orbital-independent shift. Yet, on the other hand, we have shown, Section B, that an orbital-dependent one-particle potential actually does capture spectral properties to a surprising degree.

Experimental details and prelude to the calculation.   We now turn to the first real application of the formalism described in Chapter 4 to an actual compound. In the following we present results for the optical conductivity of VO$_2$ in the metallic rutile, and the insulating M1 phase.

In order to compute the optical conductivity also for high energies, we employ the upfolding scheme detailed in Section D, Chapter 4. In the many-body Cluster-DMFT calculation of [Biermann *et al.* (2005)] that stood at the beginning of our work, all orbitals other than the vanadium t_{2g} were downfolded. The latter thus constitute the low energy sector, L according to Equation (4.95). For the calculation of the Fermi velocities we use a larger Hamiltonian that comprises for the high energy part, H, in particular the vanadium e_g^σ and the oxygen 2p orbitals, and, moreover, the oxygen 2s[35]. We sketchily write s,p,e_g^σ in the graphics. When indicating, in the graphics, that transitions are from s,p,e_g^σ into the t_{2g} orbitals, this mainly accounts for transitions from the occupied O2p into empty t_{2g} orbitals, since, e.g., the e_g^σ to t_{2g} transitions are derived only from the little occupied weight of e_g^σ character that stems from hybridizations with occupied orbitals.

When referring to the orientation of the electric field, or the light polarization, we use the simple monoclinic lattice as reference[36]. Since for the Peierls Fermi velocity, Equation (4.70), we perform the numerical derivative of the Hamiltonian on a discrete momentum mesh, not all directions are accessible in a straight forward manner. Yet, the important polarizations, $E \parallel [001]$ and $E \perp [001]$, are capturable. In an experiment, the polarization is varied by choosing different orientations of the sample, or different

---

[34]This work appears in : [Tomczak and Biermann(2007b)]

[35]In the M1 phase, though not necessary, we further include the vanadium 4s and 4p orbitals.

[36]See e.g. Fig.10 in [Eyert(2002)] for the first Brillouin zone

substrates, which, in the case of thin films, favor different growth directions. Herewith, all orientations that lie within the plane of the surface are probed, when using unpolarized light. In our calculations, however, we evaluate the response of a single given polarization only, without averaging over an ensemble of in-plane directions.

As a comparison to our theoretical curves, we include results from three experiments that we already mentioned in the beginning. We will display measurements on single crystals by [Verleur *et al.* (1968)], performed for different orientations of the sample. Moreover, recently, experiments were carried out on different types of thin films. The work of [Okazaki *et al.* (2006)] used thin films (T$_c \approx$ 290 K) with [001] orientation, i.e. for the electric field $E \perp$ [001]. [Qazilbash *et al.* (2006)] on the other hand used polycrystalline films with preferential [010] orientation (T$_c \approx$ 340 K).

D.a   Rutile VO$_2$ – The metal

In Figure 5.25 we show, along with the mentioned experimental data, the theoretical optical conductivity of rutile VO$_2$, which we obtain for the different light polarizations as indicated.
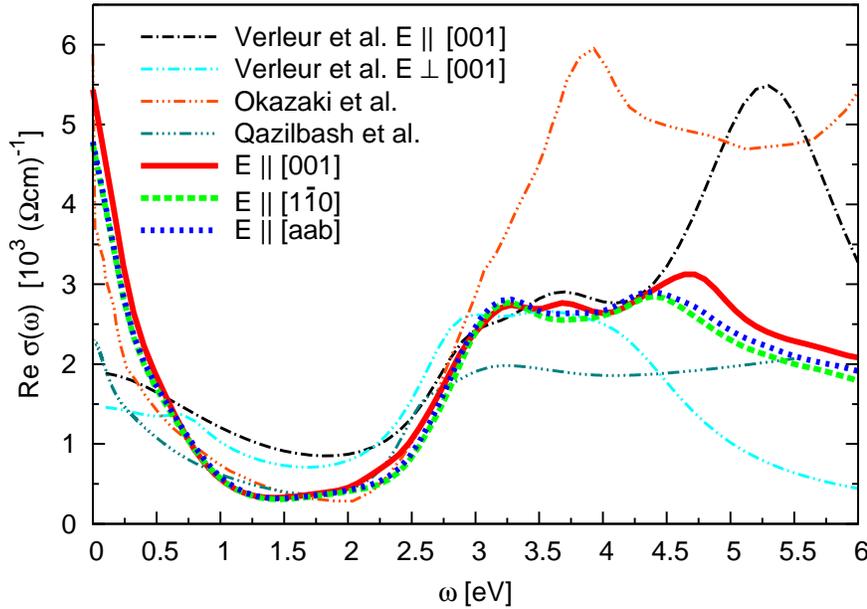

Figure 5.25 : *LDA+CDMFT optical conductivity of the rutile phase of VO$_2$ for the indicated polarizations ([aab]=[0.85 0.85 0.53]). The velocity matrix elements were calculated using the scheme of Section D, Chapter 4. Beyond the t_{2g} orbitals this calculation includes in particular the Ve_g^σ and O2p orbitals. Experimental curves from [Verleur et al. (1968)] (single crystals, orientation as indicated), [Qazilbash et al. (2006)] (polycristalline film (T$_c \approx$ 340 K), preferential orientation $E \perp$ [010], T=360 K), and [Okazaki et al. (2006)] (thin film (T$_c \approx$ 290 K), $E \perp$ [001], T=300 K).*

As one can see, already the three experiments yield quite distinguishable spectra. The differences may point to a polarization dependence, but one cannot rule out an

influence of the sample type and the means by which multiple reflections at the sample substrate were treated in case of the thin films. Indeed, in the case of rutile VO$_2$, x-ray experiments [Haverkort *et al.* (2005)] witness a rather isotropic response. The different measurements on single crystals [Verleur *et al.* (1968)] also evidence a quite uniform conductivity up to 4 eV.
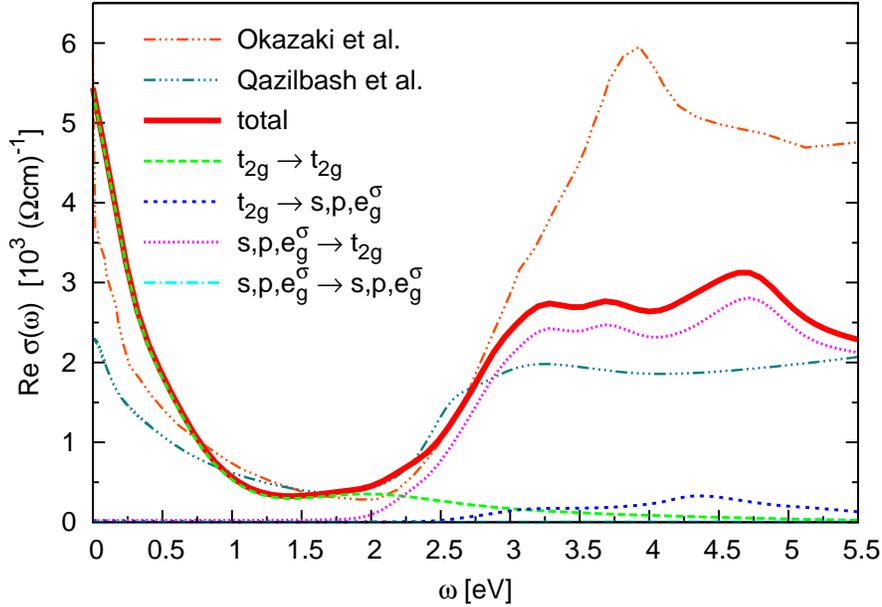

Figure 5.26 : *LDA+CDMFT optical conductivity of rutile VO$_2$ for the [001] polarization. Shown are the different orbital transitions according to their energy sector, see Equation (4.96). The contributions are additive and sum up to the total conductivity. For details see Section D, Chapter 4. Experimental curves, as above from [Okazaki et al. (2006), Qazilbash et al. (2006)].*

The polarization dependence of the theoretical conductivity is found to be rather small, too, which is of course in line with our previous statement [Tomczak *et al.* (2007)] that the t_{2g} self-energy shows no particular orbital dependence. Thus, in theory, the metallic Drude-like response is made up from a_{1g} and e_g^π density near the Fermi surface[37].

At higher energies, beyond the Drude-like tail, further inter-"band" intra-t_{2g} transitions occur. Yet, the optical response is rather structureless up to 2 eV. At this energy, however, we already expect the onset of oxygen 2p derived transitions. In order to elucidate the origin of the spectral weight of this region in greater detail, we plot in Figure 5.26 the optical conductivity resolved into the different energy sectors, according to Equation (4.96). Since the O2p and the e_g^σ orbitals were part of the downfolded high energy

---

[37] As concerns the very low frequency response, we remark that the theoretical result might overestimate the spectral weight, since we (so far) do not employ the tetrahedron method for momentum summations, and thus a very fine **k**-mesh was needed to get the current data. Therewith also the spectral weight of transitions from density near the Fermi level to higher energies will be slightly too large. This is an issue for metallic phases only.

sector, their position, within our scheme, is frozen to the LDA result (see e.g. the band-structure in [Eyert(2002)]). Therefore transitions from the O2p orbitals into the t_{2g} ones start, as expected, at around 2 eV. We remark that the polarization dependence for the oxygen derived transitions agrees very well with the single crystal experiments [Verleur *et al.* (1968)] up to 4.5 eV. Transitions from the t_{2g} orbitals into the e_g^σ set in later, at around 2.5 eV, and are rather small in magnitude. The O2p to e_g^σ transitions appear at the expected energies, but they are too low to be seen in Figure 5.26.

Overall, the LDA eigenvalues seem to give a rather good description of the e_g^σ and O2p orbitals, since the agreement with experiment is reasonably accurate, as was qualitatively noticed already in previous LDA optics calculations [Mossanek and Abbate(2007)]. When looking at photoemission results [Abbate *et al.* (1991),Koethe *et al.* (2006)], one remarks that the on-set of the oxygen 2p is compatible with the LDA, yet, their center of their gravity is shifted to slightly higher binding energies in the experiment. As to the e_g^σ orbitals, it is conceivable, when resorting to x-ray experiments [Abbate *et al.* (1991), Koethe *et al.* (2006)] as a reference, that they appear at a little larger energies and with a smaller bandwidth than within the LDA. Of course both comparisons are somewhat indirect, due to the occurrence of matrix element effects in the experiments. Yet, we emphasize that the rather incoherent nature of the t_{2g} weight in the t_{2g} spectral function is far beyond any band-structure technique, which is why the optical conductivity in the 2.5 to 4.0 eV region, derived from O2p to t_{2g} transitions, comes out too large in LDA [Mossanek and Abbate(2007)] when comparing to the experiment of Ref. [Verleur *et al.* (1968)], while we find a good agreement for the LDA+CDMFT conductivity.

At this point, we can only speculate on the origin of the shoulder and peak structure seen in one of the experiments [Qazilbash *et al.* (2006)] at 2.5 eV, and 3.0 eV, see Figure 5.25. It seems conceivable that it stems from t_{2g} to O2p transitions, rather than from e_g^σ contributions. Attributing the humps to distinct O2p to a_{1g} or e_g^π transitions is cumbersome, mostly due to the structure of the numerous oxygen bands. When looking at the momentum-resolved optical conductivity (not shown), one realizes that O2p to e_g^π transitions start for most of the **k**-regions at lower energies than transitions into the a_{1g}.

D.b Monoclinic VO$_2$ – The insulator

The optical conductivity of the scissors construction. At first, in order to further corroborate the validity of our effective band picture of M1 VO$_2$ of Section B, we calculate the optical conductivity $\Re\sigma(\omega)$ that corresponds to the scissored Hamiltonian from above. In order to go beyond the transitions within the t_{2g} manifold, we compute a full LMTO [Andersen(1975)] Hamiltonian that in particular comprises the vanadium e_g^σ and the oxygen 2p orbitals. This Hamiltonian is used to compute the Fermi-velocities in the Peierls approximation, according to Equation (4.70). We emphasize that the d-orbital wavefunctions of this non-downfolded LMTO Hamiltonian are more localized than those of the t_{2g} Hamiltonian, a fact that renders the Peierls substitution closer to the exact result. Yet, oxygen wavefuntions are much less localized, which is why the corresponding transition amplitudes within the Peierls approximation might be less reliable.

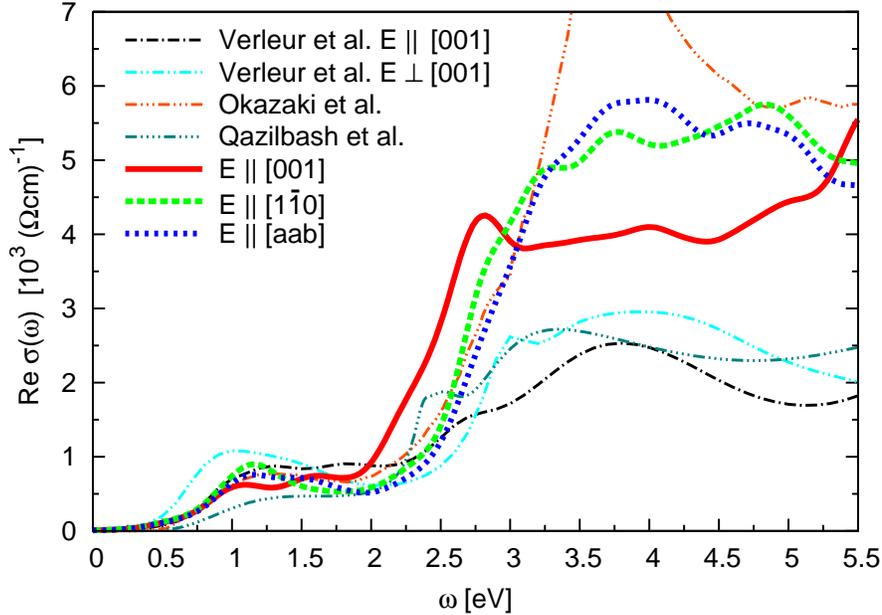For the spectral function of the system, we employ the up-folded scissored Hamilto-

Figure 5.27 : *Optical conductivity of the effective band-structure for indicated polarizations ([aab]=[0.84 0.84 0.54]). Experimental curves from [Okazaki et al. (2006)] (thin film, E ⊥ [001], T=280 K), and [Qazilbash et al. (2006)] (polycristalline film, preferential orientation E ⊥ [010], T=295 K).*

nian, i.e. a spd-Hamiltonian to which the scissors operator has been applied as described above in Equation (5.11). The reason for not computing the Fermi velocities from this "scissored" Hamiltonian is the following. In the introduction we have noted that interactions on a mean-field level can be incorporated into the kinetic part of the Hamiltonian, see Equation (1.4) and Equation (1.5). Yet the effect of the scissors operator is different, since it explicitly depends on the orbital and, in this context, thus has to be treated as a correlation effect beyond mean-field, i.e. like a self-energy, that hence does not enter the calculation of the Fermi velocities, see Chapter 4.

With the scissors procedure, all correlation induced energy shifts are captured, whereas the coherence of the excitations remains infinite, i.e. band-like. Also, in this case, we do not have to invoke the upfolding scheme of Section D, Chapter 4. However, this also means that we cannot easily distinguish the origin of the different orbital contributions to the total spectral weight in the conductivity.

In Figure 5.27 we show our theoretical results, again, in conjunction with the three experiments [Verleur *et al.* (1968), Okazaki *et al.* (2006), Qazilbash *et al.* (2006)].

As was the case for the metallic phase, the latter yield varying results. While the optical gap is roughly 0.5 eV in all cases, the higher energy response is markedly different. Not only the amplitudes, but also the peak positions differ considerably. Yet, as a matter of fact, in the current case of M1 VO$_2$, a sizable polarization dependence is expected from the structural considerations mentioned above. Indeed our calculation suggests a noticeable anisotropy in the optical response, which is congruent with the experimental

findings.

When looking first at the optical conductivity that results from the effective band-structure, "LDA+scissors", we find all polarization tendencies reproduced : Consistent with Verleur et al. [Verleur *et al.* (1968)], the $E \parallel$ [001] conductivity is lower than the $E \perp$ [001] one at energies up to 1.5 eV, after which the c-axis response develops a little maximum of spectral weight in both, experiment and theory. At energies of 2.35 eV [Qazilbash *et al.* (2006)] or 3.0 eV [Verleur *et al.* (1968)] the experimental conductivity with $E \parallel$ [001] components evidences a narrow peak. In the calculation this is prominently seen at 2.75 eV. When looking at our effective band-structure, Figure 5.19, it seems plausible that these transitions stem from a_{1g} bonding to anti-bonding orbitals. The peak is indeed very narrow for an inter-band transition, but in our picture this is simply owing to the fact that the a_{1g} anti-bonding excitation does exhibit an almost dispersionless behavior (see e.g. Figure 5.19). However, already at these frequencies we expect transitions that involve the oxygen 2p orbitals, as will be detailed below for the LDA+CDMFT conductivity.

At still higher energies the $E \parallel$ [001] response is again lower than for the perpendicular direction in both, experiment and theory. This surprising congruity with experiments further corroborates the validity of our effective band-structure picture for spectral properties and therewith strengthens our interpretation of the nature of the insulating phase of VO$_2$ as a "many-body Peierls" realization.

The optical conductivity of the LDA+CDMFT calculation. What the above theoretical conductivity is missing are the life-time effects encoded in the imaginary part of the LDA+CDMFT self-energy. These were found to be small, yet not entirely negligible (see above). When incorporating the latter, we thus have to resort to the upfolding scheme of Section D, Chapter 4 in order to compute the full-orbital LDA+CDMFT optical conductivity using the dynamical t_{2g} self-energy. Figure 5.28 displays our result, again along with the experimental curves.

When comparing with the conductivity of the effective one-particle approach (see also Figure 5.29), we realize that the LDA+CDMFT response for the t_{2g} orbitals is damped and therewith less structured, which was clearly expected. The small underestimation of the optical gap is probably owing to the elevated temperature at which the LDA+CDMFT quantum Monte Carlo calculation was performed [Biermann *et al.* (2005)].

To shed further light on the structure of the response, we resolve in Figure 5.30 the contributions to the [001] LDA+CDMFT conductivity into their respective energy sectors, according to Section D, Chapter 4. From this we first infer that the slight upturn, seen for this polarization beyond 1.5 eV in the LDA+CDMFT conductivity is indeed derived from transitions within the t_{2g} manifold, for oxygen contributions only set in at around 2.0 eV.

Besides, the prominent peak in both, the experimental and LDA+Scissors conductivity with $E \parallel$ [001] polarization that we attributed above to a_{1g}–a_{1g} transitions, is largely suppressed and only faintly discernible as a weak shoulder, when comparing with the other polarizations.

We can think of two explanations for this discrepancy between experiment and the scissors approach on the one hand, and the LDA+CDMFT result on the other. A first
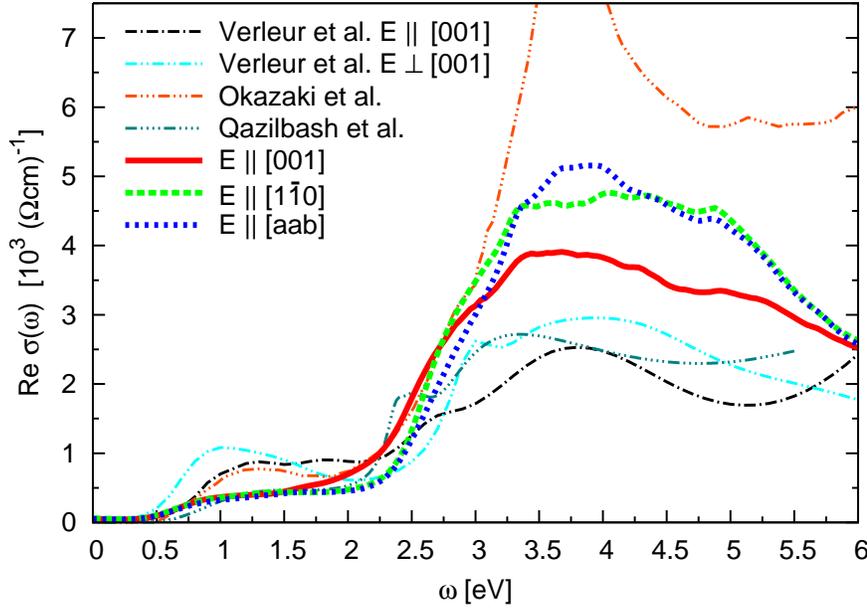
Figure 5.28 : *LDA+CDMFT optical conductivity of the M1 phase of VO$_2$ for the indicated polarizations ([aab]=[0.84 0.84 0.54]). The velocity matrix elements were calculated using the scheme of Section D, Chapter 4. Experimental curves from [Verleur et al. (1968)] (single crystals, orientation as indicated), [Okazaki et al. (2006)] (thin film, E ⊥ [001], T=280 K), and [Qazilbash et al. (2006)] (polycristalline film, preferential orientation E ⊥ [010], T=295 K)*
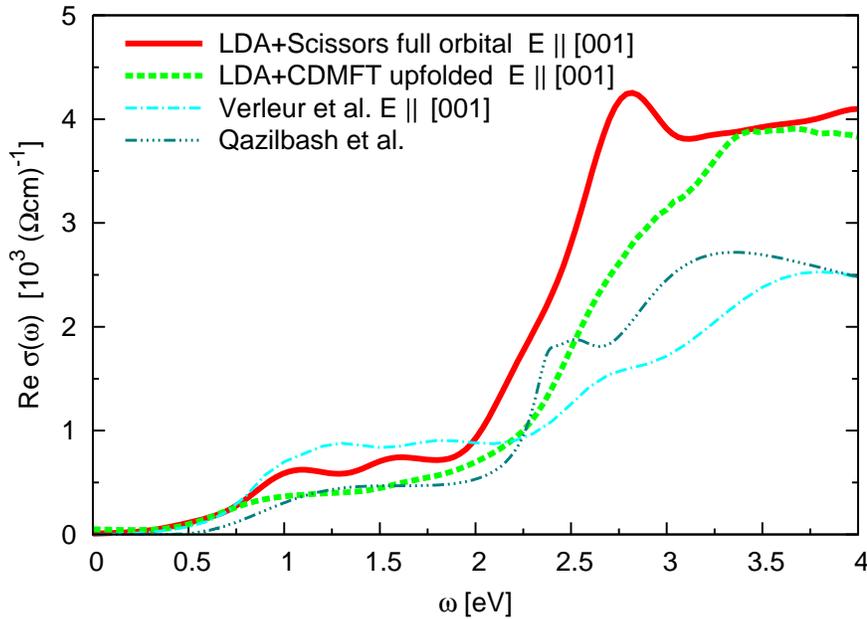

Figure 5.29 : *Comparison of the LDA+Scissors, Figure 5.27, and the LDA+CDMFT optical conductivity, Figure 5.28, for E ∥ [001] polarization, along with experimental data from [Verleur et al. (1968), Qazilbash et al. (2006)], as above.*

issue are the Fermi velocities. As mentioned above, only the LDA+CDMFT scheme makes use of the downfolding procedure of the matrix elements, whereas the other calculation uses the untransformed Peierls Fermi velocity of the large Hamiltonian.
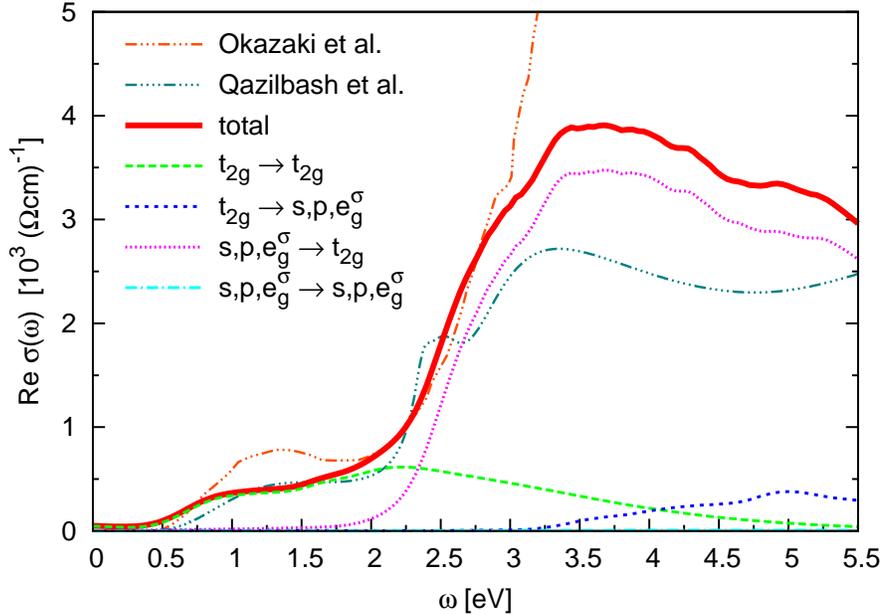

Figure 5.30 : *LDA+CDMFT optical conductivity of M1 VO$_2$ for the [001] polarization. Shown are the different orbital transitions according to their energy sector, see Equation (4.96). The contributions are additive and sum up to the total conductivity. For details see in particular Equation (4.96). Experimental curve, as above from [Okazaki et al. (2006), Qazilbash et al. (2006)].*

The second, and from our viewpoint predominant, effect is the occurrence of sizable life-time effects in the LDA+CDMFT electronic structure calculation. Indeed the a_{1g} spectral weight in the corresponding t_{2g} LDA+CDMFT spectral function is not sharply defined and extends over more than 2 eV, and is only barely discernible in the total, orbitally traced, spectrum [Biermann *et al.* (2005)]. When thinking of the conductivity in simple terms of density-density transitions, it is perfectly conceivable that the a_{1g}–a_{1g} response eventuates only in a tail of spectral weight (as seen in the energy sector resolved conductivity in Figure 5.30) and not in a well defined peak. Having said this, and referring to the experiments, one may thus conclude that these life-time effects are actually still overestimated in the LDA+CDMFT calculation [38]. We are hence led to the (speculative) conclusion that the narrow peak in the experiments indeed is a hallmark of the bonding/anti-bonding splitting, consistent with our theoretical interpretation.

Finally, we remark that despite all differences in the experimental data, they reveal (maybe apart from the single crystal for [001] polarization) a common global tendency,

---

[38]This might point to problems in the use of the maximum entropy method [Jarrell and Gubernatis(1996)] that we employed for the analytical continuation, which has problems in finding sharp structures at higher energies.

namely that, when going from the metal to the insulator, low frequency spectral weight is transfered to higher energies. Indeed, for a given polarization, the Drude-like weight that the insulator is lacking at low energies must be recovered, as requires the f-sum rule. This condition is met at 5.5 eV in one experiment [Qazilbash *et al.* (2007)], while in the other [Okazaki *et al.* (2006)] an overcompensation appears already at energies beyond 3.5 eV. Theoretically, when using the LDA+CDMFT conductivity, we find values of 3.73 eV and 4.35 eV, for the [1$\bar{1}$0] and [001] direction, respectively.

Motiviating the upfolding procedure. In Chapter 4 we already pointed out that the calculation of Fermi-velocity matrix elements from downfolded Hamiltonians is problematic, which is why in Section D, Chapter 4 we devised a "downfolding procedure" for the Fermi velocities, which are calculated using a full Hamiltonian that comprised in the current case (see above) in particular the e_g^σ and the oxygen 2p orbitals.
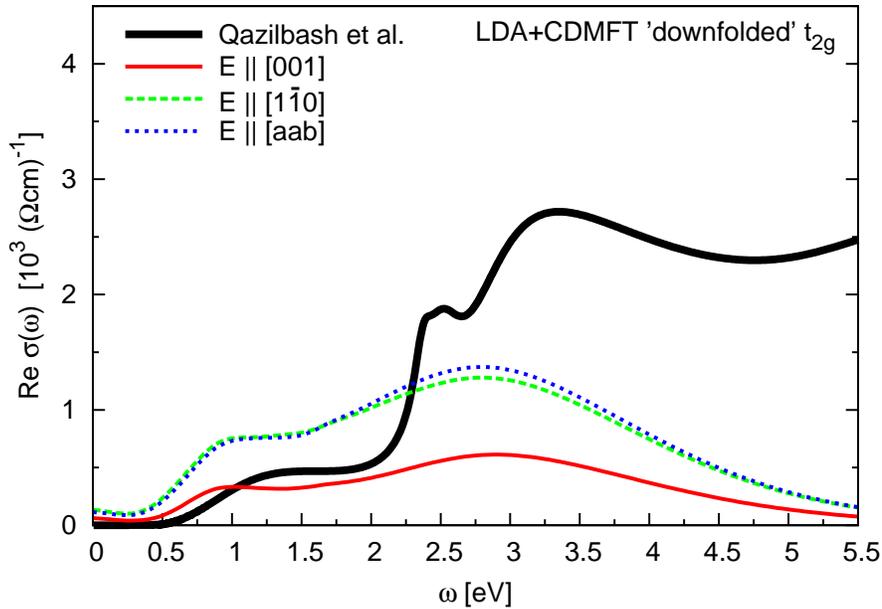

Figure 5.31 : *LDA+CDMFT optical conductivity for indicated polarizations ([aab]=[0.84 0.84 0.54]). The matrix elements were calculated from the downfolded t_{2g} Hamiltonian. Experimental curve (E $\perp$ [010]) from [Qazilbash et al. (2006)].*

For the sake of the argument we plot in Figure 5.31 the optical conductivity, resulting from the Fermi-velocities of the *downfolded t_{2g}* Hamiltonian. We clearly see that not only the absolute values of the conductivity are worse than in the preceding calculation, but also the impact of the light polarizations is somewhat different, with now the [001] conductivity having less spectral weight at all energies.
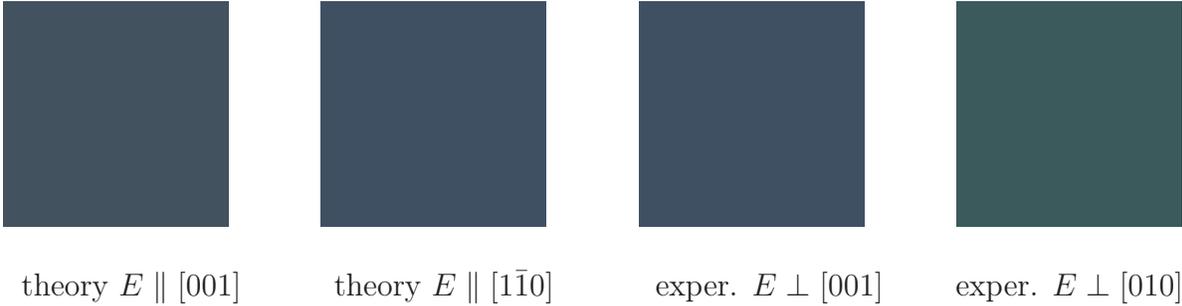
theory $E \parallel [001]$ theory $E \parallel [1\bar{1}0]$ exper. $E \perp [001]$ exper. $E \perp [010]$

Figure 5.32 : *Comparison of colours : (from left to right) as calculated from LDA+CDMFT for* [001] *polarization* [rgb] = [0.263 0.321 0.372]*,* [1$\bar{1}$0] *polarization* [rgb] = [0.245 0.314 0.390]*, and as extracted from the experiment [Okazaki et al. (2006)]* [rgb] = [0.259 0.313 0.382]*, [Qazilbash et al. (2006)]* [rgb] = [0.229 0.352 0.360]*.*

The colour of M1 VO$_2$.   From the knowledge of the optical conductivity, we can in particular calculate the reflectivity using the equations of Section A, Chapter 4, and, furthermore, the colour of the sample by the procedure described in Section E, Chapter 4.

Figure 5.32 shows the resulting RGB colours, obtained, from both, the theoretical and from the experimental conductivities [Okazaki *et al.* (2006), Qazilbash *et al.* (2006)][39]. The RGB values are indicated in the caption. Again, we remark that in the LDA+DMFT reflectivity we assume the light to be polarized along the indicated direction, whereas the experiment samples over all polarizations of a given plane.

In the current case, the optical gap does not influence the appearance in the visible range. Indeed, the energy region that is probed extends roughly from 1.75 to 3 eV. As seen in Figure 4.4, where also the corresponding colours are displayed.

We see that the theoretical colour is rather isotropic, since the different polarizations barely have any impact on the appearance of the material considerably. Hence, theoretically M1 VO$_2$ is more or less grey, with a light touch of blue[40].

The experimental conductivity yields a comparable colour, especially for the one of [Okazaki *et al.* (2006)]. For [Qazilbash *et al.* (2006)] a slightly higher green component is discernable.

We stress that the colours are computed for bulk VO$_2$. The multiple reflections of the film substrate were substracted in the deducing of the optical conductivity [Okazaki *et al.* (2006), Qazilbash *et al.* (2006)]. For instance, [Qazilbash *et al.* (2006)] used the substrate, Al$_2$O$_3$, which itself is white, and the VO$_2$ film on it appears rather yellow[41]. We have not endeavoured to reintroduce the influence of the substrate, such as to reproduce

---

[39]We note that the procedure requires the calculation of the imaginary part of the conductivity via a Kramer-Kronig transformation. Since neither the experiment nor the theoretical results reach very high energies, there is small, yet non-negligible influence by the choice of a high frequency extrapolation. For the current results, we used *no* extrapolation.

[40]This is consistent with the colour "blue-black" given e.g. in www.webelements.com : http://www.webelements.com/webelements/compounds/text/V/O2V1-12036214.html

[41]M.M. Qazilbash, private communication

the colour of the film.

D.c   Conclusions

As a first application of our optics scheme for strongly correlated materials, we evaluated the optical conductivity of VO$_2$ for both, the metallic and the insulating phase. By using our upfolding procedure we were able to include high energy orbitals that were downfolded in the LDA+CDMFT calculation of the electronic structure.

While the metal is characterized by a rather isotropic response, the insulator reveals a noticeable polarization dependence, related to the changes in the crystal-structure. The agreement with experiments is overall satisfying. The high energy conductivity is reasonably described when using the LDA band-structure. The LDA+CDMFT many-body calculation for the t_{2g} orbitals correctly describes the low-energy behaviour. In the rutile phase it accounts especially for the damping of oxygen to t_{2g} transitions. In the insulator, it allowed in particular for the reproduction of the experimental t_{2g} response, along with its polarization dependence. For the insulating phase, we moreover computed the optical conductivity corresponding to the effective band-structure of Section B. This allowed for the identifying of a prominent feature in the experiments to a_{1g} bonding to anti-bonding transitions. We interpreted this as corroborating our proposed "many-body Peierls" scenario for monoclinic VO$_2$. In the LDA+CDMFT calculation these transitions are highly damped, and we were led to the speculation that, indeed, correlation effects might still be overestimated in the insulating phase within LDA+CDMFT.

Chapter 6

Vanadium Sesquioxide – V_2O_3

Vanadium sesquioxide, V_2O_3, has been the subject of, both, extensive theoretical and experimental studies for now more than three decades. It is considered as *the* prototype of a compound that (besides other transitions) undergoes upon chemical substitution a Mott-Hubbard metal-insulator transition in its purest form, i.e. iso-structural and without acquiring any magnetic ordering. This is why early theoretical approaches almost exclusively resorted to the Hubbard model to explain the electronic properties of V_2O_3. However, over the years, mostly experimental evidence was build up, that shows that the physics of this material is indeed more involved and a realistic multi-orbital setup is needed to account for the full complexity of the correlation effects taking place.

In the following we shall briefly review experimental findings and the history of theoretical advances to V_2O_3 as far as is needed to put our work into perspective. More extensive reviews can be found e.g. in [Imada *et al.* (1998), Mott(1990)]. The current work is the result of a collaboration with the authors of [Poteryaev *et al.* (2007)]. My main contribution concerns the calculation of the real-frequency self-energy, its interpretation and related discussions, as well as the calculation of derived quantities, such as the momentum-resolved spectral functions.

Beyond this, we will show calculations of the optical conductivity of metallic V_2O_3 that were motivated by recent experiments.

After the short review, we proceed with our LDA+DMFT analysis of quasi-particle properties and questions related to the effects of the self-energy on the excitation spectra in the two paramagnetic phases, using the techniques described in the preceding section. This will allow in particular for a deeper understanding of the behaviour of the electronic degrees of freedom in the paramagnetic metal to paramagnetic insulator transition.
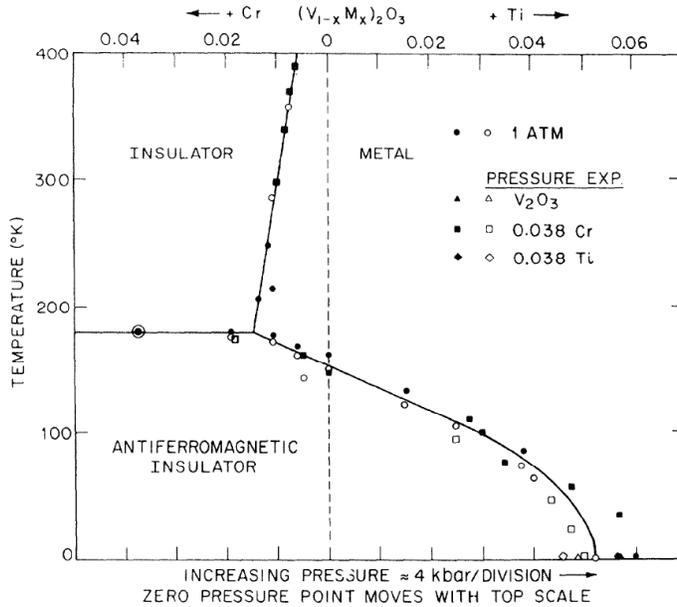
Figure 6.1 : *Temperature versus pressure or Cr-doping : Phase diagram of $(V_{1-x}M_x)_2O_3$. From [McWhan et al. (1971)].*

A   Experimental findings and theoretical understanding - a brief review

A.a   Phase diagram and crystal structure

Figure 6.1 [McWhan *et al.* (1971)] shows the phase diagram of V_2O_3 as a function of temperature versus pressure. At ambient conditions V_2O_3 is a metal and it has the corundum crystal structure. The latter, see Figure 6.2, is formed by a hexagonal close packing of oxygen atoms, with 2/3 of its octahedral sites occupied by vanadium atoms, which are arranged such as to form V-V pairs along the hexagonal/rhombohedral c-axis and a honeycomb lattice in the ab plane. The space group is R$\bar{3}$c. Upon cooling below 150 K, a peculiar antiferromagnetic order sets in and the system becomes insulating [Föex(1946), Moon(1970)]. The transition is of first order and it is accompanied by a monoclinic structural distortion (the space group becomes I2/a). Alternatively, the system can be tuned by chemical substitution $(V_{1-x}M_x)_2O_3$ and external pressure. Doping with chromium (M=Cr) amounts to applying negative hydrostatic pressure, which effectively decreases the c/a lattice constant ratio, while doping with titanium (M=Ti) is equivalent to positive pressure. Indeed, there exists an empirical relation between the chemical substitution and external pressure [McWhan *et al.* (1973)], which is $+(-)0.4$GPa per 1% substitution with Ti^{3+} (Cr^{3+}), thus allowing to cover the entire pressure range of the shown phase diagram.

At least for the Cr-doped compound series it is reasonable to assume that the global electron density is not severely changed by the additional one electron per Cr-impurity [Imada *et al.* (1998)], and that changes in the electronic structure are solely due to the
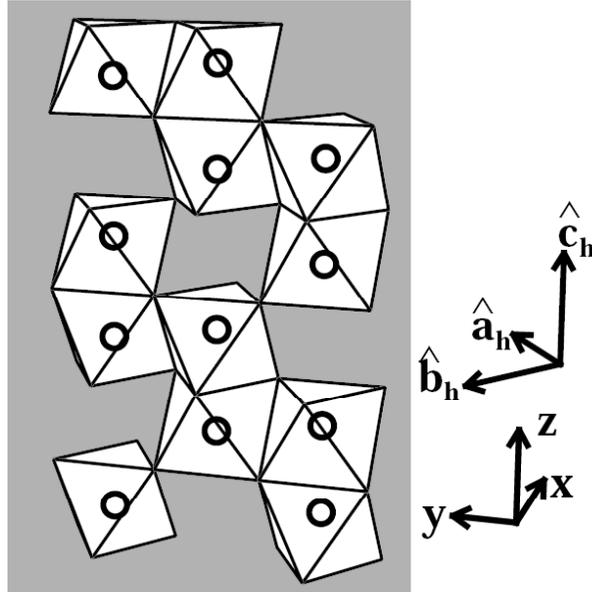
Figure 6.2 : *The corundum crystal structure of paramagnetic $(V_{1-x}M_x)_2O_3$. From [Tanaka(2004)].*

changes in the lattice parameters, i.e. one disposes of a handle to tune the bandwidth at constant filling.

This might not be true for the Ti-doped side of the phase diagram. As a matter of fact at a doping above 6 % the phase diagram differs qualitatively from the one obtained by applying external pressure [Ueda *et al.* (1979)]. It appears that the filling effect is non-negligible and that the properties actually are rather similar to the vanadium-deficient compound $V_{2-y}O_3$ [Ueda *et al.* (1980)].

Above the Néel temperature the crystal structure does not change from its corundum configuration as a function of pressure or doping. Still, as a function of Cr-doping, $(V_{1-x}M_x)_2O_3$ undergoes a first order paramagnetic metal (PM) to paramagnetic insulator (PI) transition [McWhan *et al.* (1969)]. It is this PM-PI transition that evoked the proposing of several distinct scenario in close connection with genuine Mott-Hubbard physics, as described below.

As indicated in Figure 6.1, the transition line terminates at a critical end point at about 400 K [McWhan *et al.* (1969)]. Indeed similarities with the liquid gas transition[1] can be evoked [Jayaraman *et al.* (1970),Limelette *et al.* (2003)], see also [Castellani *et al.* (1979)].

As our key interest is in the paramagnetic phases of $(V_{1-x}M_x)_2O_3$ and the transition between them, we shall limit the further discussion to precisely these two phases.

---

[1]Indeed, we mentioned already such a similarity for the metal-insulator transition of the one-band Hubbard model, see Section C, Chapter 2.
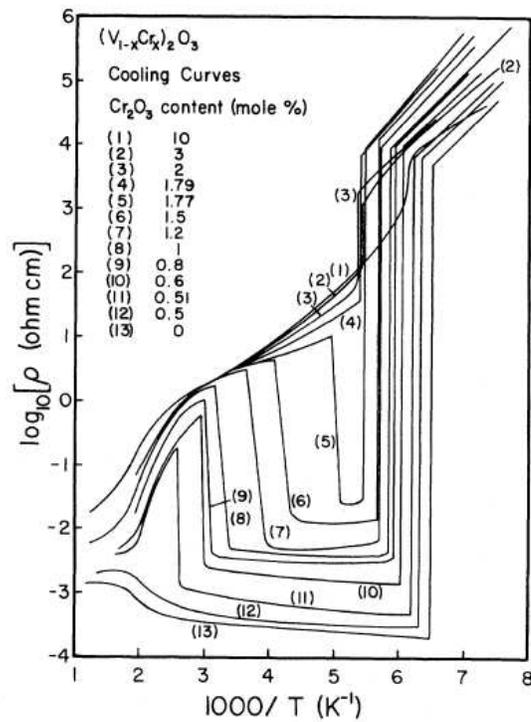
Figure 6.3 : *Resistivity of $(V_{1-x}Cr_x)_2O_3$ (upon cooling). The curves follow vertical lines in the phase diagram, Figure 6.1. From [Kuwamoto et al. (1980)].*

A.b   Experimental facts on the PM-PI transition

Experimentally the transition is signaled by a sizable discontinuity in the resistivity, which jumps by several orders of magnitude [McWhan *et al.* (1969), Kuwamoto *et al.* (1980)], as can be seen in Figure 6.3 which shows the resistivity as a function of temperature for various doping levels, thus corresponding to vertical lines in the phase diagram Figure 6.1. Unfortunately, no optical conductivity data is available for $(V_{1-x}M_x)_2O_3$ for x$\neq$ 0. Only the metal-insulator transition in vanadium deficient $V_{2-y}O_3$ has been studied in detail both experimentally and theoretical [Thomas *et al.* (1994a), Thomas *et al.* (1994b), Rozenberg *et al.* (1995)]. It was concluded that the phenomenology of the temperature dependence in the conductivity can be understood by appealing to the physics of the one-band Hubbard model. However, as in the Ti-doped case, it is not completely ruled out that filling effects play a role in the $V_{2-y}O_3$ series [Imada *et al.* (1998)].

Already the paramagnetic metallic phase exhibits signatures of strong correlations. Indeed, photoemission experiments, [Schramme(2000), Mo *et al.* (2003), Mo *et al.* (2006)], show, besides a quasi-particle peak at the Fermi edge, a lower Hubbard at around 1.25 eV binding energy (see Figure 6.7), long before oxygen contributions set in.

Also x-ray absorption spectroscopy (XAS) reveals structures broader than calculated from band-theory [Müller *et al.* (1997), Keller *et al.* (2004)], pointing to the importance of electronic correlations.

As mentioned above, the transition to the paramagnetic insulator is iso-symmetric and in particular no magnetic long-range order appears [McWhan *et al.* (1969)]. The crystal structure thus is of corundum-type in both phases. However, at ambient conditions, the volume expands by 1% at 0.9% Cr-doping and beyond this point the c/a lattice parameter ratio displays an important reduction upon further doping [McWhan *et al.* (1969)]. Such a volume expansion is a common feature of Mott-Hubbard metal-insulator transitions, since the charges that are localized in the insulating phase no longer participate in the bonding. Moreover, susceptibility measurements and entropy considerations [McWhan *et al.* (1969), McWhan *et al.* (1973)] show the presence of local moments in the insulating phase of $(V_{1-x}M_x)_2O_3$. Hence the metal-insulator transition exhibits all qualitative features that are expected for a Mott-Hubbard type transition.

A.c   Electronic configuration and early theoretical work

Atomic vanadium has the electronic configuration $[Ar]3d^34s^2$. In the present case vanadium is in its V^{3+} oxidation state, thus leading to a nominal $3d^2$ configuration. Owing to its octahedral oxygen surrounding, the vanadium 3d-manifold splits into two higher lying e_g^σ orbitals and the lower lying t_{2g} manifold, which are isolated in energy both from each other and from other orbitals. The trigonal part of the crystal field further splits the t_{2g} into a non-degenerate a_{1g} and lower lying doubly degenerate e_g^π orbitals.

The crucial question that arises is which are the positions in energy and thus the occupations of the respective e_g^π and the a_{1g} orbitals in the corundum structured *solid*. In an early series of papers by Castellani *et al.* [Castellani *et al.* (1978b), Castellani *et al.* (1978a), Castellani *et al.* (1978c)], it was assumed that the occurrence of vanadium-

pairs, oriented parallel to the hexagonal/rhombohedral c-axis, would lead, via V-V cova-
lent bonding, to a strong bonding / antibonding splitting of the a_{1g} orbitals such as to push
the resulting bonding orbital below, and the anti-bonding well above the e_g^π. The bonding
band thus filled, the remaining two electrons of a vanadium pair would partially populate
the e_g^π orbitals, forming an S=1/2 state per vanadium atom. Therefore it was assumed
that the quarter-filled degenerate Hubbard model might yield an adequate description of
the physics of V$_2$O$_3$ [Castellani *et al.* (1978a)].

A.d   The S=1 reality

Combining neutron measurements of the magnetic moment [Moon(1970)] with non-re-
sonant magnetic X-ray scattering [Paolasini *et al.* (1999)] was found to result in $\langle S \rangle =$
$0.85\mu_B$ [Di Matteo *et al.* (2002)], already querying the S=1/2 state of the vanadium atoms.
Eventually, polarization dependent X-ray-absorption experiments [Park *et al.* (2000)] re-
vealed that the vanadium atoms have actually Hund's rule S=1 character in *all* the phases,
since it was shown that the low lying *excitation* states are not of pure e_g^π character but
comprise sizable a_{1g} admixtures.

   Hence the a_{1g}-bonding / antibonding scenario is not the exclusive mechanism for the
understanding of electronic structure of $(V_{1-x}M_x)_2O_3$[2]. On the theory side this evoked
new model approaches for the PM-AFI transition in pure V$_2$O$_3$ [Di Matteo *et al.* (2002),
Mila *et al.* (2000), Tanaka(2004)] which mainly dealt with the peculiar magnetic ordering
below the Néel temperature. Also, the suggestion to investigate the electronic structure
of $(V_{1-x}M_x)_2O_3$ with a degenerate Hubbard model is thus overcome, calling for a more
sophisticated setup allowing for the full orbital complexity of the compound.

A.e   An LDA reminder

Electronic structure calculations using density functional theory within LDA were first
performed by [Mattheiss(1994)]. As expected, neither the insulating nature of the PI
phase, nor the signatures of strong correlations in the metallic phase, are captured within
this approach. For instance no V 3d spectral weight appears below -0.5 eV, in contradiction
to photoemission, as will be seen below. Indeed, at first sight, the band-structure of
$(V_{1-x}M_x)_2O_3$ reveals only minor changes when going from the PM lattice parameters to
the PI ones. However, as we shall see below in our LDA+DMFT analysis, only minor
changes are needed to describe a metal-insulator transition in the series $(V_{1-x}M_x)_2O_3$ as
a function of Cr-doping. Nonetheless the LDA can give valuable insights and a qualitative
picture of the chemical interactions, which also provides the starting point for techniques
that go beyond LDA in their description of local Coulomb interactions, such as LDA+U
or LDA+DMFT.

   Figure 6.4 shows the band-structure of pure V$_2$O$_3$ within the LDA [Saha-Dasgupta
et al. (2007)]. Displayed is the energy-range of the V 3d-orbitals, that are well separated
from all other bands. Shown is the "fat band" representation for the a_{1g} (a) and e_g^π (b)

---

[2]As we have seen before, this is to be contrasted with the case of vanadium dioxide VO$_2$.
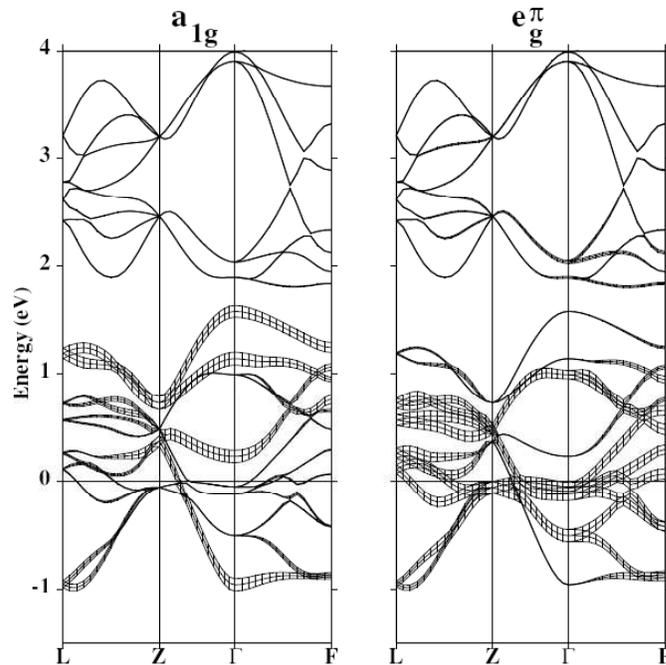
Figure 6.4 : *Bandstructure of pure V_2O_3 in the rhombohedral representation of the unit cell. The width of the lines corresponds to the magnitude of a_{1g} and e_g^π admixtures, respectively. From [Saha-Dasgupta et al. (2007)].*
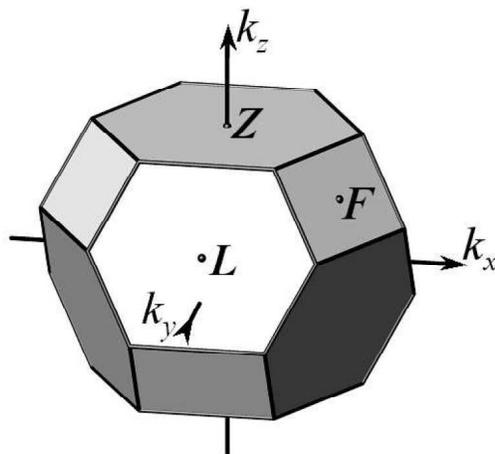

Figure 6.5 : *First rhombohedral Brillouin zone of corundum V_2O_3, indicating high symmetry points. From [Saha-Dasgupta et al. (2007)].*

orbitals, i.e. the width of the lines indicates the amount of V 3d a_{1g} and e_g^π contributions, respectively. The upper block of bands corresponds to the aforementioned e_g^σ orbitals, and the lower lying one to the t_{2g} orbitals. Clearly seen is a pronounced bonding / antibonding structure in the dispersion of the a_{1g} bands along various symmetry directions. Only in the $\Gamma - Z$ direction, along which the a_{1g}-orbitals are oriented, a sizable dispersion of the a_{1g} bands is seen, compatible with a quasi-dimensional behaviour of these orbitals. However it was demonstrated [Elfimov *et al.* (2003)] that in the corundum structure the shape of the a_{1g} orbital is not solely determined by the intra-pair hopping along the c-axis but that the hoppings in the ab basal plane are non-negligible. Moreover, for symmetry reasons the bonding part of the a_{1g} band hybridizes with the e_g^π bands to a considerable extent, leading to a sizable asymmetry of the a_{1g} density of states of pure V_2O_3 [Eyert *et al.* (2005)], with an anti-bonding peak that has less weight than expected from a pure molecular picture. As a consequence, the e_g^π manifold is more than quarter-filled.

In the antiferromagnetic low-temperature phase the insulating behaviour was correctly described within LDA+U [Ezhov *et al.* (1999)] calculations that proved also to be consistent rather with a S=1 picture of the ground state, since it was found to have two e_g^π electrons and the a_{1g} band empty.

In consequence, also from the band-structure side, the S=1 picture of V_2O_3 with almost two e_g^π electrons and nearly empty a_{1g} orbitals seemed to be favored over the S=1/2 scenario.

A.f   Previous LDA+DMFT calculations

LDA+DMFT calculations were first performed by [Held *et al.* (2001),Keller *et al.* (2004)]. They used the numerically exact Hirsch-Fye quantum Monte Carlo algorithm to solve the effective DMFT impurity problem. However, instead of using a downfolded LDA Hamiltonian in the DMFT self-consistency, they employed the LDA local density of states (DOS) projected onto a_{1g} and e_g^π components[3] and then used the Hilbert-transform to compute the local Green's function. This approach is mathematically correct only in the case of degenerate bands, a prerequisite clearly not verified in the case of V_2O_3. Indeed, as detailed below, in this approximation inter-orbital effects such as the correlation enhancement of crystal field splittings are completely neglected.

Yet, the calculations captured the correlated metal state, with the formation of an upper and lower Hubbard band, as seen in photoemission and x-ray absorption. However the quasi-particle peak appears much too narrow with respect to experiment. As we will argue below, this is possibly due to the fact that within DOS-type calculations a too large value of the Coulomb interaction (U=5.0 eV) is needed to reproduce the overall shape of the spectrum. Using the same approach, though with an increased value of the Coulomb interaction (U=5.5 eV), the insulating character of the PI phase was captured. It is argued, that the gap is opened by a divergence of the effective mass of the e_g^π electrons, while the a_{1g} Z-factor remains finite, and a_{1g} spectral weight is shifted away, or gapped-out, from

---

[3]Within the LMTO formalism [Andersen(1975)] this means: Projection on partial waves, with truncation outside the vanadium atomic sphere.

the Fermi level by the real-part of the self-energy.

Performing Hamiltonian-based calculations, using t_{2g} Wannier functions, [Anisimov *et al.* (2005)] improved their previous work [Held *et al.* (2001), Keller *et al.* (2004)] but contented themselves to show comparisons with photoemission and x-ray experiments, without analyzing their results in depth.

[Laad *et al.* (2003), Laad *et al.* (2006b)], using a multi-band generalization of the iterative perturbation theory (IPT) for solving the DMFT equations, and also the DOS approximation, even found an "orbital selectivity" in the metallic phase : In their calculation the metallic character stemmed only from the a_{1g} orbitals, while the e_g^π ones were already insulating. Further they found important differences in the orbital occupations in the two phases, with a transfer into the e_g^π in the insulating phase.

B   LDA+DMFT results and discussion

B.a   Technicalities

Poteryaev *et al.* performed LDA+DMFT calculation using in the DMFT self-consistency an *NMTO* t_{2g} Hamiltonian, where all other orbitals have been downfolded [Poteryaev *et al.* (2007),Saha-Dasgupta *et al.* (2007)]. As interaction parameters were used U=4.2 eV and J=0.7 eV.

As can be seen in the $(V_{1-x}M_x)_2O_3$ phase-diagram, pure V$_2$O$_3$ at zero pressure is metallic down to ∼150 K, the Néel temperature, below which antiferromagnetic order sets in. Due to the considerable cost of the quantum Monte Carlo (QMC), the calculations were performed at a rather elevated temperature of T=390 K. We note that this is however lower in temperature than the critical end-point of the pressure induced metal-insulator transition.

B.a.i   Full Hamiltonian vs. density of states calculation

As mentioned above, most of the previous LDA+DMFT calculations for V$_2$O$_3$ employed a density of states approach, whereas we [Poteryaev *et al.* (2007)] used the correct full Hamiltonian implementation. In the following we shall rationalize what are the particular short-comings of the DOS approach, which from here on we shall refer to as the "fixed hybridization approximation" as will become clear below. To this end, we compare both approaches within a simple two-band model. We assume that the symmetries are such that the local Green's function, $G(\omega) = \sum_{\mathbf{k}} G(\mathbf{k}, \omega)$, is a purely diagonal in orbital space, which leads to a diagonal self-energy $\mathbf{\Sigma}$. Further, for the sake of simplicity, we shall assume the self-energy to be independent of frequency, taking e.g. only $\mathbf{\Sigma}(0)$ into account. The argument is of course more general but staying within a Hamiltonian form allows for a discussion in terms of an eigenvalue problem, where the effects are is more readily explained. The momentum-resolved Green's function within DMFT then reads

$$
\begin{aligned}
G(\mathbf{k}, \omega) &= [\omega + \mu - \mathbf{H}(\mathbf{k}) - \mathbf{\Sigma}]^{-1} \\
&= \left[\omega + \mu - \begin{pmatrix} \epsilon_{\mathbf{k}}^1 & V_{\mathbf{k}}^* \\ V_{\mathbf{k}} & \epsilon_{\mathbf{k}}^2 \end{pmatrix} - \begin{pmatrix} \Sigma_1 & 0 \\ 0 & \Sigma_2 \end{pmatrix} \right]^{-1} \\
&= \frac{1}{(\omega + \mu - \epsilon_{\mathbf{k}}^1 - \Sigma_1)(\omega + \mu - \epsilon_{\mathbf{k}}^2 - \Sigma_2) - |V_{\mathbf{k}}|^2} \begin{pmatrix} \omega + \mu - \epsilon_{\mathbf{k}}^2 - \Sigma_2 & V_{\mathbf{k}} \\ V_{\mathbf{k}}^* & \omega + \mu - \epsilon_{\mathbf{k}}^1 - \Sigma_1 \end{pmatrix}
\end{aligned}
\tag{6.1}
$$

Clearly, the self-energy enters not only in the diagonal part of the Green's function, but, via the denominator, also affects the off-diagonal elements. Naturally this has important consequences for the poles of the Green's function, i.e. in this case for the eigenvalues of $\mathbf{H}(\mathbf{k}) + \mathbf{\Sigma}$ and the corresponding eigenvectors, that determine the orbital character. During the DMFT convergence process these will adjust according to the self-consistency, in particular they may change considerably with respect to the free problem. The fixed hybridization approximation consists in replacing the Hamiltonian matrix by its diago-

nalized version while keeping the self-energy in the form above, i.e.

$$G(\mathbf{k},\omega) \;=\; \left[\omega + \mu - \begin{pmatrix} E_{\mathbf{k}}^{(+)} & 0 \\ 0 & E_{\mathbf{k}}^{(-)} \end{pmatrix} - \begin{pmatrix} \Sigma_+ & 0 \\ 0 & \Sigma_- \end{pmatrix}\right]^{-1} \tag{6.2}$$

where

$$E_{\mathbf{k}}^{(\pm)} = \frac{1}{2}\left(\epsilon_{\mathbf{k}}^1 + \epsilon_{\mathbf{k}}^2\right) \pm \frac{1}{2}\sqrt{\left(\epsilon_{\mathbf{k}}^1 - \epsilon_{\mathbf{k}}^2\right)^2 + 4|V_{\mathbf{k}}|^2} \tag{6.3}$$

are the eigenvalues of the free (or LDA) Hamiltonian. Technically, this form is easier to handle because in the inversion the orbital components decouple and thus the $\mathbf{k}$-sum can be replaced by an integral over the partial densities of states of the Hamiltonian. Then however, the eigenvectors do not evolve via the self-consistency and the orbital character is not influenced by the correlation effects but is fixed once and for all. In fact, assuming the two bands split by a crystal-field Δ but otherwise degenerate (i.e. $\epsilon_{\mathbf{k}}^1 = \epsilon_{\mathbf{k}}^2 + \Delta$), the eigenvectors of the full matrix problem, Equation (6.1), are

$$\sin(\theta_{1,2})\,|\begin{pmatrix}1\\0\end{pmatrix}\rangle \;+\; \cos(\theta_{1,2})\,|\begin{pmatrix}0\\1\end{pmatrix}\rangle \tag{6.4}$$

with

$$\tan(\theta_{1,2}) = \frac{\Delta_{eff}}{2V_{\mathbf{k}}} \pm \sqrt{\left(\frac{\Delta_{eff}}{2V_{\mathbf{k}}}\right)^2 + 1} \tag{6.5}$$

They depend on the self-energy via the re-normalized crystal-field splitting $\Delta_{eff} = \Delta + \Sigma_1 - \Sigma_2$. The orbital character is controlled by $\Delta_{eff}/V_{\mathbf{k}}$, the ratio of the *re-normalized* crystal-field splitting and the hybridization. In the fixed hybridization approximation, the re-normalized crystal field splitting Δ_{eff} in the above decomposition of the eigenvectors onto the basis of the non-interacting non-hybridized single-particle states $|\begin{pmatrix}1\\0\end{pmatrix}\rangle$, $|\begin{pmatrix}0\\1\end{pmatrix}\rangle$ is replaced by the *bare* crystal field splitting Δ. Hence, an adjustment away from the starting point cannot take place.

In practice, it often looks as if the error induced by using the fixed hybridization approximation could be partially compensated by a slightly bigger choice of the Coulomb interaction parameter U, see e.g. [Mo *et al.* (2003)] in comparison with [Pavarini *et al.* (2004), Pavarini *et al.* (2005)] or the discussion in [Anisimov *et al.* (2005)]. However, in case of strong correlation induced shifts in the orbital occupation and positions, the effect of the hybridization approximation is particularly severe: as will be discussed below, one of the key effects of the correlations in V$_2$O$_3$ indeed is the suppression of hybridization of the a_{1g} and e_g^π bands by the correlation enhanced crystal field splitting, analogue to the current model case. Thus it is not surprising that within the fixed hybridization approximation, that neglects any correlation-driven changes in the hybridization, one arrives at quite different results, which, as a matter of fact, mask the genuine physics at work in the current compound of interest.

B.b   The paramagnetic metal (PM) phase

B.b.i   Comparison with photoemission

Figure 6.6 shows the LDA+DMFT spectral function, and Figure 6.7 displays a comparison of recent photoemission experiments [Mo *et al.* (2006)], and our theoretical result, i.e. the spectral function multiplied with the Fermi function at the experimental temperature (T=175 K) and broadened with the experimental resolution (90 meV). Despite the difference in temperature, the overall agreement is excellent. Both, the width of the quasi-particle peak, and the position and size of the lower Hubbard band are satisfactory reproduced. This is to be contrasted with the above cited earlier LDA+DMFT results [Held *et al.* (2001), Keller *et al.* (2004)] that in order to correctly describe the lower Hubbard band, had to use a higher value for the Coulomb interaction ($U = 5.0$ eV), which resulted in a quasi-particle peak twice as narrow as the experimental data.
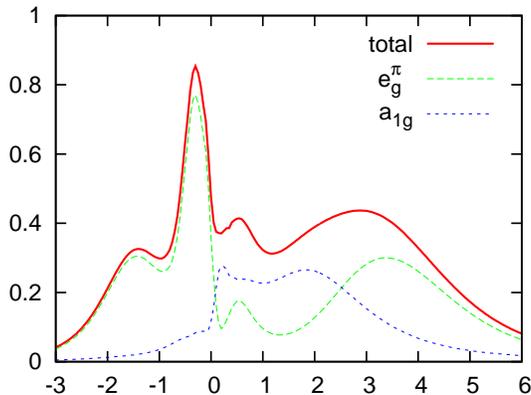

Figure 6.6 : *Indicated are the total and the orbitally resolved LDA+DMFT spectral function at $T = 390$ K for $U = 4.2$ eV, and $J = 0.7$ eV.*

Compared with the calculations of [Laad *et al.* (2003), Laad *et al.* (2006b)] we find the quasi-particle peak of mixed a_{1g} and e_g^π character, which is more compatible with the results from polarization dependent x-ray experiments [Park *et al.* (2000)], which find a $e_g^\pi : a_{1g}$ ratio of $3 : 1$.

B.b.ii   The real-frequency self-energies

However interesting it is, the local spectral function shown above does not allow for a detailed analysis of the implications of the strong Coulomb correlations present in V_2O_3. In order to see more thoroughly how and to what extent the interactions modify the (LDA) band-picture, we shall compute the DMFT self-energy on the real-frequency axis. As described in Chapter 3, we thus analytically continue the local Green's function in orbital space to the real axis and extract from it the self-energy by a root-finding algorithm. This brings us not only into the position to calculate momentum-resolved spectral functions for comparison with future ARPES measurements (see below), and the calculation of the optical conductivity according to Chapter 4, but, on a yet more basic level, it allows us to
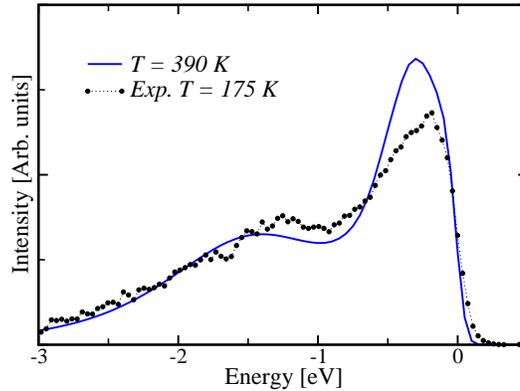
Figure 6.7 : *Photoemission spectrum [Mo et al. (2006)] of pure V_2O_3 at T=175 K (dots). The theoretical spectral function (solid line) is for T=390 K, but convoluted with the Fermi function at the experimental temperature and broadened with a Gaussian mimicking the experimental resolution of 90 meV. From [Poteryaev et al. (2007)].*

understand in greater detail the impacts on the excitation spectrum and the disentangling of the mechanisms at work.

Figure 6.8 shows the result of our analytical continuation procedure. Before discussing the real-frequency self-energy in detail, we assess in Figure 6.9 the quality of the continuation process by showing a comparison between the Matsubara self-energy as obtained from the QMC with the Hilbert transform of the continued self-energy. We see that at low energy, the agreement between the original and the processed data is excellent. Only at higher energies slight discrepancies are discernible. Our procedure thus yields satisfactory results, and the real-frequency self-energy is reliable.

Effects of the imaginary parts of the self-energy: orbital selective coherence. First, we shall examine the imaginary parts of the individual orbital components, which encode the correlation induced lifetime effects and thus the coherence of the spectrum, as discussed for the example of the half-filled one-band Hubbard model in Section C, Chapter 2.

Figure 6.8 b shows the imaginary parts of the LDA+DMFT real-frequency self-energy for the a_{1g} and e_g^π orbitals. As far as the a_{1g} orbitals are concerned, one observes a dip in the imaginary part of the self-energy at the Fermi level, leading to a small value of $\Im\Sigma_{a_{1g}}(0)$ in accordance with the low frequency expansion Equation (2.24), telling us that the a_{1g} electrons are in (or least very close to) their Fermi-liquid regime.

For the e_g^π orbitals, on the contrary, one finds $\Im\Sigma_{e_g^\pi} \approx -0.45$ eV – a considerably large value – indicating that at T=390 K the e_g^π orbitals are still well above their coherence regime. This can also be inferred from the temperature dependence of the Matsubara self-energy (not shown, for details see [Poteryaev *et al.* (2007)]). Indeed the zero frequency limit of $\Im(\imath\omega_n)$ of the a_{1g} orbitals decreases drastically between the two temperatures 1160 K and 580 K, and stays rather unchanged upon a further lowering of temperature, indicating that the coherence temperature of the a_{1g} orbitals lies between the two tem-
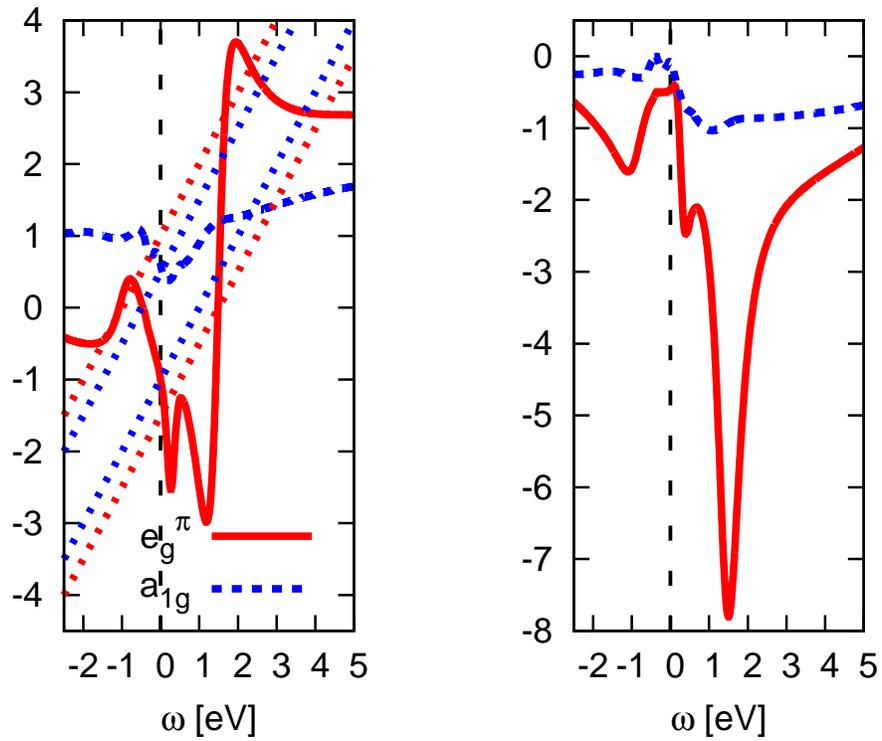
Figure 6.8 : *LDA+DMFT self-energy* $(\Sigma - \mu)$ *of* V_2O_3 *on the real frequency axis: (a) real parts (b) imaginary parts. In the left panel are moreover indicated the bandwidth of the un-hybridized LDA bands, that is used for the graphical construction, see text for a discussion.*
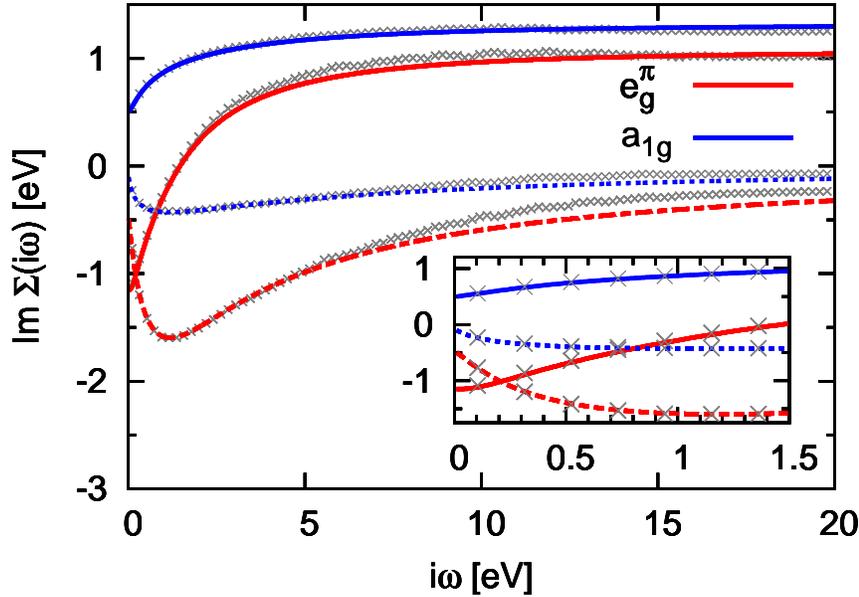
Figure 6.9 : *Assessment of the quality of the analytical continuation. Shown are the original QMC self-energy on the Matsubara axis (crosses) in comparison with the self-energy obtained from a Hilbert transform of the real-frequency self-energy of Figure 6.8. Solid lines indicate real-parts, dashed lines corresponding imaginary parts. The inset shows the low energy region.*

peratures first mentioned. The e_g^π component, on the other hand, displays changes down to the lowest temperature at which calculations were performed.

With this orbital selective coherence we will venture to explain the temperature dependence seen in recent measurements of the optical conductivity, see Section B.

At higher energies the imaginary parts grow, and, especially for the e_g^π, display large features that will, like in the one-band model, see Section C, Chapter 2, suppress spectral weight in between the remainders of the former one-particle bands and the upper and lower Hubbard band.

Effects of the real parts of the self-energy in the band-picture.   From a band-picture perspective, the real-parts of the self-energy are the more interesting quantities. While the imaginary parts tell us about the coherence of excitations, the real-parts describe the shifting of one-particle poles with respect to the non-interacting or LDA case and the possible formation of correlation satellites.

Before resorting to numerically solving the quasi-particle Equation (3.9) for the case in point, we shall, on a more basic, yet insight-full level, examine the real-parts of the self-energy as displayed in Figure 6.8.

Clearly, both the frequency dependence and the magnitudes of the self-energy are very different for the a_{1g} and e_g^π components. In particular, the zero-frequency values differ considerably, they even have the opposite sign, $\Re\Sigma_{a_{1g}}(0) - \mu > 0$, $\Re\Sigma_{e_g^\pi}(0) - \mu < 0$, which

results in an upward (downward) shift of a_{1g} (e_g^π) spectral weight at the Fermi level. In other words, the correlations effectively enhance the crystal-field splitting:

$$\Delta_{\text{eff}} = \Delta_{\text{bare}} + \Re\Sigma_{a_{1g}}(0) - \Re\Sigma_{e_g^\pi}(0) \quad , \tag{6.6}$$

where Δ_{bare} is the crystal-field splitting of the bands that result from the LDA Hamiltonian when (artificially) setting to zero the a_{1g}–e_g^π hybridizations. The reason for working with these "un-hybridized" bands is the same as was discussed for the graphical construction, Section A, Chapter 3, which we will also apply to the current case, below. With $\Delta_{\text{bare}} \approx 0.27$ eV, we find $\Delta_{\text{eff}} \approx 1.9$ eV, i.e. an enhancement by almost an order of magnitude. In return, this consequently leads to a charge-transfer into the e_g^π orbitals, thus increasing the overall orbital polarization. As a result of the low occupancy of the a_{1g} orbital, the corresponding self-energy does not vary enormously with frequency and it is much lower in absolute magnitude than its e_g^π counterpart.

Despite the appealing picture of shifting the former LDA bands according to the "new" crystal-field splitting, we emphasize that due to both, the frequency dependence of the self-energy and the momentum dependent hybridization between a_{1g} and e_g^π orbitals, the effects on the band-structure and the Fermi surface are highly non-uniform.

As a next step, we shall incorporate the renormalization effects of the real-parts of the self-energy up to linear order in frequency, as described in Section C, Chapter 2 (Equation (2.25)), a development formally only valid in the Fermi-liquid regime.

As stressed above, the e_g^π orbitals are beyond their coherence regime, and thus, the interpretation of $Z = (1 - \partial_\omega \Re\Sigma(\omega)\mid_{\omega=0})^{-1}$ as quasi-particle weight is not admissible. Formally, we find $1/Z_{e_g^\pi} \approx 5$. The a_{1g} orbitals, that are much more coherent, are subject to a sizable mass enhancement $1/Z_{a_{1g}} \approx 2.5$, in other words 60% of a_{1g} spectral weight is transferred to incoherent satellite features.

Using these values, we can compute the corresponding renormalized quasi-particle band-structure that emerges if one takes into account only this low energy-behaviour of the self-energy. This procedure was explain in Section A, Chapter 3. The resulting quasi-particle band-structure will not capture the incoherent features containing the missing weight, but it will give an accurate picture of what happens at the Fermi energy, which still is interesting inasmuch as it reveals how much more correlations, bandwidth-narrowing or crystal-field splitting are needed to drive the system insulating. The left panel of Figure 6.10 shows the result. Compared to the LDA band-structure (Figure 6.4), the energies are renormalized towards the Fermi energy, as expected.

Due to the crystal field enhancement, mentioned above, and also the different renormalizations by the Z-factors, the a_{1g} and e_g^π bands get reshuffled and almost move apart at the Fermi level. We stress again, that these "bands" carry the reduced weight $Z < 1$, which is why having more than four "bands" below the Fermi level is not in contradiction with the particle occupation. It simply shows that the band-picture, resulting from an effective one-particle Hamiltonian, is too artificial a notion to account for the richness of the true system. Concomitant with the enhancement of the crystal-field splitting, the a_{1g}–e_g^π hybridizations are expected to decrease, as was discussed in Section B. Since the orbital character of the bands is controlled by the ratio $V_{\mathbf{k}}/\Delta_{\text{eff}}$, see Section B, one expects a
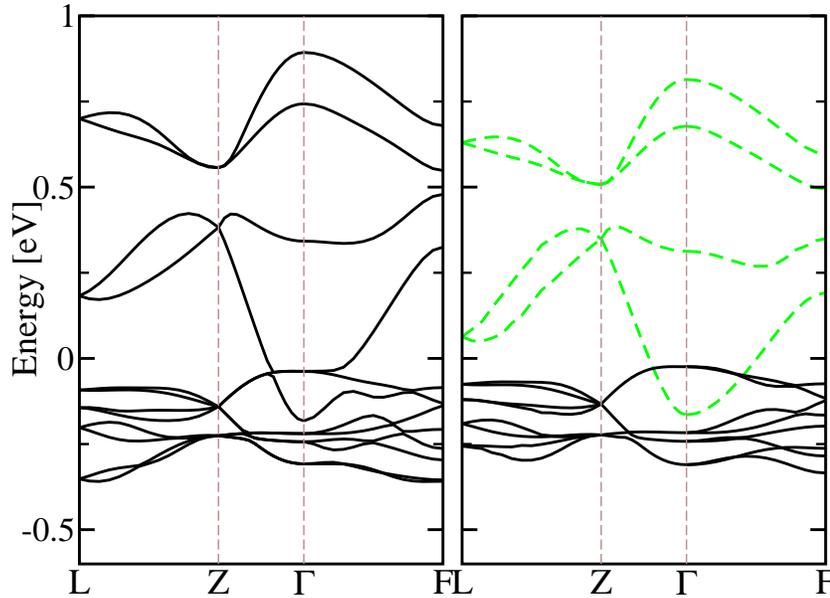
Figure 6.10 : *LDA+DMFT quasi-particle bands obtained by truncating the self-energies after linear order in ω. The left-hand panel gives the eigenvalues of the re-normalized Hamiltonian, Equation (3.11), and the right-hand side gives the un-hybridized e_g^π (black) and a_{1g} (dashed green) band structure, scaled individually according to the scalar expression, Equation (6.7). The self-energy parameters are $Z_{a_{1g}} = 1/2.5$, $Z_{e_g^\pi} = 1/5.0$, $\Sigma_{a_{1g}}(0) = 0.59$ eV, and $\Sigma_{e_g^\pi}(0) = -1.01$ eV, for U=4.2 eV, J=0.7 eV and T ∼390 K. See text for a discussion. From [Poteryaev et al. (2007)].*

decreasing importance of the former LDA hybridization $V_\mathbf{k}$. This is clearly demonstrated in the right panel of Figure 6.10, where are shown the quantities

$$Z_m \left[\epsilon_{mj}(\mathbf{k}) - \mu + \Re\Sigma_m(0)\right] \sim \omega_{mj}(\mathbf{k}), \tag{6.7}$$

where $\epsilon_{mj}(\mathbf{k})$ are the eigenvalues of the LDA Hamiltonian when the a_{1g}–e_g^π hybridizations are set to zero, and Z_m, as above, is the renormalization factor obtained from the self-energy up to linear order. The close resemblance to the renormalized bands (left panel) is quite remarkable and proves the statement that the hybridizations of the starting point are made less relevant, once the correlations are in place.

The above procedure being based on a low-frequency expansion, while shedding light on the situation at the Fermi level and hence indicating how the insulating gap is finally opened at the transition, it will not give a reasonable description at high or even intermediate energies, where the real-parts of the self-energy are far from linear and the imaginary parts considerable. If we still neglect the latter, excitations are given by the poles of the Greeen's function with $\Im\Sigma = 0$, as described in Section A, Chapter 3.

Before solving numerically the quasi-particle Equation (3.9), we shall appeal to the graphical construction mentioned in section A.b.iii, even if this is of course an oversimplified approach in the current case of a non-degenerate multi-orbital calculation, Even though, as we have seen, the correlations effectively renormalize downwards the hybridizations.

In Figure 6.8 b we have thus indicated the position and the width of the un-hybridized LDA dispersion[4], individually for the a_{1g} and the e_g^π components by the stripes of slope one in frequency. Solutions are expected over a wide range of frequency, extending roughly from -2 eV to 4 eV. However, only in regions where the imaginary parts of the self-energies are small, these will give rise to coherent quasi-particles, which is basically true within ± 0.5 eV around the Fermi level, at least for the a_{1g} orbital. The e_g^π solutions at around 1.5 eV will not appear as spectral weight in the spectral function since the corresponding imaginary part is most prominent in this frequency range. The intersections between 2.5 and 4 eV correspond to the upper Hubbard band, as seen in the local spectral function above, Figure 6.6. The lower Hubbard band, see Figure 6.6, Figure 6.7, on the contrary is not due to poles in the one-particle Green's function, as will be confirmed below by numerically solving the full quasi-particle equation. It manifests itself in the self-energy rather by a low magnitude of the imaginary-part and an *almost* pole-like behaviour in the Green's function.

B.b.iii   Momentum-resolved spectra and quasi-particle poles

Figure 6.11 shows the colour-coded momentum resolved spectral function $A(\mathbf{k}, \omega) = -\frac{1}{\pi} \text{tr}\Im G(\mathbf{k}, \omega)$ of V$_2$O$_3$ for our usual parameters. The first observation is that, as expected from the self-energy considerations above, only within a quite narrow region around the Fermi level, sharp features appear and the spectral intensity is otherwise rather broadly distributed. The dots indicate the solutions $\omega_\mathbf{k}$ of the quasi-particle Equation (3.9). To further analyze the spectrum, it is useful to combine information from

---

[4]See Section A, Chapter 3
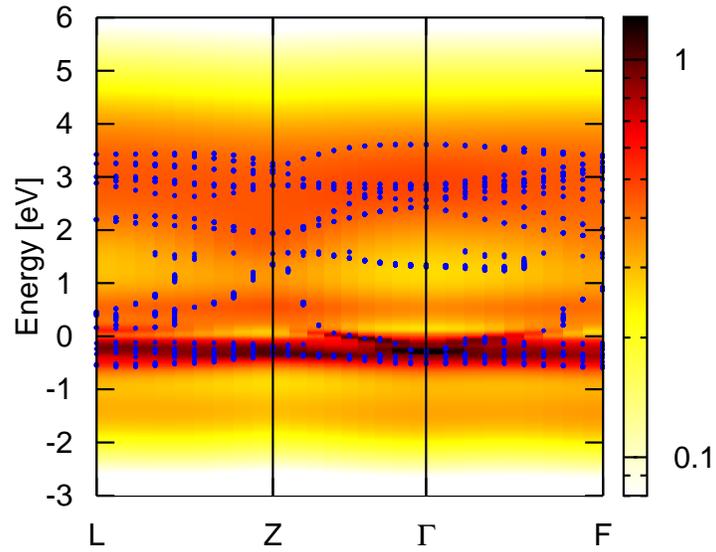
Figure 6.11 : *Momentum resolved spectral function $A(\boldsymbol{k},\omega)$ of V_2O_3 along various symmetry lines. The Fermi level corresponds to zero frequency. The (blue) dots indicate the quasi-particle solutions of Equation (3.9).*

the different figures, Figure 6.6, Figure 6.8, Figure 6.11, in order to attribute the spectral intensities to originating from a specific orbital character and whether the appearing poles represent shifted LDA bands or stem from Hubbard satellites. In the occupied part of the spectrum the poles follow closely the Z-renormalized bands from above, Figure 6.10, which is not very surprising, since the real parts of the self-energy are linear within the stripe in the Figure 6.8. In the unoccupied part, however, this is not true for the a_{1g} component. Apart from the sharp a_{1g} band that is crossing the Fermi-level near the Γ-point, the dots deviate considerably from the linearized band-structure. In particular the upper a_{1g} bands at around 1 eV in the LDA, Figure 6.4, are pushed up to around 2 eV, as inferred from the self-energy, an effect clearly lost in the linearization procedure. At intermediate energies, around 1.5 eV poles do appear, e.g. around the Γ-point, also seen in the graphical construction, however, as anticipated, the spectral weight is efficiently damped away by the large structure in the corresponding imaginary part. Beyond 2 eV the poles mirror the former e_g^π bands as poles of the upper Hubbard band, as we have already seen to be the case for rutile VO$_2$. The fact that the dispersion of the poles reflect the band-dispersions can be seen e.g. in the atomic limit and related approximations [Hubbard(1963)].

Thus, in total, the LDA+DMFT excitation spectrum evolves from the LDA band-structure by the following effects :

- a considerable enhancement of the a_{1g}– e_g^π crystal-field splitting, combined with a decrease of hybridizations leading to a depletion of spectral weight at the Fermi level and a charge transfer into the e_g^π orbitals,

- a bandwidth-narrowing à la Brinkman-Rice [Brinkman and Rice(1970)], particularly noticeable in the occupied part of the spectrum,

- a considerable transfer of spectral weight into the upper Hubbard bands beyond 2 eV, that mirror the dispersion of their renormalized bands.

As a matter of consequence, the Fermi surface is strongly modified with respect to the LDA. As seen in the local spectral function, Figure 6.6, the Fermi level already resides in a sort of pseudo gap and only minor changes in e.g. the crystal-structure may drive the system insulating.

B.b.iv   The optical conductivity of V$_2$O$_3$

In this paragraph we shall present theoretical results on the optical conductivity of the metallic phase of V$_2$O$_3$ in comparison with recent experimental results [Qazilbash(2007)]. In particular, we shall endeavour to identify the appearing spectral weight by referring to the underlying LDA+DMFT electronic structure calculation that has been presented before.
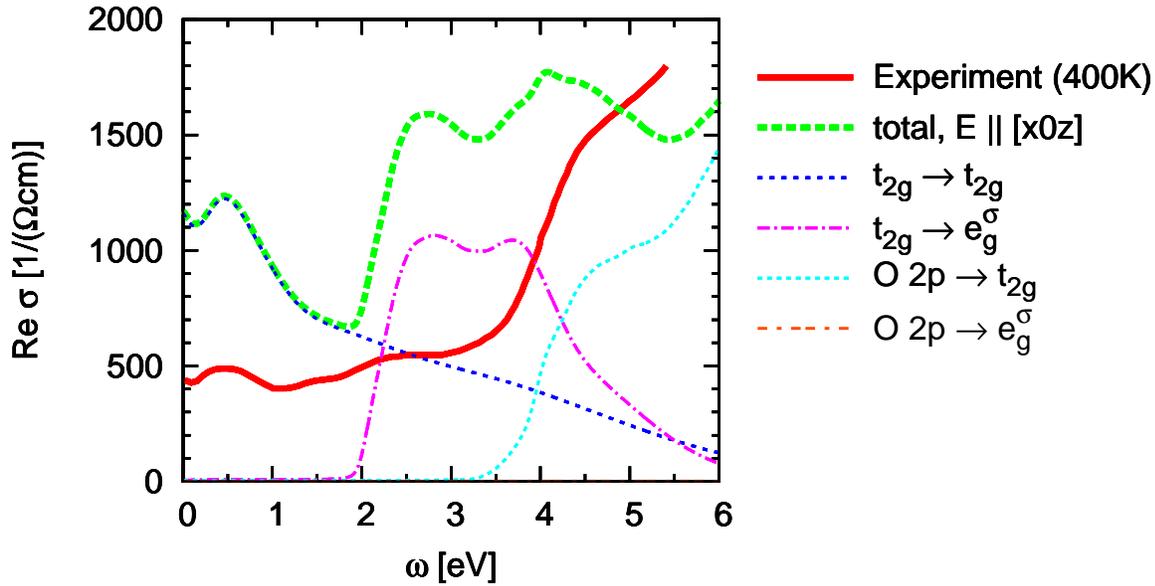

Figure 6.12 : *Optical conductivity for metallic V$_2$O$_3$. Shown is a comparison between our theoretical curve for [x0z]=[0.133 0 0.041] polarization with experimental results for T = 400 K on polycrystalline films [Qazilbash(2007)].*

Figure 6.12 shows our theoretical results, that were computed along the full-orbital scheme that we introduced in Section D, Chapter 4. The individual orbital contributions are indicated in the legend. The experimental data [Qazilbash(2007)] were obtained from a polycrystalline sample at 400 K[5].

Above, in Section B, we remarked on the orbital selective coherence, i.e. the different coherence temperatures of the a_{1g} and e_g^π quasi-particles. We found that while the a_{1g} orbitals are reasonably, yet not fully, coherent at the temperature of the calculation, the e_g^π ones are actually far above their coherence. The fact that the a_{1g} excitations are in the vicinity of their coherence regime makes them quite sensitive to changes in temperature. This is why spectral weight transfers as a function of temperature are mainly to be expected for transitions that involve a_{1g} orbitals.

Together with the local, Figure 6.6, and momentum-resolved spectral function, Figure 6.11, we shall try to identify the origin of spectral weight from the viewpoint of the

---

[5]As a matter of fact, a careful study as a function of temperature was performed. We state that only the "Drude" peak and the first feature at ~ 0.5 eV shows an appreciable temperature dependence. We thank M. M. Qazilbash for making his data available prior to publication.

LDA+DMFT results. Helpful in this vein will be Figure 6.13 in which we plot contributions to the optical conductivity at two different points in the Brillouin zone.

However, two remarks are to be made before doing so. First of all, we note that the experiment used polycrystalline samples, i.e. the optical response will be a complicated average over all possible light polarizations. Our calculations were performed for *one* polarization only. One has to keep in mind that the optical response in V$_2$O$_3$ might depend strongly on the polarization.

Furthermore, as we will see, the overall intensity of the optical conductivity is overestimated with respect to experiment. In fact, this problem is purely technical, and related to our simple **k**-summation, which does not use the tetrahedron method. As a result, a large number **k** points is needed in order to yield converged results. Our implementation, therewith, has problems with the correct accounting for transitions that involve spectral weight in the vicinity of the Fermi level, which is why it is much better suited for insulating systems than for metals. Improvement in this respect is possible but numerically expensive. Still, though the weights of the transitions will change, we expect no shiftings in energy of the appearing peaks, i.e. the physical analysis that follows should remain correct.

- The metallic response at low energy is due to the a_{1g} band that crossed the Fermi level, as can be seen in the momentum resolved spectral function, Figure 6.11, where the crossings are between the Z and the Γ, and between the Γ and the F-point. Indeed this could be further corroborated by calculating the conductivity for a momentum where a crossing occurs (not shown). The temperature dependence of this feature in the experimental data (not shown, [Qazilbash(2007)] unpublished) can be understood from the above considerations, namely that the metallic behaviour increases upon cooling, since the a_{1g} excitations evolve towards their quasi-particle regime.

- The contributions to the hump at roughly 0.5 eV in the optical conductivity is twofold : At lower energies the occurring spectral weight is mainly due to transitions from the a_{1g} into low lying e_g^π orbitals, that are restricted to a small region in the Brillouin zone, whereas at slightly higher energies, 0.6 eV and above, contributions are in majority deriving from e_g^π to e_g^π transitions, which are possible in a wide region of the Brillouin zone, yet should be largely suppressed at the Γ-point. This is clearly confirmed from the momentum-resolved spectral function, Figure 6.11, in conjunction with the momentum selective conductivity of Figure 6.13. The temperature dependence is thus expected to be more pronounced in the lower energy part of the peak, which is actually evidenced by the experiment.

- At 1.5 eV the experiment displays a small peak in the conductivity, which gets slightly more pronounced upon lowering the temperature. In the theoretical curve, on the contrary, the conductivity rather decreases. We are led to the speculation that these correspond to transitions from the a_{1g} orbitals into incoherent a_{1g} and e_g^π weight, in particular around the Γ-point. Indeed in the calculation, there appear both a_{1g} and e_g^π poles in the corresponding energy range ~ 1.5 eV, yet the spectral

weight of the latter is largely suppressed by the imaginary part of the self-energy, and also the former is subject to considerable life-time effects, as can be seen in the self-energy, Figure 6.8, as well as in the spectral function, Figure 6.11.

- At around 2 eV transitions into the e_g^σ orbitals set in, and are responsible for two features in the calculation. The first appears at 2.5 eV and may thus be identified with the peak that emerges at the same energy in the experiment. We however stress that in our formalism, the e_g^σ orbitals (as well as the oxygen 2p ones) are frozen with respect to their LDA position and shape. An inclusion of correlation effects is expected to alter, both, their position and sharpness.

- Transitions into the oxygen 2p orbitals set in at about 4 eV in the calculation which is congruent with experiment. Analyzing transition amplitudes is cumbersome. Our technique overestimates transitions involving states at the Fermi level, furthermore the oxygen weight is frozen to its LDA result, and also the way in which we calculate our Fermi velocity is less suited for the oxygens due to their larger spatial extensions.
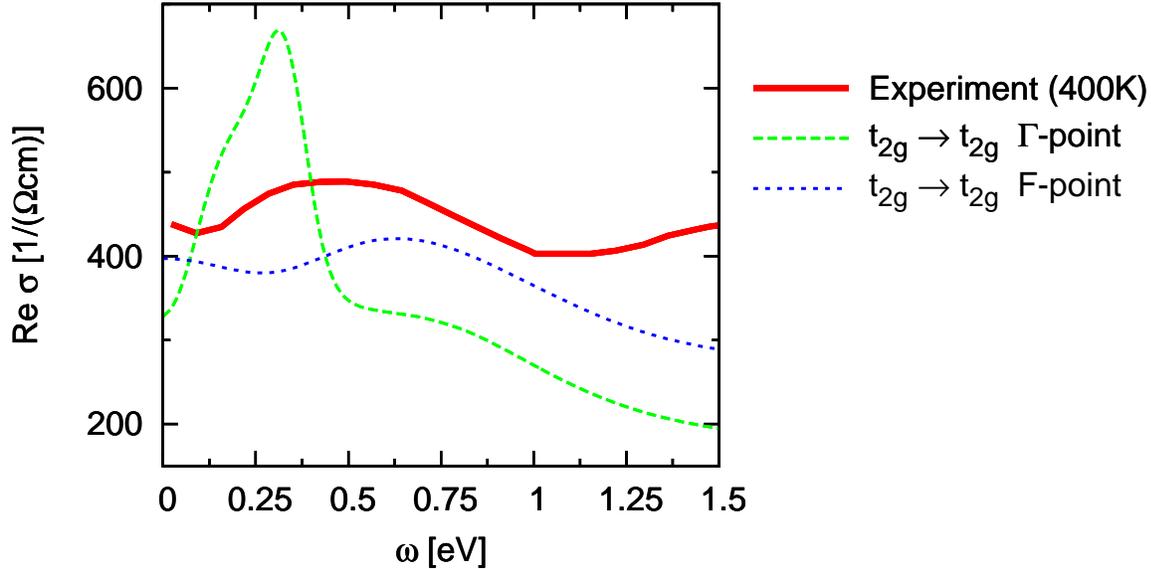

Figure 6.13 : *Optical conductivity for metallic V_2O_3. Shown is a comparison between our theoretical curve for [x0z]=[0.133 0 0.041] polarization with experimental results for $T = 400$ K [Qazilbash(2007)]. In particular shown are two contributions to the total conductivity at different points in the Brillouin zone, as indicated. Note that here the theoretical curves were rescaled such that the total conductivity matches the experimental one at 0.5 eV.*

In conclusion, most of the qualitative features of the experimental optical conductivity were reproduced by our calculation. The temperature dependence and the spectral weight transfer found in the experiment could be rationalized by evoking the orbital selective coherence that we evidenced in our calculation of the electronic excitation spectrum. The

fact that the positions in energy of the identified transitions compare favourably with our theoretical approach, further corroborates the validity of our LDA+DMFT results. The discrepancy in the transition amplitudes is mainly technically derived and improvements are possible and under way.

B.c   The paramagnetic insulating (PI) phase

Figure 6.14 shows the local spectral function of $(V_{0.962}Cr_{0.038})_2O_3$ as obtained from a maximum entropy treatment of the LDA+DMFT local Green's function. The inset shows a comparison with photoemission experiments [Mo *et al.* (2006)]. The agreement is fairly good. Compared to the PM phase, a strong depletion of spectral weight at the Fermi level is seen in the calculation. Still, the weight at zero frequency is finite. We note, that the value for the Coulomb interaction was taken to be the same as for the metallic phase (U=4.2 eV). However, less efficient screening in the insulator might be responsible for a slightly increased value, which would open the gap further. Also, the calculation was performed at a rather elevated temperature (T=580 K) due to the high numerical cost. For this phase a continuous time quantum Monte Carlo algorithm (for details see [Poteryaev *et al.* (2007)]) was used.
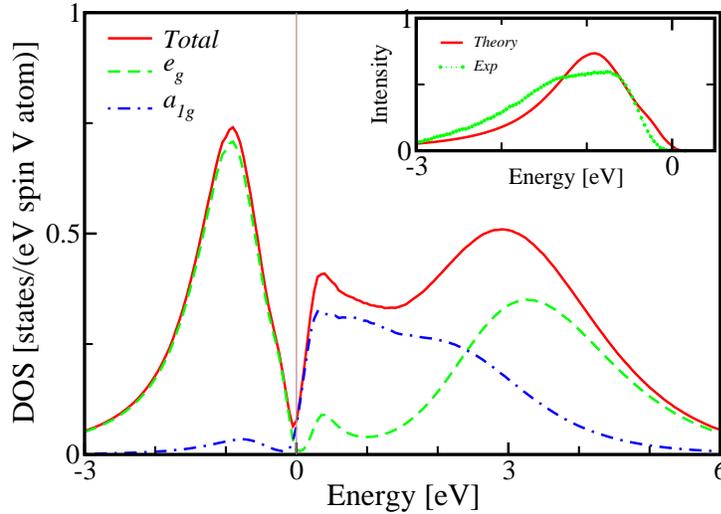
Figure 6.14 : *Spectral function of $(V_{0.962}Cr_{0.038})_2O_3$ at T=580 K. The inset shows a comparison with recent PES experiments [Mo et al. (2006)]. The theoretical curve is obtained by multiplying the spectral function with the Fermi function at the experimental temperature T=175K and a broadening with the experimental resolution of 90 meV. From [Poteryaev et al. (2007)].*

Comparing the self-energy of the Cr-doped compound, Figure 6.15 , with the self-energy of pure V_2O_3, see Figure 6.8, we first notice that the scales are very different. The insulating phase indeed exhibits stronger signs of correlations than the metallic phase. The a_{1g} element, however, which anyway is rather flat, due to the low occupation, does

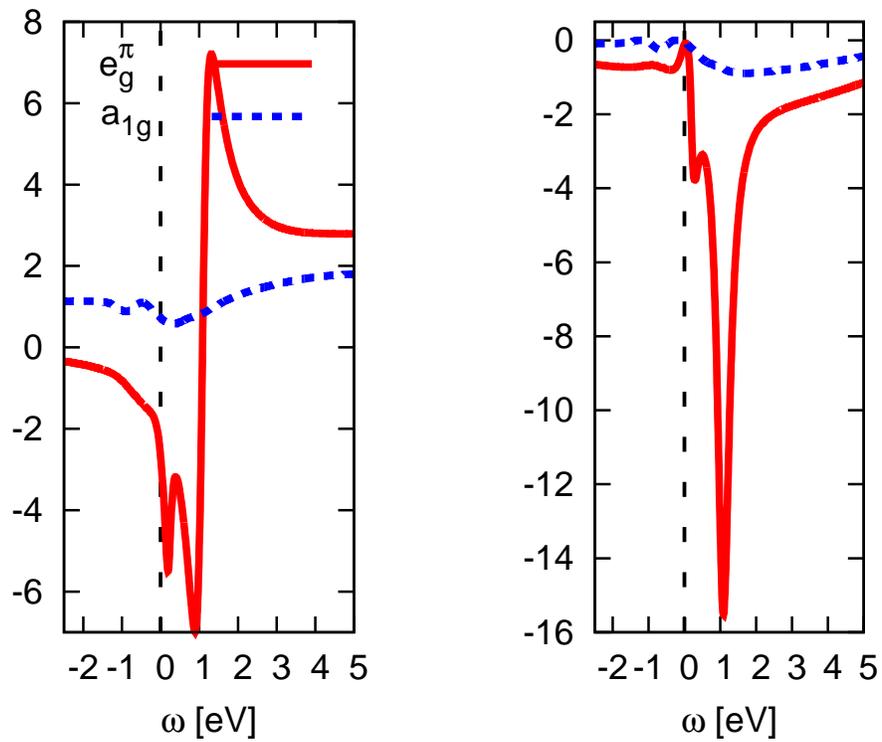**Figure 6.15 :** *LDA+DMFT self-energy $(\Sigma - \mu)$ of $(V_{0.962}Cr_{0.038})_2O_3$ on the real frequency axis: (a) real parts (b) imaginary parts.*

not change tremendously. Still, $\Re\Sigma_{a_{1g}}(0)$ is larger in the insulator, further pushing up the a_{1g} band at the Fermi level. However, the coherence of the a_{1g} bands, especially for the one seen near the Γ-point does slightly increase. The occupied e_g^π, on the contrary, become more incoherent and go further down in energy, thus again, working in favour of an insulating state. In the unoccupied part, the differences in the real parts of the self-energy subside at 2 eV and higher, which will lead to a similar spectrum as for the metal in this energy range.
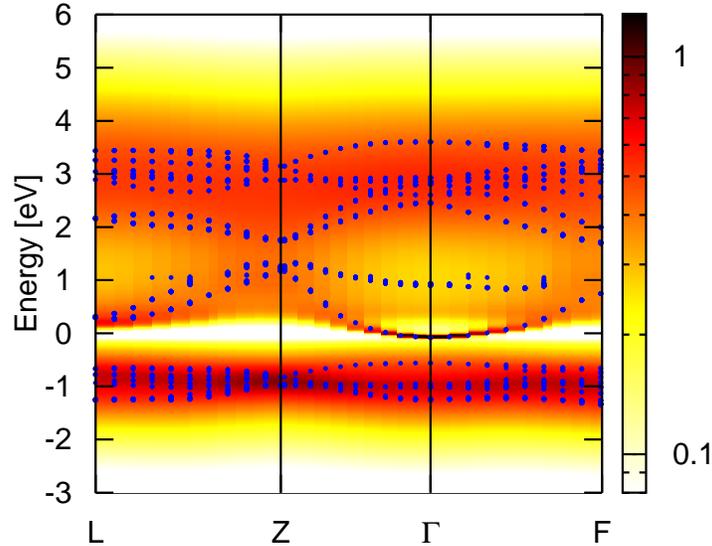

Figure 6.16 : *Momentum resolved spectral function of $(V_{0.962}Cr_{0.038})_2O_3$ along various symmetry lines. The Fermi level corresponds to zero frequency. The (blue) dots indicate the quasi-particle solutions of Equation (3.9).*

Figure 6.16 shows the momentum resolved spectral function, along with the quasi-particle poles as obtained from Equation (3.9). As mentioned above, the spectrum looks like the metallic one for energies of 2 eV or higher. The a_{1g} band around the Γ-point is sharper than in the metallic phase and got shifted up in energy. A close inspection however shows, that it still crosses the Fermi level by about 0.08 eV.

The potential reasons for this discrepancy were given above. Still, the basic mechanism of the metal-insulator transition in the $(V_{1-x}M_x)_2O_3$ series has been identified as the crystal-field enhancement induced by the correlations. Indeed, it seems that in the case of V_2O_3 correlations favour the polarization of orbitals. The opposite trend is found in the d^1 compound BaVS$_3$ [Lechermann *et al.* (2005)].

B.d Conclusions

In conclusion, we have presented a detailed analysis of the excitation spectrum of the paramagnetic metal and paramagnetic insulator phases of $(V_{1-x}M_x)_2O_3$ within LDA+DMFT. The main result is the identification of a correlation induced crystal-field enhancement that is responsible for the insulating behaviour upon Cr-doping[6].

The analytical continuation scheme that was developed in this thesis allowed not only for a refined understanding of the physical phenomena at work, but also allowed for the calculation of momentum-resolved spectral functions, that constitute our prediction for future angle resolved photoemission experiments.

Moreover an orbital selective coherence was evidenced, which led to an understanding of recent temperature-dependent optical measurements. The theoretical optical conductivity was found to exhibit the same qualitative features as the experimental one.

---

[6]For a detailed investigation on the interplay of correlations and crystal-field splittings see subsequent work by Poteryaev *et al.*

Chapter 7

Optical properties of rare-earth sesquioxides

This chapter is devoted to the investigation of optical properties of the early rare-earth sesquioxide series, RE_2O_3, with RE=La, Ce, Pr, Nd, and Pm. This part of the series is iso-structural, their members crystallize in a hexagonal structure with space group $P\bar{3}m1$, as shown in Figure 7.1. In order to avoid impacts of the crystal structure to our reasoning on the electronic structure, we shall limit ourselves in this work to this early sequence of the oxide series. All the mentioned compounds are wide gap (Mott) insulators, and the determination of the gap evolution along the series from the theoretical point of view will be one of our major concerns.

The challenge in the calculation of the electronic structure in these compounds is the presence of a partially filled RE4f shell, that gets consecutively filled with the increasing of the atomic number. Indeed, the rare-earth ions are in their 3+ oxidation state, leading to a nominal f-shell occupation of 0, 1, 2, 3, 4 electrons, for La-, Ce-, Pr-, Nd- and Pm-sesquioxide, respectively.

As we will review below, standard band-structure methods do not capture the insulating behaviour, due to the partial filling of the f-shell. Yet, from the many-body point of view, the situation is simpler than in the case of e.g. the 3d orbitals of transition metal oxides or the 5f shell of actinide systems, in the sense that the correlated orbitals, here the RE4f, do not struggle between itinerant and localized behaviour, but are strongly localized. It is this fact that allows for the application of simplified techniques, namely the Hubbard-I approximation, to treat these large systems within LDA+DMFT.

The present work relies on LDA+DMFT electronic structure calculations of the early rare-earth sesquioxide series that were performed by L. V. Pourovskii (see also prior work [Pourovskii *et al.* (2007a)]). Our contribution to this collaboration is the calculation of optical properties of the compounds in question, in particular their optical conductivity. This work will appear in [Pourovskii *et al.* (2007b)].
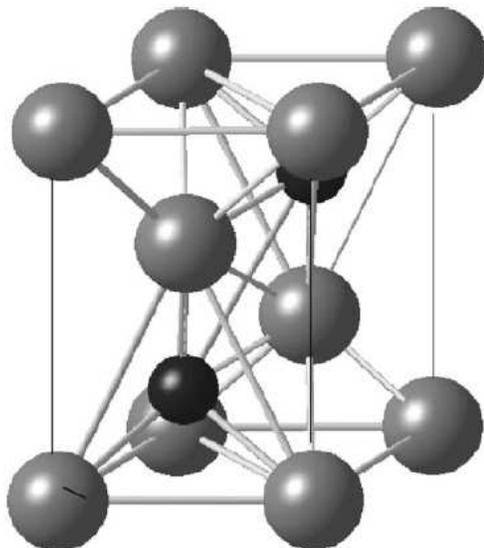
Figure 7.1 : *Hexagonal lattice of RE_2O_3. The atoms are black (RE) and grey (O), respectively. From [Skorodumova et al. (2001)].*

A   Experimental work – a brief review

An interesting question is whether the localized RE4f states have any impact on the physics of the compounds.

In the pure lanthanide series one observes that the Wigner-Seitz radius decreases only slightly, from La to Pm, with the increased filling of the f-orbitals. Contrary to early transition metals or the early actinide series, the additional electrons in the open shell do not contribute to the bonding of the solid, due to the atomic-like nature of their states. Thus, more important than the filling of the f-shell is the increase in the atomic number along the series, leading to the *lanthanide contraction*, namely to a diminution of the atomic/ionic radius.

Therefore, from a purely crystallographic point of view, one would expect a monotonic behaviour of the charge gap along the sesquioxide series, from La_2O_3 to Pm_2O_3, namely a slight increase due to band narrowing. However, experimentally one finds the (optical) gap dependence shown in Figure 7.2 [Golubkov *et al.* (1995)], and also in Figure 7.6. As one can see, when going from the $4f^0$ compound La_2O_3 to Ce_2O_3, which has a nominal $4f^1$ configuration, the optical gap decreases tremendously, and recovers higher values in the continuation of the series.

A similar dependence is found in the sulfide and selenide series, RE_2S_3 and RE_2Se_3. From this the authors [Golubkov *et al.* (1995)] concluded that the f-electrons play a fundamental role in the electronic excitation spectrum. It was thus suggested that in the case of Ce_2O_3, the gap in the excitation spectrum is determined by Ce4f-Ce5d transitions, while for the remainder of the series the lower Ce4f Hubbard band merges with the O2p orbitals, thus resulting in a O2p-RE5d character of the gap [Golubkov *et al.* (1995), Prokofiev *et al.* (1995)]. In other words, it is the shifting of the lower RE4f Hubbard band
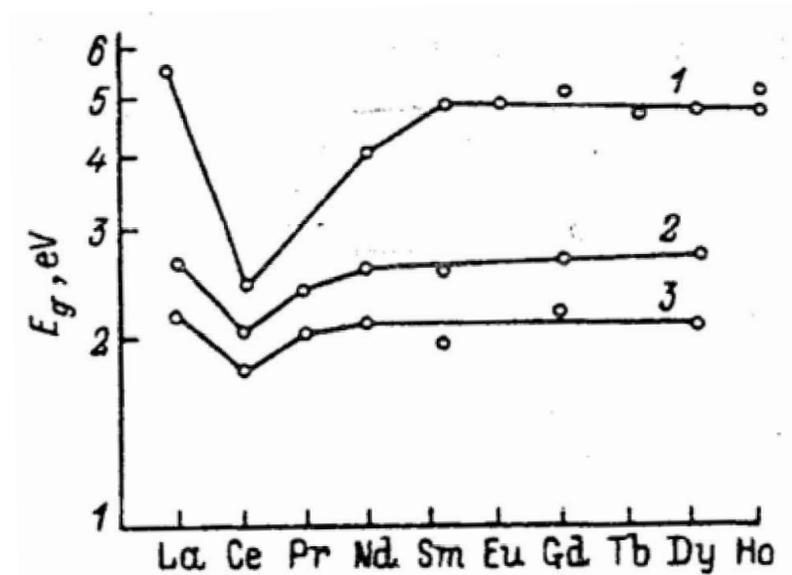
Figure 7.2 : *Optical gaps of (1) the sesquioxide (RE$_2$O$_3$), (2) the sesquisulfide (RE$_2$S$_3$), and (3) the sesquiselenide (RE$_2$Se$_3$) series. From [Golubkov et al. (1995)].*

as a function of its filling which is supposed to be responsible for the interesting changes in the low energy region of the electronic structure.

Evidence for the merging of the 4f lower Hubbard band with the O2p states came from resonant photoemission studies, which for the particular cases of Pr$_2$O$_3$, and Nd$_2$O$_3$ found a large degree of RE4f-O2p mixing [Arai *et al.* (1998)].

The fact, that in the case of Ce$_2$O$_3$ the valence part of the gap is determined by the lower 4f Hubbard band was evidenced in valence band photoemission (XPS) experiments [Mullins *et al.* (1998)]. Figure 7.5 shows their results in comparison with the occupied part of the LDA+DMFT spectral function, whose calculation we will discuss later on. However, the measured sample was obtained by exposing a metallic Ce foil to oxygen. Though indications for a Ce^{3+} oxidation state were found, no structural characterization was done.

The susceptibility of Ce$_2$O$_3$, shown in Figure 7.3, exhibit an antiferromagnetic behaviour $\chi(T) \sim (T + \theta)^{-1}$, with a Weiss constant $\theta = 27.7$ [Pinto *et al.* (1982)]. However, no indications for the magnetic transition are visible down to 9 K. The gap size being of the order of 2.5 eV, the magnetic ordering cannot be the origin of the insulating behaviour. On the contrary, the local moment behaviour above the Néel temperature, is a hallmark of a Mott insulating state.
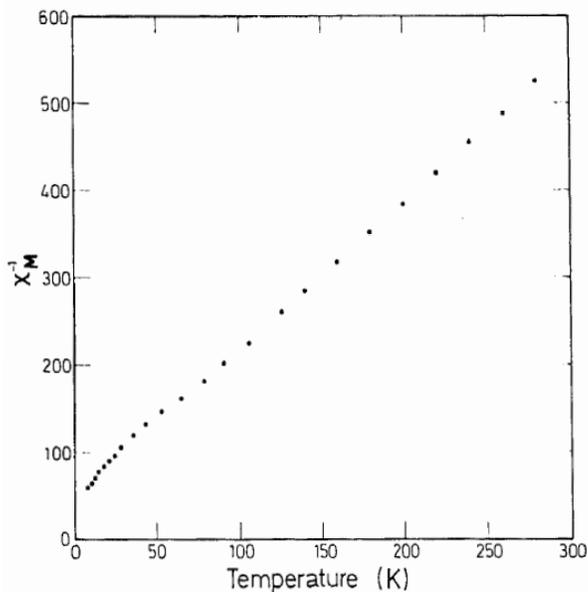
Figure 7.3 : *The inverse susceptibility of Ce$_2$O$_3$. From [Pinto et al. (1982)].*

B Theoretical work – a brief review

On the theoretical side, several computational methods were applied to the compounds of the rare-earth oxide series.

DFT-LDA. Conventional DFT-LDA calculations are not capable of producing the correct insulating behaviour of any of the compounds having 4f electrons [Skorodumova *et al.* (2001), Naoto Hirosaki and Kocer(2003), Mikami and Nakamura(2006), Fabris *et al.* (2005)], which, once more, shows the incapacity of DFT-LDA to deal with Mott insulators. In the same vein, especially in the case of Ce$_2$O$_3$, the unit-cell volume is considerably underestimated [Skorodumova *et al.* (2001)]. This is owing to the fact that the f-electrons, that are necessarily itinerant within DFT-LDA, contribute to the bonding which is unphysical.

As already indicated in experiments, the influence of the f-states on structural properties might, in reality, be not so important. Indeed DFT calculations in which the f electrons are treated as core states, lead to rather satisfactory estimates of the lattice parameter [Skorodumova *et al.* (2001), Naoto Hirosaki and Kocer(2003)].

These evidently insufficient theoretical capabilities of DFT-LDA have triggered the application of more involved electronic structure techniques to the compounds in question.

SIC. Self-interaction-corrected calculations yield good agreement in structural properties, without the need of treating the f-electrons as core states [Petit *et al.* (2005)]. However, the optical gaps are much too large as compared to experiment, and the above mentioned trend along the series is not reproduced.

Hybrid functionals. Ce$_2$O$_3$ was further investigated using hybrid density functionals [Hay *et al.* (2006)]. In this approach, the DFT exchange correlation potential is made to include some Hartree-Fock type exchange. In this spirit it might be said to be somewhat akin to the LDA+U scheme, albeit without an adjustable parameter. In the above work, insulating behaviour was found for an antiferromagnetic ground state of Ce$_2$O$_3$, using the HSE functional. The gap size is in reasonable agreement with experiments. Yet, the other members of the zoology of hybrid functions lead to quite different results [Hay *et al.* (2006)][1,2].

LDA/GGA+U. A very popular technique for insulators is the LDA+U approach. However, due to its Hartree-Fock-like nature, any insulating solution necessitates some kind of ordering. However, as shown experimentally, the rare-earth sesquioxides are paramagnetic at least down to 9 K [Pinto *et al.* (1982)], which is why, as said already above, the antiferromagnetism cannot be at the origin of the charge gap. As a matter of fact, in LDA+U calculations, an antiferromagnetic ground state was found for Ce$_2$O$_3$ [Fabris *et al.* (2005), Loschen *et al.* (2007), Andersson *et al.* (2007)]. Both, structural and electronic properties are in reasonable agreement with experiment, albeit with the caveat that the nature of the insulating state within LDA+U arises from the magnetic ordering. Best results were obtained with an effective Coulomb interaction $U_{eff} = U - J = 6$ eV, with U being the on-site interaction, and J the Hund's rule coupling.

Further, in an LSDA+U setup, [Singh *et al.* (2006)] calculated the band-structure for ferromagnetic RE$_2$O$_3$ (RE=La, Pr, Nd). The trend in the optical gap along the series was not reproduced. However, they also computed the optical conductivity for the compounds in question. The large overall features in the conductivity are not severely affected by the f-electrons, as we shall see below. Of course this not not true for the onset of transitions, and the optical gap. A comparison with our calculation illustrates this point in the following.

LDA+DMFT. Very recently, the LDA+DMFT scheme was applied to one of the compounds, namely Ce$_2$O$_3$ [Pourovskii *et al.* (2007a)]. As a matter of fact, among all the approaches mentioned so far, the realistic extension of dynamical mean-field theory is most suited to deal with the electronic structure of the materials in question, since it is capable of describing correctly the Mott insulating state, namely without the assumption of an ordering that is unphysical at room temperature.

It is these calculations that our optics calculations in the next section are based on. Due to the atomic nature of the f-states, the DMFT impurity model was solved, using the Hubbard-I approximation [Hubbard(1963)], in which the self-energy of the correlated

---

[1] In this sense the adjustable parameter U in the LDA+U scheme is replaced by the choice of the exchange correlation potential. Calling this approach *ab initio* is problematic.

[2] Another point is that the derivative of the true exchange correlation potential is discontinuous [Perdew *et al.* (1982)], while all potentials applied in practice are not. Thus, one might even say that the finding of a correct gap value indicates that the used potential is actually wrong. The undeniable merit of good results is thus diminished by the loss of control in the theory.

orbitals, RE4f, is calculated from the atomic limit of the Hubbard model, which consists of discrete levels exposed to the usual Coulomb repulsion. In other words, the hybridization with other orbitals is neglected and the correlated subset of orbitals is treated in the narrow band limit, leading to an atomic self-energy.

The interaction parameters were chosen as U=6.46 eV, and J=0.46 eV. Constrained LDA calculations [Anisimov and Gunnarsson(1991)] for Ce$_2$O$_3$ yield U values between 5.5 and 8 eV [Pourovskii *et al.* (2007a)].

The relative position of the f-states with respect to the O2p and RE5d states is largely determined by the double counting correction, which is meant to remove correlation effects in the f-states already taken into account by the LDA. Pourovskii *et al.* use the so-called fully-localized limit of the LDA+U as double counting correction : $\Sigma^{dc} = U(N - 1/2) - J(N - 1)/2$, with N being the atomic occupancy[3].

Further, we note that Pourovskii *et al.* employed the fully self-consistent LDA+DMFT scheme, i.e. after convergence of the DMFT, the charge density was updated and fed back into the LDA, such as to yield a new Hamiltonian for the next LDA+DMFT iteration. For details see [Pourovskii *et al.* (2007a)]. The effect of this charge consistency is shown to be important for the systems in question.

C   Optical properties of RE$_2$O$_3$ within LDA+DMFT

C.a   Spectral properties

Recently, L. V. Pourovskii extended prior electronic structure work on Ce$_2$O$_3$ [Pourovskii *et al.* (2007a)] to cover the entire series of early rare-earth sesquioxides, RE$_2$O$_3$, with RE=Ce, Pr, Nd, Pm. The interaction parameters were chosen the same as for Ce$_2$O$_3$, namely U=6.46 eV, and J=0.46 eV.

Figure 7.4 shows the spectral functions as obtained from the above described charge-self-consistent LDA+DMFT scheme. Clearly seen is the evolution of the lower 4f Hubbard band : While in Ce$_2$O$_3$ it lies between the O2p and RE5d bands, and thus determines the charge gap, it moves downwards in energy along the series, and already in the case of Pr$_2$O$_3$ it merges with the O2p excitations. Therefore a sharp increase of the absorption edge is expected in the optical spectra when going from Ce$_2$O$_3$ to Pr$_2$O$_3$, whereas the gap evolution in the remainder of the series is characterized by the changes of the oxygen bands with respect to the lowest conduction band. The shifting of the lower Hubbard band finds its origin in the consecutive lowering of the f energy levels in rare-earth atoms/ions with increasing filling of the f states.

Figure 7.5 shows a comparison of the LDA+DMFT spectral function with the photo-emission results [Mullins *et al.* (1998)], mentioned above. In both, theory and experiment, the 4f lower Hubbard band is well distinguished above the O2p bands. However, the relative positions are different, the experimentally determined oxygen weight occurring at sizable higher binding energy than in the theory. This might well be related to the

---

[3]Since the Hubbard-I solver neglects hybridizations of the f-orbitals with all others, also the double counting correction should do so, which is why the *atomic* and not the *total* f-occupation is used.

common underestimation of p-d gaps within the LDA. We remember that the DMFT treatment, though affecting all other bands through the self-consistency, improves only on the correlation effects of the 4f states.

Coming back to the discussion of the evolution of the charge gap along the series, we show in Figure 7.6 the results of the LDA+DMFT along with the experimental results from above. The overall experimental tendencies are well reproduced. In the case of La$_2$O$_3$, which has no f electrons, the underestimation of the p-d gap within LDA, as already mentioned above, explains the discrepancy with the experiment. In the remainder of the series, the agreement is much better. The gap value approaches that of La$_2$O$_3$ with increasing atomic number, as the influence of the f-states becomes more and more negligible for the determination of the gap size.

Yet, not only the upper valence states, but also the conduction band changes in character. While in Ce$_2$O$_3$ it is mostly formed by RE5d contributions, the multiplet structure of the upper 4f Hubbard band evolves towards lower energy, corresponding to the overall lowering of the f levels along the rare-earth series, mentioned above, and becomes responsible for the lowest unoccupied excitation in Pm$_2$O$_3$.

The occupation of the f-states are found to be close to their nominal atomic configuration, namely 1.16, 2.10, 3.10 and 4.08 for Ce, Pr, Nd, and Pm, respectively.

C.b Optical properties

In this section we present results on the optical conductivity using the formalism described in Part II. Contrary to our earlier examples no analytical continuation is required, since results of the Hubbard-I solver are directly obtained on the real-frequency axis.

Figure 7.7 shows our results along with experimental data [Kimura *et al.* (2000)] and LDA+U conductivities [Singh *et al.* (2006)]. Unfortunately, no experimental data is, to the best of our knowledge, available for the most interesting case, namely Ce$_2$O$_3$[4]. Our theoretical curves were obtained for [100] light polarization. No appreciable polarization dependence was evidenced. Figure 7.8 shows a zoom into the low energy region of the spectrum.

As anticipated, the influence of the f-orbitals in the case of Ce$_2$O$_3$ is clearly evidenced : Optical transitions from the lower RE4f Hubbard band into the conduction band, RE5d, lead to an absorption feature in the optical conductivity, which also determines the onset of the conductivity at ~ 2.25 eV.

For comparison we show for the case of Ce$_2$O$_3$ the optical conductivity resulting from an LDA calculation in which the f electrons were treated as core electrons, and thus are absent from the spectrum. Apart from the f-d transitions at low energy, the overall behaviour is roughly the same as for Ce$_2$O$_3$ within LDA+DMFT. However, we remark a perceptible downshift in energy of the features in the conductivity. This is in line with the

---

[4]Electron energy loss spectroscopy results on Ce$_2$O$_3$ foils did not show any features associated to the 4f lower Hubbard band [Mullins *et al.* (1998)]
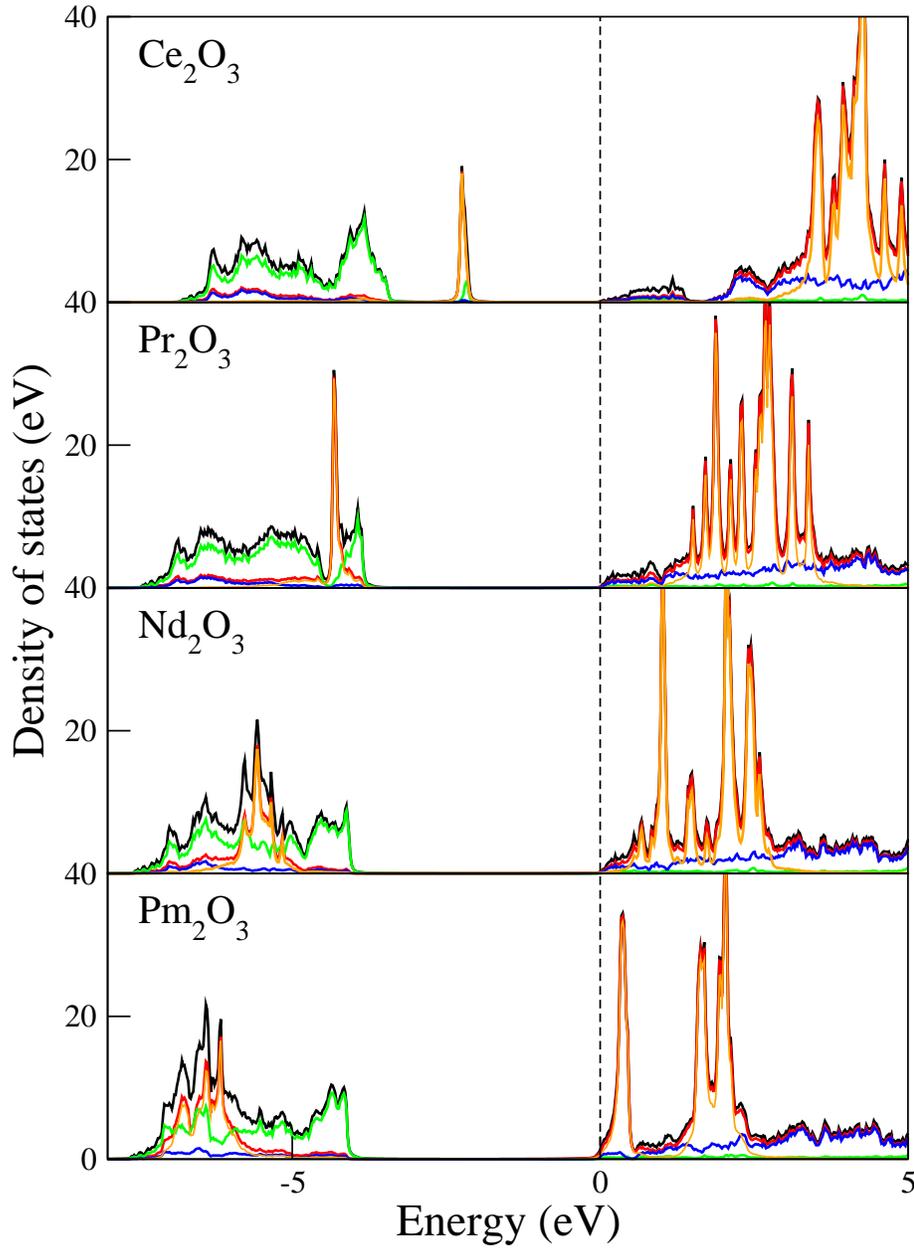
Figure 7.4 : *Spectral function of the sesquioxide series within LDA+DMFT (Hubbard I solver). Shown is the total spectral weight (black), and the individual contributions : RE4f (yellow), O2p (green), RE5d (blue), as well as RE5d+4f (red). From [Pourovskii et al. (2007b)].*
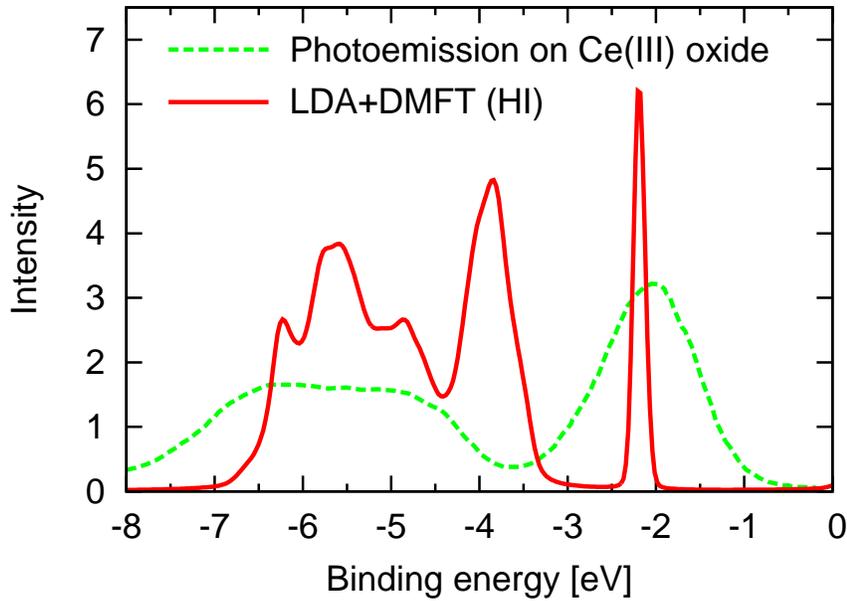
Figure 7.5 : *Comparison of the LDA+DMFT spectral function with photoemission (XPS at 340 eV) results on Ce(III) oxide of [Mullins et al. (1998)]. The experimental curve was normalized such as to yield the same integral as the spectral function (10 electrons/spin). See text for a discussion.*

Figure 7.6 : *Experimental optical, and theoretical (LDA+DMFT) direct band gap of the early RE$_2$O$_3$ series. From [Pourovskii et al. (2007b)].*

above observation that while yielding acceptable lattice parameters, spectral properties deteriorate when the f electrons are ignored. Indeed the hybridizations with the other orbitals[5] lead to considerable changes in the band-structure, in 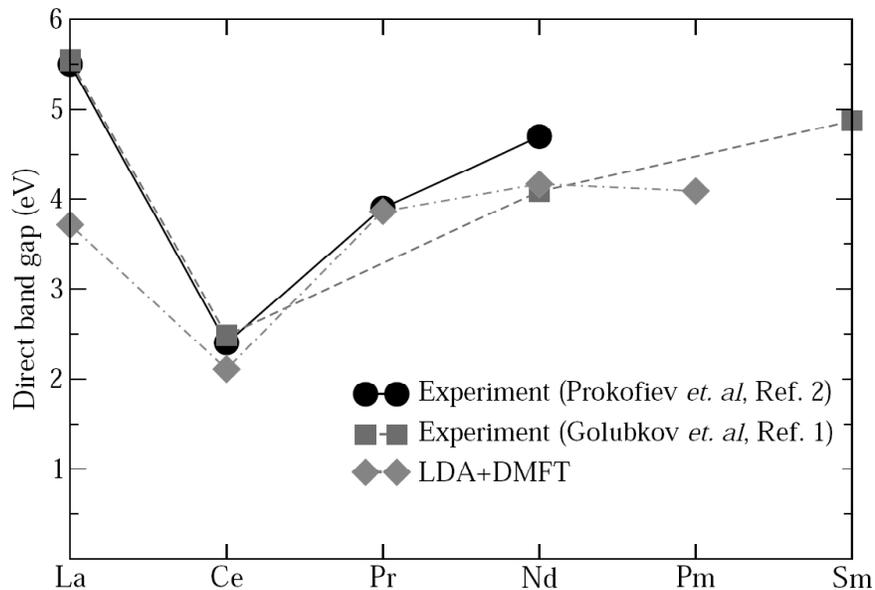particular the O2p-RE5d gap is increased when taking the f-orbitals properly into account, i.e. as correlated valence electrons.

In all RE$_2$O$_3$ other than Ce$_2$O$_3$, the onset of transitions is determined by O2p-RE5d (in the conduction band mixed with RE4f) transitions, and, though being crucial for the calculation of the correct excitation spectrum, their role in the optical spectrum is only a minor one. The optical gap, Figure 7.8, is of course congruent with the evolution of the direct band gap shown in Figure 7.6. The high energy behaviour is very similar in all the compounds.

Finally a word on the absolute value of the optical conductivities. Indeed, our theoretical findings differ from the experimental data by roughly a factor of 2.5. This is so far an unresolved issue. We did benchmark our method for pure LDA optical conductivities and found good agreement[6]. Indeed also other LDA+DMFT, and LDA+U optics approaches seem to suffer from a tendency to overestimate the absolute magnitude of optical transitions, see e.g. [Haule *et al.* (2005)]. Further investigations are needed.

Yet, it might also be quite enlightening to perform more experimental measurements, in particular for Ce$_2$O$_3$, for which our calculation constitutes a prediction.

D   Conclusions

In conclusion, we have investigated the optical properties of the early rare-earth oxide series, RE$_2$O$_3$. We studied in particular the evolution of the influence of the RE4f electrons along the series. While it was known from early on that structural properties do not considerably depend on the f electrons, their effect on spectral properties is immense. The finite hybridizations of the quasi-localized 4f states with other bands is crucial to account for a correct band-structure. While LDA+U calculations also succeed in capturing this effect, they violate the paramagnetic nature of the compound at room temperature and imply a magnetic ordering to be at the origin of the insulating behaviour, which contradicts experimental findings, as described. In the optical properties, the f electrons only play an important role in Ce$_2$O$_3$, in which they determine the absorption edge, while their impact in all other compounds is smaller on a qualitative level.

---

[5]which were only neglected in the calculation of the self-energy (Hubbard-I solver), but not in the DMFT self-consistency

[6]We also note that, apart from the maximum values, the magnitude of our RE$_2$O$_3$ conductivity compares well with LDA+U results [Singh *et al.* (2006)]. The discrepancy in the region of maximum intensity might by due to our approximation to the Fermi velocities, see Section , Chapter 4, which is less well suited for wider extending orbitals, such as the O2p ones.
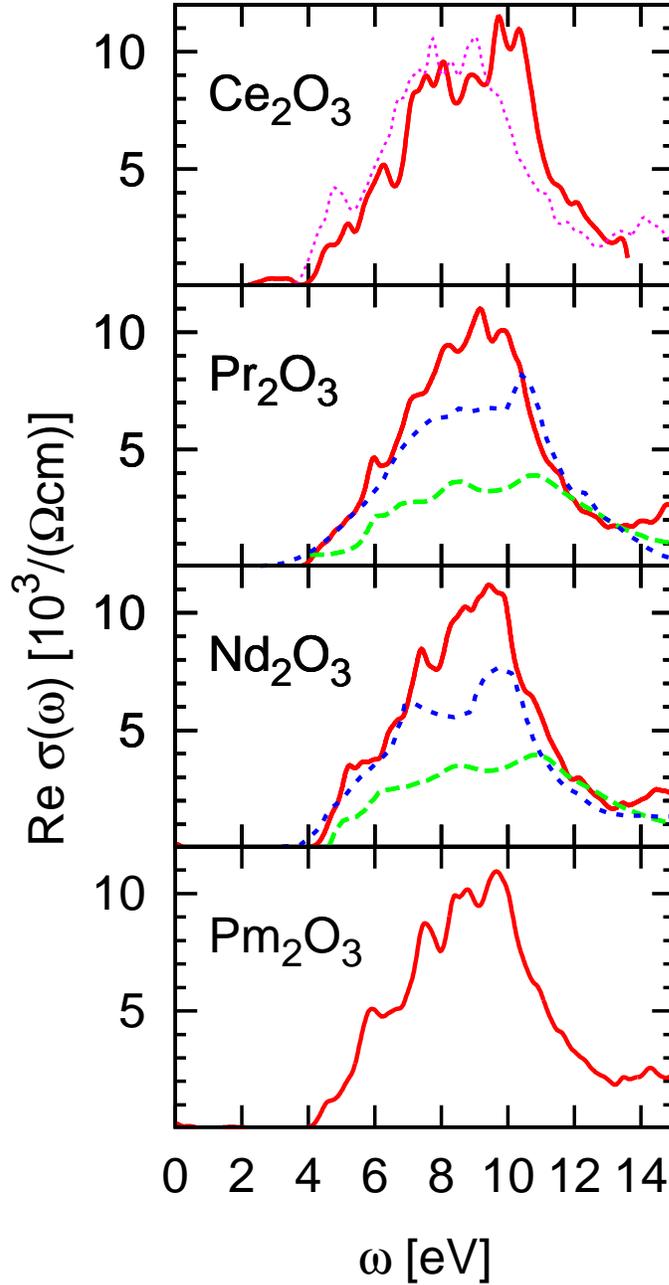
Figure 7.7 : *Optical conductivity of the rare-earth sesquioxide series : Theoretical LDA+DMFT curves (solid red) for [100] polarization, experiment [Kimura et al. (2000)] (dashed green) with E ⊥ (001) and LDA+U results (short dashed blue) with E ⊥ (001), from [Singh et al. (2006)]. For the case of Ce$_2$O$_3$ we additionally show the optical conductivity of an LDA calculation in which the f-orbitals were treated as core states (dotted pink).*
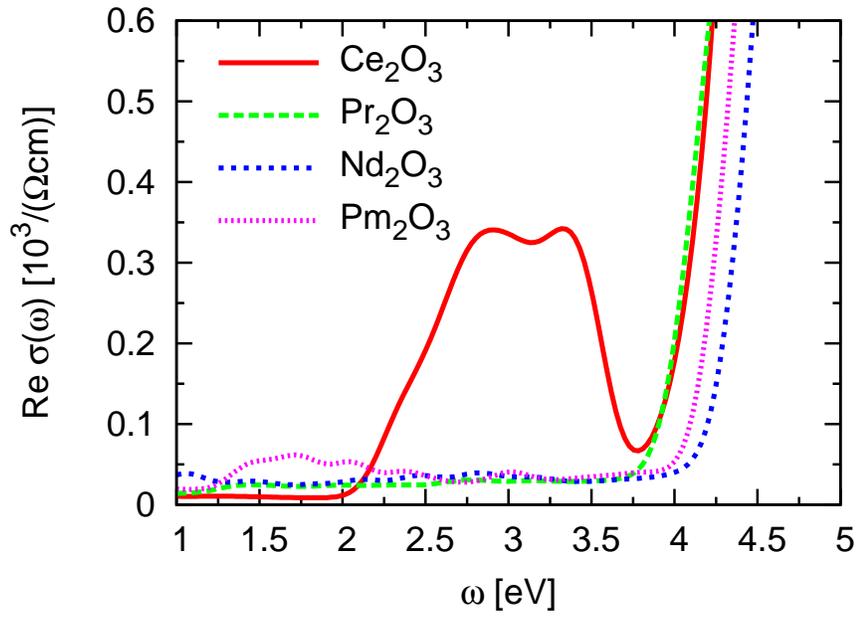
Figure 7.8 : *LDA+DMFT optical conductivity of the rare-earth sesquioxide series. Shown is the low energy region of Figure 7.7.*

Chapter 8

Conclusions and Outlook

In conclusion, this thesis has dealt with the electronic structure of correlated materials. Special emphasize has been laid on spectral and optical properties.

Using a generalized analytical continuation scheme that allowed for the calculation of the real-frequency self-energy from quantum Monte Carlo data, we were in the position to analyze in detail the outcome of dynamical mean field calculations in the realistic context. Furthermore, we explored which prerequisites have to met in order to to allow for an excitation spectrum to be cast into an effective band-structure.

A second focus was geared on optical properties of correlated materials. In this vein, we developed a versatile formalism that is well suited for calculations that use a localized basis, as is in particular verified for dynamical mean field computations. In our derivation we extended the Peierls substitution approach to the case of multi-atomic unit cell, and gave expressions for the correction terms that are missing with respect to the full Fermi velocity. It was shown, in the actual calculations, that in the case of well-localized orbitals, this generalized Peierls scheme resulted in optical conductivities in reasonable agreement with experiment. The approach is, moreover, method independent, since the only intervening matrix elements is the Hamiltonian.

Specifically, for the case of VO_2, a detailed analysis of the excitation spectrum as calculated from LDA+(C)DMFT, revealed important dynamical correlations and lifetime effects in the metallic phase, while for the low temperature phase, we described in detail a new scenario for the nature of the insulating behaviour. In particular, we have shown that spectral properties are well reproducible from a static, yet orbital-dependent, one-particle potential. Yet, the true many-body ground state was explained to be well beyond a static one-particle description, which induced us to introduce the notion of a "many-body Peierls" picture. The seemingly contradictory result of a correlation driven metal to insulator transition in which the insulator exhibits less (spectral) signatures of correlations was thus resolved. Moreover, we calculated the optical conductivity of the M1 phase in a full-orbital setup, using the LDA+CDMFT self-energy. The results are in good agreement with experiment.

In the case of V_2O_3, the mechanism of the doping-driven metal–insulator transition was investigated and identified to originate from a correlation enhancement of the e_g^π–a_{1g}

crystal field splitting. This resulted in an effective de-hybridization between these orbitals. Both, the metallic and the insulating phases were found to exhibit strong satellite features in their spectral function, the dispersion of which reflects those of the renormalized one-particle excitations. Furthermore we evidenced an orbital-selectivity in the coherence scale in the metallic phase : While a_{1g} excitations were found to be close to the Fermi liquid regime, e_g^π excitations remained incoherent down to the lowest temperatures of the calculation. This selectivity was confirmed by recent optical experiments. By identifying the orbital origins of different optical transitions, we explained the temperature dependence of the measured optical conductivity.

As a last example, we presented a study of the optical conductivity of rare-earth sesquioxides. In the series RE_2O_3, with RE=Ce, Pr, Nd, Pm, we tracked the behaviour of the localized f-states and their influence on the optical absorption. While the overall spectrum was shown to be dominated by O2p to RE5d orbitals, the low frequency onset of the absorption spectrum is determined by the position of the rare earth 4f states. The occupation of the latter increases along the series from one (Ce) to four (Pm) electrons. This change in filling resulted in a moving of the 4f Hubbard bands. In Ce_2O_3 the lower Hubbard band was evidenced to sit between the Fermi level and the uppermost oxygen bands and thus it is fully responsible for the low-lying optical excitations, whereas already in Nd_2O_3 the Hubbard band had moved sufficiently downwards to merge with the oxygen bands, resulting in an oxygen dominated absorption edge that varied only little along the remaining rare earth series.

In the future one might address some extensions of the presented work. In the cases of VO_2 and V_2O_3 the electronic structure calculations used Hamiltonians that were downfolded on a small subset of correlated orbitals. However, as we have seen in the optical spectra, the influence of the other orbitals becomes important already at quite low energies. In this work, we fixed their shape and position to the LDA results, which proved insufficient under quantitative considerations. This calls for a setup, in which these orbitals are fully taken into account. In the LDA+DMFT framework this means to include the uncorrelated orbitals into the DMFT self-consistency.

This has been done in the case of the rare-earth sesquioxides. Here we realized that the energy difference between the oxygen and the rare-earth orbitals was too small, owing to the gap underestimation common to the LDA. This will trigger new investigations with techniques that go beyond the LDA+DMFT. Particular promising in this respect seems the GW+DMFT scheme.

Finally, we hope that our approach for the calculation of optical properties, using the generalized Peierls substitution, will prove valuable in future investigations of optical properties of strongly correlated materials.

Part IV

Appendices

Appendix A

Analytical Continuation of off-diagonal Self-Energies

The starting point for the analytical continuation scheme for the self-energy, that we described in Section , Chapter 3, is the Green's function in imaginary time. In the most general case, the latter will have off-diagonal elements in orbital space. As the standard implementation of the maximum entropy (MaxEnt) algorithm in this context has, to our knowledge, so far been used for diagonal elements only, some comments are in order.

In contrast to the diagonal elements of the spectral function, which are normalized to one and are positive at all frequencies, off-diagonal elements have vanishing zeroth moment and hence change sign as a function of energy.

For mending this difference, the idea is simply to add a function $f(\omega)$ of zeroth moment one to $const \cdot A(\omega)$, and to calculate the corresponding shift in $G(\tau)$. However the function f has to be chosen such, that the resulting fictitious spectral function is non-negative for all frequencies. To this end, we construct it in the following way. Given the orthogonal orbital transformation $\widetilde{A} = U^\dagger A U$ with

$$
U_{ll'} = \tfrac{1}{\sqrt{2}}
\begin{pmatrix}
1 & & & -1 & & \\
 & \ddots & & & & \\
1 & & & 1 & & \\
 & & & & \ddots & \\
 & & & & & 1
\end{pmatrix}
\begin{array}{l} \\ \\ \leftarrow l \\ \\ \\ \end{array}
\qquad \text{(A.1)}
$$

the ll-element $(l \lessgtr l')$ of the spectral function in the new basis reads

$$
\widetilde{A}_{ll} = \frac{A_{ll} + A_{l'l'}}{2} \pm A_{ll'}
\qquad \text{(A.2)}
$$

and is thus per construction a proper diagonal element of the spectral function in the rotated basis, i.e. in particular it is positive for all ω. Therefore $f = 1/2(A_{l'l'} + A_{ll})$ is a suitable shift for $\pm A_{ll'}$ in the original basis.

Hence, after having continued the original diagonal elements, one constructs as input the function

$$\widetilde{G}_{ll}(\tau) = \left(U^\dagger G(\tau)U\right)_{ll} = \int d\omega \widetilde{A}_{ll}(\omega)K_\beta(\tau,\omega) \tag{A.3}$$

from which, using Equation (A.2), the off-diagonal spectral function $A_{ll'}(\omega)$ is then deduced.

As to the robustness of this approach, we remark that since already maxent-continued diagonal elements enter the calculation, there is an increased incertainty for the off-diagonal elements. This calls for high precision Monte Carlo data.

We have assessed the quality of this approach by performing two-band calculations and (a) continuing the Green's functions in the standard way, and (b) by artificially producing off-diagonal elements by performing a unitary transformation, then applying the above scheme, and transforming back into the original basis. The results were in more than qualitative agreement, yet differences were discernable.

We note that the above rotation has the same geometrical interpretation as the transformation into the a_{1g} bonding / antibonding basis, that we used in the case of M1 VO$_2$, but the construction is more general and does not require special symmetry properties of the system. Indeed, in the cluster case, the above unitary transformation diagonalizes the self-energy since the original diagonal elements are equivalent. This is however not true in the presence of general inter-orbital off-diagonal elements. In that case the presented scheme is still working, inasmuch as it provides a suitable transformation that allows the analytical continuation, yet it is no longer equivalent to a diagonalization of the Green's function. Indeed the latter will in general require energy dependent transformation matrices.

Appendix B

The Hubbard Molecule

1 The exact solution at zero temperature and half-filling

By the Hubbard molecule, we understand a simple one-orbital, two-site cluster with on-site interactions.

$$\text{U} \;\bullet\!\!-\!\!\overset{\text{t}}{-\!\!-\!\!}\!\!\bullet\; \text{U}$$

Its Hamiltonian, at half-filling, reads in the particle-hole symmetric form :

$$\mathbf{H} = -t \sum_{\sigma} \left(\mathbf{c}_{1\sigma}^{\dagger} \mathbf{c}_{2\sigma} + \mathbf{c}_{2\sigma}^{\dagger} \mathbf{c}_{1\sigma} \right) + U \sum_{l=1,2} \mathbf{n}_{l\downarrow} \mathbf{n}_{l\uparrow} - \frac{U}{2} \left(\sum_{\sigma,l=1,2} \mathbf{n}_{l\sigma} - 2 \right) \qquad \text{(B.1)}$$

The motivation for studying this rather simple model is the fact that in our LDA + CDMFT study on M1 VO_2 we evidenced a characteristic behaviour related to the vanadium dimers. Indeed, as will be clear below, the a_{1g} orbitals exhibited a typical molecular physics. The following model investigation will give insights into the nature of the ground state and its spectrum.

Moreover, since we have performed GW calculations for the same compound, a comparison of the cluster DMFT solution and the GW one in the model context will prove valuable. As a matter of fact, the CDMFT solution of the model corresponds to the exact solution, since the molecule is not coupled to a bath, and thus no self-consistency condition appears.

Here, we consider only the half-filled case of the Hubbard molecule, which corresponds to the situation of the a_{1g} orbitals in M1 VO_2.

Since the total particle number is a good quantum number, $[\mathbf{H}, \mathbf{N}] = 0$, the Hamiltonian is block-diagonal in the corresponding number representation, which allows for a

diagonalization of the individual N-sectors. We denote the states of the system by the kets $|1\ 2\rangle$ and indicate the occupations of the sites $1, 2$ by $0, \uparrow, \downarrow, \uparrow\downarrow$ [1].

One-particle sector (N=1).

Eigenvalue	decomposition of the $|\chi^{N=1}\rangle$ Eigenvector			
E_χ	$|\uparrow\ 0\rangle$	$|\downarrow\ 0\rangle$	$|0\ \uparrow\rangle$	$|0\ \downarrow\rangle$
$U/2 - t$	0	$1/\sqrt{2}$	0	$1/\sqrt{2}$
$U/2 - t$	$1/\sqrt{2}$	0	$1/\sqrt{2}$	0
$U/2 + t$	0	$-1/\sqrt{2}$	0	$1/\sqrt{2}$
$U/2 + t$	$-1/\sqrt{2}$	0	$1/\sqrt{2}$	0

Two-particle sector (N=2).

Eigenvalue	Eigenvector $|\psi^{N=2}\rangle$					
E	$|\uparrow\ \downarrow\rangle$	$|\downarrow\ \uparrow\rangle$	$|\uparrow\ \uparrow\rangle$	$|\downarrow\ \downarrow\rangle$	$|\uparrow\downarrow\ 0\rangle$	$|0\ \uparrow\downarrow\rangle$
singlet subspace						
$U/2 - 1/2\sqrt{16t^2 + U^2}$	$\frac{4t}{a(c-U)}$	$-\frac{4t}{a(c-U)}$	0	0	$1/a$	$1/a$
$U/2 + 1/2\sqrt{16t^2 + U^2}$	$-\frac{4t}{b(c+U)}$	$\frac{4t}{b(c+U)}$	0	0	$1/b$	$1/b$
triplet subspace						
0	0	0	0	1	0	0
0	0	0	1	0	0	0
0	$1/\sqrt{2}$	$1/\sqrt{2}$	0	0	0	0
U	0	0	0	0	$-1/\sqrt{2}$	$1/\sqrt{2}$

with $a = \sqrt{2\left(\frac{16t^2}{(c-U)^2} + 1\right)}$, $b = \sqrt{2\left(\frac{16t^2}{(c+U)^2} + 1\right)}$, and $c = \sqrt{16t^2 + U^2}$.

Three-particle sector (N=3).

Eigenvalue	Eigenvector $|\phi^{N=3}\rangle$			
E_ϕ	$|\uparrow\ \uparrow\downarrow\rangle$	$|\downarrow\ \uparrow\downarrow\rangle$	$|\uparrow\downarrow\ \uparrow\rangle$	$|\uparrow\downarrow\ \downarrow\rangle$
$U/2 - t$	0	$-1/\sqrt{2}$	0	$1/\sqrt{2}$
$U/2 - t$	$-1/\sqrt{2}$	0	$1/\sqrt{2}$	0
$U/2 + t$	0	$1/\sqrt{2}$	0	$1/\sqrt{2}$
$U/2 + t$	$1/\sqrt{2}$	0	$1/\sqrt{2}$	0

The subspaces of one and three particles are symmetric for the given Hamiltonian, i.e. at half-filling, the spectral function will be symmetric. Yet, in the particle-hole transformed Hamiltonian, see Equation (B.1), the hopping amplitude changes sign $(-t \to t)$, which is why the eigenvectors in the three particle sector are interchanged with respect to their eigenvalue when compared with the one-particle ones.

---

[1] We use the following convention as to the fermionic ordering : $|\uparrow\downarrow\ \ \uparrow\rangle = \mathbf{c}^\dagger_{2\uparrow}\mathbf{c}^\dagger_{1\downarrow}\mathbf{c}^\dagger_{1\uparrow}|0_1\ 0_2\rangle$.

Since $[\mathbf{H}, \mathbf{P}_{12}] = 0$ with the site-permutation operator $\mathbf{P}_{12}$, one could have further distinguished the singlet and triplet subspaces in the two-particle sector, that are also evident from the simple decomposition given in the box above[2].

The ground state at half-filling. For finite t, one has a non-degenerate ground state at half-filling (N=2), that is given by the first eigenvector in the list above. Since, this is the case we are interested in for the discussion of VO_2, we thus put

$$E_0 \quad = \quad U/2 - 1/2\sqrt{16t^2 + U^2} \tag{B.2}$$

$$|\psi_0^{N=2}\rangle \quad = \quad \frac{1}{a}\left\{ \frac{4t}{c-U}\left(|\downarrow \ \uparrow\rangle - |\uparrow \ \downarrow\rangle\right) + \left(|\uparrow\downarrow \ 0\rangle + |0 \ \uparrow\downarrow\rangle\right) \right\} \tag{B.3}$$

In this state the probability for double-occupations is $2/a^2$. For $t = 0.7$ eV, $U = 4.0$ eV, the relevant parameters for M1 VO_2, it amounts to $\sim 9\%$ per dimer. Figure B.1 shows the double occupation D as a function of the on-site interaction U. In the non-interacting ground state, which is a Slater-determinant

$$|1\ 2\rangle_{\text{SD}} = 1/\sqrt{4}\{|\downarrow \ \uparrow\rangle - |\uparrow \ \downarrow\rangle + |\uparrow\downarrow \ 0\rangle + |0 \ \uparrow\downarrow\rangle\} \tag{B.4}$$

of one-particle states, the weight of double occupations is $1/2$. For $U > 0$ their contribution decreases, and the ground state evolves towards the Heitler-London limit,

$$|1\ 2\rangle_{\text{HL}} = 1/\sqrt{2}\{|\downarrow \ \uparrow\rangle - |\uparrow \ \downarrow\rangle\} \tag{B.5}$$

in which all double-occupancies are projected out.
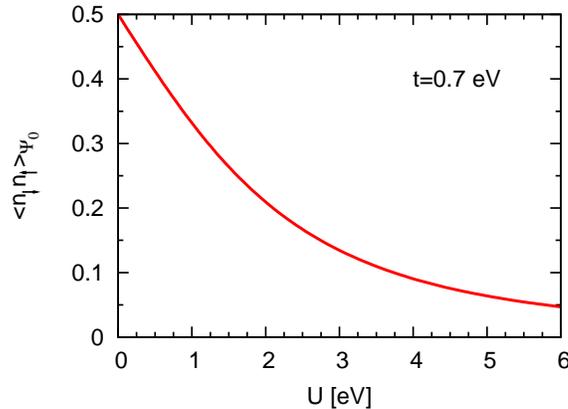
Figure B.1 : *Double occupation $D = \sum_{i=1,2} < \mathbf{n}_{i\uparrow}\mathbf{n}_{i\downarrow} >_{\psi_0}$ of the ground state $|\psi_0^{N=2}\rangle$ for $t = 0.7$ eV, as a function of the Coloumb repulsion U.*

---

[2]Note that $\mathbf{P}_{12}|\uparrow \ \downarrow\rangle = -|\downarrow \ \uparrow\rangle$.

The Green's function at half-filling.   From the definition

$$
G_{ij\sigma}(\omega) = \sum_{\phi} \frac{\langle\phi^{N=3}|\mathbf{c}_{i\sigma}^{\dagger}|\psi_0^{N=2}\rangle\langle\psi_0^{N=2}|\mathbf{c}_{j\sigma}|\phi^{N=3}\rangle}{\omega - (E_\phi - E_0) + \imath 0^+} + \sum_{\chi} \frac{\langle\chi^{N=1}|\mathbf{c}_{i\sigma}|\psi_0^{N=2}\rangle\langle\psi_0^{N=2}|\mathbf{c}_{j\sigma}^{\dagger}|\chi^{N=1}\rangle}{\omega + (E_\chi - E_0) + \imath 0^+}
\tag{B.6}
$$

one obtains

$$
\begin{aligned}
G_{11\uparrow}(\omega) &= \frac{1}{2a^2}\left(\frac{\left(1 - \frac{4t}{c-U}\right)^2}{w - (U/2 - t - E_0) + \imath 0^+} + \frac{\left(1 + \frac{4t}{c-U}\right)^2}{w - (U/2 + t - E_0) + \imath 0^+}\right) \\
&+ \frac{1}{2a^2}\left(\frac{\left(1 - \frac{4t}{c-U}\right)^2}{w + (U/2 - t - E_0) + \imath 0^+} + \frac{\left(1 + \frac{4t}{c-U}\right)^2}{w + (U/2 + t - E_0) + \imath 0^+}\right)
\end{aligned}
\tag{B.7}
$$

$$
\begin{aligned}
G_{12\uparrow}(\omega) &= \frac{1}{2a^2}\left(\frac{\left(1 - \frac{4t}{c-U}\right)^2}{w - (U/2 - t - E_0) + \imath 0^+} - \frac{\left(1 + \frac{4t}{c-U}\right)^2}{w - (U/2 + t - E_0) + \imath 0^+}\right) \\
&- \frac{1}{2a^2}\left(\frac{\left(1 - \frac{4t}{c-U}\right)^2}{w + (U/2 - t - E_0) + \imath 0^+} - \frac{\left(1 + \frac{4t}{c-U}\right)^2}{w + (U/2 + t - E_0) + \imath 0^+}\right)
\end{aligned}
\tag{B.8}
$$

or in a more compact notation (with $\omega + \imath 0^+ \to z$)

$$
G_{11\uparrow}(z) = -\frac{4w\left(36t^2 + U^2 - 4w^2\right)}{144t^4 + 8\left(3U^2 - 20w^2\right)t^2 + \left(U^2 - 4w^2\right)^2}
\tag{B.9}
$$

$$
G_{12\uparrow}(z) = -\frac{4t\left(36t^2 + 3U^2 - 4w^2\right)}{16w^4 - 8\left(20t^2 + U^2\right)w^2 + \left(12t^2 + U^2\right)^2}
\tag{B.10}
$$

with the constants a, c as given before. The above are the only independent elements in the present case. By symmetry we have $G_{11\uparrow} = G_{22\uparrow} = G_{11\downarrow} = G_{22\downarrow}$ and $G_{12\uparrow} = G_{21\uparrow} = G_{12\downarrow} = G_{21\downarrow}$.

The excitation energies are given by the poles, and thus are

$$
\begin{aligned}
\pm(U/2 - t - E_0) &= \pm(c/2 - t) = \pm\left(\sqrt{16t^2 + U^2}/2 - t\right) \\
\pm(U/2 + t - E_0) &= \pm(c/2 + t) = \pm\left(\sqrt{16t^2 + U^2}/2 + t\right)
\end{aligned}
\tag{B.11}
$$

i.e.

$$
\pm t \pm \sqrt{16t^2 + U^2}/2
\tag{B.12}
$$

from which we easily deduce the bonding / antibonding-splitting (for t>0) :

$$\Delta_{bab} = -2t + \sqrt{16t^2 + U^2} \tag{B.13}$$

Figure B.2 shows the spectral function of the Hubbard molecule in a colour-coded representation at constant hopping amplitude ($t = 0.7$ eV) as a function of the Coulomb repulsion U and frequency. At $U = 0$ there are two two-fold degenerate excitation energies ($\pm t$), since this is the non-interacting case. At finite U, the Green's function has four poles, yet the weight of the two center ones is predominant in our regime of interest. Thus, here one would call the two outer excitations correlation satellites or "Hubbard bands". We will come back to this later.
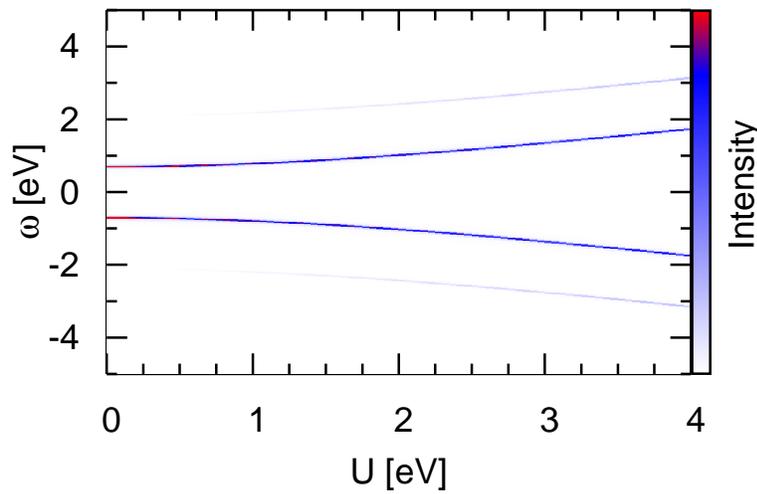
Figure B.2 : *Colour-coded local spectral function for $t = 0.7$ eV, as a function of the Coloumb repulsion U.*

The self-energy. From the Green's function, we can compute the self-energy of the Hubbard molecule by Dyson's equation :

$$\Sigma(\omega) = G^{-1}_{U=0}(\omega) - G^{-1}(\omega) \tag{B.14}$$

One finds

$$\Sigma_{11}(\omega) \;=\; \frac{U^2}{8}\left(\frac{1}{\omega - 3t + \imath 0^+} + \frac{1}{\omega + 3t + \imath 0^+} \right)$$
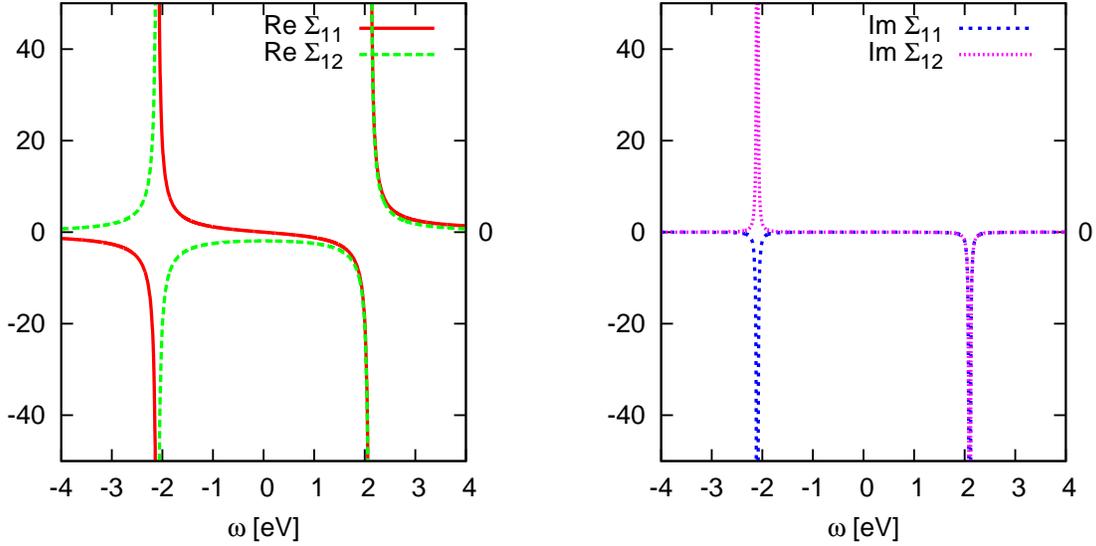
Figure B.3 : *(a) real parts, (b) imaginary parts of the self-energy of the half-filled Hubbard molecule at $T = 0$ for the parameters $t = 0.7$ eV, $U = 4.0$ eV.*

$$\Sigma_{12}(\omega) \;=\; \frac{U^2}{8}\left(\frac{1}{\omega - 3t + \imath 0^+} - \frac{1}{\omega + 3t + \imath 0^+}\right) \tag{B.15}$$

Figure B.3 shows the resulting self-energy for $t = 0.7$ eV and U=4.0 eV, the relevant parameters for the monoclinic phase of VO_2.

The symmetry of the self-energy is such that it yields the characteristic bonding / antibonding self-energies

$$\begin{aligned}\Sigma_{\substack{b\\ab}}(\omega) \;&=\; \Sigma_{11}(\omega) \pm \Sigma_{12}(\omega)\\ &=\; \frac{U^2}{4}\frac{1}{\omega \mp 3t + \imath 0^+}\end{aligned} \tag{B.16}$$

where thus in the [anti]bonding combination the imaginary part in the [un]occupied part of the spectrum is canceled, allowing for coherent weight at the respective energies. The enhancement of the bonding / antibonding splitting comes entirely from the $1/(\omega \pm 3t)$–tails in the real parts of the self-energy, seen in Figure B.3.

Figure B.4 shows the real parts of the bonding / antibonding self-energies for our favourite parameters. As usual, the excitation energies of the system are given by the intersections $\omega \pm t - \Re\Sigma_{b,ab,} = 0$, which are marked by the circles in the figure. Per bonding / antibonding component there appear two solutions. The two inner ones correspond to the renormalized bonding / antibonding excitations, i.e. to an $N - 1 \longrightarrow N + 1$ transition with an energy difference Δ_{bab} as stated above. The two others occur due to the fact that the $N = 2$ singlet subspace is two dimensional and non-degenerate. Indeed the [upper] lower satellite in the [un]occupied part of the spectrum belongs to transitions into the [high] low energy singlet with a double occupancy $[D > 1/2]$ $D < 1/2$. Thus, the
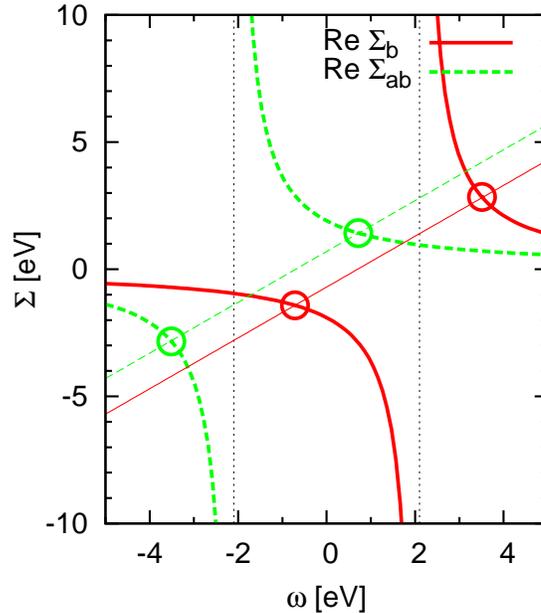
Figure B.4 : *Graphical construction for the poles of the one-particle Green's function.* $t = 0.7$ *eV,* $U = 4.0$ *eV.*

energy difference between the [anti]bonding peak and the [lower] upper satellite is just the energy splitting within the $N = 2$ singlet subspace. In this sense, the satellites are the molecular equivalent of atomic-like Hubbard bands.

The distinction between renormalized bands and those Hubbard bands becomes, however, irrelevant in the limit of $t \rightarrow 0$, in which the four pole solutions collapse and yield two pairs of solutions with equal weight, separated by the energy U. This corresponds to the limit of two isolated atoms that are Mott-Hubbard insulating. Then, all poles are to be called Hubbard bands. Hence, in the molecular context, where insulating behaviour at half-filling is realized already by a hybridization gap, the distinction and thus the notion of renormalized levels and correlation satellites is continuous.

Yet, we note the subtlety that though the spectrum of the two cases $t = 0$, and $t \rightarrow 0$ are the same, the ground state wave functions are genuinely different, the latter being the singlet state (S=0) from above, Equation (B.3), and the former corresponding to a four-fold degenerate eigenenergy, i.e. the wavefunction encompasses both the singlet and the triplet subspace, leading to the usual Mott-Hubbard (S=1/2) local moment response.

Coming back to the parameter regime of VO_2, it is clear that, when taking into account the imaginary parts of the bonding / antibonding self-energies, only the solutions near the Fermi level are fully coherent. Indeed, the outer excitations only exist due to the δ–peak nature of the self-energy. In the presence of broadening mechanisms, such as hybridizations to other orbitals and, moreover, couplings to other dimers, the divergence of the real-part of the self-energies might by removed, to an extent such that the second crossing is avoided. Yet, there might still appear satellite spectral weight at the energies in point, as evidenced in M1 VO_2.

We note that in the $U \to \infty$ limit, all four solutions acquire the same weight in the spectral function and also have the same degree of coherence.

As to the $U \to 0$ limit, we remark that only two of the four poles of the Green's function do collapse on the non-interacting solutions. Indeed it is the disappearance of the self-energy ($\Sigma \sim U^2$) which leads to the suppression of spectral weight for the two satellite structures.

Finally we note that within the $N = 2$ sector, the singlet-triplet spin excitation has an energy $\Delta_{spin} = -U/2 + 1/2\sqrt{16t^2 + U^2} = 0.44$ eV, that is much smaller than the lowest charge excitation, $\Delta_{charge} = \Delta_{bab} = 3.48$ eV, that determines the gap in the spectral function. In M1 VO$_2$ the spin gap is of about the same magnitude as given for the model above [3]. In a generic band-insulator one has $\Delta_{spin} = \Delta_{charge}$

---

[3]J. P. Pouget, private communication.

2 GW for the Hubbard molecule

In this section we will apply the GW approximation (see Section B, Chapter 2) to the above defined Hubbard molecule. This is motivated by the apparent similarities between LDA+CDMFT calculations for M1 VO_2 and the Cluster DMFT solution which corresponds to the exact solution of this model. Thus it is interesting to assess from a simple model perspective, whether an *ab initio* GW calculation might lead to the same physical picture.

Such a comparison between exact and GW solutions has been previously performed for Hubbard clusters [Schindlmayr(1997)] and Hubbard chains [Pollehn *et al.* (1998)]. This was done mostly for assessing different levels of self-consistency in the GW scheme and to study, on a model level, the implications and possible mendings of the non-conserving nature of the GW approximation.

In the following we will present the calculation in the finite temperature Matsubara formalism at half-filling and specialize later on to zero temperature. Also, since we investigate a finite system, we work in real space, and thus, matrices are written in an orbital or site basis.

The non-interacting system. In particular, we chose to work not in the eigenbasis of the system but in the site-basis of the Hamiltonian given in Equation (B.1). Then the non-interacting Green's function reads

$$\mathbf{G}^0(\imath\omega_n) = \left\{ \imath\omega_n + \mu - \begin{pmatrix} 0 & -t \\ -t & 0 \end{pmatrix} \right\}^{-1} \tag{B.17}$$

We will assume $t > 0$ and it follows

$$G_{11}^0(\imath\omega_n) = \frac{1}{2}\left(\frac{1}{\imath\omega_n + \mu - t} + \frac{1}{\imath\omega_n + \mu + t} \right) \tag{B.18}$$

$$G_{12}^0(\imath\omega_n) = -\frac{1}{2}\left(\frac{1}{\imath\omega_n + \mu - t} - \frac{1}{\imath\omega_n + \mu + t} \right) \tag{B.19}$$

In the spectral representation, the Green's function reads $G_{ij}^0(\omega) = \sum_n \frac{\langle i|\psi_n\rangle\langle\psi_n|j\rangle}{\omega - E_n + \imath 0^+}$, where the E_n and ψ_n are the eigenvalues and eigenvectors, respectively. As can be inferred from the above, the Green's function in this eigenbasis is of course diagonal and has only one pole per orbital component. This is why, contrary to more complicated cases, the weight of the poles is one and no wavefunction matrix elements $\langle\psi_n|j\rangle$ appear.

The polarization P. Within the random phase approximation (RPA), i.e. when neglecting vertex corrections, the polarization is given by

$$P_{ij}(\imath\nu_m) = \frac{2}{\beta} \sum_n G_{ij}^0(\imath\omega_n) G_{ji}^0(\imath\omega_n + \imath\nu_m) \tag{B.20}$$

from which we find

$$P_{11}(\imath\nu_m) \;=\; -a\left(\frac{1}{\imath\nu_m - 2t} - \frac{1}{\imath\nu_m + 2t}\right) \tag{B.21}$$

$$P_{12}(\imath\nu_m) \;=\; a\left(\frac{1}{\imath\nu_m - 2t} - \frac{1}{\imath\nu_m + 2t}\right) \tag{B.22}$$

$$\tag{B.23}$$

with

$$a \;=\; \frac{1}{2}\Big(\mathrm{f}(-\mu + t) - \mathrm{f}(-\mu - t)\Big) \tag{B.24}$$

$$f(z) \;=\; \frac{1}{1 + \exp(\beta z)} \tag{B.25}$$

The screened interaction W.

$$\boxed{\mathbf{W}(\imath\nu_m) = (\mathbf{1} - \mathbf{U} \cdot \mathbf{P}(\imath\nu_m))^{-1} \cdot \mathbf{U}} \tag{B.26}$$

Here the interaction vertex is written in the two-particle orbital space, and assumed to be purely local :

$$\mathbf{U} \;=\; \begin{pmatrix} U & 0 \\ 0 & U \end{pmatrix} \tag{B.27}$$

this leads to

$$W_{11}(z) \;=\; \frac{(1 - UP_{22})U}{(1 - UP_{11})(1 - UP_{22}) - U^2 P_{12}P_{21}}$$

$$=\; U - \frac{4aU^2 t}{z^2 + 8aUt - 4t^2} \tag{B.28}$$

$$W_{12}(z) \;=\; \frac{U^2 P_{21}}{(1 - UP_{11})(1 - UP_{22}) - U^2 P_{12}P_{21}}$$

$$=\; \frac{4aU^2 t}{z^2 + 8aUt - 4t^2} \tag{B.29}$$

The self-energy Σ.

$$\Sigma_{ij}(\imath\omega_n) = -\frac{1}{\beta}\sum_m G_{ij}^0(\imath\omega_n - \imath\nu_m)W_{ij}(\imath\nu_m) \tag{B.30}$$

performing the bosonic Matsubara sum yields

$$\Sigma_{11}(\imath\omega_n) = \frac{1}{2}\left\{ U\left(\mathrm{f}(\mu-t)+\mathrm{f}(\mu+t)\right) \right.$$
$$-\mathrm{f}(\mu-t)\frac{4aU^2t}{(\imath\omega_n+\mu-t+c)(\imath\omega_n+\mu-t-c)} - n(c)\frac{2aU^2t/c}{\imath\omega_n+\mu-t-c}$$
$$+n(-c)\frac{2aU^2t/c}{\imath\omega_n+\mu-t+c}$$
$$\left. +\text{ last three terms with }(\mu-t)\rightarrow(\mu+t)\right\} \tag{B.31}$$

$$\Sigma_{12}(\imath\omega_n) = \frac{1}{2}\left\{ -\mathrm{f}(\mu-t)\frac{4aU^2t}{(\imath\omega_n+\mu-t+c)(\imath\omega_n+\mu-t-c)} - n(c)\frac{2aU^2t/c}{\imath\omega_n+\mu-t-c} \right.$$
$$+n(-c)\frac{2aU^2t/c}{\imath\omega_n+\mu-t+c}$$
$$\left. -\text{ last three terms with }(\mu-t)\rightarrow(\mu+t)\right\} \tag{B.32}$$

with

$$n(z) = \frac{1}{\exp\beta z - 1} \tag{B.33}$$
$$n(x\pm\imath\omega_n) = -\mathrm{f}(x) \tag{B.34}$$
$$c^2 = 4t^2 - 8aUt \tag{B.35}$$

Now we will specialize for zero temperature and half-filling $(\mu = 0)$[4], this means

---

[4]indeed $\mu = 0$ corresponds to half-filling of the non-interacting model. For $U > 0$, however, the particle-hole symmetry is restored by putting the Hartree term into the chemical potential. Then the chemical potential of the interacting Green's function, Equation (B.42), and the non-interacting one coincide ($\mu = 0$). Away from half-filling, the latter procedure would have to be performed self-consistently. It has been shown that this alignment of the chemical potential, proposed already in [Hedin(1965)], in general improves on spectral properties [Pollehn *et al.* (1998)], here it just assures the conservation of particles. More basically, and in the spirit of Equation (1.5) this can alternatively be seen as incorporating the interactions on the mean-field, or Hartree-Fock level into the non-interacting part of the Hamiltonian by introducing an effective one-particle potential. In the current case the latter is not effective, but constant for a given particle number.

$$f(x) = \Theta(x) \tag{B.36}$$

$$n(x) = -\Theta(x) \tag{B.37}$$

$$a = -\frac{1}{2} \tag{B.38}$$

$$c^2 = 4t^2 + 4Ut \tag{B.39}$$

From which is deduced

$$
\begin{aligned}
\Sigma_{11}(\imath\omega_n) &= \frac{1}{2}\left\{ U + \frac{2U^2 t}{(\imath\omega_n - t + c)(\imath\omega_n - t - c)} + \frac{U^2 t/c}{\imath\omega_n - t + c} + \frac{U^2 t/c}{\imath\omega_n + t + c} \right\} \\
&= \frac{1}{2}\left\{ U + \frac{U^2 t}{c}\left(\frac{1}{\imath\omega_n - t - c} + \frac{1}{\imath\omega_n + t + c} \right) \right\}
\end{aligned}
$$

$$
\begin{aligned}
\Sigma_{12}(\imath\omega_n) &= \frac{1}{2}\left\{ \frac{2U^2 t}{(\imath\omega_n - t + c)(\imath\omega_n - t - c)} + \frac{U^2 t/c}{\imath\omega_n - t + c} - \frac{U^2 t/c}{\imath\omega_n + t + c} \right\} \\
&= \frac{1}{2}\frac{U^2 t}{c}\left(\frac{1}{\imath\omega_n - t - c} - \frac{1}{\imath\omega_n + t + c} \right) \tag{B.40}
\end{aligned}
$$

The term $U/2$ in the diagonal element Σ_{11}, Equation (B.40), is the aforementioned Hartree contribution, that we will drop from hereon. Figure B.5 shows the thus obtained obtained self-energy, Equation (B.40), for the parameters $t = 0.7$ eV and $U = 4.0$ eV.

When comparing the GW self-energy, Equation (B.40) and Figure B.5, with the exact one, Equation (B.15) and Figure B.3, there are several remarks to be made. First of all, the symmetries of the self-energy elements are the same, i.e. also the GW self-energy yields the characteristic bonding / antibonding combinations. The self-energy has two poles at energies $\Omega_{1\atop 2} = \pm(t + \sqrt{4t^2 + 4Ut})$. Still, the GW deviates in two respects from the exact solution :

(i) the poles of the self-energy Ω_i are not at the correct energies. Indeed the pole energies dependent on the interaction, while the exact ones are solely determined by the one-particle Hamiltonian. Still, both collapse on each other in the non-interacting limit. The deviation is given by $\left|\Omega_i^{GW} - \Omega_i^{exact}\right| = U - U^2/4t + \mathcal{O}(U^3)$.

(ii) the weights of the δ–distributions in the imaginary parts are wrong as well. Moreover, the weak-coupling expansions differ. While the exact weight is $U^2\pi/8$ for each of the two poles, as dictated by the sum rule

$$\int_{-\infty}^{\infty} d\omega' \,\Im\Sigma(\omega') = -\pi \lim_{\omega\to\infty} \omega\Re\Sigma(\omega) \overset{\text{half-filling}}{=} -\pi U^2/4 \tag{B.41}$$

GW yields $\pi U^2 t/(2\sqrt{4t^2 + 4Ut}) = \pi(U^2/4 - U^3/8t + \mathcal{O}(U^4))$ *per* pole. Though both vanish quadratically for $U \to 0$, the prefactor is twice as large in GW. As a consequence the bonding / antibonding–splitting within GW is wrong, since the $1/(\omega - \Omega_i)$ tails in the real-parts of the self-energy differ considerably.
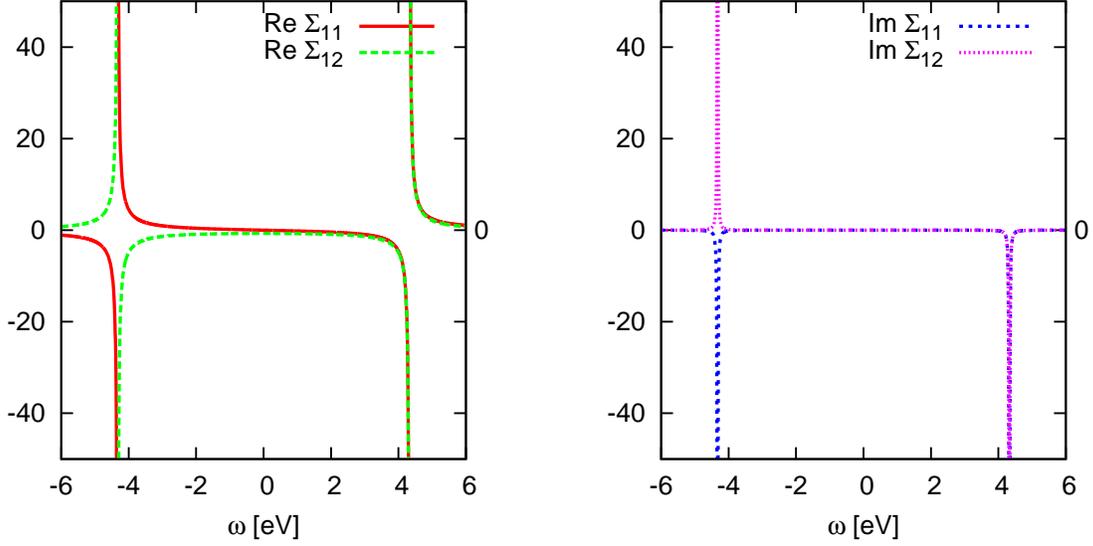
Figure B.5 : *(a) real parts, (b) imaginary parts of the GW self-energy of the half-filled Hubbard molecule at $T = 0$ for the parameters $t = 0.7$ eV, $U = 4.0$ eV according to Equation (B.40).*

Interacting Green's function G : Spectral function and one-particle excitations.

$$\mathbf{G}(\imath\omega_n) = \left\{ \imath\omega_n + \mu - \begin{pmatrix} 0 & -t \\ -t & 0 \end{pmatrix} - \mathbf{\Sigma}(\imath\omega_n) \right\}^{-1} \tag{B.42}$$

The excitation energies are as usual given by the pole-equation Equation (3.9)

$$\det(\mathbf{G}[\Re\mathbf{\Sigma}]^{-1}) = 0 \tag{B.43}$$

After continuation to the real frequency axis, the latter yields

$$(\omega - \Sigma_{11})^2 - (t - \Sigma_{12})^2 = 0 \tag{B.44}$$

i.e.

$$\omega = \pm t + \Sigma_{\substack{ab \\ b}} \tag{B.45}$$

where we have defined the bonding / antibonding–combinations

$$
\begin{aligned}
\Sigma_b = \Sigma_{11} + \Sigma_{12} &= \frac{U^2 t}{c} \frac{1}{\imath\omega_n - t - c} \\
\Sigma_{ab} = \Sigma_{11} - \Sigma_{12} &= \frac{U^2 t}{c} \frac{1}{\imath\omega_n + t + c}
\end{aligned}
\tag{B.46}
$$

The two Equations (B.45) together have the four solutions

$$\omega = \begin{Bmatrix} + \\ - \end{Bmatrix} \frac{1}{2c} \left(-c^2 \begin{Bmatrix} \pm \\ \pm \end{Bmatrix} \sqrt{c^4 + 4c^3 t + 4c^2 t^2 + 4tU^2} \right) \tag{B.47}$$

which are indicated in Figure B.6, along with the exact ones from Equation (B.12).
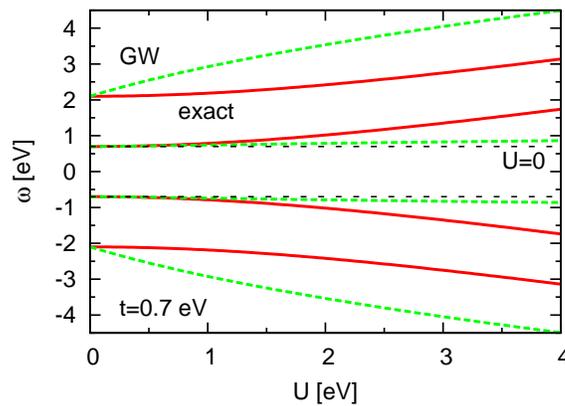

Figure B.6 : *Comparison of the GW excitation energies, Equation (B.44), with the exact ones, Equation (B.12), for $t = 0.7$ eV and as a function of U.*

As already discussed in terms of the self-energy, the excitation energies are reasonable in the weak coupling regime. Yet for $U > 0$ the positions of the satellite structures deviate considerably from the exact ones. Given the short-comings of the self-energy shown above, the weights of the respective features in the spectral function are in variance with the exact solution, as well.

Another difference concerns the $t \to 0$ limit. The exact excitations collapse on two pairs, corresponding to isolated atoms in a Mott-Hubbard insulating state. In GW the bonding / antibonding excitations merge at the Fermi level, while the satellites go towards $\pm U$. This just states that, while producing correlation satellites, GW is not able to capture Mott physics, with a self-energy that necessarily diverges at the Fermi level. This was already seen above, where we noted that the pole positions in the GW self-energy are wrong and actually interaction dependent.

The bonding / antibonding–splitting within the GW approximation is deduced as

$$\begin{aligned}
\Delta_{bab}^{GW} &= -c + \sqrt{c^2 + 4ct + 4t^2 + 4tU^2/c} \\
&= -2\sqrt{t(t+U)} + \sqrt{2\frac{2t+U}{t+U}\left(\sqrt{t(t+U)}(2t+U) + 2t(t+U) \right)}
\end{aligned} \tag{B.48}$$

However, in realistic calculation one usually does not solve the quasi-particle Equation (B.43), but rather computes the shifts relative to the Kohn-Sham energies in some

approximation. In this vein, we, alternatively, calculate the bab-splitting Δ_{bab}^{GW} by approximating the selfenergies in Equation (B.45) at the non-interacting bonding / antibonding-energies $\pm t$ [5]. Using Equation (B.46), this leads to

$$
\begin{aligned}
\Delta_{bab}^{GW\,shift} &= 2t + \Re\Sigma_{ab}(t) - \Re\Sigma_b(-t) = 2t + \frac{2U^2 t}{c}\frac{1}{2t+c} \\
&= 2t + \frac{U^2}{2\left(U + t + \sqrt{t(t+U)}\right)}
\end{aligned}
\tag{B.49}
$$

Figure B.7 compares the different bonding / antibonding–splittings. Indeed, the approximative splitting is much closer to the exact solution than the correct GW.
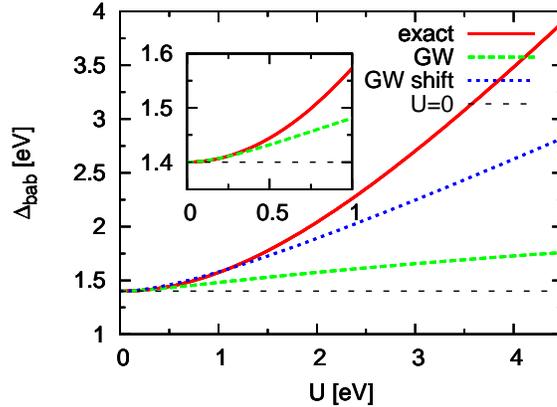

Figure B.7 : *Comparison of the bonding / antibonding–splitting: The exact $-2t + \sqrt{U^2 + 16t^2}$ expression, and the GW one, from the quasi-particle equation and from the approach leading to Equation (B.49). The inset shows a blow-up of the weak-coupling region.*

Finally, in view of LDA+U calculations for the monoclinic phase of VO_2, see Section A, Chapter 5, we comment on the applicability of Hartree-Fock theory to the current problem.
In the Hubbard molecule, as we have defined it (only local Coulomb interactions), the static part of the self-energy is given by the Hartree term. This amounts to simply setting $W_{ij}(\imath\nu_m) = U\delta_{ij}$ in Equation (B.30). Then the bonding / antibonding–splitting remains constant as a function of U, unchanged from its non-interacting value : $\Delta_{bab} = 2t$. Indeed, the Hartree term was canceled with the shift in the chemical potential that enforced the particle-hole symmetry. The reason for this is that a purely local interaction ($W_{ij} \sim \delta_{ij}$) cannot produce an off-diagonal element in the self-energy. Since both sites are equivalent ($\Sigma_{11} = \Sigma_{22}$), no relative shifts can be induced. This is no longer true, if the model is extended to non-local Coulomb interactions, i.e. non-vanishing off-diagonal elements in Equation (B.27).

---

[5]Of course one could have linearized the self-energy around the non-interacting energies.

LDA+U is in spirit a Hartree-Fock calculation. Due to the static nature of its self-energy, it cannot account for the Mott phenomenon. Further, the yielding of an insulating character for a system prerequisites the appearance of some kind of spin or orbital order[6]. In the current case, an ordering is induced by the dimerization. Nonetheless, since within LDA+U any correlation enhancement of a bonding / antibonding–splitting must come from the non-locality in the interaction, while in strongly correlated materials local interactions are likely to be predominant, we thus have to conclude that LDA+U is not suited for systems that exhibit both, correlation and dimerization effects. However, in the realistic case of M1 VO_2, though the gap-opening is largely dominated by dimer physics, a Hartree-Fock like calculation is of course able to result in an insulating band-structure, since the charge gap appears between the anti-bonding a_{1g} and low lying e_g^π orbitals.

---

[6]Often an order is forced upon the system, in order to make use of LDA+U; however this is unphysical.

Acknowledgments

Normalement, quand on ouvre la thèse de quelqu'un d'autre, ce sont les remerciements que l'on regarde tout d'abord. Et assez souvent la lecture s'arrête même là. Pour cette raison j'ai choisi de les cacher au fond du manuscrit. Comme ça, en parcourant, on voit au moins que j'ai mis des figures en couleurs.

D'où vient l'intérêt de lire les seuls mots que l'on peut considérer comme personnels dans une thèse? Est-ce que nous cherchons la personne derrière les formules (et les figures en couleurs, en particulier) ou bien voulons-nous vérifier si l'auteur nous a bien pris en compte? Ici, je vais essayer d'assurer le dernier sans en révéler trop quant au premier.

Mais commençons au début. Ce n'était point prévu que je ferai une thèse en France. En fait, j'étais juste venu pour passer une année d'études à l'étranger avant de finir mon diplôme à Heidelberg en Allemagne. En tant qu'étudiant Erasmus (un peu vieux déjà), je voulais quand même faire quelque chose de sérieux, mis à part l'expérience culturelle. C'est alors que j'ai postulé pour le DEA de physique des solides et milieux denses et je remercie particulièrement Michel Heritier de m'avoir accueilli et soutenu le long de cette année importante. Une période majeure était le stage du DEA, que j'ai eu le plaisir d'effectuer avec Ricardo Lobo au sein du laboratoire de Nicole Bontemps à l'ESPCI. C'est là où j'ai developpé un goût particulier pour les mesures optiques, ce qui, finalement, m'a mené a en faire un objet important de cette thèse théorique. De plus, je remercie Nicole Bontemps pour avoir accepté la tâche de faire partie de mon jury de thèse et de représenter le lien avec la physique expérimentale.

Réalisant la richesse des possibilités pour faire de la physique à Paris, les problèmes prévisibles de reconnaissance du DEA chez moi et le fait qu'en général, je me plaisais pas mal ici, je me suis decidé à rester pour démarrer un doctorat en France.

Avec Silke Biermann et le groupe d'Antoine Georges du Centre de Physique Théorique (CPHT) de l'Ecole Polytechnique j'ai trouvé la directrice et l'environnement qui me semblaient idéaux pour ce défi, et, à posteriori, je peux dire que je ne me suis vraiment pas trompé. Pendant les trois années suivantes, j'ai appris beaucoup. De prime d'abord je tiens à remercier ma directrice de thèse, Silke, pour son appui et son soutien infatiguables (jusqu'à des heures très avancées). Sur le chemin, elle répondait à toutes mes questions, même les plus stupides et me remontait le moral quand il le devenait nécessaire. Bien que elle ait été un guide dans tous les projets, j'ai joui de la liberté d'évoluer dans les directions qui m'intéressaient le plus. Ce serait pour moi un véritable plaisir de continuer à travailler avec elle sur des projets communs pendant mon postdoc et après. Egalement,

je dois beaucoup à Antoine. Son intérêt pour mon travail était pour moi toujours une source de motivation. En plus, il m'a fait l'honneur de présider ma soutenance de thèse.

Avec l'équipe du CPHT, j'ai eu la chance de trouver une atmosphère toujours chaleureuse et accueillante. Pour leur convivialité et leur soutien je remercie vivement mes collègues (dans l'ordre d'apparition): Luca de' Medici, Frank Lechermann, Sasha Poteryaev, Syed Hassan, Olivier Parcollet, Marcello Rozenberg, Bernard Amadon, Giovanni Sordi, Lam Dao, Leonid Pourovskii, Pablo Cornaglia, Daniel Rohe, Michel Ferrero, Lorenzo de Leo et Cyril Martins.

En dehors de l'équipe du CPHT, j'ai eu le plaisir de travailler avec des collaborateurs divers. Parmi eux, je remercie en particulier Ferdi Aryasetiawan et Takashi Miyake au AIST Tsukuba au Japon. J'ai eu le privilège de discuter avec eux à Paris et de travailler sur place à Tsukuba – une expérience considérable. C'est d'ailleurs avec eux et chez eux que je continuerai mes recherches.

De plus, je remercie Alexander Lichtenstein de Hamburg, Ole Andersen de Stuttgart, Alexey Rubtsov de Moscou et Tanusri Saha-Dasgupta de Kolkata pour notre collaboration et l'intérêt qu'ils ont porté à ce que j'ai fait. Aussi, je remercie Matteo Gatti et Lucia Reining pour des discussions très intéressantes.

Je remercie également les rapporteurs de ma thèse, Angel Rubio et Thomas Pruschke, qui m'ont fait l'honneur de faire partie de mon jury et qui ont lu mon manuscrit même pendant leurs vacances. Les discussions avec eux et leurs commentaires ont été très précieux.

Aussi, je dois exprimer ma gratitude envers Stéphane, Florence et Philippe, les informaticiens du labo, pour leur aide toujours rapide et compétente. Egalement, je remercie les secrétaires, Fadila, Florence, Malika et Jeannine pour m'avoir gentillement facilité la vie administrative en France.

Ce travail a été soutenu par une allocation internationale de thèse «Gaspard Monge» de l'Ecole Polytechnique, la Japan Society for the Promotion of Science (JSPS), la Japan Science and Technology Agency (JST) et le centre de calcul de haute performance Idris (projet 071393).

Mon contrat à l'Ecole Polytechnique disait «L'allocataire consacre l'intégralité de son activité à la préparation de son doctorat». Mais heureusement, on est en France, et la semaine de travail ne dure que 35 heures. Bien que les chiffres officiels et la réalité ne soient pas vraiment compatibles, le thésard a du temps libre pour oublier la physique et pour trouver des distractions, ou du moins pour les chercher. Dans cette entreprise, j'ai eu beaucoup d'aide et j'exprime toute ma gratitude à mes amis les plus proches en provenance de cinq continents (à nouveau dans l'ordre d'apparition) : Martin, Jan, Kenza, Melony, Eileen, Cemohn, Carlo, Riina, Angela, Kaori, Sabrina et Kristi.

Finalement, c'est du fond de mon cœur que je remercie mes parents pour leur soutien et compréhension tout au long de mon parcours. C'est à eux que je dois tout.

Paris 2007

Bibliography

[Abbate *et al.* (1991)] M. Abbate, F. M. F. de Groot, J. C. Fuggle, Y. J. Ma, C. T. Chen, F. Sette, A. Fujimori, Y. Ueda, and K. Kosuge. *Soft-x-ray-absorption studies of the electronic-structure changes through the VO_2 phase transition*. Phys. Rev. B **43** (1991)(9): 7263.

[Ahn and Millis(2000)] K. H. Ahn and A. J. Millis. *Effects of magnetic ordering on the anisotropy and temperature dependence of the optical conductivity in $LaMnO_3$: A tight-binding approach*. Phys. Rev. B **61** (2000)(20): 13545.

[Allen *et al.* (1993)] P. B. Allen, R. M. Wentzcovitch, W. W. Schulz, and P. C. Canfield. *Resistivity of the high-temperature metallic phase of VO_2*. Phys. Rev. B **48** (1993)(7): 4359.

[Andersen(1975)] O. K. Andersen. *Linear methods in band theory*. Phys. Rev. B **12** (1975)(8): 3060.

[Andersen and Saha-Dasgupta(2000)] O. K. Andersen and T. Saha-Dasgupta. *Muffin-tin orbitals of arbitrary order*. Phys. Rev. B **62** (2000)(24): R16219.

[Anderson(1961)] P. W. Anderson. *Localized Magnetic States in Metals*. Phys. Rev. **124** (1961)(1): 41.

[Andersson *et al.* (2007)] D. A. Andersson, S. I. Simak, B. Johansson, I. A. Abrikosov, and N. V. Skorodumova. *Modeling of CeO_2, Ce_2O_3, and CeO_{2-x} in the LDA + U formalism*. Phys. Rev. B **75** (2007)(3): 035109.

[Anisimov and Gunnarsson(1991)] V. I. Anisimov and O. Gunnarsson. *Density-functional calculation of effective Coulomb interactions in metals*. Phys. Rev. B **43** (1991)(10): 7570.

[Anisimov *et al.* (2005)] V. I. Anisimov, D. E. Kondakov, A. V. Kozhevnikov, I. A. Nekrasov, Z. V. Pchelkina, J. W. Allen, S.-K. Mo, H.-D. Kim, P. Metcalf, S. Suga, A. Sekiyama, G. Keller, I. Leonov, X. Ren, and D. Vollhardt. *Full orbital calculation scheme for materials with strongly correlated electrons*. Phys. Rev. B **71** (2005)(12): 125119.

[Anisimov *et al.* (1997)] V. I. Anisimov, A. I. Poteryaev, M. A. Korotin, A. O. Anokhin, and G. Kotliar. *First-principles calculations of the electronic structure and spectra*

of strongly correlated systems: dynamical mean-field theory. Journal of Physics: Condensed Matter **9** (1997)(35): 7359.

[Anisimov *et al.* (1991)] V. I. Anisimov, J. Zaanen, and O. K. Andersen. *Band theory and Mott insulators: Hubbard U instead of Stoner I*. Phys. Rev. B **44** (1991)(3): 943.

[Arai *et al.* (1998)] F. Arai, S. Kimura, and M. Ikezawa. *Resonant Photoemission Study of Electronic Structure of Rare-Earth Sesquioxides*. J. Phys. Soc. Jpn. **67** (1998)(1): 225.

[Aryasetiawan(2000)] F. Aryasetiawan. *Strong coulomb correlations in electronic structure calculations : beyond the local density approximation*. Editor: V. I. Anisimov. Amsterdam, The Netherlands : Gordon and Breach Science Publishers (2000).

[Aryasetiawan and Gunnarsson(1995)] F. Aryasetiawan and O. Gunnarsson. *Electronic Structure of NiO in the GW Approximation*. Phys. Rev. Lett. **74** (1995)(16): 3221.

[Aryasetiawan and Gunnarsson(1998)] —. *The GW method*. Rep. Prog. Phys. **61** (1998)(3): 237.

[Auerbach(1994)] A. Auerbach. *Interacting Electrons and Quantum Magnetism*. Springer Verlag (1994).

[Barker *et al.* (1966)] A. S. Barker, H. W. Verleur, and H. J. Guggenheim. *Infrared Optical Properties of Vanadium Dioxide Above and Below the Transition Temperature*. Phys. Rev. Lett. **17** (1966)(26): 1286.

[Beach(2004)] K. S. D. Beach. *Identifying the maximum entropy method as a special limit of stochastic analytic continuation*. arXiv.org (2004)(cond-mat/0403055).

[Beach *et al.* (2000)] K. S. D. Beach, R. J. Gooding, and F. Marsiglio. *Reliable Padé analytical continuation method based on a high-accuracy symbolic computation algorithm*. Phys. Rev. B **61** (2000)(8): 5147.

[Bianconi(1982)] A. Bianconi. *Multiplet splitting of final state configurations in x-ray-absorption spectrum of metal VO_2: Effect of core-hole-screening, electron correlation, and metal-insulator transition*. Phys. Rev. B **26** (1982)(6): 2741.

[Biermann(2001)] S. Biermann. *Reports of the Jülich Research Centre* **3899** (2001).

[Biermann(2006)] —. *LDA+DMFT - a Tool for Investigating the Electronic Structure of Materials with Strong Electronic Coulomb Correlations*. in Encyclopedia of Materials: Science and Technology (2006).

[Biermann *et al.* (2004)] S. Biermann, A. Dallmeyer, C. Carbone, W. Eberhardt, C. Pampuch, O. Rader, M. I. Katsnelson, and A. I. Lichtenstein. *Observation of Hubbard Bands in gamma-Manganese*. JETP Letters **80** (2004)(9): 612.

[Biermann *et al.* (2001)] S. Biermann, A. Georges, A. Lichtenstein, and T. Giamarchi. *Deconfinement Transition and Luttinger to Fermi Liquid Crossover in Quasi-One-Dimensional Systems*. Phys. Rev. Lett. **87** (2001)(27): 276405.

[Biermann *et al.* (2005)] S. Biermann, A. Poteryaev, A. I. Lichtenstein, and A. Georges. *Dynamical Singlets and Correlation-Assisted Peierls Transition in VO_2*. Phys. Rev. Lett. **94** (2005)(2): 026404.

[Blümer(2002)] N. Blümer. *Mott-Hubbard Metal-Insulator Transition and Optical Conductivity in High Dimensions*. PhD thesis, Universität Augsburg (2002).

[Blümer and van Dongen(2003)] N. Blümer and P. G. J. van Dongen. *Transport properties of correlated electrons in high dimensions* (2003).

[Brinkman and Rice(1970)] W. F. Brinkman and T. M. Rice. *Application of Gutzwiller's Variational Method to the Metal-Insulator Transition*. Phys. Rev. B **2** (1970)(10): 4302.

[Bruneval *et al.* (2006)] F. Bruneval, N. Vast, and L. Reining. *Effect of self-consistency on quasiparticles in solids*. Phys. Rev. B **74** (2006)(4): 045102.

[Bulla(2006)] R. Bulla. *Dynamical Mean-Field Theory - from Quantum Impurity Physics to Lattice Problems*. PHIL.MAG. **86** (2006): 1877.

[Byczuk *et al.* (2007)] K. Byczuk, M. Kollar, K. Held, Y. F. Yang, I. A. Nekrasov, T. Pruschke, and D. Vollhardt. *Kinks in the dispersion of strongly correlated electrons*. Nat Phys **3** (2007): 168.

[Caruthers and Kleinman(1973)] E. Caruthers and L. Kleinman. *Energy Bands of Semiconducting VO_2*. Phys. Rev. B **7** (1973)(8): 3760.

[Castellani *et al.* (1979)] C. Castellani, C. D. Castro, D. Feinberg, and J. Ranninger. *New Model Hamiltonian for the Metal-Insulator Transition*. Phys. Rev. Lett. **43** (1979)(26): 1957.

[Castellani *et al.* (1978a)] C. Castellani, C. R. Natoli, and J. Ranninger. *Insulating phase of V_2O_3: An attempt at a realistic calculation*. Phys. Rev. B **18** (1978a)(9): 4967.

[Castellani *et al.* (1978b)] —. *Magnetic structure of V_2O_3 in the insulating phase*. Phys. Rev. B **18** (1978b)(9): 4945.

[Castellani *et al.* (1978c)] —. *Metal-insulator transition in pure and Cr-doped V_2O_3*. Phys. Rev. B **18** (1978c)(9): 5001.

[Chae *et al.* (2006)] B.-G. Chae, H.-T. Kim, S.-J. Yun, B.-J. Kim, Y.-W. Lee, D.-H. Youn, and K.-Y. Kang. *Highly Oriented VO_2 Thin Films Prepared by Sol-Gel Deposition*. Electrochemical and Solid-State Letters **9** (2006)(1): C12.

[Chattopadhyay *et al.* (2000)] A. Chattopadhyay, A. J. Millis, and S. Das Sarma. *Optical spectral weights and the ferromagnetic transition temperature of colossal-magnetoresistance manganites: Relevance of double exchange to real materials.* *Phys. Rev. B* **61** (2000)(16): 10738.

[Chung and Freericks(1998)] W. Chung and J. K. Freericks. *Charge-transfer metal-insulator transitions in the spin-$\frac{1}{2}$ Falicov-Kimball model.* *Phys. Rev. B* **57** (1998)(19): 11955.

[Cohen-Tannoudji *et al.* (1992)] C. Cohen-Tannoudji, B. Diu, and F. Laloë. *Mécanique quantique.* Hermann (1992).

[Coleman(2004)] P. Coleman. *The evolving monogram on Many Body Physics* (2004).

[Continenza *et al.* (1999)] A. Continenza, S. Massidda, and M. Posternak. *Self-energy corrections in VO_2 within a model GW scheme.* *Phys. Rev. B* **60** (1999)(23): 15699.

[Cornaglia *et al.* (2007)] P. Cornaglia, A. J. Millis, and A. Georges. *to be published* (2007).

[CVRL(2006)] CVRL. *Colour and Vision Research Laboratories Institute of Ophthalmology, UCL, http://www.cvrl.org* (2006).

[Dagotto(1994)] E. Dagotto. *Correlated electrons in high-temperature superconductors.* *Rev. Mod. Phys.* **66** (1994)(3): 763.

[Di Matteo *et al.* (2002)] S. Di Matteo, N. B. Perkins, and C. R. Natoli. *Spin-1 effective Hamiltonian with three degenerate orbitals: An application to the case of V_2O_3.* *Phys. Rev. B* **65** (2002)(5): 054413.

[Dreizler and Gross(1990)] R. Dreizler and E. Gross. *Density Functional Theory – An Approach to the Quantum Many-Body Problem.* Springer Verlag (1990).

[Eguchi *et al.* (2006)] R. Eguchi, M. Taguchi, M. Matsunami, K. Horiba, K. Yamamoto, Y. Ishida, A. Chainani, Y. Takata, M. Yabashi, D. Miwa, Y. Nishino, K. Tamasaku, T. Ishikawa, Y. Senba, H. Ohashi, Y. Muraoka, Z. Hiroi, and S. Shin. *Evidence for a Mott-Hubbard metal-insulator transition in VO_2.* *cond-mat/0607712* (2006).

[Elfimov *et al.* (2003)] I. S. Elfimov, T. Saha-Dasgupta, and M. A. Korotin. *Role of c-axis pairs in V_2O_3 from the band-structure point of view.* *Phys. Rev. B* **68** (2003)(11): 113105.

[Eyert(2002)] V. Eyert. *The metal-insulator transitions of VO2: A band theoretical approach.* *Ann. Phys. (Leipzig)* **11** (2002): 650.

[Eyert *et al.* (2005)] V. Eyert, U. Schwingenschlögl, and U. Eckern. *Covalent bonding and hybridization effects in the corundum-type transition-metal oxides V_2O_3 and Ti_2O_3.* *Europhysics Letters (EPL)* **70** (2005)(6): 782.

[Ezhov *et al.* (1999)] S. Y. Ezhov, V. I. Anisimov, D. I. Khomskii, and G. A. Sawatzky. *Orbital Occupation, Local Spin, and Exchange Interactions in V_2O_3*. *Phys. Rev. Lett.* **83** (1999)(20): 4136.

[Fabris *et al.* (2005)] S. Fabris, S. de Gironcoli, S. Baroni, G. Vicario, and G. Balducci. *Taming multiple valency with density functionals: A case study of defective ceria*. *Phys. Rev. B* **71** (2005)(4): 041102.

[Fabrizio *et al.* (1999)] M. Fabrizio, A. O. Gogolin, and A. A. Nersesyan. *From Band Insulator to Mott Insulator in One Dimension*. *Phys. Rev. Lett.* **83** (1999)(10): 2014.

[Föex(1946)] M. Föex. *C. R. Acad. Sci. Paris* **B223** (1946)(1126).

[Gavini and Kwan(1972)] A. Gavini and C. C. Y. Kwan. *Optical Properties of Semiconducting VO_2 Films*. *Phys. Rev. B* **5** (1972)(8): 3138.

[Georges(2004)] A. Georges. *Strongly Correlated Electron Materials: Dynamical Mean-Field Theory and Electronic Structure*. *Lectures on the physics of highly correlated electron systems VI* **715** (2004): 3.

[Georges and Kotliar(1992)] A. Georges and G. Kotliar. *Hubbard model in infinite dimensions*. *Phys. Rev. B* **45** (1992)(12): 6479.

[Georges *et al.* (1996)] A. Georges, G. Kotliar, W. Krauth, and M. J. Rozenberg. *Dynamical mean-field theory of strongly correlated fermion systems and the limit of infinite dimensions*. *Rev. Mod. Phys.* **68** (1996)(1): 13.

[Gibson(1958)] J. B. Gibson. *Bull. Am. Phys. Soc.* **3** (1958): 146.

[Goering *et al.* (1997a)] E. Goering, M. Schramme, O. Müller, R. Barth, H. Paulin, M. Klemm, M. L. denBoer, and S. Horn. *LEED and photoemission study of the stability of VO_2 surfaces*. *Phys. Rev. B* **55** (1997a)(7): 4225.

[Goering *et al.* (1997b)] E. Goering, M. Schramme, O. Muller, H. Paulin, M. Klemm, M. L. denBoer, and S. Horn. *Angular-resolved photoemission on V2O3 and VO2*. *Physica B: Condensed Matter, Proceedings of the International Conference on Strongly Correlated Electron Systems* **230-232** (1997b): 996.

[Golubkov *et al.* (1995)] A. V. Golubkov, A. Prokof'ev, and A. I. Shelykh. *Optical characteristics of Ce_2O_3 single crystals*. *Phys. Solid State* **37** (1995)(6): 1028.

[Goodenough(1960)] J. B. Goodenough. *Direct Cation- -Cation Interactions in Several Oxides*. *Phys. Rev.* **117** (1960)(6): 1442.

[Goodenough(1971)] —. *The two components of the crystallographic transition in VO_2*. *J. Solid State Chem.* **3** (1971): 490.

[Granqvist(1990)] C. G. Granqvist. *Window coatings for the future. Thin Solid Films* **193-194** (1990)(Part 2): 730.

[Gunnarsson *et al.* (2003)] O. Gunnarsson, M. Calandra, and J. E. Han. *Colloquium: Saturation of electrical resistivity. Rev. Mod. Phys.* **75** (2003)(4): 1085.

[Gutzwiller(1963)] M. C. Gutzwiller. *Effect of Correlation on the Ferromagnetism of Transition Metals. Phys. Rev. Lett.* **10** (1963)(5): 159.

[Gygi and Baldereschi(1989)] F. Gygi and A. Baldereschi. *Quasiparticle energies in semiconductors: Self-energy correction to the local-density approximation. Phys. Rev. Lett.* **62** (1989)(18): 2160.

[Haule *et al.* (2005)] K. Haule, V. Oudovenko, S. Y. Savrasov, and G. Kotliar. *The alpha $->$ gamma Transition in Ce: A Theoretical View from Optical Spectroscopy. Physical Review Letters* **94** (2005)(3): 036401.

[Haverkort *et al.* (2005)] M. W. Haverkort, Z. Hu, A. Tanaka, W. Reichelt, S. V. Streltsov, M. A. Korotin, V. I. Anisimov, H. H. Hsieh, H.-J. Lin, C. T. Chen, D. I. Khomskii, and L. H. Tjeng. *Orbital-Assisted Metal-Insulator Transition in VO_2. Phys. Rev. Lett.* **95** (2005)(19): 196404.

[Hay *et al.* (2006)] P. J. Hay, R. L. Martin, J. Uddin, and G. E. Scuseria. *Theoretical study of CeO_2 and Ce_2O_3 using a screened hybrid density functional. The Journal of Chemical Physics* **125** (2006)(3): 034712.

[Hedin(1965)] L. Hedin. *New Method for Calculating the One-Particle Green's Function with Application to the Electron-Gas Problem. Phys. Rev.* **139** (1965)(3A): A796.

[Hedin(1999)] —. *On correlation effects in electron spectroscopies and the GW approximation. Journal of Physics: Condensed Matter* **11** (1999)(42): R489.

[Held *et al.* (2001)] K. Held, G. Keller, V. Eyert, D. Vollhardt, and V. I. Anisimov. *Mott-Hubbard Metal-Insulator Transition in Paramagnetic V_2O_3: An LDA + DMFT(QMC) Study. Phys. Rev. Lett.* **86** (2001)(23): 5345.

[Held *et al.* (2003)] K. Held, I. A. Nekrasov, G. Keller, V. Eyert, N. Blümer, A. K. McMahan, R. T. Scalettar, T. Pruschke, V. I. Anisimov, and D. Vollhardt. *Realistic investigations of correlated electron systems within LDA+DMFT. Psi-k Newsletter* **56** (2003)(65).

[Hérbert *et al.* (2002)] C. Hérbert, M. Willinger, D. Su, P. Pongratz, P. Schattschneider, and R. Schlögl. *Oxygen K-edge in vanadium oxides: simulations and experiments. Eur. Phys. J. B* **28** (2002): 407.

[Hirsch(1983)] J. E. Hirsch. *Discrete Hubbard-Stratonovich transformation for fermion lattice models. Phys. Rev. B* **28** (1983)(7): 4059.

[Hirsch and Fye(1986)] J. E. Hirsch and R. M. Fye. *Monte Carlo Method for Magnetic Impurities in Metals*. Phys. Rev. Lett. **56** (1986)(23): 2521.

[Hoffmann(2000)] G. Hoffmann. *CIE Color Space* (2000).

[Hohenberg and Kohn(1964)] P. Hohenberg and W. Kohn. *Inhomogeneous Electron Gas*. Phys. Rev. **136** (1964)(3B): B864.

[Huang *et al.* (1998)] X. Huang, W. Yang, and U. Eckern. *Metal-insulator transition in VO_2: a Peierls-Mott-Hubbard mechanism. cond-mat/9808137* (1998).

[Hubbard(1963)] J. Hubbard. *Electron Correlations in Narrow Energy Bands*. Royal Society of London Proceedings Series A **276** (1963): 238.

[Imada *et al.* (1998)] M. Imada, A. Fujimori, and Y. Tokura. *Metal-insulator transitions*. Rev. Mod. Phys. **70** (1998)(4): 1039.

[Jaebeom Yoo and Baranger(2005)] R. K. K. D. U. Jaebeom Yoo, Shailesh Chandrasekharan and H. U. Baranger. *On the sign problem in the Hirsch and Fye algorithm for impurity problems*. Journal of Physics A: Mathematical and General **38** (2005)(48): 10307.

[Jarrell *et al.* (1995)] M. Jarrell, J. K. Freericks, and T. Pruschke. *Optical conductivity of the infinite-dimensional Hubbard model*. Phys. Rev. B **51** (1995)(17): 11704.

[Jarrell and Gubernatis(1996)] M. Jarrell and J. E. Gubernatis. *Physics Reports* **269** (1996): 133.

[Jayaraman *et al.* (1970)] A. Jayaraman, D. B. McWhan, J. P. Remeika, and P. D. Dernier. *Critical Behavior of the Mott Transition in Cr-Doped V_2O_3*. Phys. Rev. B **2** (1970)(9): 3751.

[Jones and Gunnarsson(1989)] R. O. Jones and O. Gunnarsson. *The density functional formalism, its applications and prospects*. Rev. Mod. Phys. **61** (1989)(3): 689.

[Kanamori(1963)] J. Kanamori. *Electron Correlation and Ferromagnetism of Transition Metals*. Progress of Theoretical Physics **30** (1963)(3): 275.

[Keiter and Kimball(1970)] H. Keiter and J. C. Kimball. *Perturbation Technique for the Anderson Hamiltonian*. Phys. Rev. Lett. **25** (1970)(10): 672.

[Keller *et al.* (2004)] G. Keller, K. Held, V. Eyert, D. Vollhardt, and V. I. Anisimov. *Electronic structure of paramagnetic V_2O_3: Strongly correlated metallic and Mott insulating phase*. Phys. Rev. B **70** (2004)(20): 205116.

[Khurana(1990)] A. Khurana. *Electrical conductivity in the infinite-dimensional Hubbard model*. Phys. Rev. Lett. **64** (1990)(16): 1990.

[Kimura *et al.* (2000)] S. Kimura, F. Arai, and M. Ikezawa. *Optical Study on Electronic Structure of Rare-Earth Sesquioxides*. J. Phys. Soc. Jpn. **69** (2000)(10): 3451.

[Koethe *et al.* (2006)] T. C. Koethe, Z. Hu, M. W. Haverkort, C. Schussler-Langeheine, F. Venturini, N. B. Brookes, O. Tjernberg, W. Reichelt, H. H. Hsieh, H.-J. Lin, C. T. Chen, and L. H. Tjeng. *Transfer of Spectral Weight and Symmetry across the Metal-Insulator Transition in VO_2*. Phys. Rev. Lett. **97** (2006)(11): 116402.

[Kohn(1964)] W. Kohn. *Theory of the Insulating State*. Phys. Rev. **133** (1964)(1A): A171.

[Kohn and Sham(1965)] W. Kohn and L. J. Sham. *Self-Consistent Equations Including Exchange and Correlation Effects*. Phys. Rev. **140** (1965)(4A): A1133.

[Korotin *et al.* (2002)] M. A. Korotin, N. A. Skorikov, and V. I. Anisimov. *Phys. Met. Metallogr.* **94** (2002)(1): 17.

[Kotliar(1999)] G. Kotliar. *Landau theory of the Mott transition in the fully frustrated Hubbard model in infinite dimensions*. The European Physical Journal B **11** (1999)(1): 27.

[Kotliar *et al.* (2000)] G. Kotliar, E. Lange, and M. J. Rozenberg. *Landau Theory of the Finite Temperature Mott Transition*. Phys. Rev. Lett. **84** (2000)(22): 5180.

[Kotliar *et al.* (2006)] G. Kotliar, S. Y. Savrasov, K. Haule, V. S. Oudovenko, O. Parcollet, and C. A. Marianetti. *Electronic structure calculations with dynamical mean-field theory*. Rev. Mod. Phys. **78** (2006)(3): 865.

[Kotliar and Vollhardt(2004)] G. Kotliar and D. Vollhardt. *Strongly Correlated Materials: Insights from Dynamical Mean-Field Theory*. Physics Today **57** (2004)(3): 53.

[Kurmaev *et al.* (1998)] E. Z. Kurmaev, V. M. Cherkashenko, Y. M. Yarmoshenko, S. Bartkowski, A. V. Postnikov, M. Neumann, L. C. Duda, J. H. Guo, J. Nordgren, V. A. Perelyaev, and W. Reichelt. *Electronic structure of VO2 studied by x-ray photoelectron and x-ray emission spectroscopies*. J. Phys.:Cond. Matter **10** (1998): 4081.

[Kuwamoto *et al.* (1980)] H. Kuwamoto, J. M. Honig, and J. Appel. *Electrical properties of the $(V_{1-x}Cr_x)_2O_3$ system*. Phys. Rev. B **22** (1980)(6): 2626.

[Laad *et al.* (2003)] M. S. Laad, L. Craco, and E. Müller-Hartmann. *Orbital Switching and the First-Order Insulator-Metal Transition in Paramagnetic V_2O_3*. Phys. Rev. Lett. **91** (2003)(15): 156402.

[Laad *et al.* (2005)] M. S. Laad, L. Craco, and E. Müller-Hartmann. *VO_2: A two-fluid incoherent metal?*. Europhysics Letters (EPL) **69** (2005)(6): 984.

[Laad *et al.* (2006a)] M. S. Laad, L. Craco, and E. Müller-Hartmann. *Metal-insulator transition in rutile-based VO_2*. Phys. Rev. B **73** (2006a)(19): 195120.

[Laad *et al.* (2006b)] M. S. Laad, L. Craco, and E. Muller-Hartmann. *Orbital-selective insulator-metal transition in V_2O_3] under external pressure.* Phys. Rev. B **73** (2006b)(4): 045109.

[Ladd and Paul(1969)] L. A. Ladd and W. Paul. *Optical and Transport Properties of high quality crystals of V_2O_4 near the metallic transition temperature.* Solid State Commun. **7** (1969): 425.

[Lechermann *et al.* (2005)] F. Lechermann, S. Biermann, and A. Georges. *Importance of Interorbital Charge Transfers for the Metal-to-Insulator Transition of $BaVS_3$.* Phys. Rev. Lett. **94** (2005)(16): 166402.

[Lechermann *et al.* (2006)] F. Lechermann, A. Georges, A. Poteryaev, S. Biermann, M. Posternak, A. Yamasaki, and O. K. Andersen. *Dynamical mean-field theory using Wannier functions: A flexible route to electronic structure calculations of strongly correlated materials.* Phys. Rev. B **74** (2006)(12): 125120.

[Lederer *et al.* (1972)] P. Lederer, H. Launois, J. P. Pouget, A. Casalot, and Villeneuve. *Contribution to the stuudy of the Metal-Insulator Transition in the $V_{1-x}Nb_xO_2$ System - III. Theoretical Discussion.* J. Phys. Chem. Solids **33** (1972): 1969.

[Lichtenstein and Katsnelson(1998)] A. I. Lichtenstein and M. I. Katsnelson. *Ab initio calculations of quasiparticle band structure in correlated systems: LDA++ approach.* Phys. Rev. B **57** (1998)(12): 6884.

[Lieb(1983)] E. H. Lieb. *Density functionals for coulomb systems.* Int. J. Quant. Chem. **24** (1983)(3): 243.

[Liebsch *et al.* (2005)] A. Liebsch, H. Ishida, and G. Bihlmayer. *Coulomb correlations and orbital polarization in the metal-insulator transition of VO_2.* Phys. Rev. B **71** (2005)(8): 085109.

[Limelette *et al.* (2003)] P. Limelette, A. Georges, D. Jérome, P. Wzietek, P. Metcalf, and J. M. Honig. *Science* (2003)(302): 89.

[Loschen *et al.* (2007)] C. Loschen, J. Carrasco, K. M. Neyman, and F. Illas. *First-principles LDA + U and GGA + U study of cerium oxides: Dependence on the effective U parameter.* Phys. Rev. B **75** (2007)(3): 035115.

[Mahan(1990)] G. D. Mahan. *Many-particle Physics.* Plenum Press (1990).

[Maldague(1977)] P. F. Maldague. *Optical spectrum of a Hubbard chain.* Phys. Rev. B **16** (1977)(6): 2437.

[Marezio *et al.* (1972)] M. Marezio, D. B. McWhan, J. P. Remeika, and P. D. Dernier. *Structural Aspects of the Metal-Insulator Transitions in Cr-Doped VO_2.* Phys. Rev. B **5** (1972)(7): 2541.

[Marzari and Vanderbilt(1997)] N. Marzari and D. Vanderbilt. *Maximally localized generalized Wannier functions for composite energy bands*. Phys. Rev. B **56** (1997)(20): 12847.

[Massidda *et al.* (1995)] S. Massidda, A. Continenza, M. Posternak, and A. Baldereschi. *Band-Structure Picture for MnO Reexplored: A Model GW Calculation*. Phys. Rev. Lett. **74** (1995)(12): 2323.

[Mattheiss(1994)] L. F. Mattheiss. *Band properties of metallic corundum-phase V2O3*. J. Phys.: Condens. Matter **6** (1994): 6477.

[McWhan *et al.* (1973)] D. B. McWhan, A. Menth, J. P. Remeika, W. F. Brinkman, and T. M. Rice. *Metal-Insulator Transitions in Pure and Doped V_2O_3*. Phys. Rev. B **7** (1973)(5): 1920.

[McWhan *et al.* (1971)] D. B. McWhan, J. P. Remeika, T. M. Rice, W. F. Brinkman, J. P. Maita, and A. Menth. *Electronic Specific Heat of Metallic Ti-Doped V_2O_3*. Phys. Rev. Lett. **27** (1971)(14): 941.

[McWhan *et al.* (1969)] D. B. McWhan, T. M. Rice, and J. P. Remeika. *Mott Transition in Cr-Doped V_2O_3*. Phys. Rev. Lett. **23** (1969)(24): 1384.

[Metzner and Vollhardt(1989)] W. Metzner and D. Vollhardt. *Correlated Lattice Fermions in $d = \infty$ Dimensions*. Phys. Rev. Lett. **62** (1989)(3): 324.

[Mikami and Nakamura(2006)] M. Mikami and S. Nakamura. *Electronic structure of rare-earth sesquioxides and oxysulfides*. Journal of Alloys and Compounds **408-412** (2006): 687.

[Mila *et al.* (2000)] F. Mila, R. Shiina, F.-C. Zhang, A. Joshi, M. Ma, V. Anisimov, and T. M. Rice. *Orbitally Degenerate Spin-1 Model for Insulating V_2O_3*. Phys. Rev. Lett. **85** (2000)(8): 1714.

[Millis(2004)] A. J. Millis. *Optical Conductivity and Correlated Electron Physics*. In *Strong Interactions in Low Dimensions* (edited by L. D. D. Baeriswyl), vol. 25, (p. 195ff). Physics and Chemistry of Materials with Low-Dimensional Structures (2004).

[Minar *et al.* (2005)] J. Minar, L. Chioncel, A. Perlov, H. Ebert, M. I. Katsnelson, and A. I. Lichtenstein. *Multiple-scattering formalism for correlated systems: A KKR-DMFT approach*. Phys. Rev. B **72** (2005)(4): 045125.

[Mo *et al.* (2003)] S.-K. Mo, J. D. Denlinger, H.-D. Kim, J.-H. Park, J. W. Allen, A. Sekiyama, A. Yamasaki, K. Kadono, S. Suga, Y. Saitoh, T. Muro, P. Metcalf, G. Keller, K. Held, V. Eyert, V. I. Anisimov, and D. Vollhardt. *Prominent Quasiparticle Peak in the Photoemission Spectrum of the Metallic Phase of V_2O_3*. Phys. Rev. Lett. **90** (2003)(18): 186403.

[Mo et al. (2006)] S.-K. Mo, H.-D. Kim, J. D. Denlinger, J. W. Allen, J.-H. Park, A. Sekiyama, A. Yamasaki, S. Suga, Y. Saitoh, T. Muro, and P. Metcalf. *Photoemission study of $(V_{1-x}M_x)_2O_3$ (M = Cr,Ti)*. Phys. Rev. B **74** (2006)(16): 165101.

[Moon(1970)] R. M. Moon. *Antiferromagnetism in V_2O_3*. Phys. Rev. Lett. **25** (1970)(8): 527.

[Morin(1959)] F. J. Morin. *Oxides Which Show a Metal-to-Insulator Transition at the Neel Temperature*. Phys. Rev. Lett. **3** (1959)(1): 34.

[Mossanek and Abbate(2007)] R. J. O. Mossanek and M. Abbate. *Optical response of metallic and insulating VO2 calculated with the LDA approach*. Journal of Physics: Condensed Matter **19** (2007)(34): 346225 (10pp).

[Mott(1990)] N. F. Mott. *Metal-Insulator transition*. Taylor and Francis, London (1990).

[Müller et al. (1997)] O. Müller, J. P. Urbach, E. Goering, T. Weber, R. Barth, H. Schuler, M. Klemm, S. Horn, and M. L. denBoer. *Spectroscopy of metallic and insulating V_2O_3*. Phys. Rev. B **56** (1997)(23): 15056.

[Müller-Hartmann(1989)] E. Müller-Hartmann. *The Hubbard model at high dimensions: some exact results and weak coupling theory*. Zeitschrift für Physik B Condensed Matter **76** (1989)(2): 211.

[Mullins et al. (1998)] D. R. Mullins, S. H. Overbury, and D. R. Huntley. *Electron spectroscopy of single crystal and polycrystalline cerium oxide surfaces*. Surface Science **409** (1998)(2): 309.

[Naoto Hirosaki and Kocer(2003)] S. O. Naoto Hirosaki and C. Kocer. *Ab initio calculation of the crystal structure of the lanthanide Ln2O3 sesquioxides*. Journal of Alloys and Compounds **351** (2003)(1-2): 31.

[Nassau(2001)] K. Nassau. *The Physics and Chemistry of Color: The Fifteen Causes of Color, 2nd Edition*. Wiley Series in Pure & Applied Optics (2001).

[Nekrasov et al. (2006)] I. A. Nekrasov, K. Held, G. Keller, D. E. Kondakov, T. Pruschke, M. Kollar, O. K. Andersen, V. I. Anisimov, and D. Vollhardt. *Momentum-resolved spectral functions of $SrVO_3$ calculated by LDA + DMFT*. Phys. Rev. B **73** (2006)(15): 155112.

[Okazaki et al. (2006)] K. Okazaki, S. Sugai, Y. Muraoka, and Z. Hiroi. *Role of electron-electron and electron-phonon interaction effects in the optical conductivity of VO_2*. Phys. Rev. B **73** (2006)(16): 165116.

[Okazaki et al. (2004)] K. Okazaki, H. Wadati, A. Fujimori, M. Onoda, Y. Muraoka, and Z. Hiroi. *Photoemission study of the metal-insulator transition in $VO_2/TiO_2(001)$: Evidence for strong electron-electron and electron-phonon interaction*. Phys. Rev. B **69** (2004)(16): 165104.

[Onida *et al.* (2002)] G. Onida, L. Reining, and A. Rubio. *Electronic excitations: density-functional versus many-body Green's-function approaches*. Rev. Mod. Phys. **74** (2002)(2): 601.

[Oudovenko *et al.* (2004)] V. S. Oudovenko, G. Palsson, S. Y. Savrasov, K. Haule, and G. Kotliar. *Calculations of optical properties in strongly correlated materials*. Phys. Rev. B **70** (2004)(12): 125112.

[Pálsson(2001)] G. Pálsson. *Computational studies of thermoelectricity in strongly correlated electron systems*. PhD thesis, Rutgers, The State University of New Jersey (2001).

[Paolasini *et al.* (1999)] L. Paolasini, C. Vettier, F. de Bergevin, F. Yakhou, D. Mannix, A. Stunault, W. Neubeck, M. Altarelli, M. Fabrizio, P. A. Metcalf, and J. M. Honig. *Orbital Occupancy Order in V_2O_3: Resonant X-Ray Scattering Results*. Phys. Rev. Lett. **82** (1999)(23): 4719.

[Park *et al.* (2000)] J.-H. Park, L. H. Tjeng, A. Tanaka, J. W. Allen, C. T. Chen, P. Metcalf, J. M. Honig, F. M. F. de Groot, and G. A. Sawatzky. *Spin and orbital occupation and phase transitions in V_2O_3*. Phys. Rev. B **61** (2000)(17): 11506.

[Pavarini *et al.* (2004)] E. Pavarini, S. Biermann, A. Poteryaev, A. I. Lichtenstein, A. Georges, and O. K. Andersen. *Mott Transition and Suppression of Orbital Fluctuations in Orthorhombic $3d^1$ Perovskites*. Physical Review Letters **92** (2004)(17): 176403.

[Pavarini *et al.* (2005)] E. Pavarini, A. Yamasaki, J. Nuss, and O. K. Andersen. *How chemistry controls electron localization in $3d^1$ perovskites: a Wannier-function study*. New Journal of Physics **7** (2005): 188.

[Peierls(1933)] R. Peierls. *Z. Physik* **80** (1933): 763.

[Perdew *et al.* (1982)] J. P. Perdew, R. G. Parr, M. Levy, and J. L. Balduz. *Density-Functional Theory for Fractional Particle Number: Derivative Discontinuities of the Energy*. Phys. Rev. Lett. **49** (1982)(23): 1691.

[Petit *et al.* (2005)] L. Petit, A. Svane, Z. Szotek, and W. M. Temmerman. *First-principles study of rare-earth oxides*. Phys. Rev. B **72** (2005)(20): 205118.

[Pines and Noziere(1965)] D. Pines and P. Noziere. *Theory of Quantum Liquids*. Oxford University (1965).

[Pinto *et al.* (1982)] H. Pinto, M. N. Mintz, M. Melamud, and H. Shaked. *Neutron diffraction study of Ce_2O_3*. Physics Letters **88A** (1982)(2): 81.

[Pollehn *et al.* (1998)] T. J. Pollehn, A. Schindlmayr, and R. W. Godby. *Assessment of the GW approximation using Hubbard chains*. Journal of Physics: Condensed Matter **10** (1998)(6): 1273.

[Poteryaev *et al.* (2007)] A. I. Poteryaev, J. M. Tomczak, S. Biermann, A. Georges, A. I. Lichtenstein, A. N. Rubtsov, T. Saha-Dasgupta, and O. K. Andersen. *Enhanced crystal-field splitting and orbital-selective coherence induced by strong correlations in V[sub 2]O[sub 3]*. *Physical Review B (Condensed Matter and Materials Physics)* **76** (2007)(8): 085127.

[Pouget and Launois(1976)] J. P. Pouget and H. Launois. *Metal Insulator Phase Transition in VO_2*. *J.Phys. France* **37** (1976): C4.

[Pouget *et al.* (1975)] J. P. Pouget, H. Launois, J. P. D'Haenens, P. Merenda, and T. M. Rice. *Electron Localization Induced by Uniaxial Stress in Pure VO_2*. *Phys. Rev. Lett.* **35** (1975)(13): 873.

[Pouget *et al.* (1974)] J. P. Pouget, H. Launois, T. M. Rice, P. Dernier, A. Gossard, G. Villeneuve, and P. Hagenmuller. *Dimerization of a linear Heisenberg chain in the insulating phases of $V_{1-x}Cr_xO_2$*. *Phys. Rev. B* **10** (1974)(5): 1801.

[Pouget *et al.* (1972)] J. P. Pouget, P. Lederer, D. S. Schreiber, H. Launois, D. Wohlleben, A. Casalot, and Villeneuve. *Contribution to the stuudy of the Metal-Insulator Transition in the $V_{1-x}Nb_xO_2$ System - II. Magnetic Properties*. *J. Phys. Chem. Solids* **33** (1972): 1961.

[Pourovskii *et al.* (2007a)] L. V. Pourovskii, B. Amadon, S. Biermann, and A. Georges. *Self-consistency over the charge-density in dynamical mean-field theory: a linear muffin-tin implementation and some physical implications* (2007a).

[Pourovskii *et al.* (2007b)] L. V. Pourovskii, J. M. Tomczak, A. Georges, R. Windiks, E. Wimmer, and S. Biermann. *Impact of strong correlations on optical properties of the rare-earth sesquioxides* (2007b). In preparation.

[Prokofiev *et al.* (1995)] A. Prokofiev, A. I. Shelykh, and B. T. Melekh. *Periodicity in the band gap variation of Ln_2X_3 (X=O, S, Se) in the lanthanide series*. *J. of Alloys and Comp.* **242** (1995): 41.

[Pruschke *et al.* (1993a)] T. Pruschke, D. L. Cox, and M. Jarrell. *Europhys. Lett.* **21** (1993a): 593.

[Pruschke *et al.* (1993b)] —. *Hubbard model at infinite dimensions: Thermodynamic and transport properties*. *Phys. Rev. B* **47** (1993b)(7): 3553.

[Pruschke *et al.* (1995)] T. Pruschke, M. Jarrell, and J. K. Freericks. *Anomalous normal-state properties of high-Tc superconductors: intrinsic properties of strongly correlated electron systems?*. *Advances in Physics* **44** (1995)(2): 187.

[Pruschke *et al.* (1996)] T. Pruschke, J. Obermeier, J. Keller, and M. Jarrell. *Spectral properties and bandstructure of correlated electron systems*. *Physica B: Condensed Matter, Proceedings of the International Conference on Strongly Correlated Electron Systems* **223-224** (1996): 611.

[Qazilbash *et al.* (2007)] M. Qazilbash, A. Schafgans, K. Burch, S. Yun, B. Chae, B. Kim, H. Kim, and D. Basov. *Electrodynamics of the vanadium oxides VO_2 and V_2O_3. unpublished* (2007).

[Qazilbash(2007)] M. M. Qazilbash. *private communication* (2007).

[Qazilbash *et al.* (2006)] M. M. Qazilbash, K. S. Burch, D. Whisler, D. Shrekenhamer, B. G. Chae, H. T. Kim, and D. N. Basov. *Correlated metallic state of vanadium dioxide. Phys. Rev. B* **74** (2006)(20): 205118.

[Rini *et al.* (2005)] M. Rini, C. A., R. W. Schoenlein, R. Lopez, L. C. Feldman, R. F. Haglund Jr., L. A. Boatner, and T. E. Haynes. *Photoinduced phase transition in VO2 nanocrystals: ultrafast control of surface-plasmon resonance. Opt. Lett.* **30** (2005): 558.

[Rozenberg *et al.* (1996)] M. J. Rozenberg, G. Kotliar, and H. Kajueter. *Transfer of spectral weight in spectroscopies of correlated electron systems. Phys. Rev. B* **54** (1996)(12): 8452.

[Rozenberg *et al.* (1995)] M. J. Rozenberg, G. Kotliar, H. Kajueter, G. A. Thomas, D. H. Rapkine, J. M. Honig, and P. Metcalf. *Optical Conductivity in Mott-Hubbard Systems. Phys. Rev. Lett.* **75** (1995)(1): 105.

[Saha-Dasgupta *et al.* (2007)] T. Saha-Dasgupta, O. K. Andersen, and A. Poteryaev. *Wannier orbitals and first-principles modeling of V_2O_3: an NMTO study. unpublished* (2007).

[Savrasov *et al.* (2001)] S. Y. Savrasov, G. Kotliar, and E. Abrahams. *Correlated electrons in δ-plutonium within a dynamical mean-field picture. Nature* **410** (2001)(6830): 793.

[Sawatzky and Post(1979)] G. A. Sawatzky and D. Post. *X-ray photoelectron and Auger spectroscopy study of some vanadium oxides. Phys. Rev. B* **20** (1979)(4): 1546.

[Scalapino *et al.* (1992)] D. J. Scalapino, S. R. White, and S. C. Zhang. *Superfluid density and the Drude weight of the Hubbard model. Phys. Rev. Lett.* **68** (1992)(18): 2830.

[Schindlmayr(1997)] A. Schindlmayr. *Violation of particle number conservation in the GW approximation. Phys. Rev. B* **56** (1997)(7): 3528.

[Schramme(2000)] M. Schramme. PhD thesis, Universität Augsburg (2000).

[Shastry and Sutherland(1990)] B. S. Shastry and B. Sutherland. *Twisted boundary conditions and effective mass in Heisenberg-Ising and Hubbard rings. Phys. Rev. Lett.* **65** (1990)(2): 243.

[Shin *et al.* (1990)] S. Shin, S. Suga, M. Taniguchi, M. Fujisawa, H. Kanzaki, A. Fujimori, H. Daimon, Y. Ueda, K. Kosuge, and S. Kachi. *Vacuum-ultraviolet reflectance and photoemission study of the metal-insulator phase transitions in VO_2, V_6O_{13}, and V_2O_3*. Phys. Rev. B **41** (1990)(8): 4993.

[Singh *et al.* (2006)] N. Singh, S. M. Saini, T. Nautiyal, and S. A. luck. *Electronic structure and optical properties of rare earth sesquioxides (R_2O_3, R = La, Pr, and Nd)*. Journal of Applied Physics **100** (2006)(8): 083525.

[Skorodumova *et al.* (2001)] N. V. Skorodumova, R. Ahuja, S. I. Simak, I. A. Abrikosov, B. Johansson, and B. I. Lundqvist. *Electronic, bonding, and optical properties of CeO_2 and Ce_2O_3 from first principles*. Phys. Rev. B **64** (2001)(11): 115108.

[Sommers and Doniach(1978)] C. Sommers and S. Doniach. *First principles calculation of the intra-atomic correlation energy in VO_2*. Solid State Commun. **28** (1978): 133.

[Tanaka(2003)] A. Tanaka. *A New Scenario on the Metal-Insulator Transition in VO_2*. J. Phys. Soc. Jpn. **72** (2003)(10): 2433.

[Tanaka(2004)] —. *Electronic Structure and Phase Transition in V2O3: Importance of 3d Spin-Orbit Interaction and Lattice Distortion*. J. Phys. Soc. Jpn. **71** (2004)(4).

[Thomas *et al.* (1994a)] G. A. Thomas, D. H. Rapkine, S. A. Carter, A. J. Millis, T. F. Rosenbaum, P. Metcalf, and J. M. Honig. *Observation of the Gap and Kinetic Energy in a Correlated Insulator*. Phys. Rev. Lett. **73** (1994a)(11): 1529.

[Thomas *et al.* (1994b)] G. A. Thomas, D. H. Rapkine, S. A. Carter, T. F. Rosenbaum, P. Metcalf, and J. M. Honig. *Optical properties of a correlated electron system: V2O3*. J. Low Temp. Phys. **95** (1994b)(1-2): 33.

[Tomczak(2004)] J. M. Tomczak. *La Réponse Optique de $Pr_{1.89}Ce_{0.11}CuO_4$* (2004). Rapport de stage du DEA de Physique de Solids et Milieux Denses.

[Tomczak *et al.* (2007)] J. M. Tomczak, F. Aryasetiawan, and S. Biermann. *Effective bandstructure in the insulating phase versus strong dynamical correlations in metallic VO_2* (2007). Submitted to Phys. Rev. Lett., preprint: arXiv:0704.0902.

[Tomczak and Biermann(2007a)] J. M. Tomczak and S. Biermann. *Effective band structure of correlated materials: the case of VO_2*. Journal of Physics: Condensed Matter **19** (2007a)(36): 365206.

[Tomczak and Biermann(2007b)] —. *Optical properties of strongly correlated materials – Generalized Peierls approach and its application to VO_2* (2007b). In preparation.

[Ueda *et al.* (1980)] Y. Ueda, K. Kosuge, and S. Kachi. *Phase Diagram and Some Physical Properties of V2O3 x(0<=x<=0.080)*. J. Solid State Chem. **31** (1980)(171).

[Ueda *et al.* (1979)] Y. Ueda, K. Kosuge, S. Kachi, and T. Takada. *J. Phys. (Paris), Colloq.* **C2** (1979)(275.a).

[van Schilfgaarde *et al.* (2006)] M. van Schilfgaarde, T. Kotani, and S. Faleev. *Quasiparticle Self-Consistent GW Theory*. *Physical Review Letters* **96** (2006)(22): 226402.

[Verleur *et al.* (1968)] H. W. Verleur, A. S. Barker, and C. N. Berglund. *Optical Properties of VO_2 between 0.25 and 5 eV*. *Phys. Rev.* **172** (1968)(3): 788.

[Villeneuve *et al.* (1972)] G. Villeneuve, A. Bordet, A. Casalot, J. P. Pouget, H. Launois, and P. Lederer. *Contribution to the stuudy of the Metal-Insulator Transition in the $V_{1-x}Nb_xO_2$ System - I. Crystallographic and Transport Properties*. *J. Phys. Chem. Solids* **33** (1972): 1953.

[Vollhardt(1991)] D. Vollhardt. *Investigation of correlated electron systems using the limit of high dimensions – Lecture-Notes for the 9th Jerusalem Winter School for Theoretical Physics, Jerusalem 30. Dec. 1991 - 8. Jan. 1992*. V. J. Emery (World Scientific, Singapore) (1991).

[Wannier(1962)] G. H. Wannier. *Dynamics of Band Electrons in Electric and Magnetic Fields*. *Rev. Mod. Phys.* **34** (1962)(4): 645.

[Wentzcovitch *et al.* (1994)] R. M. Wentzcovitch, W. W. Schulz, and P. B. Allen. *VO_2: Peierls or Mott-Hubbard? A view from band theory*. *Phys. Rev. Lett.* **72** (1994)(21): 3389.

[Zimmers(2004)] A. Zimmers. *Etude par spectroscopie infrarouge de l'électrodynamique du supraconducteur $Pr_{2-x}Ce_xCuO_4$ et de la manganite $La_{2/3}Ca_{1/3}MnO_3$*. PhD thesis, ESPCI, Paris (2004).

[Zlatic and Horvatic(1990)] V. Zlatic and B. Horvatic. *The local approximation for correlated systems on high dimensional lattices*. *Solid State Communications* **75** (1990)(3): 263.

[Zylbersztejn and Mott(1975)] A. Zylbersztejn and N. F. Mott. *Metal-insulator transition in vanadium dioxide*. *Phys. Rev. B* **11** (1975)(11): 4383.